**Title**
Dielectric Elastomers for Fluidic and Biomedical Applications



**Author**
McCoul, David

**Publication Date**
2015

Peer reviewed|Thesis/dissertation

UNIVERSITY OF CALIFORNIA

Los Angeles

# Dielectric Elastomers for Fluidic and Biomedical Applications

A dissertation submitted in partial satisfaction of the

requirements for the degree Doctor of Philosophy

in Materials Science and Engineering

by

**David James McCoul**

2015

ABSTRACT OF THE DISSERTATION

# Dielectric Elastomers for Fluidic and Biomedical Applications

by

**David James McCoul**

Doctor of Philosophy in Materials Science and Engineering

University of California, Los Angeles, 2015

Professor Qibing Pei, Chair

Dielectric elastomers have demonstrated tremendous potential as high-strain electromechanical transducers for a myriad of novel applications across all engineering disciplines. Because their soft, viscoelastic mechanical properties are similar to those of living tissues, dielectric elastomers have garnered a strong foothold in a plethora of biomedical and biomimetic applications. Dielectric elastomers consist of a sheet of stretched rubber, or elastomer, coated on both sides with compliant electrode materials; application of a voltage generates an electrostatic pressure that deforms the elastomer. They can function as soft generators, sensors, or actuators, and this last function is the focus of this dissertation. Many design configurations are possible, such as stacks, minimum energy structures, interpenetrating polymer networks, shape memory dielectric

elastomers, and others; dielectric elastomers are already being applied to many fields of biomedicine.

The first part of the original research presented in this dissertation details a PDMS microfluidic system paired with a dielectric elastomer stack actuator of anisotropically prestrained VHB™ 4910 (3M™) and single-walled carbon nanotubes. These electroactive microfluidic devices demonstrated active increases in microchannel width when 3 and 4 kV were applied. Fluorescence microscopy also indicated an accompanying increase in channel depth with actuation. The cross-sectional area strains at 3 and 4 kV were approximately 2.9% and 7.4%, respectively. The device was then interfaced with a syringe pump, and the pressure was measured upstream. Linear pressure-flow plots were developed, which showed decreasing fluidic resistance with actuation, from 0.192 psi/($\mu$L/min) at 0 kV, to 0.160 and 0.157 psi/($\mu$L/min) at 3 and 4 kV, respectively. This corresponds to an ~18% drop in fluidic resistance at 4 kV. Active de-clogging was tested *in situ* with the device by introducing ~50 μm diameter PDMS microbeads and other smaller particulate debris into the system. After a channel blockage was confirmed, three actuation attempts successfully cleared the blockage. Further tests indicated that the device were biocompatible with HeLa cells at 3 kV. To our knowledge this is the first pairing of dielectric elastomers with microfluidics in a non-electroosmotic context. Applications may include adaptive microfilters, micro-peristaltic pumps, and reduced-complexity lab-on-a-chip devices.

Dielectric elastomers can also be adapted to manipulate fluidic systems on a larger scale. The second part of the dissertation research reports a novel low-profile, biomimetic dielectric elastomer tubular actuator capable of actively controlling hydraulic flow. The tubular actuator has been established as a reliable tunable valve, pinching a secondary silicone tube completely shut in the absence of a fluidic pressure bias or voltage, offering a high degree of resistance against fluidic flow, and able to open and completely remove this resistance to flow with an applied low power actuation voltage. The system demonstrates a rise in pressure of ~3.0 kPa when the dielectric elastomer valve is in the passive, unactuated state, and there is a quadratic fall in this pressure with increasing actuation voltage, until ~0 kPa is reached at 2.4 kV. The device is reliable for at least 2,000 actuation cycles for voltages at or below 2.2 kV. Furthermore, modeling of the actuator and fluidic system yields results consistent with the observed experimental dependence of intrasystem pressure on input flow rate, actuator prestretch, and actuation voltage. To our knowledge, this is the first actuator of its type that can control fluid flow by directly actuating the walls of a tube. Potential applications may include an implantable artificial sphincter, part of a peristaltic pump, or a computerized valve for fluidic or pneumatic control.

The final part of the dissertation presents a novel dielectric elastomer band with integrated rigid elements for the treatment of chronic acid reflux disorders. This dielectric elastomer ring actuator consists of a two-layer stack of prestretched VHB™ 4905 with SWCNT electrodes. Its transverse prestretch was maintained by

selective rigidification of the VHB™ using a UV-curable, solution-processable polymer network. The actuator exhibited a maximum vertical (circumferential) actuation strain of 25% at 3.4 kV in an 24.5 g weighted isotonic setup. It also exhibited the required passive force of 0.25 N and showed a maximum force drop of 0.11 N at 3.32 kV during isometric tests at 4.5 cm. Modeling was performed to determine the prestretches necessary to achieve maximum strain while simultaneously exerting the force of 0.25 N, which corresponds to a required pinching pressure of 3.35 kPa. Modeling also determined the spacing between and number of rigid elements required. The theoretical model curves were adjusted to account for the passive rigid elements, as well as for the addition of margins; the resulting plots agrees well with experiment. The performance of the DE band is comparable to that of living muscle, and this is the first application of dielectric elastomer actuators in the design of a medical implant for the treatment of gastrointestinal disorders. Related applications that could result from this technology are very low-profile linear peristaltic pumps, artificial intestines, an artificial urethra, and artificial blood vessels.

The dissertation of David James McCoul is approved.

Yong Chen

Warren Grundfest

Suneel Kodambaka

Qibing Pei, Committee Chair

University of California, Los Angeles

2015

Dedicated to my family for their unremitting support and encouragement throughout my journey at UCLA.

# TABLE OF CONTENTS

# LIST OF FIGURES

# LIST OF TABLES

# ACKNOWLEDGMENTS

I am deeply grateful to all whom I acknowledge in this section. Without them, the research presented in this dissertation would not have been possible.

Above all, I would like to thank my advisor, Professor Qibing Pei, for his guidance and support throughout my time at UCLA. His unfaltering attention to the quality of my research and unremitting encouragement have made me a better scientist and engineer. His mentorship helped to equip me with qualities essential to a successful career.

I would also like to thank my committee members: Professor Yong Chen, Professor Warren Grundfest, and Professor Suneel Kodambaka. I greatly appreciate their support in serving on my committee, and their insights were invaluable to further improve the quality of my research efforts.

I would like to thank Professor Dino Di Carlo and his group members Coleman Murray, Dr. Elodie Sollier, and Taylor Ruggiero from the Bioengineering Department, as well as Dr. Mohsen Khoshnevisan, in collaborating to perform the research in Chapter 2. Their contribution of resources as well as of intellect was unmatched in enhancing the quality of the microfluidic project.

I am grateful to Weili Hu, Mengmeng (Katrina) Gao, and Vishrut Mehta for their assistance in compiling the review article on compliant conductors listed in the Vita, and portions of which appear in Chapter 1 and the Appendix.

I would like to thank Dr. Jianwen Zhao and Junshi Zhang for requesting that I assist in the preparation of several of their publication manuscripts as a co-author.

I would also like to thank Junshi Zhang for helping to review portions of the modeling work presented in Chapter 3 and Chapter 4.

I would like to thank my present and former colleagues in the Soft Materials Research Laboratory, especially Dr. Paul Brochu and Dr. Xiaofan Niu for their close mentorship in my first couple years in the group. They helped to teach me the dedication and attention to detail necessary to succeed in materials research and device fabrication. I am thankful to Wei (Maggie) Hu and Zhi Ren, as well as to Tibor (Jake) Hajagos and David Kishpaugh, for their close help and support throughout the years. I thank Dr. Jiajie Liang and Kwing Tong for assisting with the UV polymerization in Chapter 4. I would like to thank Dr. Hristiyan Stoyanov, Dr. Wei Yuan, Dr. Sung Ryul Yun, Dr. Jiang Liu, and Dr. Chaokun Gong for their assistance. I would also like to thank the undergraduates Haroula Kyriacou, Joseph Shire, and Nicole Voyen for helping me to reach my research goals.

I would like to give a special thank you to SPIE and my friends and colleagues from around the world who attend the yearly SPIE Smart Structures conferences, such as the research groups of Professors Herbert Shea, Ian Anderson, Federico Carpi, Siegfried Bauer, and many others. They helped to provide me with a strong sense of community in the dielectric elastomer field, and their research presentations inspired and motivated me.

I would also like to thank my family and friends for their immense support and encouragement while earning my Ph.D. They were by my side through my

successes and my failures, and they taught me arguably one of the most important attributes of success: tenacity.

Finally, I am grateful to the Defense Advanced Research Projects Agency (Contract # N66001-10-1-4072), the United States National Science Foundation (Award # 1207975), the United States Air Force Office of Scientific Research (FA9550-12-1-0074, Dr. Charles Lee), the National Science Foundation (Awards # ECCS-1028412 and IIP-1414415), the U.S. National Robotic Initiative (NSF Award # IIS 1207975), the General Motor Corporation, and the University of California Discovery Program for financial support.

# VITA

2008 B.S., Biomedical Engineering, Northwestern University, Evanston, IL

2012 M.S., Materials Science and Engineering, UCLA, Los Angeles, CA

2009 Mechanical Engineering Intern, Rehabilitation Institute of Chicago, IL

2007 Clinical Research Assistant, National Institutes of Health, NINDS, MNB, LSS, Bethesda, MD

2011–15 Teaching Fellow, Department of Materials Science and Engineering, UCLA, Los Angeles, CA

2014–15 Teaching Fellow, Department of Mechanical and Aerospace Engineering, UCLA, Los Angeles, CA

2010–15 Graduate Student Researcher, Department of Materials Science and Engineering, UCLA, Los Angeles, CA

# PUBLICATIONS AND PRESENTATIONS

Murray, C.* and McCoul, D.*, Sollier, E., Ruggiero, T., Niu, X., Pei, Q., and Di Carlo, D. "Electro-adaptive microfluidics for active tuning of channel geometry using polymer actuators". *Microfluidics and Nanofluidics*, **14**(1-2), pp. 345-358 (2013). DOI: 10.1007/s10404-012-1055-y

**Equal Contribution*

McCoul, D., Murray, C., Di Carlo, D., and Pei, Q. "Dielectric elastomer actuators for active microfluidic control." *Proc. SPIE*, **8687**, p. 86872G (2013). DOI: 10.1117/12.2009576

McCoul, D. and Pei, Q. "Tubular dielectric elastomer actuator for active fluidic control." *Smart Materials and Structures*, submitted.

McCoul, D., Hu, W., Gao, M., Mehta, V., and Pei, Q. "Advances in Compliant Conductors for Dielectric Elastomers and Flexible Electronics." *Progress in Materials Science*, submitted.

McCoul, D. and Pei, Q. "Lower Esophageal Sphincter Dielectric Elastomer Ring Actuator for the Treatment of Gastroesophageal Reflux Disorder." In preparation.

Zhao, J., Niu, J., McCoul, D., Ren, Z., and Pei, Q. "Phenomena of nonlinear oscillation and special resonance of a dielectric elastomer minimum energy structure rotary joint." *Applied Physics Letters*, **106**, p. 133504 (2015). DOI: 10.1063/1.4915108

Zhang, J., Wang, Y., McCoul, D., Pei, Q., and Chen, H. "Viscoelastic creep elimination in dielectric elastomer actuation by preprogrammed voltage." *Applied Physics Letters*, **105**(21), pp. 212904-1-4 (2014). DOI: 10.1063/1.4903059

Zhao, J., Niu, J., McCoul, D., and Pei, Q. "A rotary joint for a flapping wing actuated by dielectric elastomer: design and experiment." In preparation.

Zhang, J., Chen, H., Li, B., McCoul, D., and Pei, Q. "Tunable active vibration attenuation by highly deformable dielectric elastomers." In preparation.

Zhang, J., Chen, H., Li, B., McCoul, D., and Pei, Q. "Coupled nonlinear oscillation and stability evolution of viscoelastic dielectric elastomers." In preparation.

# CHAPTER 1

# Introduction

## 1.1 Motivation

In the history of animal evolution, mass transport has been a life-essential emergent phenomenon. It is intriguing to realize that the survival of multicellular organisms— such as ourselves— relies heavily on the transport of other living cells. The heart pumps red blood cells through the body to oxygenate its other living cells. The intestines digest the cells of plants or other animals to extract essential nutrients. In both of these cases, moving living matter is involved. The transport of living cells is also critical in reproduction. The study of fluidics, then, holds key significance to our understanding of biology and the advancement of biomedical science.

One of the logical consequences of the study of living systems is to emulate them artificially. So doing can allow for a deeper understanding of the underlying physical principles governing the biological function under study. Put another way, the ability to design a system with the same structure and function as another system requires a deep understanding of the imitated system. One technological consequence of this process is the creation of artificial organs, which require very similar structure and function as living organs in order to replace them and integrate well with the body as implants. Additionally, mimicking living systems allows for *in vitro* biomedical studies in a controlled, noninvasive environment.

These principles are foundational to the field of biomimetics, in which one can take advantage of biological refinement millions of years in the making to guide engineering design. Certainly, biomimetics is not limited to the design of artificial biological systems, but can inspire solutions to a myriad of other non-biological engineering problems. Still, biomedical design is the most obvious application of biomimetic techniques, and biomedical devices often require biologically-inspired designs over more traditional approaches. For example, artificial heart designs cannot rely on conventional motor-driven pumps, which are often too large and heavy to sit within the chest. In this vein, while electrical motors have served robotic systems well, they are not the best solution for the most realistic of prosthetic limbs, which would require higher energy-density actuation and many more degrees of freedom than traditional electromagnetic rotary motor systems can offer.

Attempting to solve biomedical engineering design problems such as these—where imitating biological structure is equally important as imitating function—has motivated the search for new actuators and actuator materials. Indeed, technological advancement in virtually every discipline is largely limited by the sophistication of the underlying materials; one beneficial outcome of the field of materials science has been the advancement of technology though new materials. Potentially one of the best alternative actuator material candidates for biomimetic design has been the dielectric elastomer, a type of electroactive polymer that converts electrical energy into mechanical work. Dielectric elastomer actuators have

been shown to have similar power density, efficiency, speed, force, and strain to living muscle, and so they are often referred to as "artificial muscle" (Figure 1.1). [1] The research presented herein focuses on biomimetic devices related to fluidics, some of which have biomedical applications, and all of which were designed and fabricated utilizing dielectric elastomer soft actuators.

| Actuator | Strain | Actuation Pressure | Density | Efficiency | Speed (fast AND slow) |
|---|---|---|---|---|---|
| Natural Muscle | ● | ● | ● | ● | ● |
| Electromagnetic | ● | ● | ○ | ● | ○ |
| Piezoelectric | ○ | ● | ◐ | ● | ● |
| Shape Memory Alloy | ◐ | ● | ◐ | ○ | ○ |
| Magnetostrictive | ○ | ● | ○ | ● | ○ |
| Electrostatic | ● | ○ | ● | ● | ● |
| Dielectric Elastomers | ● | ● | ● | ● | ● |

○ = Poor ◐ = Fair ● = Good

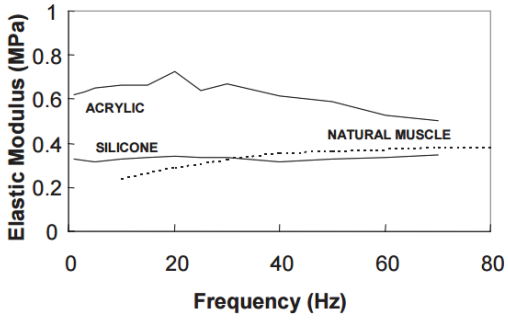


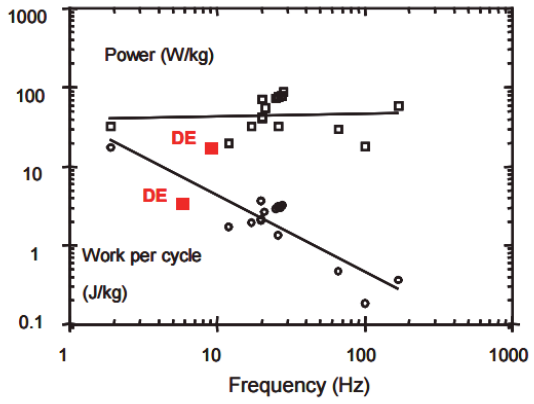


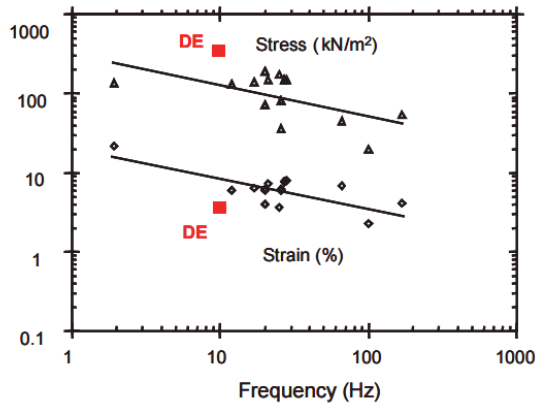


**Figure 1.1** Dielectric elastomer actuators as compared to living muscle, exhibiting comparable power, work, stress, strain, elastic modulus, efficiency, speed and force. [1]

## 1.2 Dielectric Elastomer Transducers

Dielectric elastomers (DEs) are essentially soft parallel plate capacitors. They consist of an insulating elastomer, typically of acrylic or silicone, sandwiched between flexible conductive electrodes. DEs function as electromechanical transducers, operating through several regimes. As energy harvesters, dielectric elastomer generators (DEGs) convert mechanical work into electrical energy. In this mode, energy can be generated either through a constant charge or a constant voltage process. Constant charge is the most commonly used, in which: (1) the DE is stretched; (2) a small seed voltage charges the DE surface, but is less than enough voltage to result in any significant actuation; (3) relaxation separates the charges to create a potential difference; and (4) the charge is removed. Figure 1.2 depicts this cycle, where the energy generated ($E_{gen}$) is related to the difference in the voltage generated from film relaxation in (3) and the input voltage to charge the film in (2). The input mechanical energy is represented by $E_{mech}$ from (1), and the ratio of $E_{gen}$ to $E_{mech}$ is the electromechanical coupling, or energy conversion efficiency. [2, 3]

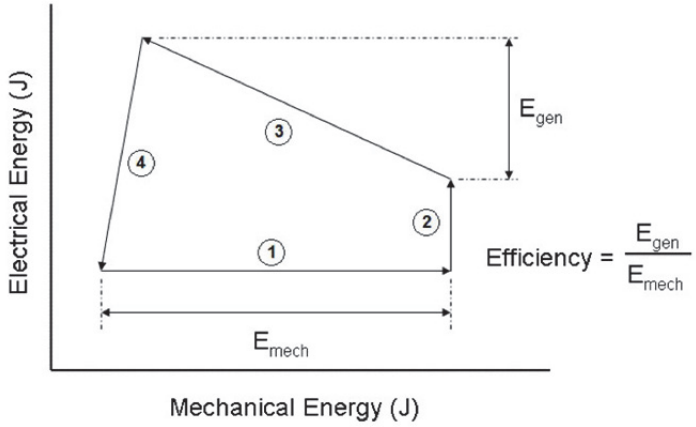


**Figure 1.2** The general constant-charge energy harvesting cycle, depicting the calculation of energy conversion efficiency. [2]

DEs can also function as sensors, where changes in capacitance can be monitored. Calibration of a DE sensor would involve finding the scaling relationship between these voltage or capacitance changes and the degree of input mechanical deformation. Self-sensing is also possible, in which sensing and actuation can occur simultaneously. [4] See Section 1.4.3.4 for more on the topic of DE sensors.

Finally, DEs can function as actuators when they convert electrical energy into mechanical work. Dielectric elastomer actuators (DEAs) form the focus of the research presented in this dissertation. DEAs are a type of electroactive polymer (EAP) known as electric field-activated EAPs. The other primary type of electroactive polymer in use today is the ionic EAP. [5] A good example of an ionic EAP is the ionic polymer-metal composite (IPMC), which bends in solution due to ion and solvent fluxes that reversibly swell the polymer membrane. Ionic EAPs operate at low voltages, but because they actuate due to ion and solvent fluxes, their response times are slow and they require encapsulation. On the other hand,

electronic EAPs (i.e., DEAs) require high voltages but are often preferable since they are still low-power, do not require fluidic encapsulation, output greater force and strain, and have faster response times, on the order of microseconds. [6] As with DEGs, DEAs can operate under either constant voltage or constant charge conditions, although constant voltage is the most commonly utilized for DEAs.

### 1.2.1 Columbic Electrostriction of Elastomers

The physical operation of a dielectric elastomer actuator is depicted in Figure 1.3. When an electric field is applied across the elastomer, charge accumulates on the electrodes, and electrostatic forces result in a deformation. [7] Specifically, electrostatic attraction between the overlapping electrodes creates a pressure that decreases the elastomer thickness and also expands the in-plane area due to material incompressibility. [8] This so-called Maxwell pressure (or stress) is given by the following equation:

$$\sigma_{\mathrm{M}} = \varepsilon_r \varepsilon_0 E^2 = \varepsilon_r \varepsilon_0 \left( \frac{V}{t} \right)^2 \tag{1.1}$$

where $\varepsilon_r$ is the dielectric constant (or relative permittivity), $\varepsilon_0$ is the permittivity of a vacuum (or of "free space"), and $E$ is the applied electric field, defined as the applied voltage $V$ divided by the distance of separation, or elastomer thickness, $t$. Response times are fast, typically on the order of microseconds. [6]

Values of $\varepsilon_r$ typically range from 2 to 12 for soft DE materials. [9-11] This is in stark contrast to conventional rigid dielectrics used for capacitors, such as the

ceramic barium titanate that has a dielectric constant of over 3,000. [12] Section 1.3.2 describes the incorporation of high dielectric constant powders, such as those of barium titanate, into the DE matrix. In addition, like all dielectrics, DE materials have an electrical breakdown strength $E_{BD}$, an electric field above which the material will begin to conduct electricity, but which often results in catastrophic failure because of the resistance of the DE material. Stable actuation is possible only below $E_{BD}$.

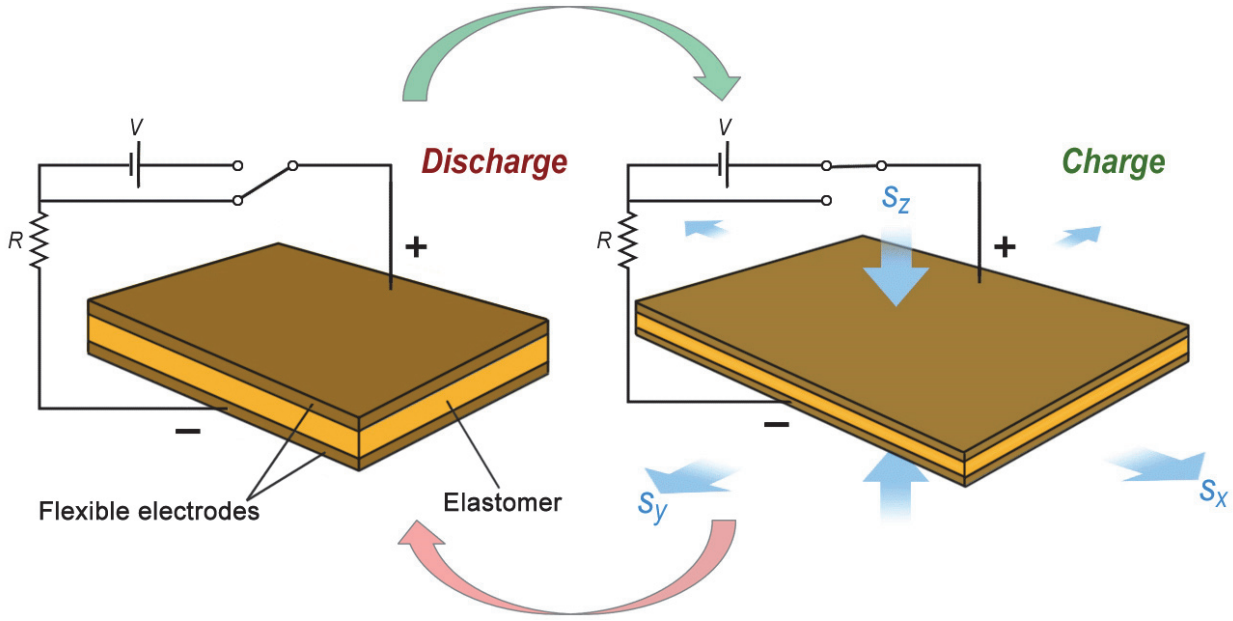


**Figure 1.3** Physical operation of the dielectric elastomer actuator, shown with a standard capacitor charge/discharge circuit. Application of a voltage charges the flexible electrodes, causing a compressive strain $s_z$ in the thickness direction and a positive area strain $s_x s_y$. Short-circuiting, the electrodes discharge, causing full relaxation. As a footnote, the illustration shows a section of a DEA; the entire DEA requires a passive margin at the edges where no electrodes are patterned in order to avoid short-circuiting during charging.

Let us assume a Hookean approximation of the Maxwell stress $\sigma_{\mathrm{M}}$ and strain in the thickness direction $s_z$, as

$$\sigma_{\mathrm{M}} = Y s_z \tag{1.2}$$

where $Y$ is the Young's (or elastic) modulus. Strain $s$ is defined as the percent change in length:

$$s(\%) = \frac{\Delta l}{l_0} = \frac{l_f - l_0}{l_0} \times 100 \tag{1.3}$$

in which $l_f$ is the final length, and $l_0$ is the initial length. Combining Equations 1.1 and 1.2, we can write the strain in the thickness direction as

$$s_z = \frac{\varepsilon_r \varepsilon_0}{Y} \left( \frac{V}{t} \right)^2 \tag{1.4}$$

ignoring that $s_z$ is negative from compression. From (1.4), we can see that the achievable strain in a DE is directly proportional to the dielectric constant and the square of the applied voltage, and inversely proportional to the elastic modulus and the square of the DE thickness. In order to achieve maximum actuation strain at the same applied voltage— or equivalently, to achieve the same actuation strain at lower applied voltages— the dielectric constant of the DE can be raised, the Young's modulus of the DE can be decreased, and/or the thickness of the DE can be decreased.

We can re-write (1.4) in terms of the area strain by noting some definitions. Firstly, stretch $\lambda$ is defined as the final length $l_f$ divided by the initial length $l_0$:

$$\lambda = \frac{l_f}{l_0} \tag{1.5}$$

The strain as a decimal equals the stretch $\lambda$ minus unity:

$$s = \lambda - 1 = \frac{l_f}{l_0} - 1 = \frac{l_f - l_0}{l_0} \tag{1.6}$$

For example, let us stretch a rubber band with initial length 1 in to a final length of 5 in. You would have stretched the band by 5 times, or strained it by 4 (or 400%). Next, we can assume that the elastomer is incompressible, meaning that its volume remains constant during electrostriction or other loading:

$$V_0 = V_f \tag{1.7}$$

or

$$l_0 w_0 t_0 = l_f w_f t_f \tag{1.8}$$

where $l$, $w$, and $t$ are the length, width, and thickness, respectively. Dividing by the right hand side, and noting the definition of stretch from (1.6), we write

$$\lambda_x \lambda_y \lambda_z = 1 \tag{1.9}$$

or

$$(s_x + 1)(s_y + 1)(s_z + 1) = 1 \tag{1.10}$$

Rearranging, we have

$$(s_x + 1)(s_y + 1) = (s_z + 1)^{-1} \tag{1.11}$$

If we assume that $s_x = s_y = s$, then (1.11) becomes

$$s = (s_z + 1)^{-1/2} - 1 \tag{1.12}$$

and the area strain $s_A$ is

$$s_A = s^2 = \left[\left(s_z + 1\right)^{-1/2} - 1\right]^2 \tag{1.13}$$

Therefore, substituting (1.4) into (1.13), we have

$$s_A = \left\{\left[\frac{\varepsilon_r \varepsilon_0}{Y}\left(\frac{V}{t}\right)^2 + 1\right]^{-1/2} - 1\right\}^2 \tag{1.14}$$

We can also rewrite Equation 1.4 in terms of force output in the thickness direction $F_z$. Since

$$\sigma_M = \frac{F_z}{lw} \tag{1.15}$$

where $l$ and $w$ are the length and width of the overlapping electrode area of the DE, we have that

$$F_z = \varepsilon_r \varepsilon_0 \left(\frac{V}{t}\right)^2 lw \tag{1.16}$$

In this case, a similar logic as before applies. To output a greater force at the same voltage— or to achieve the same force output at a lower voltage— the active area $lw$ can be increased, the dielectric constant can be increased, or the thickness can be decreased.

### 1.2.2 Prestrain and Electromechanical Instability

Prestrain, or stretching a DEA film prior to actuation, enhances performance by overcoming electromechanical instability, lowering operating voltages, and increasing actuation speed, force, and strain. [7, 13, 14] Electromechanical instability (EMI) occurs typically in voltage-controlled actuation, wherein above a

certain electric field an exponential thinning of the DEA can occur until catastrophic failure. This occurs when the Maxwell Pressure generated by the applied field intersects the stress strain curve of the elastomer, as shown in Figure 1.4. At this point, the applied electrostatic stress exceeds the internal restoring stress in the elastomer, and this runaway effect occurs. However, prestraining prior to actuation effectively stiffens the elastomer to the point where the internal stress always exceeds the stress from the applied field, and EMI can be avoided. [5] This enables the creation of fast, high-strain soft devices that are made from DEAs.

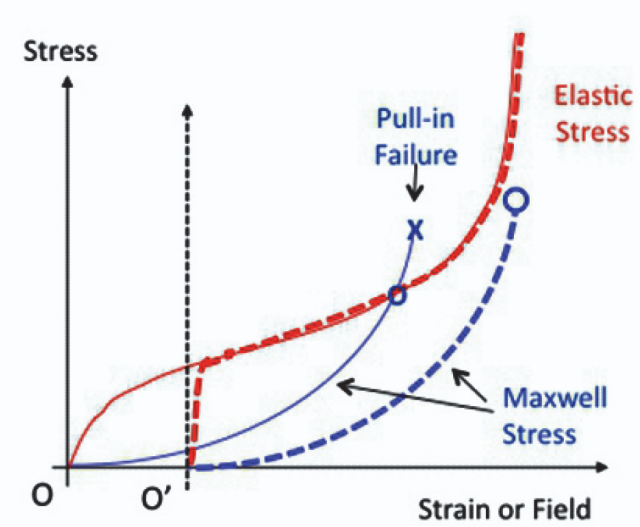


**Figure 1.4** Passive DE stress-strain curve overlaid with active Maxwell stress curve. EMI occurs above the intersection of the passive stress-strain curve with the Maxwell stress curve, at which point the restoring stress in the DE is less than the electrostatic Maxwell stress. Prestretching to *O′* increases the stress in the DE to be always greater than the applied Maxwell stress, thus avoiding EMI. [5]

Typically, isotropic biaxial prestrains (BAPS) are applied, in which a DEA is stretched equally in both in-plane directions. Anisotropic, or unequal, prestrains might also be chosen in order to bias actuation along a preferred direction. [7] In this scenario, the direction with the higher prestrain is stiffer and will deform less than the direction with less prestrain, which is effectively softer. Noteworthy is that a 500% × 100% prestrain will exhibit larger strains in one direction than a 500% BAPS will exhibit in any direction. Thus, anisotropic prestraining is superior when high-strain, unidirectional actuation is desired. As shown in the next section, modeling confirms that prestretching higher in the transverse direction results in stable, high actuation strains in the orthogonal direction.

After prestraining, the new thickness $t_f$ of the DE can be determined by using a variant of Equations 1.8 and 1.9:

$$t_f = \frac{t_0}{\lambda_x \lambda_y} = \frac{t_0}{\left(s_x + 1\right)\left(s_y + 1\right)} \tag{1.17}$$

wherein the initial thickness $t_0$ is divided by the area stretch $\lambda_x \lambda_y$. For example, VHB™ 4905 has an initial thickness of 0.5 mm, or 500 microns. Given a BAPS of 400% × 400%, or an area stretch of $\lambda_x \lambda_y = \left(5\right)\left(5\right) = 25,$ the final thickness is $t_f = \left(500\ \mu\text{m}\right)/25 = 20\ \mu\text{m}$. Prestraining VHB™ 4910 by 500% × 100% results in a film thickness of $t_f = \left(1{,}000\ \mu\text{m}\right)/\left(6 \cdot 2\right) \approx 83.3\ \mu\text{m}$ before actuation. Similarly, we can rewrite Equation 1.1 in terms of the area stretches as

$$\sigma_{\mathrm{M}} = \varepsilon_r \varepsilon_0 \left( \frac{V}{t_0} \right)^2 \lambda_x{}^2 \lambda_y{}^2 \tag{1.18}$$

in which $t_0$ is the original thickness, before prestretching by $\lambda_x \lambda_y$. The terms "prestrain" and "prestretch" are often used interchangeably when discussing DEs.

#### 1.2.2.1 Modeling

As mentioned above, prestretching higher in the transverse direction results in stable, high actuation strains in the perpendicular direction, especially under isotonic (constant force) conditions. As shown in Figure 1.5(a), a DEA is grounded on one end, and a freely-hanging weight is affixed to the other end. In this case, there is no prestretch in the transverse direction. The resulting stretch voltage curves exhibit a so-called "snap through" instability, wherein small changes in actuation voltage lead to large jumps in actuation stretch. [15, 16] In the plot in (a), snap through results in almost immediate failure as the vertical stretch curves intersect the red dielectric breakdown curve very soon. The result is low vertical strain in the case where the transverse stretch is not constrained. On the other hand, Figure 1.5(b) shows an actuator with transverse fibers reinforcing prestretch in that direction. The resulting actuation plot shows stable actuation with no snap through, and high vertical strains are possible. Further discussion about this latter actuation modality will follow in the modeling section of Chapter 4.

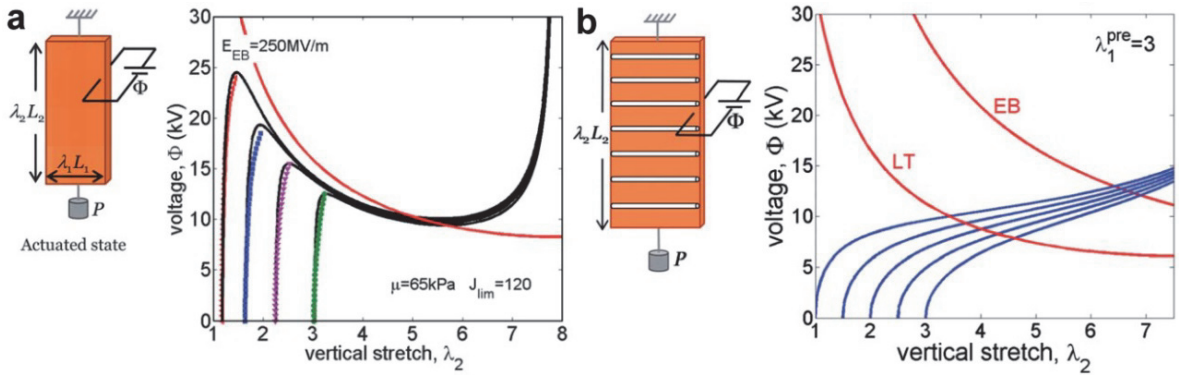


**Figure 1.5** **(a)** Isotonic setup of a DEA with no horizontal prestretch, resulting in snap through instability and low actuation stretch. **(b)** Isotonic setup of a DEA with a transverse prestretch of 3 maintained by fibers, resulting in high vertical stretch, instability-free actuation. [15]

#### 1.2.2.2 Electrode-Free, Charge-Controlled DEAs

As one can ascertain from the following sections, material choice is quintessential in determining the electromechanical properties of DEs. In most cases, the electrode material is the charge carrier on the surface of an elastomer. Perhaps the purest category of DE electrodes is one that eliminates using electrode materials altogether, spraying charges directly onto both sides of an elastomer thin film to cause a deformation. This peculiar class of electrode-free DEAs was first explored by Röntgen in 1880. Röntgen was the first known researcher to study the electrostrictive properties of rubbers. While this makes him the pioneer of dielectric elastomer actuators, he did not focus on the utility of this phenomenon, and applications of dielectric elastomers would lay unrealized until roughly a century later. [17]

Recently, Keplinger and Bauer et al. attempted to replicate the setup used by Röntgen for further study of elastomeric electrostriction. They actuated freestanding and minimum energy DEs (see Section 1.5.3, below) of prestrained VHB™ by charging the elastomer surface using two opposing corona needles, depicted in Figure 1.6. Unusually high voltages of up to 25 kV could be applied, in part because pull-in electromechanical instability can be avoided. In typical voltage-controlled electrodes, increasing voltage leads to an increase in electric field and an accompanying increase in Maxwell pressure in the elastomer. Beyond the restoring stress in the elastomer, the increase in field creates a positive feedback loop that proceeds to thin out the elastomer to failure. However, in a charge-controlled setup of spraying charges, the electric field cannot increase by a positive feedback mechanism since charge-controlled electrostatic stress decreases with stretch, and EMI is avoided.

Additionally, electrode degradation or plastic deformation is avoided since no electrode material is needed to conduct the charges. Optical transparency is also not of concern since it would be limited only by the clarity of the elastomer, not by any electrode material. The only theoretical limitation to actuation strain for this class of devices is the breakdown field of the dielectric elastomer. However, spraying charges onto such devices in situ could pose a variety of practical problems, such as difficulty in confining charges to the device and using obtrusive needles, which is why charge-controlled actuation is not commonly used in DEA devices. Still, the experiment is useful at least in a laboratory setting in understanding the function

of dielectric elastomer actuation, as well as the fundamental function of physical electrodes of any material with respect to voltage-controlled versus charge-controlled phenomena. [18, 19]

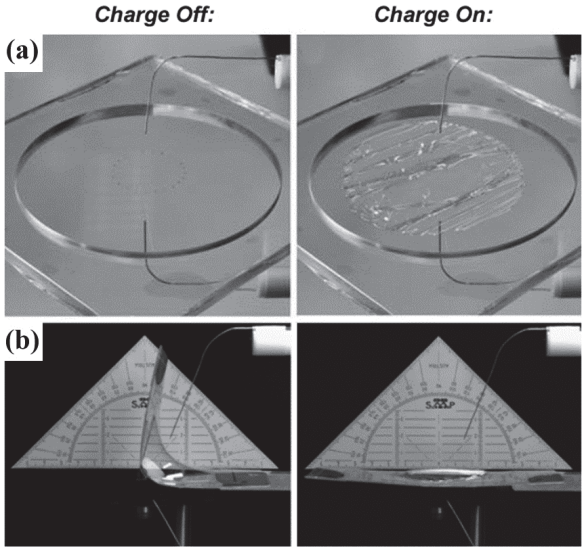


**Figure 1.6** Spraying charges onto electrode-free dielectric elastomers using corona needles. Charge off and on for **(a)** a planar dielectric elastomer film and **(b)** a minimum energy structure. [19]

## 1.3 Dielectric Elastomer Materials

### 1.3.1 Conventional DE Materials

Conventional dielectric elastomer materials fall broadly into the categories of acrylics, silicones, or polyurethanes, as shown in Figure 1.7. The most common acrylic dielectric elastomer material is VHB™ ("very high bonding") manufactured by 3M™. As the name suggests, VHB™ was originally formulated to serve as an industrial-grade double-sided adhesive tape that is just as strong as a weld between two metal surfaces. VHB™ is sticky, soft, and viscoelastic, allowing rough surfaces to easily join with the proper pressure and/or time. As a DE material, VHB™ is capable of exhibiting the highest possible actuation strains once prestrained, and several prestrain suggestions are given in the table in Figure 1.7 for VHB™ and several types of silicones. Silicones are becoming more popular as a DE material because they exhibit little to no viscoelastic behavior, but their application is generally limited to those which require slightly lower strains. Certain modifications can be made to these base materials to change their electrical and/or mechanical properties, as will be discussed in detail in the next section.

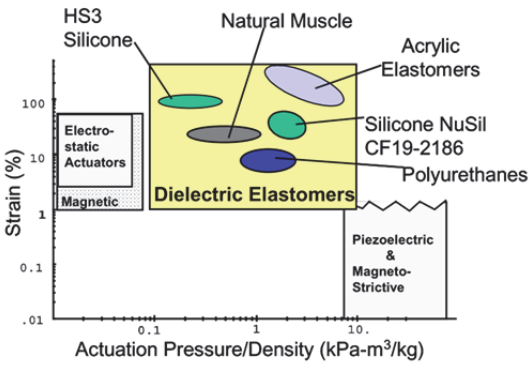


| Material | Prestrain (x,y) (%) | Actuated relative thickness strain (%) | Actuated relative area strain (%) | Field strength (MV/m) | Effective compressive stress (MPa) | Estimated ½e (MJ/m³) |
|---|---|---|---|---|---|---|
| | | | *Circular strain* | | | |
| HS3 silicone | (68,68) | 48 | 93 | 110 | 0.3 | 0.098 |
| | (14,14) | 41 | 69 | 72 | 0.13 | 0.034 |
| CF19-2186 silicone | (45,45) | 39 | 64 | 350 | 3.0 | 0.75 |
| | (15,15) | 25 | 33 | 160 | 0.6 | 0.091 |
| VHB 4910 acrylic | (300,300) | 61 | 158 | 412 | 7.2 | 3.4 |
| | (15,15) | 29 | 40 | 55 | 0.13 | 0.022 |
| | | | *Linear strain* | | | |
| HS3 | (280,0) | 54 | 117 | 128 | 0.4 | 0.16 |
| CF19-2186 | (100,0) | 39 | 63 | 181 | 0.8 | 0.2 |
| VHB 4910 | (540,75) | 68 | 215 | 239 | 2.4 | 1.36 |

**Figure 1.7** Dielectric elastomer materials fall into a similar category as natural muscle in terms of the specific mechanical work output. [1] The table lists several commonly used silicone and acrylic DEs, recommended prestrains, and associated properties. [7]

### 1.3.2 High Dielectric Constant Elastomers

One of the practical challenges facing DEAs are their high required driving voltages, often in the thousands of volts. Although this has been of concern for use in implantable medical devices, their low-current ($\mu$A), low-power operation likely does not pose a safety concern. Nonetheless, lower required voltages can cut back on the bulk of required DC power converters, as well as make interfacing with logic circuits more feasible. As mentioned in Section 1.2.1, one method to lower the driving voltages needed for DEAs is to increase the dielectric constant. This has been accomplished through a variety of approaches. The most common method has been to "dope" the DE with high-dielectric constant fillers, such as Titanium-based nanoparticles, functionalized graphene sheets, and encapsulated polyaniline. [20-23] Let us discuss first the use of Titanium-based nanoparticles.

Gallone and colleagues enhance the dielectric constant of a silicone elastomer filled up to 30% by volume with lead magnesium niobate-lead titanate (PMN-PT, $Pb(Mg_{1/3}NB_{2/3})O_3$-$PbTiO_3$), a ferroelectric ceramic powder. [20] PMN-PT is thought to be a promising compound due to its astonishingly high dielectric constant of 28,000 at 1 kHz. They reported both an increase in the storage $\varepsilon'$ and loss $\varepsilon''$ dielectric constants ($\varepsilon = \varepsilon' + i\varepsilon''$) with increasing filler content, as shown in Figure 1.8. Here, a four-fold increase in the dielectric constant $\varepsilon'$ was observed at 10 Hz and 30% filler content by volume. It will be useful to define the (complex) dielectric loss tangent, given by

$$\tan\delta = \frac{\varepsilon''}{\varepsilon'}. \tag{1.19}$$

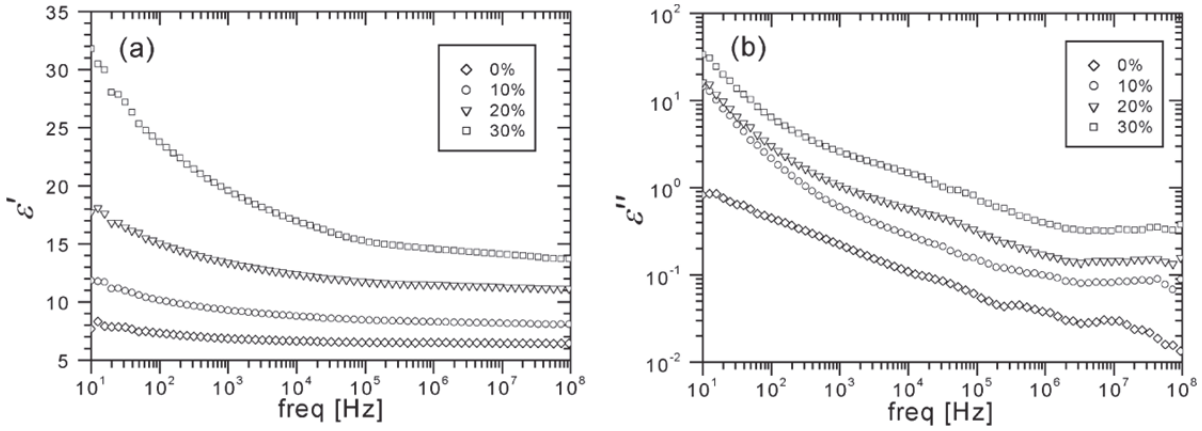


**Figure 1.8** **(a)** Dielectric constant and **(b)** dielectric loss show an increase for the Silicone-PMN-PT composite with increasing content by volume. [20]

Because adding a hard filler effectively stiffens the material, they also observed a simultaneous increase in Young's Modulus with increasing filler content, as depicted in Figure 1.9. As mentioned before, this is the downside of using the

filler approach, since increasing the Young's Modulus has a counteracting effect to raising the dielectric constant for a given strain, by Equation 3. Fortunately, this increase is not as pronounced as the increase in dielectric constant.

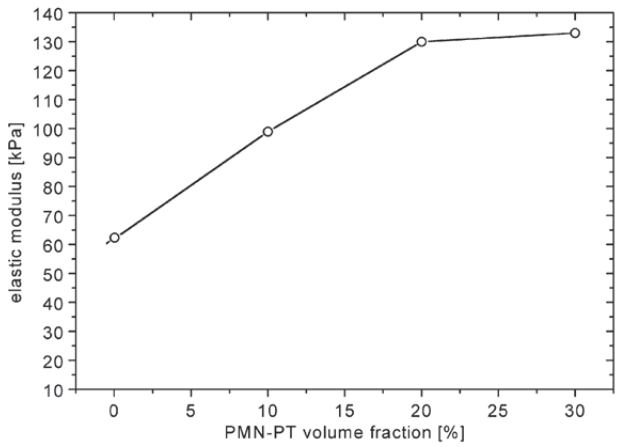


**Figure 1.9** Increasing Young's Modulus for the Silicone-PMN-PT composite with increasing filler content. [20]

Similar results were obtained when Stoyanov et al. used block copolymer elastomers filled with surface-treated nanoparticles. [21] They utilized poly-Styrene-*co*-Ethylene-*co*-Butylene-*co*-Styrene (SEBS) as the matrix elastomer to silicone (PDMS) oil-coated $TiO_2$ nanoparticles. They chose a tri-block copolymer to prevent networking effects upon addition of the $TiO_2$ filler. As shown in Figure 1.10, dielectric constant increases for coated nanoparticles (closed symbols), while uncoated nanoparticles show only significant changes in dielectric constant at 25% $TiO_2$ by volume.

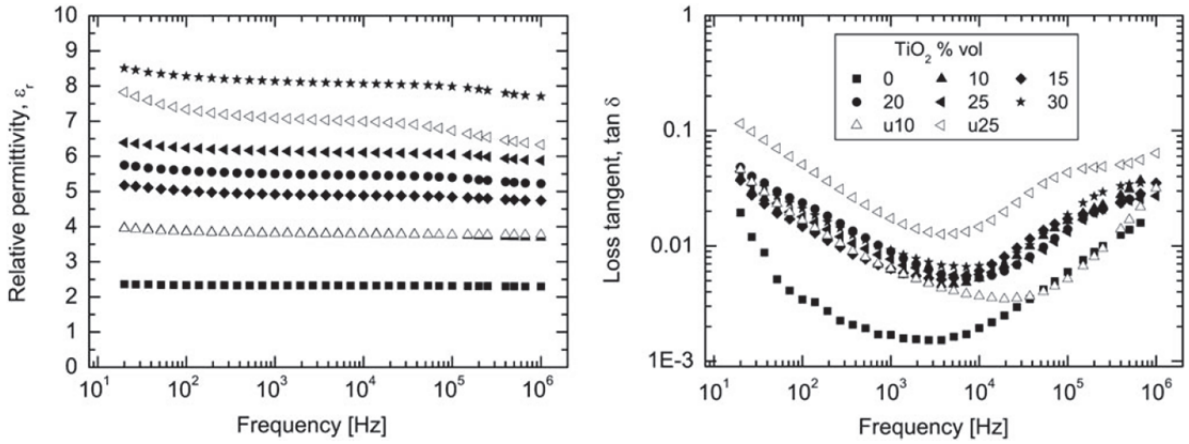


**Figure 1.10** *Left:* Increasing dielectric constant with filler content for SEBS-PDMS-coated $TiO_2$ composite. Open symbols represent samples with uncoated $TiO_2$ nanoparticles. *Right:* Loss tangent ($\varepsilon''/\varepsilon'$) is nearly identical for all treated nanoparticle samples, except for untreated nanoparticle samples above the percolation threshold of ~15 vol. %. [21]

An interesting feature of the dielectric constant here is its relatively flat frequency response, which implies minimized surface (Maxwell-Wagner) polarization effects due to the $TiO_2$ surface treatment. This treatment (PDMS oil coating) is thought to lead to reduced charge accumulation at the polymer/filler interface that leads to these surface polarization effects. Reduction of these surface polarization effects also results in a smaller loss tangent (dielectric loss $\varepsilon'$), explained as follows. In the case of untreated particles (open symbols), a so-called Chapman-Stern interfacial layer is created between nanoparticle and polymer matrix. Above a certain percolation threshold of roughly 15%, charge begins to accumulate at the interface, resulting in a higher dielectric constant, but also an inevitably greater loss tangent (shown in Figure 1.10, right). All treated nanoparticles have higher dielectric losses than the neat polymer, but they all

appear independent of the nanoparticle concentration, and they avoid losses above the percolation threshold.

Figure 1.11(a) shows the chemical structure of the SEBS matrix and the PDMS-oil-coated $TiO_2$ nanoparticles, as well as the homogenous dispersion of nanoparticles to matrix as a result of the increased nanoparticle miscibility in the matrix from the methyl groups of the PDMS oil. Figure 1.11(b) shows the stress-strain results of mechanical testing of the PDMS-treated $TiO_2$ nanoparticle/SEBS composite from 0 to 30% nanoparticle by volume. As expected, Young's Modulus (below 5% strain) increases with filler content, as plotted in the inset. Nevertheless, the PDMS oil coating does serve to mechanically lubricate the polymer/nanoparticle interfaces, increasing slip and effectively lowering the Young's Modulus. For example, for 10% by volume, untreated samples had a Young's Modulus of 790 kPa, more than twice that for treated samples at 340 kPa.

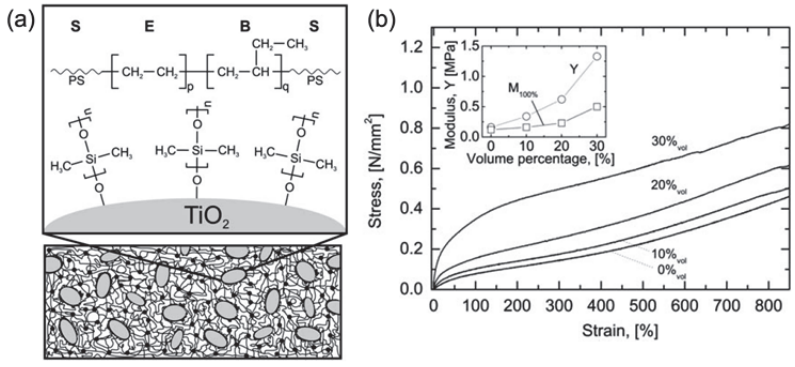


**Figure 1.11** **(a)** SEBS matrix/PDMS-treated $TiO_2$ nanoparticle interface and homogenous phase distribution. Black dots represent PS phase clusters, and the gray ovals are the treated nanoparticles. **(b)** Mechanical testing of the composite, showing an increase in Young's Modulus with increasing doping concentration. [21]

Romasanta and co-workers report PDMS elastomer with increased dielectric constant by using functionalized graphene sheets (FGSs) and carbon nanotubes. [22] As before, Maxwell-Wagner (or Maxwell-Wagner-Sillars) surface percolation effects from such elastomer/dopant composites result in uneven dielectric constant frequency responses and higher loss tangents. This was the motivation to produce functionalized graphene from the thermal decomposition of graphite oxide. Carbon nanotubes (CNTs) were also used for comparison. Figure 1.12(a) shows the effect of the CNT filler on dielectric constant and loss tangent, and (b) shows the same for the FGSs.

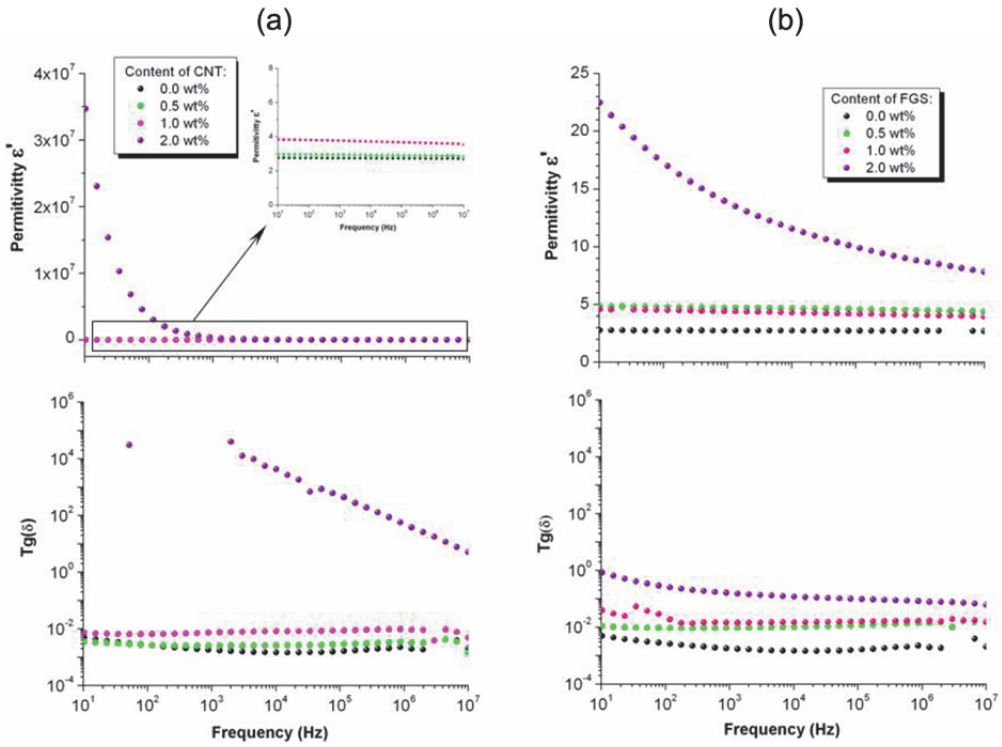


**Figure 1.12** **(a)** CNT and **(b)** FGS effects on PDMS dielectric constant and loss tangent. [22]

At 1.0 wt.% CNT, the dielectric constant of the PDMS-CNT composite increases by 1.5 times compared to neat PDMS, and the loss tangents are comparable. However, at 2.0 wt.%, there is an abrupt frequency-dependent rise in dielectric constant and a significant loss tangent. This rise in loss tangent and frequency dependence of dielectric constant indicate the presence of interfacial polarization phenomenon from surface percolation at a critical CNT wt.% somewhere between 1.5 and 2.0 wt.%. In addition, the enormous rise in low-frequency dielectric constant implies that the CNT clusters have now formed electrically continuous pathways, and the PDMS-CNT composite is now conductive. This scenario is not desired for DE applications since the dielectric must remain insulating; otherwise, premature dielectric breakdown at only modest actuation strains will result.

By contrast, the FGSs show more promise. At 1.0 wt.% FGS, the dielectric constant doubles to ~5, and there is no significant rise in the loss tangent. Even at 2.0 wt.% FGS, although there is once again a sharp, frequency-dependent rise in the dielectric constant, this rise is not as high (only 23 vs. $3.5 \times 10^7$ at 10 Hz), implying surface effects but not as high of conductivities. Nevertheless, even the FGS approach is inferior to the previous  (by Stoyanov et al.) since the low-loss, frequency-independent increases in dielectric constant are not as high. And, the significant dielectric constant increases that occur between 1.5 and 2.0 wt.% FGS have a high dependence on frequency, making the case non-ideal for all dielectric applications. This said, at 2.0 wt.% FGS, the dielectric losses are low, and the

minimum increase in dielectric constant (to ~10 at $10^7$ Hz) is about the same as the maximum increase in dielectric constant shown by Stoyanov et al. with their functionalized $TiO_2$ nanoparticles. [21]

Molberg and colleagues successfully created high dielectric constant PDMS filled with encapsulated polyaniline (PANI). [23] As shown in Figure 1.13, this approach eliminates any PANI conducting paths that may agglomerate by encapsulating the PANI particles in insulating shells of poly(divinyl benzene) (PDVB).

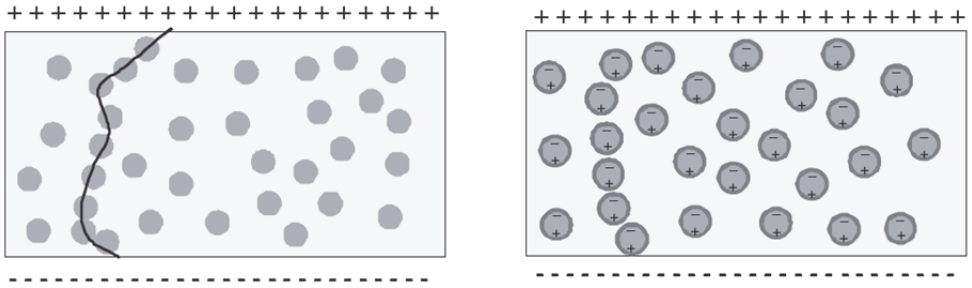

**Figure 1.13** PDVB-encapsulated PANI particles in a PDMS host matrix. Shown left, a conducting path can form along contiguous PANI particles, but encapsulation (right) addresses this issue. [23]

Mechanical testing reveals a 20-fold increase in the Young's Modulus at 31.7 vol.% of PANI filler, which is comparable to the results of Stoyanov and company. As seen in Figure 1.14, all percentages of filler exhibit comparable loss tangents greater than neat PDMS, and increasing the filler content increases the dielectric constant. However, these results are inferior to those of Stoyanov since the maximum dielectric constant is only ~7.5 at 100 Hz (vs. 8.25 at 100 Hz), and the

dielectric constant curves are more dependent on frequency, implying surface charge effects.

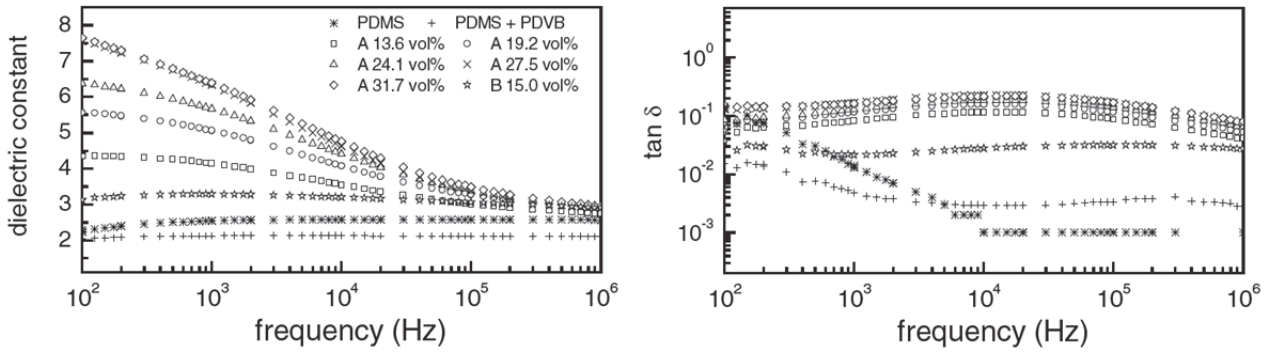


**Figure 1.14** Dielectric performance of PDVB-PANI/PDMS. Frequency dependence of the dielectric constant and high loss tangents compared to neat PDMS imply undesirable surface charge effects. [23]

An alternative approach currently being researched is to graft conducting polymers or organic dipoles to the molecular chain of the elastomer. [24, 25] In a variation of the PANI composite above, doped conductive PANI is grafted to a matrix of poly-styrene-*co*-ethylene-*co*-butylene-*co*-styrene-*g*-maleic anhydride (SEBS-*g*-MA) to form a molecular composite elastomer, the chemical structure of which is illustrated in Figure 1.15 and was verified via FTIR. [24]

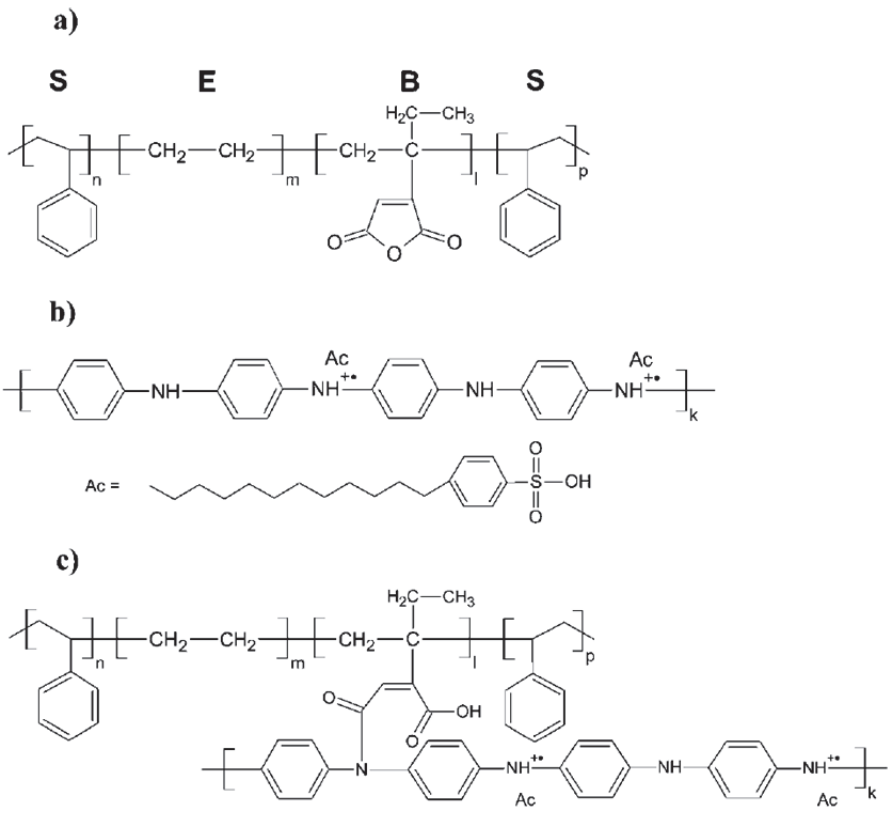


**Figure 1.15** **(a)** SEBS-*g*-MA, **(b)** emeraldine salt form of DBSA-doped PANI, and **(c)** a molecular composite of PANI-grafted SEBS-*g*-MA. [24]

The dielectric performance in Figure 1.16 identifies two critical regions: I and II. In Region I, at or below 2.0 vol.% PANI, PANI chains are sufficiently insulated by the SEBS-*g*-MA elastomer matrix, giving comparable dielectric losses. However, above 2.0 vol.% PANI, the conductive *p*-doped PANI chains are no longer fully-insulated by the matrix, and charge hopping begins to occur between chains, leading to much higher loss tangents.

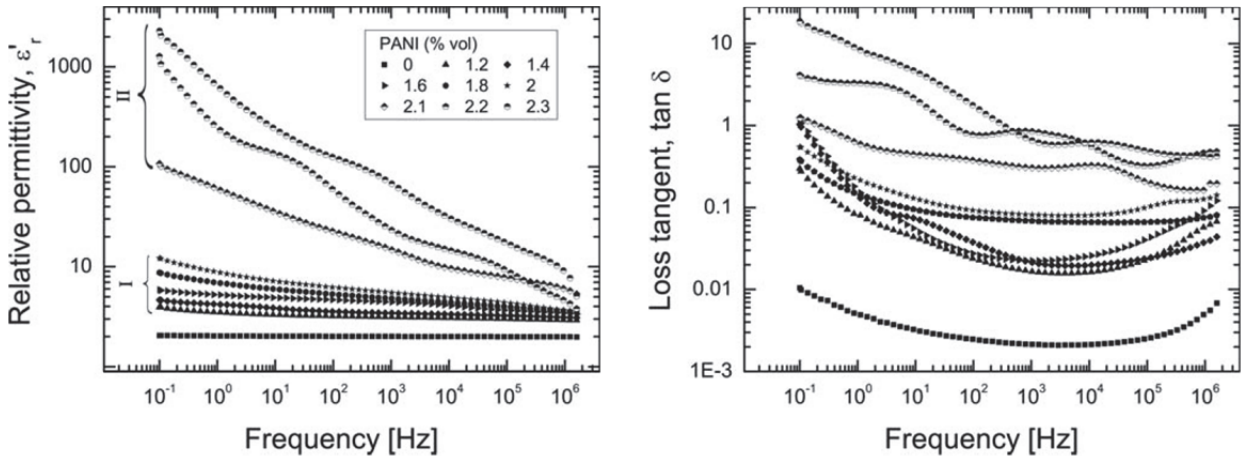


**Figure 1.16** Dielectric constant and loss tangent for PANI/SEBS-*g*-MA molecular composite. Region I at and below 2.0 vol.% PANI represents fully-insulated PANI chains with comparable losses, while in Region II above the critical 2.0 vol.% PANI, charge hopping can occur, leading to leakage current, high dielectric losses, and low breakdown strength. [24]

This increased conductivity also manifests itself in low breakdown strengths in actuation mode, as seen in Figure 1.17(a). Here, the inset shows an increasing actuation strain at a given field up to and including 2.0 vol.% PANI. However, above this weight percent, the elastomer becomes conductive, and the actuators fail from dielectric breakdown before achieving higher strains.

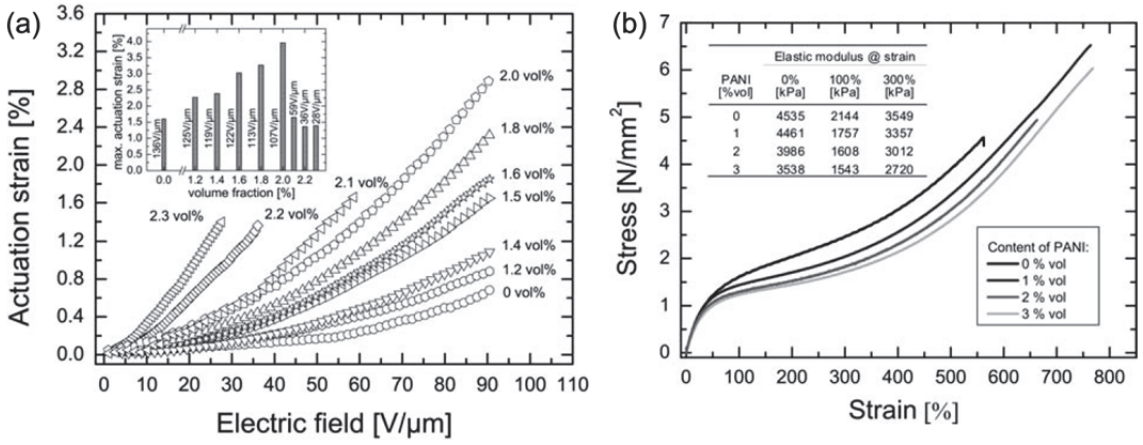


**Figure 1.17** **(a)** Actuation mode performance of PANI/SEBS-*g*-MA molecular composite, exhibiting enhanced strains at a given field at or below 2.0 vol.% PANI and low breakdown strength above this volume fraction. **(b)** Mechanical performance, showing a slightly decreasing Young's Modulus with increasing PANI content. [24]

Noteworthy, however, is that Figure 1.17(b) shows a slight decrease in the Young's Modulus with increasing PANI concentration. The presence of PANI chains effectively function as plasticizers, allowing the SEBS-*g*-MA chains to more easily slide past one another and lowering the stiffness or Young's Modulus of the composite. This approach of both increasing the dielectric constant while simultaneously decreasing the Young's Modulus appears to be most advantageous method to lowering required driving voltages, as given by Equation 1.4.

Finally, Kussmaul and coworkers have recently made a promising contribution to this effort by grafting high-dielectric constant organic dipoles to a PDMS elastomer chain, which not only increases the dielectric constant, but also decreases the Young's Modulus more drastically than any other aforementioned method. [25] Figure 1.18(a) shows their concept of grafting small molecules with

permanent dipoles to a PDMS elastomer chain via crosslinker. Figure 1.18(b) shows the process of functionalizing the dipole molecule (with high dielectric constant of ~56.3) with a vinyl group to allow for grafting to the crosslinker. This Pd-catalyzed allyl alcohol allylation resulted in the functionalized dipole N-allyl-N-methyl-p-nitroaniline (NANMPN). The crosslinker allows for greater homogenization of the dipoles during grafting to the PDMS.

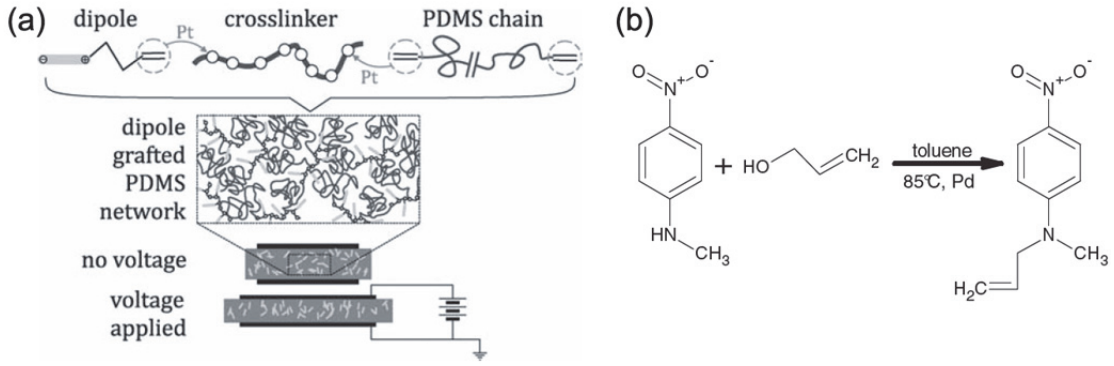


**Figure 1.18** **(a)** Concept of attaching small molecular dipoles to a crosslinker, which is then grafted to a PDMS elastomer chain for use in DE applications. **(b)** The vinyl functionalization of an aniline to create NANMPN. [25]

The resulting elastomer exhibits dielectric behavior, shown in Figure 1.19(a), that is comparable to that of the PANI-grafted SEBS-*g*-MA elastomer (Figure 1.16) in dielectric constant frequency response, maximum value of ~10, and dielectric losses. However, this elastomer achieved astonishingly lower Young's Moduli, dropping from 1900 kPa for neat PDMS down to 550 kPa at 13.4 wt.% dipole. Moreover, while there may be some surface charge effects from the frequency-dependent dielectric constant spectrum, there is no secondary region with

abnormally high dielectric constants, nor are the loss tangents too far apart from each other. This implies a dielectric elastomer with a high energy density, low conductivity, and high breakdown strength. Figure 1.19(b) shows actuation mode tests using the NANMPN/PDMS molecular composite, exhibiting superior actuation strains at a given field, increasing with wt.% of dipole content.

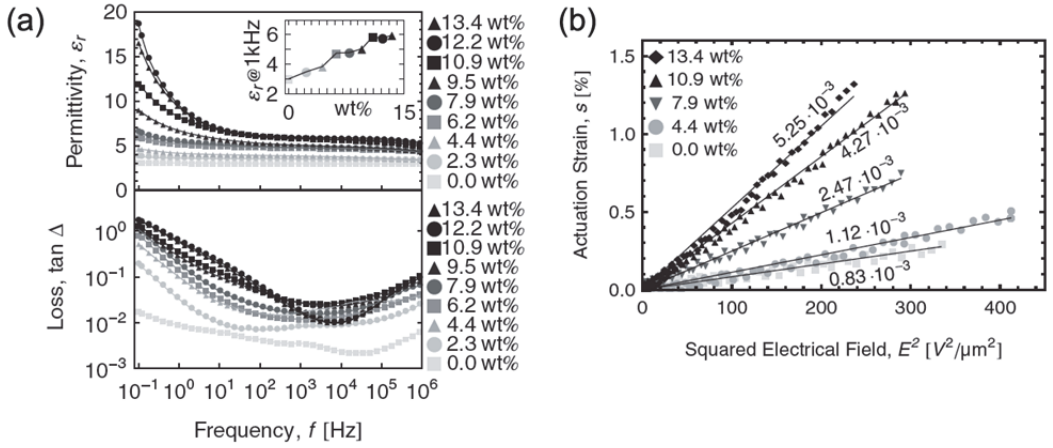


**Figure 1.19 (a)** Dielectric response of NANMPN/PDMS molecular composite; **(b)** Actuation mode testing of the molecular composite. [25]

All of the previously mentioned methodologies have their benefits, but all also have their drawbacks. In the case of the ferroelectric ceramic nanoparticles of PMN-PT, we see quite a dramatic rise in dielectric constant $\varepsilon'$ with few losses, but this is generally always accompanied by an opposing increase in the Young's Modulus $Y$. Using $TiO_2$ coated with PDMS oil in SEBS results in a favorable rise in the $\varepsilon'$ with few losses and supposedly also decreased interfacial friction, yet the reported increase in $Y$ is much larger than would be expected. Use of FGSs in PDMS appears promising at first glance due to its substantial rise in $\varepsilon'$, but the loss

tangent reveals an accompanying undesirable increase in conductivity. PANI fillers in PDMS show a steep rise in $\varepsilon'$ with astonishingly low losses at 100 Hz, but the rise in $Y$ is abnormally high. PANI grafts on SEBS-*g*-MA show a favorable rise in $\varepsilon'$ and even an accompanying lowering of $Y$, but the loss tangent seems to indicate a similar fate to the FGS/PDMS composite: dielectric losses are too high for the material to have a useful breakdown strength in actuation mode. Finally, while the NANMPN/PDMS graft increase in $\varepsilon'$ is a tad modest, losses are reasonably low and significantly, the material shows a substantial drop in $Y$. These key properties are summarized in Table 1.1.

**Table 1.1 High Dielectric Constant Elastomer Composites**

| Neat Elastomer | Filler/Graft | $\Delta\varepsilon'$ at $10^2$ Hz / Δ% | $\Delta\tan\delta$ at $10^2$ Hz / Δ% | $\Delta Y$ (kPa) at 0% Strain / Δ% | Ref. |
|---|---|---|---|---|---|
| PDMS | 30 v.% PMN-PT | 23 – 7 = +16 / +229% | 0.25 – 0.01 = +0.24 / +240% | 130 – 60 = +70 / +117% | [20] |
| SEBS | 30 v.% PDMS oil/$TiO_2$ | 8.25 – 2.25 = +6 / +267% | 0.02 – 0.003 = +0.017 / +567% | 1,300 – 300 = +1,000 / +333% | [21] |
| PDMS | 2.0 w.% FGS | 17 – 3 = +14 / +467% | 0.2 – 0.004 = +0.196 / +4,900% | 990 – 330 = +660 / +200% | [22] |
| PDMS | 31.7 v.% PDVB-PANI | 7.6 – 2.25 = +5.4 / +315% | 0.095 – 0.09 = +0.005 / +6% | 11,751 – 578 = +11,173 / +1,900% | [23] |
| SEBS-*g*-MA | 2.0 v.% PANI graft | 5 – 1 = +4 / +400% | 0.09 – 0.0015 = +0.0885 / +5,900% | 3,986 – 4,535 = –549 / –12% | [24] |
| PDMS | 13.4 w.% NANMPN graft | 6 – 3 = +3 / +100% | 0.05 – 0.003 = +0.047 / +1,567% | 550 – 1,900 = –1,350 / –71% | [25] |

## 1.4 Stretchable Electrode Materials for Dielectric Elastomers

### 1.4.1 Physical Attributes

Electrical conductors that are compliant and retain their electrical conduction at high strain deformation are one of the crucial materials behind high performance DEAs. Aside from the practical engineering attributes of low cost and simple fabrication, good compliant conductors should exhibit low electrical resistance at the maximum operational strain, and perform with little degradation over its cycle lifetime. Low electrical resistance helps to minimize the $RC$ time constant and $I^2R$ power consumption, enabling faster, more efficient devices. Typically, the resistance of compliant conductors is given as the sheet resistance $R_S$ in Ohms per square (Ω/sq.). By Pouillet's Law,

$$R = \frac{\rho}{t}\frac{l}{w} = R_S\frac{l}{w}, \text{ and } \sigma = \frac{1}{\rho} \qquad (1.20, 1.21, 1.22)$$

where the resistance $R$ (Ω) equals the bulk resistivity $\rho$ (Ω-m) divided by the thickness $t$, times the ratio of the electrode length $l$ (in the direction of the current) to width $w$; the electrical conductivity $\sigma$ (S/m) is the inverse of the bulk resistivity. [26] Figures of merit are often given interchangeably as sheet resistance in Ohms per square or conductivity in Siemens per centimeter. This is because the thickness is sometimes difficult to measure accurately for thin films of conductors on or near the surface of soft substrates.

Secondly, compliant conductors should exhibit low impedance to mechanical deformation and adhere well to their substrates. Accordingly, stretchable

conductors should be much less viscoelastic than their substrates to prevent interference with the mechanical response time. Also, these conductors should be much more compliant than their substrates to not restrict the strain. In the case of compliant electrodes, the product of thickness and elastic modulus should be less than that of the substrate. If we assume a Hookean approximation, then

$$P = \frac{F}{wt} = Y\varepsilon \qquad (1.23, 1.24)$$

where the pressure, or stress, $P$ is defined as a force $F$ divided by the cross-sectional area, or width $w$ times thickness $t$. This in turn approximates the product of the Young's modulus $Y$ and the strain $\varepsilon$. At a constant load $F$ and width $w$,

$$\varepsilon \propto \frac{1}{tY} \text{ and so } \varepsilon_S \propto \frac{1}{t_S Y_S} \text{ and } \varepsilon_E \propto \frac{1}{t_E Y_E} \qquad (1.25, 1.26, 1.27)$$

where $\varepsilon_S$ and $\varepsilon_E$ are the achievable strains of the substrate and stretchable electrode, respectively. Therefore, for $\varepsilon_E \gg \varepsilon_S$, it follows that

$$t_E Y_E \ll t_S Y_S \qquad (1.28)$$

in which the product of thickness and Young's modulus of the electrode should be much less than that of the substrate to not interfere with strain. In addition, some DE applications may desire transparency. This parameter is often quantified as percent transmittance (%$T$) averaged over a range of frequencies, or at a single frequency, typically 550 nm since it is in the middle of the visible spectrum.

The challenge to engineering compliant conductors for a given application lies in obtaining the intersection of desirable electronic, mechanical, and optical properties. This set of design requirements is graphically illustrated by the Venn

diagram in Figure 1.20. At first glance, creating conductors with high compliance, conductivity, and transparency is not a trivial matter, as these properties are often mutually exclusive. Furthermore, engineering reliable compliant conductors with a desired set of properties that remain fairly unchanged over long service lifetimes is an additional criterion that merits careful attention.

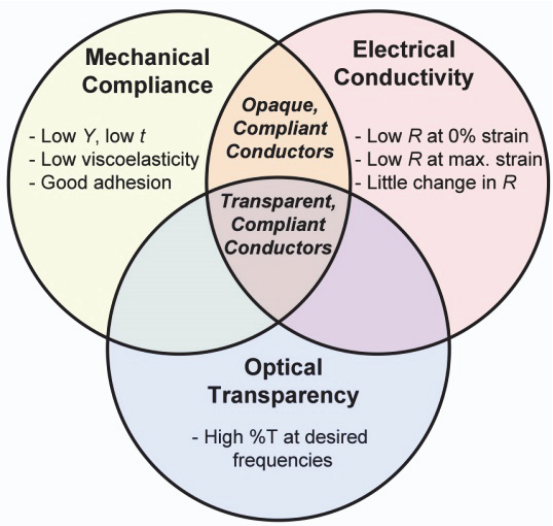


**Figure 1.20** Engineering compliant conductors must find an intersection of mechanical, electrical, and optical properties for the given application. Conductors with both high mechanical compliance and high electrical conductivity form a class of opaque, complaint conductors; transparent, complaint conductors also possess high optical transparency.

To address these challenges, most compliant conductors for DEs have been fabricated by filling elastomers with conductive particles or by depositing conductive particles on or just beneath the surface of elastomers. Metal and carbon powders and nanoparticles, conducting polymers, carbon nanotubes and other carbon allotropes, and metal nanowires have been composited with synthetic

rubbers of acrylic, silicone, and others. This approach creates a class of DE electrode materials that are said to be intrinsically stretchable.

To put the discussion into context, Table 1.2 lists the bulk resistivities of conventional, non-compliant conductors that are also mostly opaque. These are among the raw materials often utilized to create soft and transparent conductors. Also provided are the calculated sheet resistances of hypothetical thin films of these materials at an arbitrary thickness of 100 nm, unless stated otherwise. For nanowires and nanotubes, a hypothetical solid thin film is considered with thickness equivalent to the average diameter of a single tube or wire; for graphene the thickness is that of a single monolayer. This will allow for comparison to the sheet resistances of the compliant and transparent conductors summarized in Table 1.3. The discussion that follows will cover more conventional electrode materials for dielectric elastomer transducers. An extension of this discussion detailing less conventional or novel DE electrodes is given in the Appendix.

## Table 1.2 Electrical Properties of Rigid Conductors[a]

| Pure Material | | Bulk Resistivity (Ω-cm) | Sheet Resistance at $t$ = 100 nm[b] (Ω/sq.) | Ref. |
|---|---|---|---|---|
| **Metals** | Silver | $1.62 \times 10^{-6}$ | 0.16 | [27] |
| | Copper | $1.7 \times 10^{-6}$ | 0.17 | [27] |
| | Copper Nanowires | $1.7 \times 10^{-6}$ | 0.19[c,d] | [28-30] |
| | Gold | $2.26 \times 10^{-6}$ | 0.23 | [27] |
| | Aluminum | $2.71 \times 10^{-6}$ | 0.27 | [27] |
| | Silver Nanowires | $3.08 \times 10^{-6}$ | 0.51[c,e] | [31-33] |
| | Nickel | $7.12 \times 10^{-6}$ | 0.71 | [27] |
| | Indium | $8.37 \times 10^{-6}$ | 0.84 | [34] |
| | Platinum | $10.7 \times 10^{-6}$ | 1.1 | [27] |
| | Tin | $11.5 \times 10^{-6}$ | 1.2 | [27] |
| | Chromium | $12.6 \times 10^{-6}$ | 1.3 | [27] |
| | Gallium | $13.6 \times 10^{-6}$ | 1.4 | [27] |
| | Lead | $21.1 \times 10^{-6}$ | 2.1 | [27] |
| | Mercury | $96.1 \times 10^{-6}$ | 9.6[f] | [27] |
| | Indium Tin Oxide | $1 \times 10^{-4}$ | 10 | [35] |
| **Carbons** | Single-Walled Carbon Nanotubes | $1 \times 10^{-6}$ | 3[c,g] | [36-38] |
| | Graphene | $1.7 \times 10^{-6}$ [h] | 41.6 | [39, 40] |
| | Multi-Walled Carbon Nanotubes | $5.1 \times 10^{-6}$ | 2.6[c,i] | [41-44] |
| | Graphite (Crystalline) | $3.8 \times 10^{-5}$ | 3.8 | [34, 43, 45] |
| **Conducting Polymers** | Polyacetylene (Iodine-Doped) | $9.09 \times 10^{-6}$ | 0.91 | [46] |
| | Polypyrrole ($FeCl_3$/ $FeCl_2$-Doped) | $4.55 \times 10^{-3}$ | 455 | [47] |
| | Polyaniline (HCl-Doped) | $1.25 \times 10^{-2}$ | 1,250 | [48] |
| | PEDOT:PSS (Untreated) | $1 \times 10^{-1}$ | 10,000 | [49] |

[a]Properties at or near Ambient Standard Temperature and Pressure (25°C, ~1 atm); [b]Unless stated otherwise; [c]Equivalent sheet resistance, assuming such a material could retain its electronic properties in the form of a solid sheet of thickness equal to the diameter of one nanotube or nanowire; [d]For a diameter of $t \approx 90$ nm; [e]For a diameter of $t \approx 60$ nm; [f]Assuming this liquid metal has a uniform thickness of 100 nm, as if solid; [g]For a diameter of $t \approx 3$ nm; [h]Calculated from an electron mobility of 15,000 $cm^2$/V-s and a carrier concentration of $10^{13}$ /$cm^2$, which gives the sheet resistance rather than the resistivity. For resistivity, this value was multiplied by the thickness of a single graphene sheet ($t \approx 0.4$ nm); [i]For a diameter of $t \approx 20$ nm

### 1.4.2 Opaque Compliant Conductors

#### 1.4.2.1 Metals

Metals have long been an obvious choice as a conventional electrode material due to their high electrical conductivity, on the order of $10^5$ S/cm. However, because metals possess very high elastic moduli near $10^2$ GPa, adapting them to become stretchable has proven challenging. [27] Perhaps the simplest approach has been to deposit a metallic thin film onto a compliant substrate via printing, painting, sputtering, electron beam evaporation, or other surface deposition strategies. On the other hand, metal nanoparticle/elastomer compositing and metal ion beam implantation techniques offer much higher stretchability while still maintaining reasonable levels of conductivity. These methods are outlined below.

##### *1.4.2.1.1 Inks and Paints*

Suspending metallic nanoparticles in a solution has been a traditional approach to creating conducting inks and paints. Typically, paints— sometimes referred to as pastes— are more viscous than inks and must be brushed or stamped onto the substrate. Inks may be stamped, but also printed, offering a manufacturing platform capable of high resolutions and versatile computer control. Inks require a very specific composition to meet all the criteria for inkjet printing. For example, the ink must have the correct viscosity and surface tension to avoid nozzle clogging and ensure optimal droplet resolution, the surface energy of the ink should match that of the substrate well for optimal wetting, and the vapor pressure of the ink

solvent should allow for uniform drying yet not be so volatile that the nozzle clogs when not jetting. [50] These three physical properties of ink viscosity, surface tension, and vapor pressure must meet the requirements of the printer manufacturer, as well as those of the substrate, to be effectively printed. [51] In addition, the desired electrode properties after printing must be considered when designing the conducting ink. Ideally, the nanoparticle loading is as high as possible for optimal conductivity, yet not so high that the ink is overly viscous or stiff when dry, or that maintaining a homogeneous dispersion is difficult. Carbon-based inks are also possible, and the same requirements for metallic inks apply to carbon inks. Carbon grease can be considered to be a type of carbon paint, and will be discussed further below.

Unlike carbon grease, metallic paints are not as commonly used as a flexible electrode material because they are much more brittle and rigid when dry. Silver paints— available from Structure Probe, Inc. or Ted Pella, Inc.— are more commonly utilized for static electrical contacts, such as between a flexible conductor of a different material and leads to other electronics. [52-55] Sliver inks may offer more flexibility, although they can still be quite brittle. One approach to overcome this limitation is to improve the wettability and adhesion of the printed silver ink to the DE substrate.

Chung et al. inkjet printed silver electrodes onto the UV-treated surface of PDMS using ANP Corp. DGP-40 ink with 32 wt.% silver nanoparticle loading. UV ozone treatment of the PDMS nearly doubled the wettability of the ink, which

contained the polar solvent triethylene glycol monoethyl ether. The ink was printed with the Dimatix DMP-2831, a piezoelectrically-actuated material printer that enables inkjet printing of nonaqueous ink dispersions. Various printing parameters were fine-tuned, such as cartridge temperature (33°C), ink drop velocity (6–7 m/s), and drop spacing (20 $\mu$m). This drop spacing was chosen for the best resolution and uniformity since each ink droplet wets the activated PDMS surface to a 40 $\mu$m-diameter circle. The PDMS substrate was kept at a constant 60°C during printing, followed by a 100°C sintering step post-printing. Doubly-printed silver electrodes have a sheet resistance of 0.55 Ω/sq.; the increase in resistance was less than three times that of the initial resistance after 1,000 stretching cycles at 10% strain and 1 mm/s. [56]

#### *1.4.2.1.2 Nanoparticle/Polymer Composites*

Metallic nanoparticles can not only be processed into inks, but also incorporated into an elastomer matrix to form a stretchable composite conductor. Use of metal powder fillers has been the simplest, most conventional approach to this end, and metal powders of aluminum, nickel, copper, silver, and gold have been used as fillers in metal/polymer composites of poly(vinyl chloride) (PVC), thermosetting resins, and elastomers such as natural rubber. [57-61] Metallic fibers such as of aluminum and stainless steel have also been explored as an alternative filler material in various polymers, with some Al/polypropylene composites reaching percolation near ~10 vol.% Al fibers. [62, 63] Mixing colloidal dispersions of metal

nanoparticles with polymers is a more recent direction, such as gold nanoparticle colloids in polyethylene (PE) and poly(methyl methacrylate) (PMMA) or polystyrene (PS) functionalized gold nanoparticles in a PS matrix. [64, 65] In a slightly more novel approach, silver, gold, and platinum nanoparticles can be formed in situ inside a PDMS elastomer matrix by the same reaction that crosslinks the elastomer. [66] This process utilizes a metal salt reduction process that is very similar to that used to form Pt electrodes, which will be described below in the discussion of photopatterned platinum electrodes. A similar in situ approach reports the formation of silver and gold nanoparticles in PDMS concomitant with crosslinking, as well as the in situ formation of silver nanoparticles in polyacrylonitrile (PAN) elastomers accompanying UV curing in the absence of a solvent or additional reducing agent. [67, 68]

In all of these examples of conducting particle/elastomer composites, as well as for conductive inks, the primary conduction mechanism is percolation. According to percolation theory, conductivity increases sharply above the percolation threshold, i.e., once the volume fraction of conductive filler is high enough to form contacting conductive pathways throughout the composite (Figure 1.21). [69, 70] In general, this phenomenon near the percolation threshold can be described by the power law

$$\sigma \propto \sigma_{\mathrm{f}} \left(V - V_{\mathrm{c}}\right)^{n} \text{ for } \; V > V_{\mathrm{c}} \tag{1.29}$$

where $\sigma$ is the conductivity of the composite, $\sigma_{\mathrm{f}}$ is the conductivity of the filler, $V$ is the volume fraction of the filler, $V_{\mathrm{c}}$ is the critical volume fraction at percolation, and

$n$ is an empirically determined power. [71-73] Below $V_c$, $\sigma$ is essentially zero. Several non-contact conduction mechanisms are also possible— such as quantum tunneling, charge hopping, and thin film conductivity— but are beyond the scope of this discussion. [74, 75] As a result, the Young's modulus of the metal/elastomer composite is kept to a minimum stiffness, and the composite is able to withstand high strains before losing electrical conduction. Further discussion of percolation phenomena will follow when discussing Carbon/Polymer Nanocomposites. More recent advances have utilized metal ion implantation to create flexible, patterned metal electrodes just under the surface of silicone elastomers. This allows for the direct creation of DE devices with metal/polymer composite electrodes without the need for additional manufacturing steps. [76]

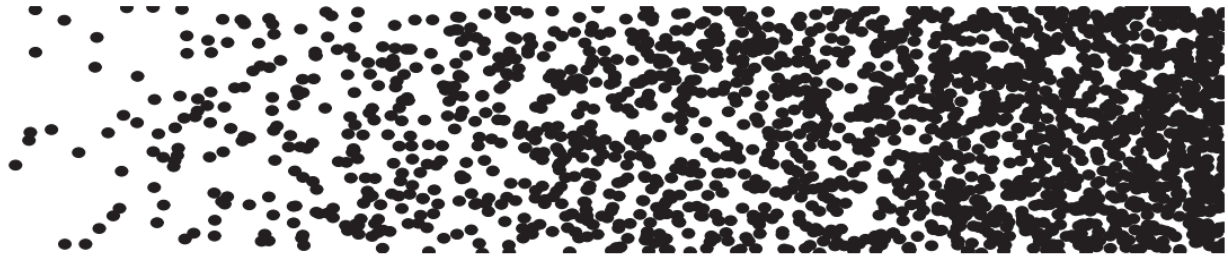

**Figure 1.21** Simulation of conducting particles in an elastomer matrix, shown with increasing probability density from left to right. The composite reaches high conductivity when the density of conducting particles is sufficient to form adequate conducting pathways. [70]

*1.4.2.1.2.1 Metal Ion Implantation*

An emerging direction of stretchable conductor fabrication is the use of a specialized form of physical vapor deposition called metal ion implantation. During metal ion implantation, charged nanoparticles of a metal are collided with a target substrate at high velocity. Typically, an ion source vaporizes a metal into a plasma, which is then electrostatically accelerated at the target. [77] The distribution of ion diameters varies, so an electromagnetic filter may be necessary to exclude the less-useful large-diameter ions, as in filtered cathodic vacuum arc (FCVA) implantation. This filtering is usually accomplished by using a solenoid coil to arc the trajectory of the ions; heavier species will have larger radii of curvature and will be caught on the sidewalls of a 90° duct. [78] Supersonic cluster beam implantation (SCBI) is a slight variation, wherein a pressure gradient, formed from supersonic expansion, is used to aerodynamically accelerate pre-fabricated, non-charged metal nanoparticles into the target. These nanoparticles are typically produced by the same vaporization method used in FCVA, but are then rapidly cooled by a pulse of inert gas, allowing the formation of neutrally charged clusters. [79-81]

Rosset et al. have utilized low-energy FCVA metal ion implantation to create compliant electrodes of gold, palladium, and titanium in PDMS with a low surface resistance (< 1 kΩ/sq.) that does not drift with time. [82, 83] The incoming metallic particles have low acceleration energies between 2.5 and 10 keV in order to result in penetration depths of only ~10 to 50 nm below the elastomer surface. [84, 85] Additionally, a high ion flux near $10^{14}$ ions/pulse is required to reach the desired

film conductivity (at doses of 1 to 5 × $10^{16}$ ions/$cm^2$) after a reasonable amount of time. Unlike plasma-based implanters, conventional beamline implanters are inadequate since they typically cannot deliver high ion fluxes at low energies. [86] For example, metal vapor vacuum arc (MEVVA) implantation delivers high ion fluxes but at energies in excess of 30 keV, and so stiffer target substrates such as PI or polyethylene terephthalate (PET) must be utilized. [87-91]

FCVA implantation can usually produce Au electrodes in silicone with a surface resistance below 1 kΩ/sq. after only 3 minutes. [84] Typically, FCVA electrodes have a resistance of ~200 Ω/sq. and can be patterned to a resolution of 10 $\mu$m by utilizing a photolithographically patterned mask on the substrate surface prior to implantation. [84, 92] These electrodes can be stretched up to 175% strain and survive for more than $10^5$ cyclic deformations at 30% strain. [82, 84, 93] SCBI has also been utilized effectively to produce durable, stretchable metallic circuits on thermoplastic elastomers. This process can be carried out at room temperature, and unlike FCVA, it does not charge or carbonize the polymer substrate. Corbelli and colleagues fabricated deformable elastomeric electrodes that can withstand deformations of 40% strain for more than $10^5$ cycles and that can actually decrease their resistance upon uniaxial cyclical stretching, which is caused by the formation of a percolating network. Moreover, they utilized stencil mask lithography to pattern the SCBI electrodes, wherein a grid was interposed between the cluster beam and the substrate. [81] Figure 1.22 schematically illustrates the FCVA implantation and SCBI methods.

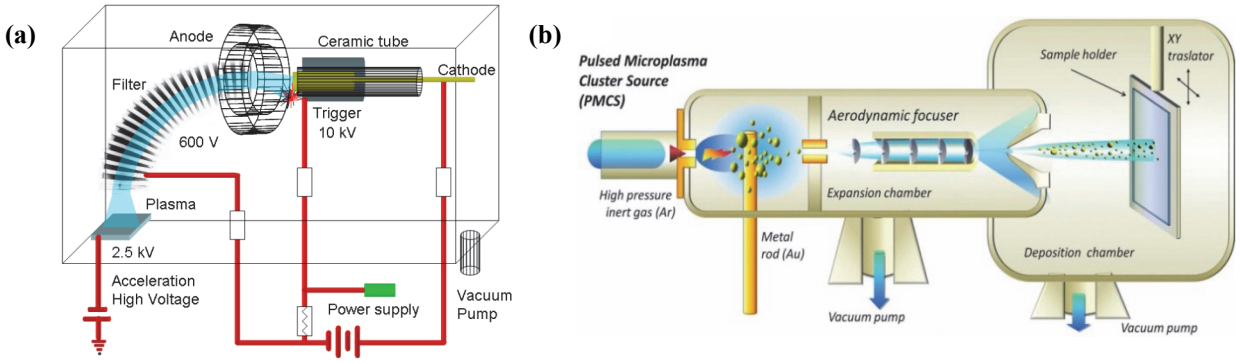


**Figure 1.22** **(a)** FCVA implantation accelerates a charged ion source to a grounded substrate, through a 90° magnetic filter. [75] **(b)** SBCI, on the other hand, accelerates neutralized nanoparticles toward a substrate using air pressure. [81]

Metal ion implantation leads to the formation of nanosized (2–20 nm) clusters in the polymer matrix. Although these clusters may touch each other, they are free to slide past one another. Because there are no strong mechanical bonds among nanoparticles, the Young's modulus of the composite can remain low. As is the case with other metal-filled polymer composite conductors, the primary conduction mechanism follows percolation theory, in which sufficient implantation doses are required to exceed the percolation threshold. As a result, metal ion implantation typically produces semi-transparent to opaque electrodes, which are generally not well-suited where optical transmittance is a design requirement. Wu et al. conducted research on the modification of polyethylene terephthalate (PET) films via Ag, Cr, Cu, and Si metal ion MEVVA implantation. [88] They found that the colorless, clear PET film became a semi-transparent light brown at a dose of 5 ×

$10^{15}$ cm$^{-2}$, and when the dose reached $5 \times 10^{16}$ cm$^{-2}$, the color changed to dark brown and became opaque. At a dose of $1 \times 10^{17}$ Ag ions per cm$^2$, the PET adopted a bright, metallic sheen. Figure 1.23(a) shows the microstructure of the PET cross section, where three discrete regions are present: a lighter upper layer 20 nm deep, a darker 80 nm-thick region with dense clusters of Ag nanoparticles and carbon-enriched species, and the bottommost layer where Ag nanoparticle precipitation into the PET is evident. The total penetration depth was roughly 170 nm. Figure 1.23(b) shows a transmission electron micrograph (TEM) cross section of Au-implanted PDMS, with a Au ion penetration depth of about 60 nm.

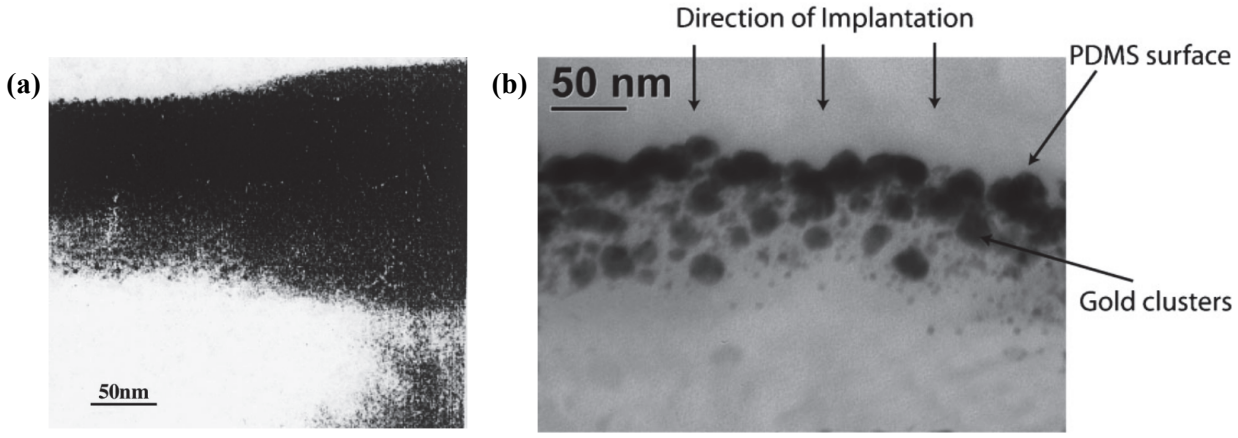


**Figure 1.23** **(a)** TEM bright field image of a cross section of MEVVA Ag-implanted PET with the three-layers visible. The center layer, containing dense Ag nanoparticles and carbonized particles, is shown between 20 and 100 nm from the surface (top of the image). [88] **(b)** TEM cross section of FCVA Au ion implantation in PDMS (dose: $1.5 \times 10^{16}$ cm$^{-2}$ at 5 keV). [84] In both cases, the touching nanoparticles can slide relative to each other upon flexing or stretching.

Moreover, Wantanabe et al. performed Ag, Pd, and W ion MEVVA implantation in polyimide films of Kapton™ tape, specifically to study the surface carbon formation that contributes to a reported 20 order of magnitude drop in sheet resistivity. [87] Using laser Raman spectroscopy, the researchers ascertained the structure of the carbonization layer: Diamond-like carbon formed from high-dose implantation with W or Ag, graphite with W implantation, amorphous C for low-dose Ag, and a so-called transparent carbon structure for Pd implantation. Thus, the specific carbon structure that is formed is dependent on the type of metal element implanted, as well as on the dose. As mentioned above, MEVVA metal ion implantation is not typically utilized with elastomer substrates, and SCBI may be preferred over FCVA for certain applications because the implanted metal nanoparticles are neither charged nor carbonized.

*1.4.2.1.2.2 Photopatterned Platinum*

While metal ion implantation offers patternability and low modulus for the fabrication of miniature DEAs, the substrate size is limited, and the resulting electrodes have a rather high sheet resistance. Electrodes with lower sheet resistances and larger areas can be fabricated by mixing a metal salt into a photopatternable elastomer precursor, then immersing this mixture in a reducing solution. Reminiscent of photolithography, UV light and a shadow mask can photochemically pattern stretchable Pt metal electrodes on the surface of an elastomer. Specifically, an uncured elastomer mixed with 11 vol.% Pt salt is spread

atop a previously cured elastomer. Then, a shadow mask is placed between the sample and a UV curing source, and the undeveloped mixture is washed away with water and ethyl acetate. What remains on the elastomer surface is a photocured pattern containing a Pt salt, with a feature resolution of ~310 μm. This process is feasible since UV radiation is not readily absorbed by Pt in its salt form. To render the pattern conductive, the sample is immersed in a reducing solution of 30 mM sodium borohydride in a solvent of 50% water and 50% methanol. The salt $Pt(NH_3)_4 \cdot Cl_2$ then diffuses to the surface and is reduced to form conductive Pt nanoparticle precipitates. The final result is a patterned electrode of Pt on the elastomer surface. In addition, the reduction itself is essentially identical to the manufacture of ionic polymer-metal composites (IPMCs), wherein a reducing agent is used to metallize a Pt salt-soaked polymer. [94-96] These electrodes demonstrate good electromechanical performance, capable of 150% elongation before loss of electrical conduction and can survive 1,000 stretching cycles at 30% strain. Figure 1.24 depicts the macro- and microscale structure of the photopatterned Pt electrodes. [97]

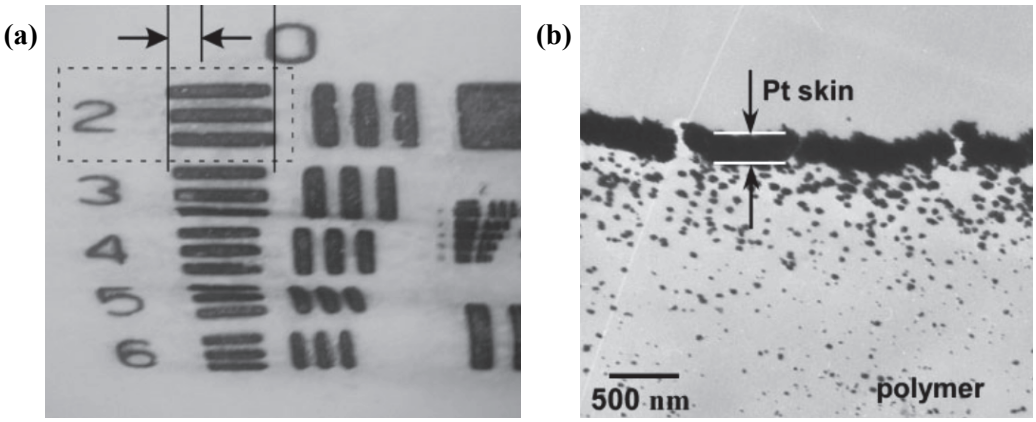


**Figure 1.24** **(a)** Photograph of Pt electrodes, patterned with a USAF 1951 mask, after being stretched uniaxially by ~45%. **(b)** TEM micrograph revealing the microstructure of the composite, with a "skin" of Pt nanoclusters aggregated near the polymer surface. [97]

Swelling of the elastomer during immersion is an important step. It increases porosity, in turn increasing the diffusion of Pt into the elastomer. In addition, swelling mechanically strains the polymer during metallization, and on relaxation following reduction, the Pt folds into out-of-plane corrugations. When actuated the folds flatten, and as a result higher actuation strains are possible. Methanol was chosen since it swells the chosen acrylated polyurethane elastomer (Loctite 3180) by 55%, versus 10% by water alone. The samples prepared with the methanol mixture exhibited a resistance decrease after increasing the Pt salt concentration past the percolation threshold of ~7% by volume, reaching as high as ~1 S/cm (2.2 Ω/sq.) at 15 vol.%. With increasing Pt salt concentration, there was an observed increase in average strain before failure, from ~73% at 9 vol.% to 150% at 14 vol.%. The higher salt loading allowed the film to be stretched more before the area density of Pt nodules dropped below the percolation threshold. In addition, the Pt electrodes

demonstrated conduction recovery after being stressed beyond electrical failure. [97-99] In short, Pt salt electrodes offer a variety of desirable characteristics, such as high strain, high conductivity, low elastic modulus, and high feature resolution via photopatternability.

#### 1.4.2.2 Carbons

Originally investigated as an alternative to metals, carbons are now one of the most widely-researched conducting materials for stretchable conductors. Carbon powders are the simplest form of carbon-based electrode, but they are not capable of maintaining reasonable levels of conductivity at high strains. Carbon grease incorporates carbon powder into an oil-based matrix and can maintain conductivity at higher strains than carbon powder alone, but it is messy and inconvenient to work with. More advanced carbon materials such as carbon nanotubes (CNTs) address these shortcomings, offering high conductivity at high strains and little mess. Further, carbon nanotubes have been functionalized to allow for inorganic solution processing.

##### *1.4.2.2.1 Carbon Black*

Carbon black, also known as carbon powder, is the industrial byproduct of hydrocarbon thermal decomposition. Its microstructure consists of agglomerates of loose spherical carbon particles that can be spray or brush deposited onto a substrate. [100] Thus, no strong binding forces are formed between the agglomerates, and the powders do not contribute to the stiffness of the membrane onto which they are applied. Combined with easy application, carbon blacks were

widely utilized as some of the first stretchable electrode materials. Many forms of carbon black are commercially available, such as Ketjenblack® EC-300J (AkzoNobel), VULCAN® XC72 (Cabot Corp.), Raven® 7000 (Aditya Birla Chemicals), and Shawinigan Black® Acetylene Black (Chevron Phillips). [69]

Although metallic powders are intrinsically more conductive than carbon powders, metallic powders tend to form insulating surface oxide layers. Carbon powders do not present this difficulty, and their smaller particle size assists in the creation of sufficient electrical contacts at low strains. Additionally, as long as the electrical time constant of the device does not exceed its intended mechanical bandwidth, the relatively high electrical resistance of carbon black electrodes becomes less of a concern for actuators. For example, a 1 $cm^2$, 40 $\mu$m-thick silicone dielectric elastomer actuator (DEA) with electrodes whose resistance would be in the megohm range could still be driven up to 1 kHz. [50] In this case, carbon powders prove sufficient compared to metallic powders, in applications where large strains are not required.

However, large strains are hard to attain with carbon powder electrodes since their small particle size makes it difficult to maintain sufficient electrical contacts above a critical strain. Second, carbon particles are sensitive to static charges and are difficult to handle. Third, carbon black electrodes have a limited lifetime because the carbon particles tend to detach from the substrate. To prevent this, these loose carbon powders are sometimes used as the electrode material on acrylic elastomers, such as 3M™ VHB™ industrial adhesive tape, which are sufficiently adhesive to bind carbon particles to the surface. Alternately, loose carbon black may

be bound to the substrate by incorporating it into a curable elastomer matrix, which is usually the same material as the dielectric elastomer. [50, 101]

O'Brien et al. tested different carbon electrodes when creating a smart DEA with an integrated extension sensor. [102] The carbon-based electrode of choice for the sensor was selected from among loose carbon powders, bound carbon powders, and carbon grease electrodes, which will be discussed in the next section. They found that significant amounts of carbon powder would fall off, leading to the poorest mechanical performance of the three. However, these loose carbon powders demonstrated the best electrical performance, with little noise and a resistance of about 10 kΩ/cm at rest. On the contrary, bound carbon powder electrodes (silicone:carbon black = 1:5) demonstrated the best mechanical performance, preventing the shedding of carbon powder during mechanical cycling. However, the bound powder was the least suitable for self-sensing due to significant electrical time dependent effects. And although carbon grease was easier to apply than carbon powder, electrically it appeared to be the noisiest of these three electrodes. Therefore, loose carbon powder was ultimately chosen for the sensor since it behaved the best electrically with little noise and hysteretic problems, and since its electrical properties play a more significant role as a sensor electrode. Figure 1.25 compares the appearance of bound carbon powder, loose carbon powder, and carbon grease electrodes on their silicone extension sensor.

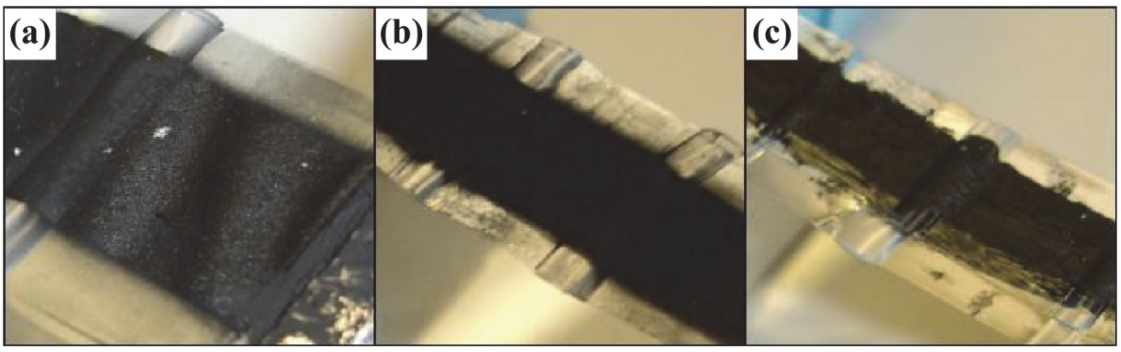


**Figure 1.25** Comparison of carbon-based electrodes on a silicone elastomer used as an extension sensor. **(a)** Carbon black bound in a cured silicone elastomer, **(b)** loose carbon black powder, and **(c)** carbon grease. [102]

#### *1.4.2.2.2 Carbon Grease*

As seen above, loose carbon powders can be unreliable and difficult to work with. Other than incorporating these loose particles into a curable matrix or potentially using an adhesive substrate, a third option is to transform carbon black into a grease. Carbon grease, with a sheet resistance of 100 kΩ/sq., is formed by binding loose carbon powders, usually with silicone oil, into a viscous matrix. [103, 104] Carbon grease is capable of sustaining much larger strains while still remaining conductive. When actuated below 50% strain, there is no significant migration of the electrode material; only above 100% strain can any visible migration be observed. [105] Carbon grease is relatively inexpensive and is commercially available as NyoGel® from Nye Lubricants, Inc. or as 846 Carbon Grease from MG Chemicals®.

Pelrine et al. demonstrated that prestraining dielectric elastomer films can enable high strains and high energy densities, further improving device

performance. [7] Strains five to six times those previously reported, higher pressures (up to 7 MPa), and energy densities about 23 times those described earlier were demonstrated. Carbon grease was chosen as the compliant electrode material of choice because it can maintain relatively high conductivities at high actuation strains, allowing these high strains to be realized. Compared to loose carbon powders, carbon grease adheres better to the elastomer, preventing its resistance from increasing as rapidly. In addition, Kofod et al. have utilized carbon grease electrodes with polyacrylate dielectric elastomers for extremely large strain and elastic energy density measurements. [11] In this case, carbon grease electrodes enabled the stretchable devices under test to realize the highest practical strains, stresses and efficiencies.

While easier to handle and apply than loose powders, carbon grease can still be quite messy and can easily rub off of the elastomer substrate. Carbon grease can also reduce interlayer adhesion of dielectric elastomer stack actuators. Devices with carbon grease electrodes have limited shelf life due to drying out of the grease or due to diffusion of the oil-based emulsifier into the dielectric membrane, which can cause short circuits or membrane swelling. Additionally, the viscoelasticity of carbon grease causes it to creep under the influence of gravity, especially for vertically-stored devices, and can be subject to mechanical abrasion. [50] Moreover, it is difficult to deposit carbon grease in a uniform thickness. [105, 106] In the earlier days of dielectric elastomer development, carbon grease was the electrode material of choice and is still used widely today in laboratories for proof of concept

actuator configurations and experiments. However, the disadvantages have driven researchers to investigate more sophisticated alternatives for commercial products.

#### *1.4.2.2.3 Graphite*

Like carbon black, graphite powder electrodes usually require an adhesive substrate or a binding agent and can be brushed or spray coated. When spray deposited, graphite electrodes demonstrate good performance at high electric fields, optimally above 25 V/$\mu$m. [105] When brushing graphite electrodes onto the substrate, the thickness uniformity and resulting resistances cannot be easily controlled, leading to sub-optimal performance. [8, 107] In lieu, spray coating can address these issues, improving uniformity, lowering resistance, and increasing performance. [106]

To evaluate different electrode materials, Carpi et al. sprayed planar actuators (2 × 3 cm) of an acrylic elastomer film with compliant electrode materials. [103] Graphite powders were smeared on the two sides of the elastomer strip, as well as spray deposited. The powder was sprayed onto a separate substrate, the solvent was left to evaporate, and then the remaining powder was transferred onto the elastomer substrate. The sprayed graphite electrodes demonstrated superior uniformity and low resistances (40 kΩ/sq.) compared to graphite powder (160 kΩ/sq.), in part due to the homogenous dispersion in the solvent and in part due to the deposition technique (Figure 1.26(a)). On the other hand, Schlaak et al. reported the opposite result: Spraying nearly doubled the sheet resistance of their electrodes

at ~20% strain (Figure 1.26(c)). Intending to increase the absolute strain at lower voltages, the group developed an automated spin-coating process to fabricate elastomer stack actuators with up to 100 layers. The combination of a highly elastic silicone elastomer with thin, highly-conductive graphite electrodes was shown to achieve strains of up to 20%. [108, 109]

As Schlaak et al. confirmed by SEM micrographs, the homogeneity of spraying was markedly lower than with brushing (Figure 1.26(b)). Of importance here is to note that electrode resistance and homogeneity are inversely proportional: resistance decreases with increasing homogeneity. Thus, we can assume that the spray coating method and/or type of graphite used by Carpi et al. likely produced more homogenous graphite electrodes than the methodology and/or type of graphite utilized by Schlaak at the time. Indeed, Carpi used graphite dispersed in a solvent (N-77, Due-ci electronic, Italy) and used a transfer technique, while Schlaak likely used dry graphite powder with a pressurized air system sprayed directly onto the elastomer, although the exact graphite material is not published.

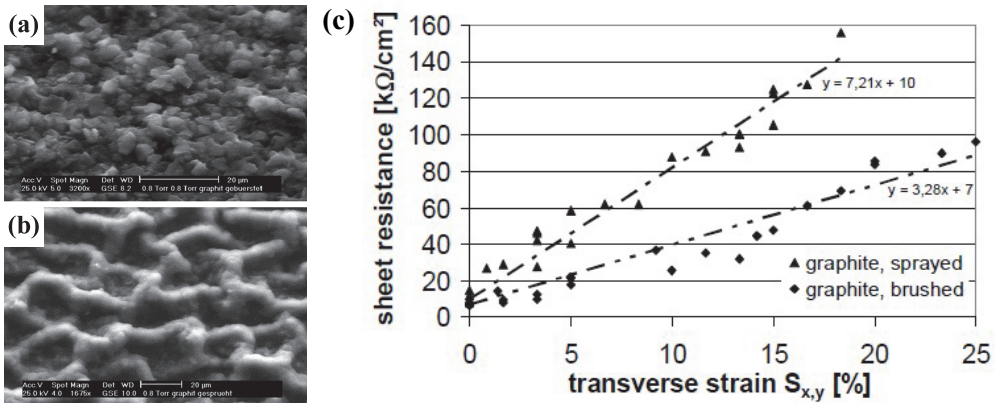


**Figure 1.26** Scanning electron micrographs of **(a)** homogenous brushed and **(b)** inhomogeneous sprayed graphite electrodes, and their **(c)** sheet resistance with increasing transverse strain. Both the graphite powder and the graphite spray electrodes have low starting sheet resistances (< 10 kΩ/cm²), but at ~20% transverse strain, the sprayed electrode has roughly twice the sheet resistance as the brushed. [108] Using a dry versus a solution-based graphite deposition technique may explain the differences in resistance and underlying homogeneity.

#### *1.4.2.2.4 Carbon Nanotubes*

CNTs are poised as an ideal stretchable conductor and electrode material, possessing high aspect ratios (with lengths up to 1 mm or more), nanoscale diameters (as small as 0.4 nm), excellent mechanical strength (~0.64 TPa Young's modulus), high thermal stability, and superior electrical conductivity along the tube axis (~$10^6$ S/cm). [37, 110-112]

#### *1.4.2.2.4.1 Raw Single-Walled Carbon Nanotubes*

Single-walled carbon nanotubes (SWCNTs, also commonly referred to as SWNTs) on prestrained VHB™ have been shown to exhibit linear strains greater than 700% before losing conduction. SWCNT films may appear uniform to the naked eye, but clusters and boundaries exist in the nanotube network at the microscale. While these clusters may break apart at large strains, the high aspect ratio of the nanotubes allows them to maintain contact with neighboring clusters and ensure the continuity of the conduction pathway . Perhaps the simplest method of SWCNT film formation is via spray deposition. This technique allows the opacity and resistivity of the resulting films to be directly controlled, and high packing densities are possible when transparency is not required. SWCNT films have a high absorption coefficient, leading to optical transmission loss. However, as the electrodes stretches, the nanotube density decreases, thus increasing the transmittance. SWCNTs have been explored as a transparent stretchable conductor; however, like metal ion implantation, increasing the conducting material reduces electrical resistivity, but at the cost of optical transmittance. In other words, both film opacity and conductivity are proportional to the amount sprayed. Fortunately, some applications do not require high conductivities— such as with actuators— which is useful when transparency is desired. A following section will briefly touch upon the use of SWCNTs as a transparent conductor. [113]

*Self-Clearing Fault Tolerance*

Microstructural defects in dielectric elastomer films can cause a short-circuit through the membrane under an applied electric potential, leading to premature dielectric breakdown well before maximum actuation strains can be obtained. Possible such defects could include gel particles, uneven thickness, nonuniform crosslinking, and stress concentration introduced during processing. [114] Dielectric elastomer actuators with electrodes of carbon grease, carbon powder, or most other electrode materials will become inactive after puncture and permanently fail, often setting the device on fire. [105, 106] To address this and extend device lifetimes, our group has pioneered the use of SWCNT electrodes for their self-clearing properties, which can circumvent electrothermal failure while maintaining almost identical actuation strain performance following a breakdown event. [115]

The nanometer-sized dimensions and high aspect ratios of SWCNTs amplify the electric field at the tip of the nanotubes. When a short-circuit passes through a defect in the dielectric elastomer, an electric arc discharge results from the amplified electric field. This arc discharge, in turn, causes the vaporization of a thin layer of the electrode radially outward from the fault. This forms isolated, non-conductive patches of SWCNTs near the fault (Figure 1.27(b)). As a result, the short-circuit through the elastomer is isolated from the intact electrodes, and the device can continue operation virtually unabated. This entire process is known as "self-clearing". SWCNTs are prone to thermally decompose during an arcing event because of their low vaporization energy. Despite being in the same family of

materials, multi-walled carbon nanotubes (MWCNTs) do not exhibit the same self-clearing behavior because multiple walls require more energy to vaporize by localized electrical breakdowns. Interestingly, charcoal powder has recently been shown to possess self-clearing properties due to its low vaporization energy (unlike graphite powder or carbon grease), but its actuation strain is far inferior to that of SWCNTs. [115-118]

Yuan et al. first demonstrated this self-clearing principle using 200% biaxially-prestrained VHB™ 4905 with SWCNT electrodes. Using a pin, they punctured the dielectric elastomer to create a temporary short between the electrodes, inducing a dielectric breakdown event. This in turn caused the voltage across the polymer dielectric to drop and the current to surge. Following the puncture, they demonstrated an 80% actuation strain at 3 kV following several self-clearing events, or 100% actuation strain excluding the cleared areas. [115] Moreover, because of the many conducting pathways available to the intact SWCNT networks (Figure 1.27(a)), many self-clearing events can occur without interrupting the overall conducting integrity of the network. [119]

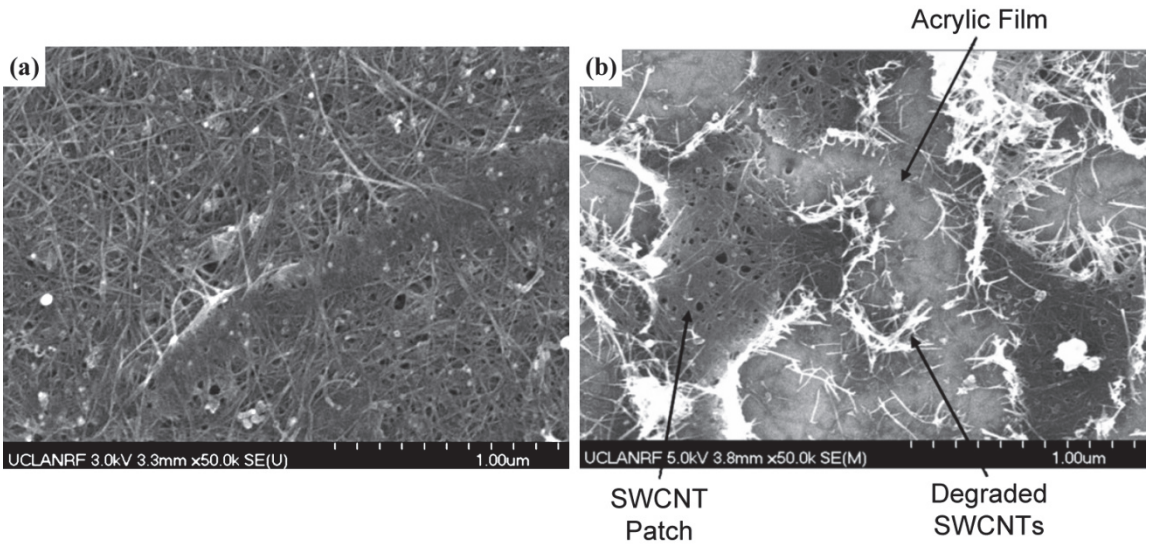


**Figure 1.27** SEM images of **(a)** an intact SWCNT electrode network and **(b)** a self-cleared SWCNT electrode surface near a fault. Isolated patches/islands of SWCNTs are visible, surrounded by insulating conduits of the acrylic film. [115]

As seen in Figure 1.28(a)–(d), puncturing a carbon grease DEA renders it nonfunctional, while introducing a puncture defect in a SWCNT DEA does not interfere with its ability to continue actuating. Figure 1.28(e) compares the actuation cycling reliability of carbon grease versus SWCNT DEAs. Actuators of 300% biaxially prestrained VHB™ 4905 were coated with carbon grease or spray-coated with P3-functionalized SWCNTs. They were then cycled between 0 and 3 kV at 80 mHz with a duty cycle ("on" percentage) of 50%. In this test, the SWCNT DEA does not reach failure until ~140 minutes, while the carbon grease DEA failed after only ~30 minutes. Breakdown events occurred in the SWCNT DEA, leading to gradually decreasing actuation strain and highly delayed catastrophic failure.

However, once even a single breakdown event occurred in the carbon grease DEA, it ceased to function. [120]

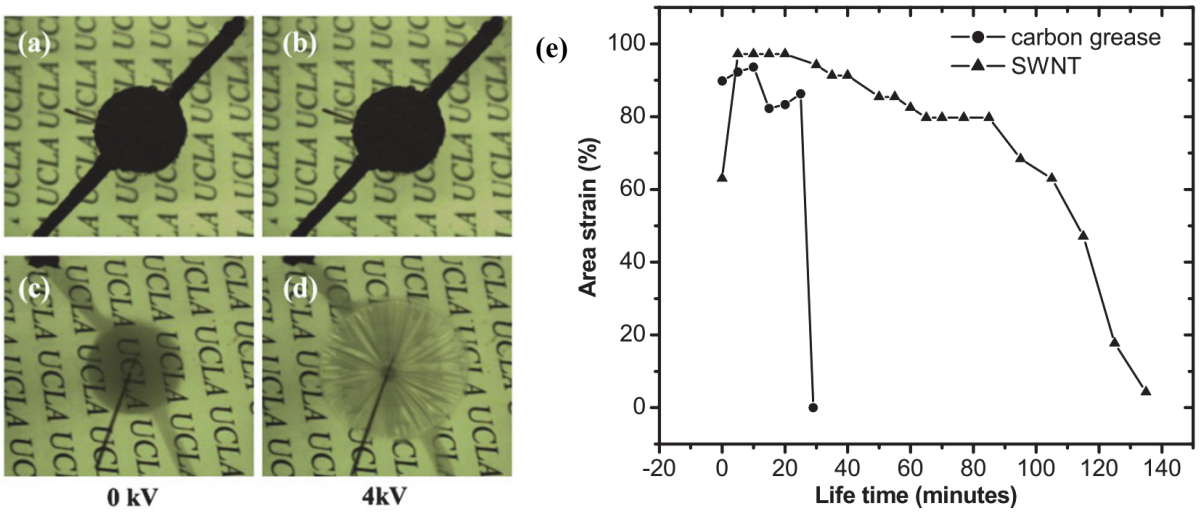


**Figure 1.28** **(a)** A carbon grease DEA punctured with a pin **(b)** no longer functions when 4 kV is applied, while **(c)** puncturing a SWCNT DEA does not drastically interfere with **(d)** its function at 4 kV. Therefore, one clearing event could lead to catastrophic failure for carbon grease DEAs, while SWCNT DEAs can continue to function, as evidenced by: **(e)** Actuation strains with time for 300% biaxially prestrained VHB™ 4905 DEAs coated with carbon grease or SWCNT electrodes, and driven with a 0 to 3 kV square wave at 80 mHz, 50% duty cycle. [120]

Thickness is a very important parameter in dielectric elastomer manufacturing, both of the electrode material, as well as of the elastomer. In the case of SWCNT electrodes, actuation performance appears to be optimal when the SWCNT thickness is between 15 and 60 nm, inclusive. As one might expect, actuation strains were lower than for a carbon grease control (Figure 1.29(a)) at a 5

nm thickness, likely due to the sheet resistance being too high. However, the 125 and 250 nm-thick samples drastically underperformed. This seems to be due to an added rigidity that the SWCNTs impart on the dielectric elastomer system when at high enough nanotube network densities. Because of the high modulus of SWCNTs, the thickness of the network must be sufficiently thin to not interfere with actuation strain. This test was performed for a 300% biaxially prestrained VHB™ 4905 DEA. [115] In addition, elastomer thickness has been shown to affect the length of time of SWCNT self-clearing events. For example, tripling the thickness of a silicone DEA (Dow Corning LC-20-2004, 25% biaxial prestrain) from 50 to 160 $\mu$m decreased the clearing period from 2 to 6 minutes for the former to only tens of seconds for the latter. One can see this in Figure 1.29(b), in which the widths of the clearing peaks noticeably decrease. This could be attributable to 15 $\mu$m-long SWCNTs moving through the fault hole to form a conductive path. Indeed, this possibility would increase with decreasing film thickness. [121] In short, because of the marked improvement in reliability, the self-clearing process is a potentially valuable discovery toward the commercialization of dielectric elastomer actuators and other compliant electronic products. [122]

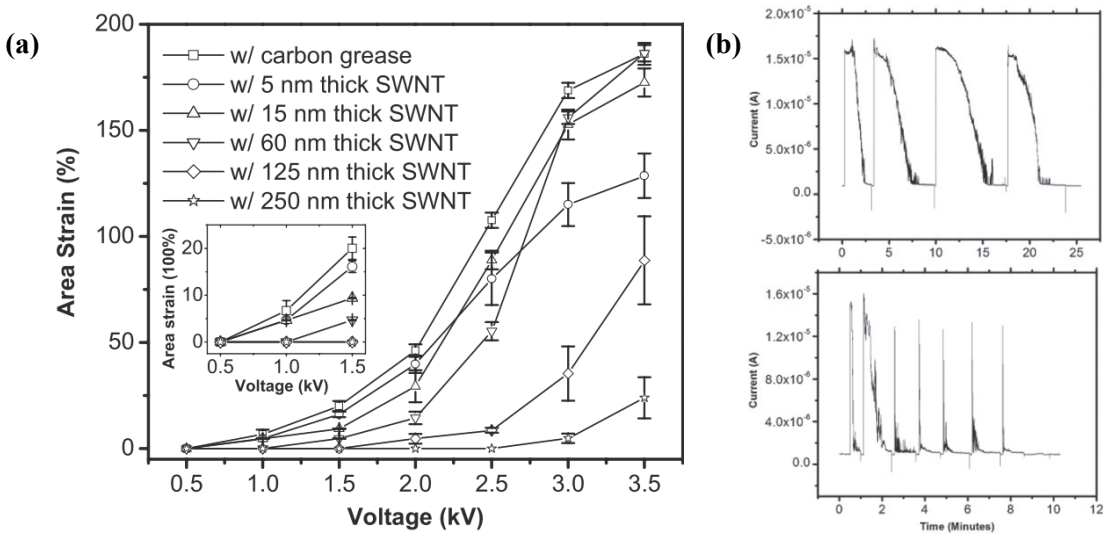


**Figure 1.29** **(a)** Area actuation strain with applied voltage for a 300% biaxially prestrained VHB™ 4905 DEA. While 5 nm SWCNT thickness is not conductive enough, thicknesses above 60 nm may overly stiffen the electrode. [115] **(b)** Chronoamperic (Time-current) plots for a silicone DEA (Dow Corning LC-20-2004, 25% biaxial prestrain) with thickness: *Top:* 50 $\mu$m and *Bottom:* 160 $\mu$m. Self-clearing peak widths are narrower for the thicker film. [121]

*Dielectric Oil*

One critical step in the self-clearing process is the generation of a coronal arc discharge prior and concomitant to the nanotube vaporization phase. If the coronal discharge can be suppressed, then the self-clearing process can be mitigated, and SWCNT electrode reliability would be advanced even further. To this end, Yuan et al. coated the SWCNT electrodes of a DEA with a dielectric oil to insulate the electrodes from air (Figure 1.30(c) and (d)). They applied 3 kV continuously at a limited current of ~3.5 $\mu$A to a 300% biaxially prestrained VHB™ film. While they do not state the initial thickness of the actuator, it is likely 0.5 mm VHB™ 4905, as

the authors utilized this tape in a separate publication on the same topic. Under these test conditions, clearing events commenced after roughly 25 minutes and continued unabated until the end of the experiment. The control SWCNT actuator area strain dropped from ~170% to ~110% after ~80 minutes, while the dielectric oil-coated SWCNT actuator maintained a ~150% area strain during the entire 1,200 minute test, as shown in Figure 1.30(e). [116, 123] This is a clear improvement in actuation performance. Practical device implementation for freestanding films may require encapsulation, although dielectric oil may be unnecessary in stack actuators or for space applications, such as the DEA satellite gripper designed by the Shea group. [124]

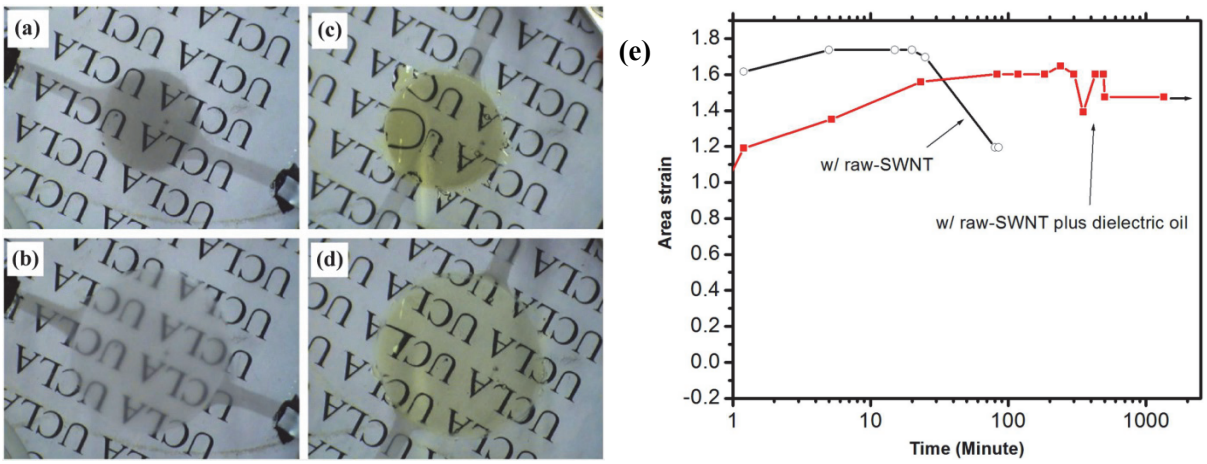


**Figure 1.30** SWCNT electrodes on 300% biaxially prestrained VHB™ 4905 at **(a)** 0V, **(b)** 3 kV, and with dielectric oil at **(c)** 0V and **(d)** 3 kV. [123] **(e)** Continuous actuation strain of these actuators at 3 kV for raw SWCNTs and for SWCNTs coated with dielectric oil. The former experiences a drop in actuation strain after ~100 minutes, while the latter continues to maintain roughly the same strain for over 1,000 minutes. [116]

*1.4.2.2.4.2 P3-Functionalized SWCNTs*

To improve solution processing versatility, manufacturers (e.g., Carbon Solutions, Inc.) have functionalized SWCNTs with hydrophilic carboxyl groups. [125] These so-called "P3-SWCNTs" (or "P3-SWNTs") are miscible in water or other non-toxic, inorganic solvents. Because the carbon nanotube structure remains intact, this functionalization does not drastically alter the electronic properties of the SWCNTs themselves. However, DEA performance using P3-SWCNTs has been observed to be slightly compromised at high strains over time, as compared to raw SWCNTs. In a continuous actuation test similar to that in the previous Dielectric Oil Section, after 35 minutes the current dropped from 3.5 to 0.2 $\mu$A, accompanied by a drop in area strain from 160% to only 20%. The loss in strain is permanent, and Yuan et al. comment that this is attributed to the P3-SWCNT electrodes losing their conductive paths. Specifically, a shorter tube length and fairly strong hydrogen bonding among –COOH groups increases the self-attraction of P3-SWCNTs as compared to raw SWCNTs, leading to the formation of isolated islands at high strains. Some nanotubes remain between these P3-SWCNT patches, but the resistance is much higher. After continuous actuation, these higher-resistance intermediate nanotubes readily thermally decompose from Joule heating, leading to the observed permanent loss of electrode conduction and actuation strain. [116, 120] Since potentially carcinogenic organic solvents (e.g., chloroform) need not be utilized during spray deposition, P3-SWCNTs may hold promise as a low-strain stretchable conductor with safe and environmentally-friendly manufacturing processes.

However, raw SWCNTs may be a more reliable stretchable conductor choice for DEA applications that require strains greater than 100%.

#### *1.4.2.2.5 Carbon/Polymer Nanocomposites*

Three primary forms of carbon-based electrodes consist of loose particles, particles suspended in a gel or polymer oil as with carbon grease, or carbon particles mixed into a soft elastomer matrix. In this latter form, the loose carbon particles are first homogenously dispersed in a viscous polymer mixture, then cured to form chemical crosslinks among the polymer chains, which entraps the conducting filler. This electrode solution addresses the lifetime and handling issues with carbon powders and carbon grease, but could potentially add stiffness to the device. [50] Traditional approaches involve mixing carbon black with a one-component silicone rubber, then dissolving the mixture in a volatile solvent and ultrasonicating for spraying onto an elastomer substrate with an airbrush. The resulting electrodes can then cure at room temperature after several hours. Kofod reports using 20 wt.% Ketjenblack carbon black in Wacker Elastosil® E43 RTV-1 silicone glue, dissolved in heptane for airbrushing. [70] In a slight variation, Carpi et al. have loaded Rhodorsil CAF 4 with Vulcan XC-72 carbon black, then dissolved in trichloroethylene for the spray deposition. [126] In yet another variant, Sau et al. filled a nitrile rubber/ethylene propylene diene rubber blend with short carbon fibers, which is shown to provide higher conductivity at lower loadings than carbon black due to their higher aspect ratios. [127-129]

Thus far, most of the methods of transferring a conducting medium onto an elastomer substrate have been reviewed: brushing, painting, spray coating, implantation, deposition, photopatterning, and inkjet printing. Stamping, also known as pad printing, is yet another such technique of flexible electrode deposition. Pad printing is quite versatile, and arrays of entire flexible electronic devices have been manufactured using this material transfer process. [130] The use of pad printing for electrode deposition was first introduced by Aschwanden and Stemmer, wherein they utilized a PDMS stamp to transfer 100 $\mu$m-wide carbon black electrodes onto a prestrained VHB™ substrate for a tunable diffraction grating. [131] Through an automated stamping process, the Shea group have improved on this technique, patterning flexible, UV-curable electrodes using a Teca Print TPM 101 industrial pad-printing machine. It operates by doctor blading a small amount of a curable electrode ink onto a shallow reservoir, which is then transferred to a stamp. The stamp in turn applies the ink to the elastomer substrate, atop a laser-cut PET mask for electrode patterning. The electrode ink is subsequently cured at 80°C, and the process is repeated for the reverse side. The ink consists of carbon black suspended in a low-modulus silicone elastomer matrix, which is typically the same elastomer used in the dielectric elastomer membrane (Sylgard® 186, Dow Corning, 10:1 ratio), or softer (< 0.7 MPa). [9, 132, 133] Post-curing, the stamped carbon black/silicone ink electrodes were 2 $\mu$m thick. [124] Figure 1.31 shows electrodes patterned with (a) a PDMS stamp and (b) the Teca Print pad-printing machine.

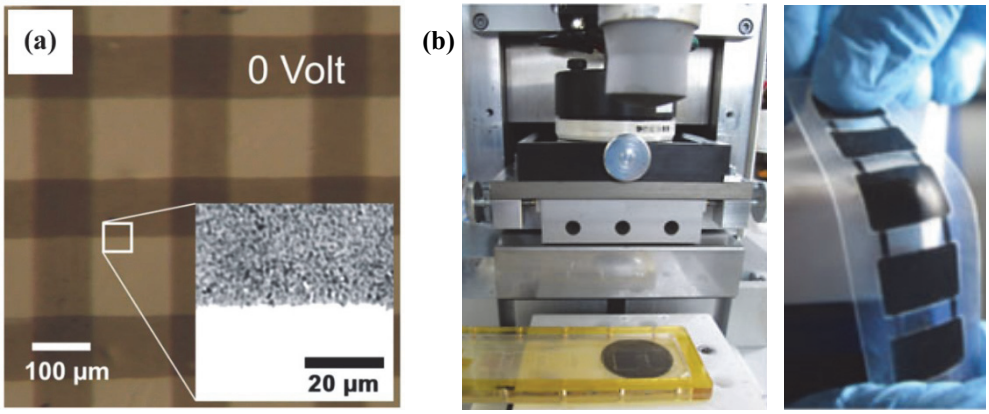


**Figure 1.31** **(a)** Microscale carbon black electrodes patterned with a PDMS stamp onto an acrylic substrate. [131] **(b)** Stamping carbon/silicone electrodes onto a silicone substrate with a Teca Print TPM 101 pad-printing machine through a laser-cut PDMS mask. [124]

#### 1.4.2.3 Conducting Polymers

Polyaniline (PANI) and polypyrrole (PPy) are two of the most widely researched conjugated conducting polymers. Pei et al. established the use of PANI as a bending ionic electroactive polymer by laminating it to flexible, semi-rigid substrates of polyethylene (PE) or polyimide (PI) and immersing in an electrolyte solution. [134, 135] More recently, encapsulated PANI was explored as a high dielectric constant filler for DEs, and PANI has also been considered for use as a stretchable electrode material in various forms for dielectric elastomers. [23, 114, 136] This section will focus on the more opaque form of PANI nanofibers, while some transparent forms of PANI will be addressed in a future section. Moreover, PPy has found application as a conductive filler in insulating epoxies, as an ionic electroactive polymer, and as a compliant electrode material in electrostrictive and

bending-electrostrictive polyurethane (PU) elastomer actuators. [137-142] The chemical structures of PANI and PPy are shown in Figure 1.32. [48, 143]

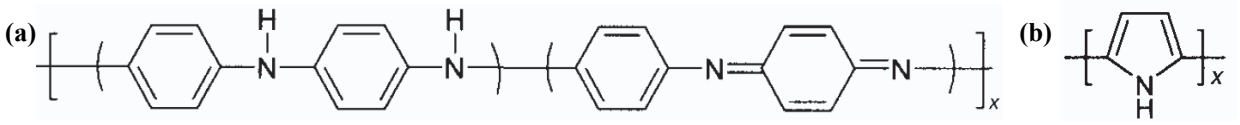


**Figure 1.32** **(a)** The half-reduced, partially protonated "emeraldine" form of polyaniline. Further protonation, such as by aqueous HCl, results in a delocalized radical cation and an increase in conductivity by $10^{10}$. **(b)** Chemical structure of undoped polypyrrole. [48, 143]

#### *1.4.2.3.1 Polyaniline Nanofibers*

PANI nanofibers have been investigated as a stretchable electrode material jointly by Lam and Tran et al. from the Pei and Kaner groups, respectively. Because of their high aspect ratios, PANI nanofibers are theoretically capable of high conductivities and actuation strains at fairly low concentrations. The PANI nanofibers were dispersed in isopropanol at a concentration of ~2 g/L, then spray deposited onto prestrained VHB™ 4905 using an airbrush. Depending on the amount sprayed, electrodes of varying thicknesses between 0.7 and 1.5 $\mu$m were created. Lam et al. postulate that in general, the thinner electrodes exhibited higher strains at lower voltages due to higher mechanical compliance, while also exhibiting lower strains than the thicker electrodes at higher voltages due to a higher reduction in conductivity from dedoping. [136]

Performance was optimal for the 1.1 $\mu$m-thick electrode, which experienced an 84% area increase and self-clearing at 3 kV. Self-clearing was observed for only

the 1.1 and 1.3 $\mu$m-thick electrodes, and of the two the 1.1 $\mu$m-thick electrode achieved the higher strains at 3.5 kV and above. The 1.1 $\mu$m-thick PANI nanofiber electrodes could also perform 700 cycles for 75 minutes at a pulsed 3 kV, and these electrodes were estimated to increase the elastic modulus of the elastomer by only ~3%. Although the PANI nanofiber films are semi-transparent at 0.7 $\mu$m thickness, they become opaque at higher thicknesses. The sheet resistance of unactuated PANI electrodes is 20–40 kΩ/sq. and they are a greenish color; after prolonged exposure to light or an electric field, the resistance increases to at least 300 kΩ/sq. and the color changes to dark blue, indicative of a dedoping process. Figure 1.33 depicts the PANI nanofiber electrodes on the microscale and macroscale. [136]

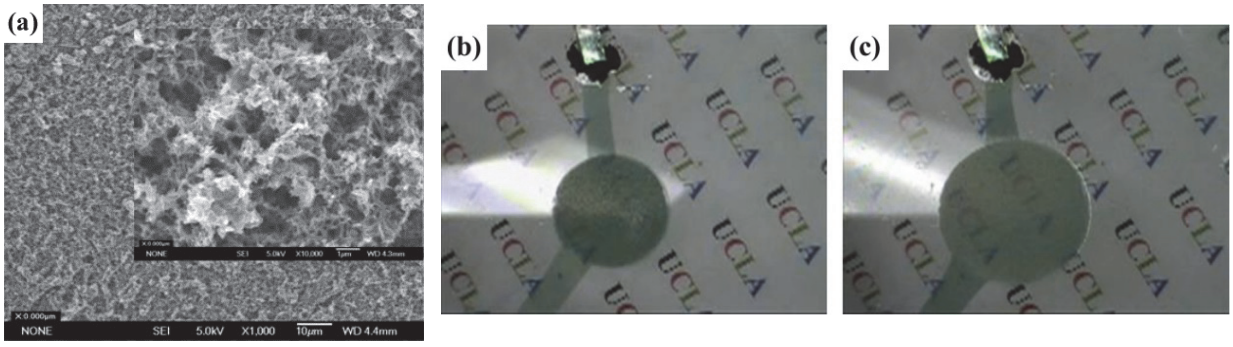


**Figure 1.33** **(a)** SEMs of PANI nanofibers at 1,000× and 10,000× magnifications. **(b)** Circular actuator of PANI nanofiber electrodes of 1.1 $\mu$m thickness at 0 V. **(c)** 84% area strain during actuation at 3 kV. [136]

#### *1.4.2.3.2 Polypyrrole*

While PPy has been traditionally used as an ionic bending actuator, Su et al. adapted it for use as a dielectric elastomer electrode material. Their ~300 Å-thick

PPy electrodes had a sheet resistance of ~1,000 Ω/sq., which is suitable for a dielectric elastomer electrode. PPy has the potential to be a transparent electrode, although specific measurements were not taken in their study to quantify the percent transmittance. These all-polymer dielectric elastomers were prepared by first casting the PU elastomer from a solution of tetrahydrofuran (THF), followed by vacuum annealing at 100°C for 30 mins. The annealed PU was then repeatedly dipped in a solution of PPy precursors to form thin, uniform electrodes with good adhesion to the PU.

To compare the electromechanical performance of the PPy electrodes to that of gold electrodes on PU, they measured the electric field induced strain coefficient $R$ at different alternating current frequencies. They define $R$ by the relationship

$$s = RE^2 \tag{1.30}$$

where $s$ is the electric field induced strain and $E$ is the applied electric field. Hence at a given electric field, a larger $R$ means a higher actuation strain results. From their observations, $R$ has a maximum at 100 $\mu$m total DE thickness for the PU films with both PPy and gold electrodes. Additionally, $R$ increases with decreasing frequency for both DEs with PPy and gold electrodes. This makes sense because the relative permittivity (dielectric constant) of materials generally decreases with increasing frequency, until only electronic polarization remains. For DEs, recall that the Maxwell pressure (or stress) $P_M$ is given by Equation 1.1. Since $P_M$ generates field induced strain $s$, $R$ is likely proportional to $\varepsilon_0\varepsilon_r$. [7, 9] Because $R$ is higher for the 100 $\mu$m PU/Au DE at 2 Hz than for the PU/PPy DE at 2 Hz, there is

strong indication of the existence of interfacial space charges building up between the Au electrodes and PU elastomer, while this effect is less pronounced for the all-polymer DE of PU/PPy, with mainly electronic polarization. [139]

Watanabe et al. improved the design of Su et al. further by creating bending-electrostrictive PU actuators using wrinkled PPy electrodes. The conductivity of these wrinkled PPy electrodes remained constant for elongations less than 40%. These actuators were fabricated by first uniaxially pre-straining a solution-cast PU film, depositing PPy electrodes by the method utilized by Su et al. above, and then relaxing the film to form wrinkled PPy electrodes. The PU films were prestrained by up to 35.3%. Application of a voltage causes a freestanding cantilever of the PU/PPy actuator to bend, and it was found that a prestrain of ~10% resulted in the largest displacement of the free end of the film. PU/PPy bending actuators at this prestrain were compared to those doped with sodium acetate, as well as to undoped, unwrinkled PU actuators with gold electrodes. At 2 V/$\mu$m, the doped, wrinkled PU/PPy actuator exhibited the highest tip displacement of ~2.75 mm, the undoped actuator displaced by only ~1.75 mm, and the PU/Au actuator bent by only ~0.5 mm. These results reinforce the observation that for the same dielectric elastomer material, actuation strain typically increases with electrode compliance and conductivity. In this case, doping increases PPy electrode conductivity and therefore actuation strain; while the gold electrodes are more conductive, their low mechanical compliance limits actuation strain. [140]

Polypyrrole has not only been used as a stretchable electrode on polyurethane elastomers, but also as a high conductivity filler in polyurethane foam elastomers. These PPy/PU composites are typically prepared by vapor phase oxidative polymerization. In this process, a prefabricated PU foam is impregnated with oxidants such as $FeCl_2$ and $FeCl_3$, usually by swelling the PU in a methanol solution of these oxidants and then vacuum drying. The oxidant-containing PU is then exposed to a PPy vapor that polymerizes inside the PU when it contacts the oxidants. The composite is then washed with methanol to remove any unreacted oxidants, then vacuum dried. [144, 145] In a solvent-free alternative, the PU foam is "doped" with oxidants by the thermally-controlled diffusion of $I_2$ and $Br_2$ vapors into the foam. The doped PU is then exposed to the PPy vapor to finish the composite. [146] The best results were obtained with a combination of $FeCl_2$ and $FeCl_3$ (1 mol to 3.5 mol, respectively), in which the resulting PPy/PU composite exhibited an elongation of 446% and a conductivity of 1.21 S/cm. This composite exhibits roughly a ten order of magnitude increase in the initial conductivity of the PU ($< 10^{-9}$ S/cm), and an almost identical elongation (463% for the initial PU).

### 1.4.3 Transparent Compliant Conductors

Many of the same basic materials can be utilized to create non-opaque stretchable conductors when transparency is required. Conducting polymers can be synthesized or processed to possess higher transparency, and carbons like CNTs can also be employed in lower concentrations, or as different allotropes such as

graphene, to render greater transparency. Metals can also be used, although more emphasis has been given to metal nanowires for transparent applications than to more opaque thin metal films, metallic fillers, or metal implantation. Moreover, metal nanowires and carbon nanotubes are capable of forming percolated networks in or on elastomers, permitting reversible deformation without drastically altering electrical continuity, as well as potentially high transparency through lower required concentrations of these materials.

#### 1.4.3.1 Ag Nanowire/Polymer Composites

Silver nanowires (AgNWs) have been shown to possess almost identical optical (sheet resistance ~3 Ω/sq.) and electronic (95% transmittance) properties to conventional transparent conductors such as indium tin oxide (ITO), yet AgNWs are much more flexible and can allow for cost-effective roll-to-roll device manufacturing through solution processing. [147-149] The high aspect ratio of AgNWs enables the formation of a percolation network with high transparency and mechanical compliance. This high aspect ratio also allows them to fuse at intercrossings at relatively low temperatures, which facilitates the formation of additional conduction pathways and further reduces the resistance of the electrode. [150, 151]

Efforts here in the Pei group have been made to improve the mechanical robustness of AgNW electrodes by making them more flexible, and even stretchable. The primary approach was to incorporate the AgNW mesh in a transparent polyacrylate elastomer to form a smooth, stretchable and/or flexible composite

electrode material. Yu et al. formed flexible composite electrodes by dispersing synthesized AgNWs in methanol, drop casting them on glass, and then drop casting the mixed polyacrylate precursor solution (an ethoxylated bisphenol A dimethacrylate, Sartomer SR-540, and photoinitiator) atop the AgNWs and UV curing to crosslink the elastomer (Figure 1.34(a)). Peeling off the cured elastomer thus transfers the AgNWs from the glass to the polymer; the result is a compliant composite conductor. The AgNW network can be seen to be embedded in the acrylate polymer in Figure 1.34(b). The AgNW/acrylate composite could withstand 16% strain when bent with virtually no change in sheet resistance, and showed a fully-recoverable ~3.9× increase in resistance when stretched by 16% strain in a tensile test. [152]

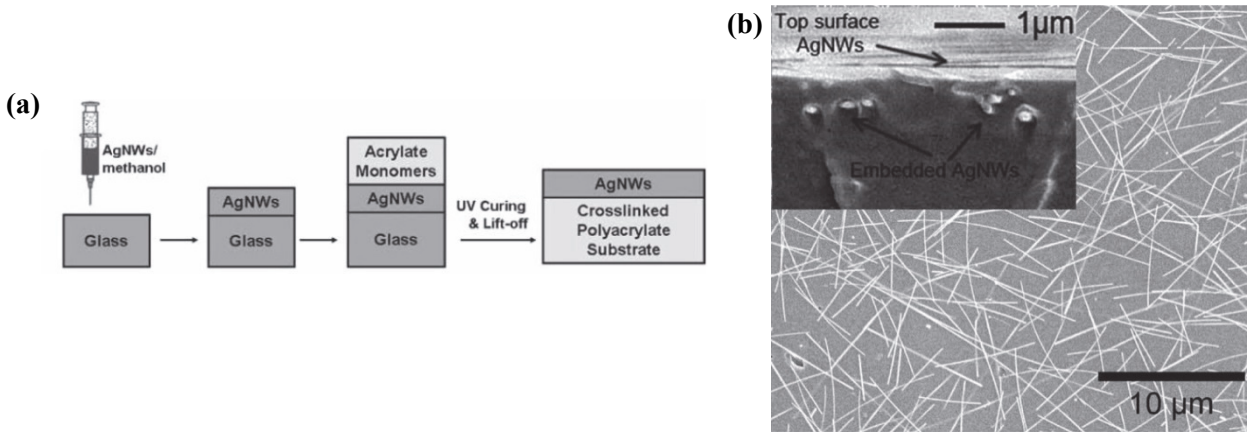


**Figure 1.34 (a)** Fabrication procedure of AgNW/polyacrylate composite electrodes, involving deposition and annealing of AgNWs, drop casting and curing the polyacrylate, and transferring the AgNWs from glass to polyacrylate. [152] **(b)** Silver nanowire network. *Inset:* Silver nanowires embedded in the upper region of the polyacrylate. [153]

Hu et al. more recently improved the performance of the AgNW/acrylate composite by including an aromatic monoacrylate (Sartomer CN-131) as well as acrylic acid (AA) to the SR-540 precursor prior to polymerization. The resulting composite exhibited an increase in sheet resistance of only 2.3× at 50% strain. The composite also exhibited transmittances at 550 nm between 90.2% and 79.6% for sheet resistances between 50.8 and 7.5 Ω/sq. The acrylate elastomer without AA had a sheet resistance 26% higher than neat AgNWs on glass, while the composite with AA had the same sheet resistance as the AgNWs on glass, indicating that the AA in the composite facilitates the complete transfer of AgNWs from glass to elastomer. Along these lines, it is thought that the presence of carboxylic acid groups from the acrylic acid enhances the bonding and reduces the void formation between the AgNWs and polymer matrix, allowing for the observed high stretchability with little increase in sheet resistance. [154]

Yun et al. developed transparent AgNW composite electrodes for use with bistable electroactive polymer (BSEP) thermoplastic DEAs. The operation of BSEP DEAs is detailed in Section 1.5.2, below. In brief, BSEPs are DEAs that are rigid at room temperature, and therefore require heating before the application of an actuation voltage. The voltage deforms the BSEP, and removing the heat locks in the actuated shape. To allow for this shape memory actuation, resistive Joule heating was originally accomplished using carbon nanotubes, [42, 155, 156] carbon black, [157, 158] Ni powders, [159] or CNT/CB composite electrodes. [160] However, high cycle lifetimes with these materials are not possible due to aggregation, and

they also require high loading content to maintain conductivity, negatively impacting mechanical strain and optical transmittance. Therefore, AgNWs were investigated as a transparent BSEP electrode material for dual Joule heating and actuation since the same resistance can be maintained at a lower AgNW content. The composite material consisted of an annealed AgNW network embedded in the top surface of a poly(*tert*-butylacrylate-co-acrylic acid) BSEP material, fabricated using a similar transfer method as with the stretchable AgNW/acrylate composite mentioned previously, shown in Figure 1.34(a). The AgNW/poly(TBA-co-AA) composite exhibited a sheet resistance as low as 10 Ω/sq., and could maintain a high level of conductivity after 5,000 continuous actuation cycles at strains from 30% to 90%. As noted above, the presence of carboxylic acid groups in the acrylic acid component of the polymer improves the bonding between AgNWs and polymer matrix. [31]

### 1.4.3.2 Carbons

#### *1.4.3.2.1 Graphene*

Graphene has recently been researched as a transparent electrode alternative where low cost and thermomechanical stability are important to the application. [161-166] Specifically, pure graphene has a thermal conductivity of ~5,000 W/m-K, a high carrier mobility in excess of 20,000 $cm^2$/V-s at room temperature, and transparency above 95%. [40, 167-171] Additionally, graphene can be grown in one or multiple layers, and its properties change with layer number.

[172] Recently, graphene has been shown to be suitable as not only a transparent conductor, but a compliant one as well.

De et al. demonstrated the use of randomly stacked graphene sheets as a flexible, transparent electrode with conductivities up to $1.5 \times 10^2$ S/cm, stable for at least 2,000 bending cycles. [173] In another study, Bae et al. utilized chemical vapor deposition (CVD) on copper substrates to create films with ~125 Ω/sq. sheet resistance and 97.4% optical transmittance, as well as four-layer films of ~30 Ω/sq. and ~90% transparency. Kim and colleagues demonstrated similar results with their graphene transparent conductors, obtaining original resistance recovery after stretching by ~6%, although typically exhibiting mechanical failure beyond this. To attempt to overcome these strain limitations, the graphene was transferred to an isotropically prestrained PDMS substrate, resulting in stable longitudinal and transverse resistances up to ~11% stretching and exhibit only one order of magnitude increase at ~25% stretch. Their graphene conductors possessed 80% optical transmittance and a minimum sheet resistance of 280 Ω/sq. and were grown by CVD on nickel before transferring to PDMS. [174]

#### *1.4.3.2.2 Carbon Nanotubes*

Due to their variable opacity, carbon nanotube films have been employed not only as an opaque electrode material, but as a transparent electrode material as well. [175-178] As mentioned in a previous section, Hu et al. have explored using SWCNT thin films as a transparent electrode material for DEs. SWCNTs spray

deposited onto a 300% biaxially prestrained film of transparent 3M™ VHB™ 4905 showed an increase in transmittance at 550 nm from 37% to 50% at 50% area strain. [113] Additionally, Yu and coworkers developed transparent SWCNT/poly(*tert*-butylacrylate) (P*t*BA) composite electrodes. The composite was fabricated using the same transfer method depicted in Figure 1.34(a). The composite electrodes exhibited a good combination of conductivity and transparency: A 500 Ω/sq. electrode has 87% transmittance at 550 nm, 200 Ω/sq. with 77% transmittance, 50 Ω/sq. with 63%, and 20 Ω/sq. with 40%. After heating to 70°C, the composite could be stretched to up to 50% strain with reversible resistance changes. [179] Atomic force micrographs depict the surface morphology of neat SWCNTs on glass and of the SWCNT/P*t*BA composite in Figure 6.3(a).

#### 1.4.3.3 Conducting Polymers

##### *1.4.3.3.1 PEDOT:PSS and P3DOT*

Poly(3,4-ethylenedioxythiophene):poly(styrenesulfonate), or PEDOT:PSS, has been widely investigated as a cost-effective, transparent, mechanically compliant, and solution-processable alternative to ITO (Figure 1.35(a)). [49] PEDOT is a positively-doped conjugated polymer, which is accompanied by an aqueous solution of PSS counteranions. [180, 181] Further doping of PEDOT:PSS using polar solvents such as ethylene glycol (EG) and other alcohols, dimethyl sulfoxide (DMSO), and *N*,*N*-dimethylformamide (DMF) has been shown to increase conductivity by up to three orders of magnitude, nearing ~100 S/cm. [182]

Polymerizing EDOT-$CH_2OH$ in lieu of the monomer EDOT resulted in a conductivity of 900 S/cm, and more recent work utilizing vapor phase polymerized PEDOT gave a conductivity of 1,100 S/cm. [183, 184] By using a novel solvent post-treatment process, Kim et al. have reported conductivities as high as 1,418 S/cm and 88% transparency. By comparison, ITO has a conductivity of up to $10^4$ S/cm and similar transparency. Their PEDOT:PSS (PH-1000 from H. C. Starck) was treated with EG, then post-treated for 30 minutes to remove excess PSS. In addition, pre-heating the PEDOT:PSS electrodes when utilized in an organic solar cell resulted in a power conversion efficiency and fill factor nearly identical to the same solar cell with ITO electrodes. [185]

Typically, PEDOT:PSS is quite rigid, with an elastic modulus of ~2 GPa and an elastic strain limit of only 2%. [186] One common alternative is to blend PEDOT with elastomers to create stretchable conducting composites. Hansen et al. blended the conductive polymer PEDOT:*p*-tosylate by up to 50 wt.% with an aliphatic polyurethane elastomer to form a stretchable conductor with a conductivity of 120 S/cm, which increased to ~160 S/cm when elongated to ~50%. Up to 50% strain this conductivity increase was recoverable, but above 50% strain, the composite unrecoverably lost conductivity to ~40 S/cm at 200% elongation, and down to ~15 S/cm at 0% strain. [187] Kwon et al. created a stretchable composite by incorporating a paste of PEDOT in a polyionic liquid into a poly(ether-b-ester) (PEEA) elastomer matrix. Its resistance increased by only a factor of two upon stretching to 350% strain, but its initial conductivity was only ~$10^{-3}$ S/cm. [188]

While these stretchable conductors are only semi-transparent, creating more transparent PEDOT/elastomer composites should be theoretically possible since PEDOT is a transparent polymer.

Perhaps the best combination of conductivity and stretchability in a PEDOT/elastomer composite was demonstrated by Lipomi et al., in which they spin-coated PEDOT:PSS with 1% Zonyl fluorosurfactant and 5% DMSO dopants onto oxygen plasma ($UV/O_3$) treated PDMS. With this material, they achieved 550 S/cm (260 Ω/sq.) and 95% transmittance at 0% strain. At 50% strain, the resistance increased by 2.7 times, and at 188% strain (at which the PDMS substrate failed), the resistance increased to 42 times its original value. Nevertheless, the conductivity and transparency are quite high for this class of stretchable conductors, and this material is capable of reversible strains up to 30%. [189] In a related work, the fluorosurfactant Zonyl was also employed as a secondary dopant to PEDOT:PSS, in which they achieved similar performance of 240 Ω/sq. and 97% transmittance at 550 nm. Multilayering can lower the sheet resistance further to 46 Ω/sq. (and 82% transmittance). They also utilized PDMS substrates, but with prestrain, resulting in a conductor capable of over 5,000 stretching cycles at 10% strain with no change in sheet resistance. The prestrain was released to form buckles prior to cyclic loading, whose presence were confirmed via optical microscopy. More discussion on buckling follows in the next section.[190]

Poly(3-decyloxythiophene-2,5-diyl) (P3DOT) (Figure 1.35(b)), a variant of PEDOT, has been investigated as a conducting polymer in various organic

electronic devices, such as organic photovoltaics. [191] Yuan et al. have explored P3DOT for use as a stretchable electrode material on VHB™ 4905 DEAs. [114] A solution of 0.5% P3DOT in chloroform was spray deposited onto the prestrained VHB™ through a shadow mask. Then, nitrosonium hexafluoroantimonate ($NOSbF_6$) in acetonitrile was added as a dopant to render the polymer conductive. Completion of the doping process was marked by the transformation of the electrode color from blue to transparent. The sheet resistance was ~300 Ω/sq. At an actuation voltage of 2.5 kV, an area strain between 70% and 100% was observed.

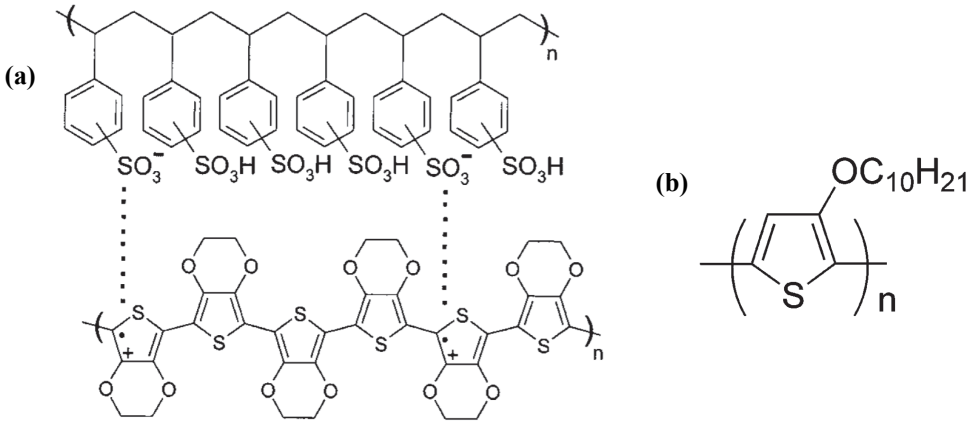


**Figure 1.35** **(a)** Chemical structure of PEDOT doped with PSS, available as BAYTRON® P. [49] **(b)** Chemical structure of undoped P3DOT, which is similar to that of undoped PEDOT. [191]

Additionally, with a 5 MΩ current-limiting resistor, self-clearing was observed for the P3DOT electrodes at 3 kV once a defect was introduced with a pin puncture. The self-clearing process proceeded for 3–4 seconds accompanying a large spike in current, after which the current subsided to a low, stable value. Because

cleared areas reverted to the original blue color, self-clearing resulted in a de-doping process, in which heat from the self-clearing rendered the affected regions nonconductive. Such is the desired property of any self-clearing electrode, in which a fault is electrically isolated from the rest of the electrode so that it does not affect actuation performance. A micrograph of the self-cleared region on a P3DOT/VHB™ actuator is shown in Figure 1.36. [114]


**Figure 1.36** P3DOT:$NOSbF_6$ electrodes on a prestrained VHB™ actuator, magnified to the vicinity of the pin contact point and self-cleared region surrounding it. The de-doped, self-cleared region has a blue color, in contrast to the transparent un-cleared area. [114]

#### *1.4.3.3.2 Polyaniline*

In addition to P3DOT, Yuan and colleagues spray deposited PANI onto VHB™ to be studied as a transparent actuator electrode material. The results of this approach contrast with those utilizing PANI nanofibers, which yielded opaque to semi-transparent stretchable electrodes, as mentioned in a previous section. The spray-deposited PANI solution consisted of a 2 wt.% polyaniline emeraldine base doped with dodecylbenzenesulfonic acid (DBSA) in toluene. The sheet resistance of the PANI electrode was ~400 Ω/sq., slightly higher than that of the P3DOT and

SWCNT electrodes tested. As observed with the SWCNT, P3DOT, and PANI nanofiber electrodes, these PANI electrodes also demonstrated self-clearing. Following a pin puncture, the self-clearing event electrically isolated the fault, reaching completion after ~10 seconds at 3 kV. Compared to SWCNTs and P3DOT, the clearing process took 2–3 times longer due to the high thermal stability of doped PANI. Area actuation strain at 2.5 kV was comparable to that of P3DOT at 70% to 100%. [114]

The above work is notable as one of the first attempts at utilizing PANI as a transparent, stretchable electrode material. Traditionally, PANI has been explored as a transparent electrode material with moderate flexibility but not stretchability. A seminal work to this end by Gustafsson and Heeger et al. explores the use of PANI as a flexible, transparent electrode in PLEDs of poly(2-methoxy-5-(2'-ethyl-hexyloxy)-1,4-phenylene vinylene) (MEH-PPV). The PLED consists of a flexible, transparent PET substrate coated with a PANI anode, followed by the MEH-PPV emissive layer and cathode. They report that the device can be bent sharply and curled without failing. [192] Future work by Yang and Heeger utilizes PANI in conjunction with a thin (< 600 Å) layer of ITO as the anode, achieving up to a 50% reduction in operating voltage and up to a 40% increase in quantum efficiency than for MEH-PPV PLEDs using ITO alone. [193]

#### 1.4.3.4 Electrolyte Electrodes

Perhaps less conventional is the use of an aqueous electrolyte, such as salt water, as an electrode material for stretchable electronics. McCoul and Ha have demonstrated actuation and capacitive sensing of biaxially prestrained, untreated VHB™ 4905 immersed in an electrolyte solution of aqueous sodium chloride (NaCl). McCoul affixed the VHB™ to the end of an electrolyte-filled tube, deformed by the hydrostatic pressure from the column of NaCl water, and then submerged in an exterior NaCl bath, as shown in Figure 1.37(a). A similar procedure was performed in the dissertation of Ha. [194] For sensing, the capacitance across the VHB™ membrane was measured between the electrolyte solution in the tube and the exterior bath with a digital multimeter. The capacitance $C$ of a dielectric elastomer is

$$C = \varepsilon_0 \varepsilon_r \frac{A}{t} \tag{1.31}$$

where $A$ is the area of electrode overlap and $t$ is the thickness of the elastomer. The observed change in capacitance is therefore related to the change in DE membrane geometry from the hydrostatically induced pressure bias. Actuation was also performed by applying a high voltage between the two electrolytes, which caused the membrane to expand outward (down). Although sensing can be quite precise (Figure 1.37(b)), proper sealing of the solutions can be difficult, and a high leakage current often results as ions are driven into the untreated elastomer when actuated at high voltages.

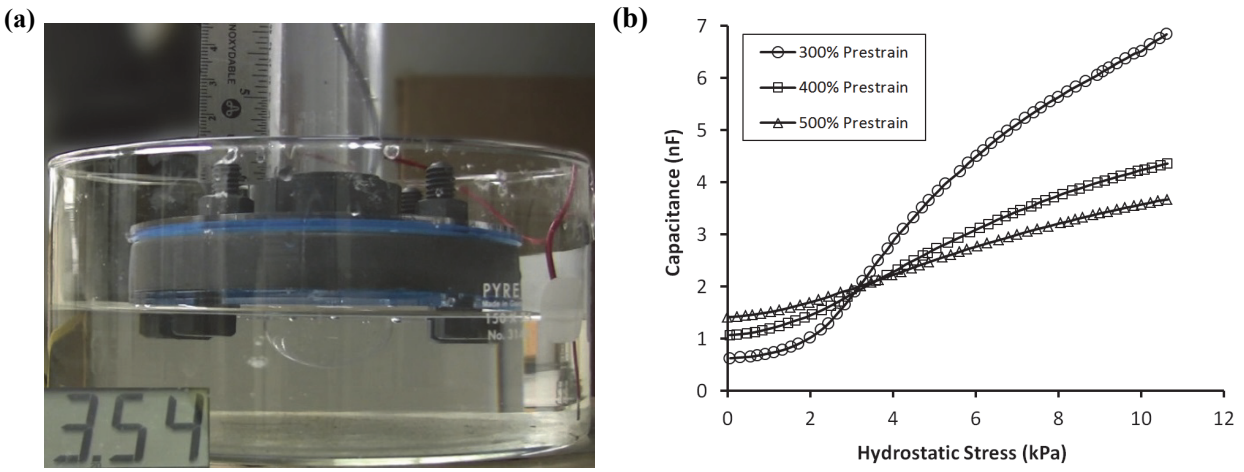


**Figure 1.37** **(a)** Capacitive sensing and actuation setup with prestrained VHB™ 4905 and NaCl electrolyte electrodes. The multimeter reads 3.54 nF across the single-layer VHB™ semisphere. **(b)** Hydrostatic pressure from the column of aqueous electrolyte versus capacitance across VHB™ 4905 at various biaxial prestrains.

In applications that will be used on land, encapsulation may be required, potentially adding bulk and complexity to the system. For applications where the active device would be submerged in an aqueous medium, however, this approach would actually simplify the system, avoiding the need to deposit additional electrodes. Shivapooja et al. have used salt water as an electrolyte electrode on the outer surface of a metal coated with an elastomer/rigid insulator laminate. They immersed PDMS bonded to Au-sputtered polyimide (PI, Kapton™) into a salt water bath containing *Cobetia marina* bacteria and let a biofilm accumulate over 4 days. After a biofilm had adhered to the PDMS, a DC voltage was applied between the metal and the salt water, and the elastomer deformed, forming craters that mechanically perturbed and released any accumulated biofilms. It is theorized that

biofilm debonding occurs when the elastomer deforms above a critical strain, wherein the elastic energy exceeds the biofilm adhesion energy, causing delamination cracks to propagate at the biofilm/polymer interface. Using this approach, the hulls of existing sea vessels could be coated with a thin layer of the PDMS/PI laminate to be used as a simple, cost-effective electroactive antifouling coating for barnacles and other accumulated biofilms. [195] Figure 1.38 shows the operating principle of this smart coating, and the strains required to release biofilms of *C. marina*. More detail on the operating principle, known as "creasing to cratering instability" is discussed in Section 1.6.3 below.

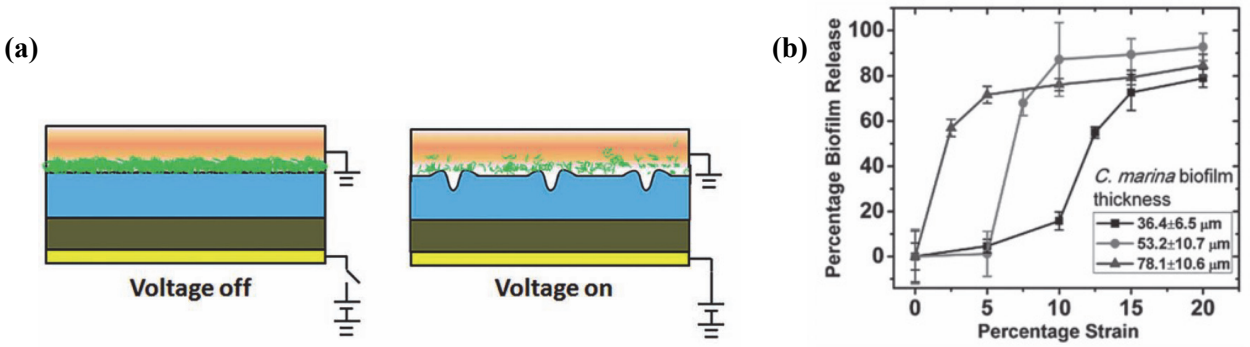


**Figure 1.38** **(a)** Operation of silicone/PI anti-biofouling smart coating, with a salt water electrolyte functioning as the top electrode. **(b)** Percentage of strain needed to release biofilms of *C. marina* of varying thicknesses. [195]

For land applications that are not in direct contact with salt water or other aqueous electrolytes, a more practical approach could utilize a hydrogel to contain an ionic electrolyte. Keplinger et al. have demonstrated a transparent actuator of VHB™ dielectric and ionic electrodes of 100 $\mu$m-thick polyacrylamide hydrogel

containing a NaCl electrolyte. The actuator system also consists of a solid Cu electrode that interfaces with the hydrogel electrode, but the solid electrode need not come in contact with the active area (Figure 1.39(a)–(d)). The Cu electrode allows for the formation of an electrical double-layer between hydrogel and metal, with a very high capacitance, due to the separation of charges over merely nanometers. The design is thus essentially two capacitors in series: the double layer (DL) and the VHB™ dielectric (D).

Charge equals the product of capacitance $C$ and voltage $V$, and both capacitors accumulate the same amount of charge under an applied voltage. Hence, $C_{DL}V_{DL} = C_D V_D$ when area is ignored. Since $C_{DL}$ is roughly $10^7$ times that of $C_D$, voltages in excess of 10 kV may be applied across the dielectric for electromechanical transduction, while still ensuring that the voltage across the metal-hydrogel interface is less than 1 V to prevent charge migration or an undesirable electrochemical reaction. [196-199] Although ions do not cross the metal-hydrogel interface under these conditions, ion migration may still be an issue across the VHB™ due to the high voltages there. Keplinger et al. applied up to 20 kV to a 1 mm-thick VHB™ 4910 elastomer, a field slightly below the breakdown field (~25 MV/m) for this unprestrained material. [200, 201] It is possible that, over a dielectric thickness of 1 mm, the effect of ion migration is mitigated. However, further testing may still be needed to ascertain the full effect of ion migration on reliability over many actuation cycles.

Using these hydrogel/electrolyte electrodes, they were able to achieve an area strain of up to 167%, which approached zero as the frequency neared $10^3$ Hz. This behavior is comparable to that of carbon grease electrodes, except that these electrolytic electrodes are highly transparent to all frequencies of visible light, with a 98.9% average transmittance at a 5.48 *M* NaCl concentration. As shown in Figure 1.39(e), the hydrogel electrodes offer the best combination of low sheet resistance and high transparency, in applications where transparency is a priority. This class of transparent, stretchable electrodes is also potentially well suited for applications where biocompatibility is of concern. [196]

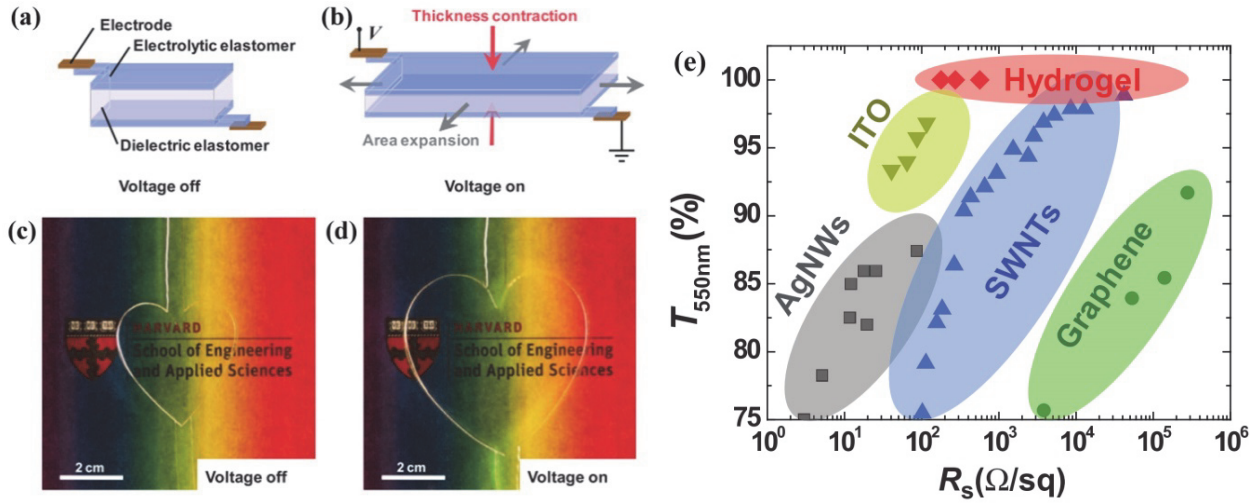


**Figure 1.39** **(a)** and **(b)** illustrate the structure and operation of the DEA with hydrogel/NaCl electrodes and Cu metal contacts. **(c)** and **(d)** depict an area expansion of a heart-shaped DEA of this actuator with highly-transparent hydrogel electrodes. **(e)** Percent transmittance as a function of sheet resistivity for the major classes of transparent electrode materials. [196]

### 1.4.4 Opaque Compliant Conductor Architectures

#### 1.4.4.1 Corrugated Metal Thin Films

While prestretching in one direction can cause fairly uniform buckling morphologies, perhaps the most uniform buckling and highest reliability can be produced by patterning corrugations directly onto the surface of an elastomer film. In this approach, a highly-ordered corrugated surface pattern can result from casting a silicone elastomer in a mold, which is typically micromachined via a photolithographic process. After curing the patterned elastomer, a metal such as silver is evaporated on the surface by physical vapor deposition. The resulting compliant conductor is stretchable only along the axis perpendicular to the corrugated rows; the axis parallel to the corrugated rows will remain stiff, constrained by the metal foil (Figure 1.40).

Corrugated stretchable conductors are commercially manufactured by Danfoss PolyPower A/S. Benslimane et al. spun cast Wacker Elastosil® RT 625 silicone precursor on their custom corrugated mold, resulting in a 20–25 $\mu$m-thick stretchable conductor with corrugations on one side. After evaporating Ag to a thickness of 70–110 nm, a pair of corrugated conductors can be stacked to form a dielectric elastomer. They demonstrated that their corrugated electrodes are capable of over 3 million actuation cycles with no change in strain or electrode damage. Their corrugated electrodes can also achieve > 80% strain with no damage to the metallic layer by using a 1:1 height-to-period ratio. [202] Xiao et al. from the Rogers group performed finite element analysis of these structures of Au thin films

on corrugated PDMS substrates, additionally deriving an analytical expression for the maximum film strain in terms of the film and substrate elastic moduli, film thickness, and the amplitude and wavelength of the corrugated profile. [203]

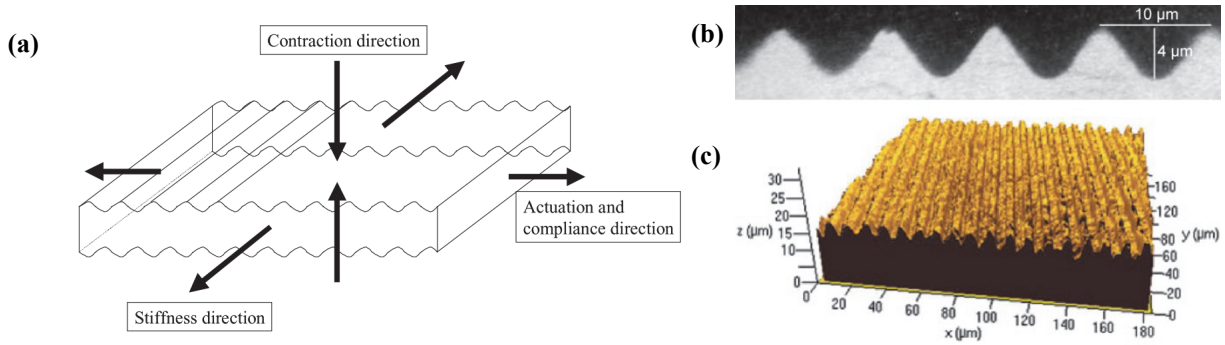


**Figure 1.40** **(a)** Illustration of a dielectric elastomer actuator with corrugated stretchable electrodes. The elongation is anisotropic since the elastomer is roughly 100× softer in the corrugated direction. [202] **(b)** Optical micrograph of the photolithographically-etched mold used to cast silicone with the corrugated surface. [202] **(c)** Laser scanning micrograph of surface of a polypyrrole actuator with corrugated gold electrodes. [204]

In a similar approach, Jeong et al. created stretchable silver electrodes 700 nm-thick deposited onto a PDMS substrate with a corrugated surface morphology, obtained from an aluminum mold. Additionally, the mold surface was roughened via wire electrical discharge machining, in turn roughening the wavy PDMS surface and improving adhesion of the evaporated silver. These silver electrodes exhibited a five-fold increase in resistance after 10,000 cycles of 10% strain, and a three-fold increase in resistance at 50% strain. [205] While these Au/PDMS electrodes are similar, it appears that the commercialized Au/Elastosil corrugated electrodes from

Danfoss exhibit superior performance. In short, corrugated metallic electrodes provide good mechanical and electrical performance for dielectric elastomers and stretchable electronic devices. Due to the corrugations, these electrodes can withstand very large displacements, while still allowing the use of metallic conductors without damage to the metal thin film. In general, the buckling structure— whether fabricated by this method or by ones mentioned previously— offers the most straightforward solution to the problem of using a metal as a stretchable electrode material without compromising performance or reliability.

#### 1.4.4.2 Zigzag Metallic Traces

Pelrine et al. could obtain strains of 80% while still retaining conductivity in gold-sputtered silicones with "zigzag" scores patterned via photolithography. Figure 1.41(a) illustrates this compliant conductor concept, in which scored traces 5 $\mu$m wide separate a Au thin film into parallel zigzag strips. The traces add compliance to the Au film, relieving stress and enabling the film segments to flex along the surface plane like springs. Figure 1.41(b) depicts crack-free ~30% strain in the zigzag direction. Surprisingly, electrical continuity is able to be maintained across the traces since the distance is small enough that even air can act as a sufficient conductor. Hence, these low-conductivity traces can also help to limit current flow in the case of catastrophic breakdown, thus mitigating the effects of such an event and acting as a safety feature. [9]

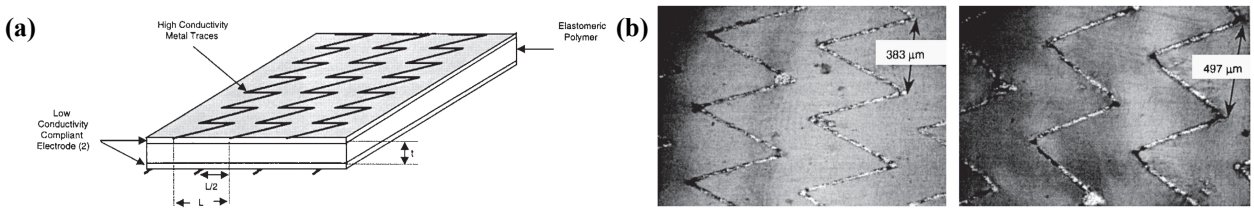


**Figure 1.41** **(a)** Schematic of the concept of zigzag Au electrodes on a dielectric elastomer. **(b)** Micrograph of the surface of a zigzag-structured Au electrode undergoing elongation in the zigzag direction. [9]

### 1.4.5 Summary

The mechanical, electrical, and optical properties of some of the compliant conductors discussed above are compared in Table 1.3. This table includes the more conventional DE electrode materials discussed above, as well as the less common DE electrode materials, which are covered in detail in the Appendix. One of the materials with the best overall performance for DEA electrodes is raw single-walled carbon nanotubes. SWCNTs have high enough aspect ratios to remain conductive enough for DEs (~120 Ω/sq.) at low concentrations, allowing for high stretchability and transparency. Along these lines, uniformly spray depositing SWCNT dispersions in small amounts renders any surface conductive with little footprint, almost like spraying charges directly onto the elastomer (except that this is still a voltage-controlled, not a charge-controlled, case). The high aspect ratios also allow SWCNTs to remain conductive at high strains (>100%), which is one of the most important requirements of DE electrodes. SWCNTs also conform and adhere remarkably well to their substrates, resulting in a high degree of reliability. And as

an added strength, the special property of self-clearing increases the service reliability even further.

Another good candidate for DE electrodes is FCVA-implanted gold and other metal ions. Such stretchable electrodes can have sheet resistances as low as 200 Ω/sq. at no strain, with reversible changes in resistance at tensile strains of 175%, and moderate transparency of 55% at 550 nm. Such electrodes have shown reliability up to 100,000 stretching cycles at 30% strain. However afterwards, the sheet resistance increases to ~11,000 Ω/sq. at no strain, which may have an effect on the actuation strain of the DE at the same electric field. Compared to FCVA-implanted Au electrodes, SCBI Au electrodes have a slightly lower calculated sheet resistance of ~138 Ω/sq. at no strain, but more importantly show an increase to only 420 Ω/sq. after 50,000 stretching cycles at 40% strain. Still, more information may be needed to conclude higher reliability, as testing at 100,000 cycles would offer the best comparison.

Of the other stretchable conductors, those composites containing metals with the best performance are opaque EGaIn in SEBS and transparent long AgNWs on Ecoflex®. For carbons, among the highest performing opaque conductors is the 15 wt.% MWCNTs in SEBS composite, and the transparent conductor with the best performance is the SWCNT aerogel. And for conducting polymers, both Metal Rubber™ and the NaCl hydrogel offer the best performance, and both have varying degrees of transparency. All of these stretchable conductors are described in the Appendix.

The opaque conductor that combines the highest overall degree of stretchability (700% strain) and conductivity ($3 \times 10^{-5}$ Ω-cm) is SEBS filled with eutectic Gallium-Indium (see Appendix). This composite is also highly reliable, showing no change in conductivity after 100 stretching cycles at 300% strain, as well as highly robust, showing only a small change in conductivity at maximum strain that is fully reversible. This is a unique case, whereby metallic conductivity is possible with a liquid metal at room temperature, then confined and mechanically reinforced by a highly resilient elastomer. When transparency is not a design requirement but ultrahigh conductivity and stretchability are required, this conductor is one of the best options. It would be well suited for stretchable interconnects, antennas, and cables. On the other hand, this material may not be as ideal for dielectric elastomer electrodes since conformability and adhesion to the elastomer are at much higher priority for DEs than is high conductivity. Nevertheless, several DE designs incorporating EGaIn as the compliant electrode material can be envisioned.

Of all these conductors, the one that combines some of the highest degrees of stretchability (530% strain), sheet conductance (150 Ω/sq. or 1.5 Ω-cm), and transparency (~99% for all visible frequencies) is the polyacrylamide hydrogel swollen with a sodium chloride electrolyte. However, the long-term reliability of this material remains a topic of future study. Another remarkable material that allegedly excels in many respects is Metal Rubber™ (see Appendix), with reported high stretchability (1,000%), conductivity ($2 \times 10^{-5}$ Ω-cm), transparency (up to 90%

at 550 nm), and reliability, showing no change in conductivity after 1,500 cycles at 10% strain.

## Table 1.3. Comparison of Compliant Conductor Properties[a]

| | | Mechanical Properties | | | Electrical Properties | | | Optical Properties | | Special Properties | Ref. |
|---|---|---|---|---|---|---|---|---|---|---|---|
| | | Max. Tensile Strain | Cyclic Reliability | | Sheet Resistance | | | Trans-mittance | Frequency | | |
| | | | *n* | at Strain | At 0% Strain | At Max. Strain | After *n* Cycles | | | | |
| | | (%) | (cycles) | (%) | (Ω/sq.) | (Ω/sq.) | (Ω/sq.) | (%) | (nm) | | |
| **Metals** | Reduced Pt Salt/Loctite® 3180 PU | 150 | 1,000 | 30 | 2.0 | 20,000[b] | ∞[c] | – | – | – | [97] |
| | FCVA-Implanted Au/PDMS | 175 | 100,000 | 30 | 199 | 550,000[d] | 10,945[b] | 55 | 550 | – | [84] |
| | SCB-Implanted Au/PDMS | 97 | 50,000 | 40 | 138[d] | 6,300[d] | 420[d] | – | – | – | [81] |
| | EGaIn/SEBS | 700 | 100 | 300 | $8.3\times10^{-4}$ [e] | $3.3\times10^{-2}$ [b,e] | $8.3\times10^{-4}$ [e] | – | – | Partial Self-Healing | [26] |
| | AgNW/Acrylate Elastomer | 50 | 600 | 50 | 7.5 | 17.25[b] | 63.75[b] | 80 | 550 | – | [154] |
| | AgNW/PtBA-AA (at 80°C) | 160 | 1,000 | 90 | 10 | 10,000 | 1,050 | 45 | 550 | Shape Memory | [31] |
| | AgNWs on Dopamine/PDMS | 20 | – | – | 35 | ∞[c] | – | 80 | 550 | – | [52] |
| | Long AgNWs on Ecoflex® | 460 | 200 | 150 | 9 | 90[b] | 90[b] | 90 | – | – | [33] |
| | Long CuNWs on PET | – | 1,000[f] | – | 30 | – | 40 | 85 | 550 | – | [29] |
| | Cu Nanofiber Mesh on PDMS | 10 | – | – | 12.0 | 12.6[b] | – | 80 | 300–1,100 | – | [206] |
| | CuNW/PU | 90 | 200 | 60 | 8.5 | 210[b] | 31.5[b] | 70 | 550 | – | [207] |
| **Carbons** | Carbon Grease on VHB™ | 215[g] | – | – | 100,000[d] | – | – | – | – | – | [7, 103] |
| | Due-ci D-77 Graphite Spray on VHB™ | 6[g] | – | – | 40,000[d] | – | – | – | – | – | [103] |
| | Raw SWCNTs on VHB™ | 700 | 300 | 100 | 120[d] | $4.0\times10^{6}$ [d] | 1,560[b,d] | 37 | 550 | Fault Tolerance | [113] |
| | Jet-Milled SWCNTs/BMITFSI/PDMS | 118 | 1,000 | 70 | 2.1[h] | – | 2.1[h] | – | – | – | [37] |
| | SWCNTs/BMITFSI/ShinEtsu KE 441 | 300 | 20 | 200 | 50 | 320 | 160 | – | – | – | [208] |
| | SWCNTs/PtBA (at 70°C) | 50 | 15 | 40 | 200 | 356[b] | 230[b] | 77 | 550 | Fault Tolerance, Shape Memory | [179] |
| | Aligned SWCNTs/PDMS | 120 | 30 | 100 | 18,800[i] | 47,300[i] | 35,500[i] | 60 | 400–800 | – | [209] |
| | SWCNT Aerogel/PDMS | 250 | 20 | 100 | 23.1[d] | – | 23.1[d] | 93 | 400–800 | – | [210] |
| | Cross-stacked Super-Aligned CNTs/PDMS | 28 | 200 | 15 | 800[j] | 920[b, j] | 800[b, j] | 69 | 550 | – | [211] |
| | 15 wt.% MWCNTs/SEBS | 611 | – | – | 3.9[j] | – | – | – | – | – | [110] |
| | MWCNTs/PU | 100 | 100 | 100 | 3.8[h] | 4.5[b,h] | 3.8[b,h] | – | – | – | [41] |
| | Graphene on PDMS | 25 | – | – | 280 | 2,800[b] | – | 83.7 | 550 | – | [174] |
| **Conducting Polymers** | PANI Nanofibers on VHB™ | 97[j] | – | – | 20,000 | – | – | – | – | Fault Tolerance | [136] |
| | PANI/DBSA on VHB™ | 100[j] | – | – | 400 | – | – | – | – | Fault Tolerance | [114] |
| | PEDOT:PSS (Clevios™ PH1000)/EG | – | – | – | 65 | – | – | 80 | 550 | – | [212] |
| | PEDOT:PSS/PU | 200 | 10 | 50 | 140[h] | 560[b,h] | 224[b,h] | – | – | – | [187] |
| | PEDOT:PSS/Zonyl®/DMSO on PDMS | 10 | 5,000 | 10 | 46 | 46 | 46 | 82 | 550 | – | [190] |
| | P3DOT:NOSbF$_6$ on VHB™ | 100[j] | – | – | 300 | – | – | – | – | Fault Tolerance | [114] |
| | Metal Rubber™ | 1,000 | 1,500 | 10 | 1.0[h] | – | 1.0[b,h] | 90 | 550 | – | [213, 214] |
| | Hydrogel/NaCl Electrolyte on VHB™ | 530 | – | – | 150 | 350[b] | – | 98.9 | 400–700 | – | [196] |
| **Architectures** | Microcracked Au on PDMS | 20 | 250,000 | 20 | 7.0[k] | 25[b,k] | 70[b,k] | – | – | – | [215] |
| | Buckled Polypyrrole/PU | 60 | – | – | 2,100[d] | 15,000[d] | – | – | – | – | [140] |
| | Ag Ink on Micropatterned PDMS | 20 | 1,000 | 20 | 3.0[k] | 12.1[b,k] | 3.0[k] | – | – | Printability | [216] |
| | Nanoporous gold/PDMS | 25 | – | – | 8.3[d] | 270[d] | – | – | – | – | [217] |
| | Buckled Au/Cr/PDMS | 100 | 30 | 15 | 38[d] | 47[d] | – | – | – | – | [218] |
| | Buckled Cu/Polyelectrolyte/PDMS | 300 | 50 | 70 | 0.21[k] | – | 0.21[k] | – | – | – | [219] |
| | Buckled Au/PPy | 70 | 2,000 | 30 | 42.8[d] | 428[b,d] | 59.9[d] | – | – | – | [220] |
| | Corrugated Au/Elastosil® RT 625 | 33 | $3\times10^{6}$ | 18[g] | 3.8[d] | 3.8[d] | 3.8[d] | – | – | – | [202] |
| | Ultrathin Au Metal Films | – | – | – | 86 | – | – | 75 | 530 | – | [221] |
| | Buckled CNT Ribbons/F4-TCNQ on PDMS | 100 | – | – | 72 | 75[b] | – | – | – | – | [222] |
| | Zigzag PEG/Ag/PDMS | 55 | 900 | 20 | 3.40[k] | 17.9[b,k] | 3.40[k] | 70 | 400–800 | – | [223] |
| **Hybrids**[o] | nAg-MWCNT/PVDF | 140 | 5,000 | 20 | 0.0125[k] | 3.57[k] | 0.0473[k] | – | – | – | [224] |
| | AgNWs/CNTs on Ecoflex® | 460 | 10,000[f] | – | 100 | 600[b] | 75[b] | 85 | – | – | [225] |

[a]Properties at or near Ambient Standard Temperature and Pressure (25°C, ~1 atm), unless otherwise stated
[b]Calculated from the given change in resistance
[c]Indicates electrical failure
[d]Calculated from the given dimensions of the sample geometry
[e]Sheet resistance does not apply for this cylindrical geometry, but for comparison the bulk resistivity of $3\times10^{-5}$ Ω-cm was divided by the smallest inner diameter of 360 μm.
[f]Bending
[g]Linear actuation strain, prestrained elastomer
[h]Calculated from an estimate of the thickness of the conductor or the equivalent thickness of the conductive volume, not necessarily the entire composite
[i]Calculated from the estimated dimensions of the sample geometry
[j]Area actuation strain, prestrained elastomer
[k]Calculated from the given thickness of the conductor or the equivalent thickness of the conductive volume, not necessarily the entire composite
[l]Calculated from an estimate of the bulk resistivity
[m]Sheet resistance does not apply for this cylindrical geometry, but for comparison the bulk resistivity of $5.2\times10^{-5}$ Ω-cm was divided by the wire diameter of 20 μm.
[n]Equivalent sheet resistance, calculated from given meander resistance (10 Ω), length (3 mm), and common width (20 μm).
[o]Compliant conductors that combine two or more conducting elements

## 1.5 Dielectric Elastomer Configurations

DEAs can be adapted to a myriad of useful geometries and architectures in order to perform useful work. Many of these design configurations require the polymer to maintain a prestrain by a rigid or semi-rigid component. [7, 8, 226, 227] As an alternative, coworkers in the Pei laboratory have developed two types of free-standing DEAs: interpenetrating polymer network (IPN) DEAs and bistable electroactive polymers (BSEPs), described below.

### 1.5.1 Interpenetrating Polymer Networks

For interpenetrating polymer network (IPN) DEAs, a secondary polymer network is cured within a prestrained DEA to internally resist prestrain relaxation. This secondary elastomer infiltrates the prestreched elastomer, which can then relax onto, and be supported by, the secondary elastomer when released from its frame or other rigid support component. [228, 229] The steps involved in an IPN DE fabrication are shown in Figure 1.42. In this depiction, a VHB™ film is prestrained by 400% biaxially. Then, a trifunctional monomer such as trimethylolpropane trimethacrylate (TMPTMA) is spray deposited onto and allowed to diffuse into the VHB™. Following thermal curing, the TMPTMA/VHB™ composite is released from its original rigid frame and let relax slightly. At equilibrium, the tension in the VHB network balances the compression of the additive network, and some prestrain is maintained.

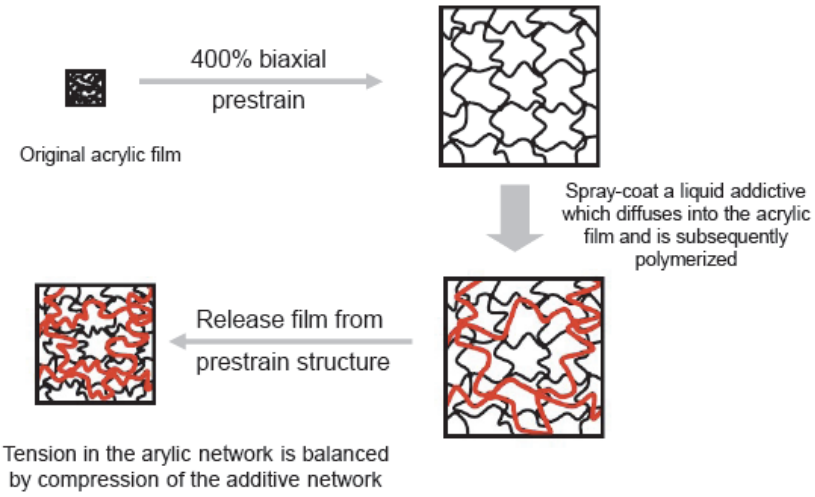


**Figure 1.42** The steps involved in the fabrication of an IPN network DEA. [229]

### 1.5.2 Bistable Electroactive Polymers

Bistable electroactive polymers (BSEPs) enable shape memory in the absence of an electric field by utilizing a polymer with a glass transition temperature ($T_g$) above ambient temperature. This means that the BSEP is initially rigid under ambient conditions. When heated above its $T_g$, the polymer becomes rubbery and may deform to a new shape under an electric field as a DEA. Joule heating can be accomplished either by a silver nanowire electrode or a microheater. [230] Once cooled below its $T_g$, the field may be removed and its actuated shape maintained. This shape memory allows the actuated shape to be locked into the BSEP material without the need to continue to apply an actuation voltage. [231] One basic BSEP material is poly(tert-butyl acrylate) (PtBA), with a $T_g$ between 50 and 70°C. One recent application of the BSEP DEA was a refreshable Braille display, discussed in Section 1.6.2.

### 1.5.3 Minimum Energy Structures

Minimum energy structures (MESs) consist of a prestrained DEA interfaced with flexible, semi-rigid components. Due to changes in the stress states of the prestrained DE between resting and actuated states, the resulting folded structure can be reversibly changed between two minimum energy conformations in the passive and active states. Specifically, the prestrain in the DEA causes the MES to fold into a minimum energy configuration, and actuation of the DEA membrane causes motion toward a second minimum energy shape. [232] The concept is illustrated in Figure 1.43, in which a DE, usually VHB™, is prestrained and affixed to a larger frame. Then, semi-rigid frames, usually made of PET, are adhered to the prestrained DE and cut around the semi-rigid edge to release from the surrounding DE. The result is a folded shape in the first equilibrium energy minimum. Flexible electrodes are put on both sides of the DE in the center hole, and application of a voltage causes a deformation.

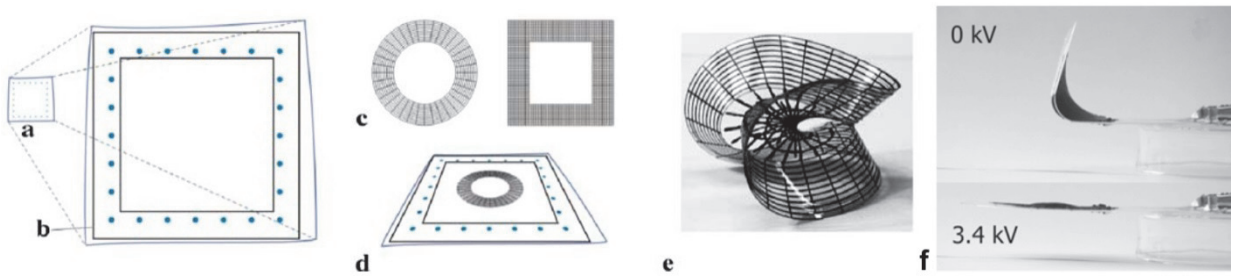


**Figure 1.43** **(a)** A DE is prestretched on **(b)** a rigid frame. **(c)** Semi-rigid frames are then **(d)** affixed to the prestretched DE. **(e)** When released from the surrounding DE, it folds into a minimum energy state. **(f)** Actuation changes the minimum energy state, resulting in motion that can perform work. [232]

### 1.5.4 Stacked and Folded Actuators

DEAs expand in area and reduce in thickness when a voltage is applied. This is unlike living muscle, however, which contracts in the direction of work and increases in thickness when stimulated. Stacking DEAs is one obvious solution. In this configuration, rather than perform work in the planar direction from an expanding area, the DEA is reoriented so that work can be performed in the thickness direction. Stacking many layers then results in a linear contractile actuator more akin to natural muscle.

The typical stack device architecture consists of layers of DE films, alternating with layers of flexible electrodes. These electrodes are then given alternating electrical biases, and global actuation occurs from the summation of the many parallel actuation events across each layer (Figure 1.44(a)). [226] Due to the many layers needed for a stack, fabrication complexity is already high, as is patterning of individual electrodes. To address this, a single sheet of dielectric

elastomer can be coated on both sides with a continuous electrode pattern and then folded multiple times into a rectangular or circular stack actuator (Figure 1.44(b),(c)). [233]

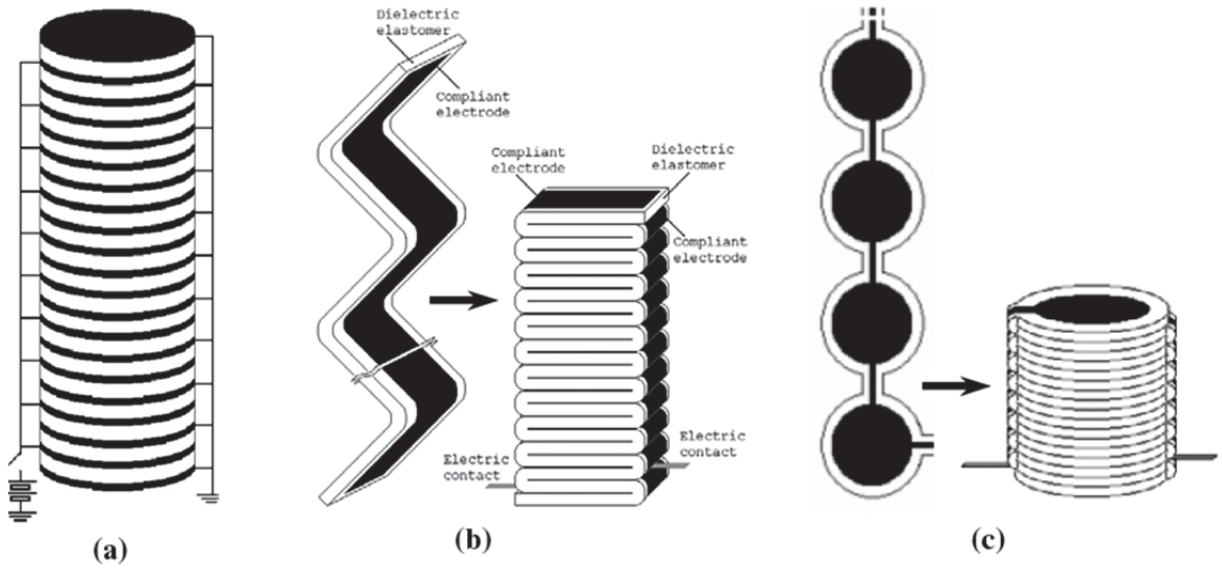


**Figure 1.44** **(a)** Concept of a DEA stack, with alternating electrodes wired in parallel to deliver equal voltage to all layers. **(b)** A folded actuator design. **(c)** A circular folded DEA design. [233]

### 1.5.5 Other Configurations

Many other DE geometries can be envisioned, some of which are shown in Figure 1.45. In the extender configuration, a DEA stack is constrained on one edge, leading to expansion parallel to the stacking plane. In the diaphragm configuration, a DE film is given a slight pressure bias from a diaphragm chamber below, which aids in actuation. The dielectric elastomer microfluidic device presented in Chapter 2 is thought to actuate as a combination of these two configurations. [227]

Next, the bowtie experiences both vertical and horizontal expansion in active area. And, the tube actuator, in which a DEA membrane is wrapped around two rigid pipe ends but is free in the center, will expand in length when actuated. The dielectric elastomer valve presented in Chapter 3 can be thought of as a combination of these two configurations. In addition, the dielectric elastomer band in Chapter 4 consists of a series of bowtie actuators, except that the DEA has free vertical edges rather than hinges.

The remaining configurations pictured are spring roll, framed, spider, bimorph, and unimorph. A spring roll actuator is a variant of the tube actuator, but with a spring placed in the hollow center to maintain the vertical prestretch in the resting state. At rest, the tension in the DEA film is in equilibrium with the compression in the spring; during actuation, the DEA film stress relaxes, relieving some of the compression in the spring and performing work. A framed push-pull actuator consists of DE membrane with two opposing active areas; when one side actuates, the other side contracts, performing work on the centerline. In the spider configuration, the in-plane expansion of a DEA is converted into expansion or contraction in the orthogonal direction.

Stacking spiders would be similar to a multilayer stack like that mentioned in the previous section, but with a couple advantages: prestretch can be maintained, leading to higher strains, and area changes can be used to amplify changes in the thickness direction, which would otherwise be small for each DEA layer. Finally, the unimorph actuator consists of a prestretched DEA membrane(s) laminated on

one side with a flexible, semi-rigid substrate; actuation causes stress relaxation in the DEA layer, leading to motion. Similarly, a bimorph consists of a flexible substrate laminated between two DEA layers and is capable of motion in either direction, depending on which DEA side is actuated. Most of these configurations can be considered to operate on principles similar to minimum energy structures, in which prestrained DE films reach an equilibrium state with some other force-exerting element, which then reaches another equilibrium state as a result of actuation, allowing movement and work to be performed.

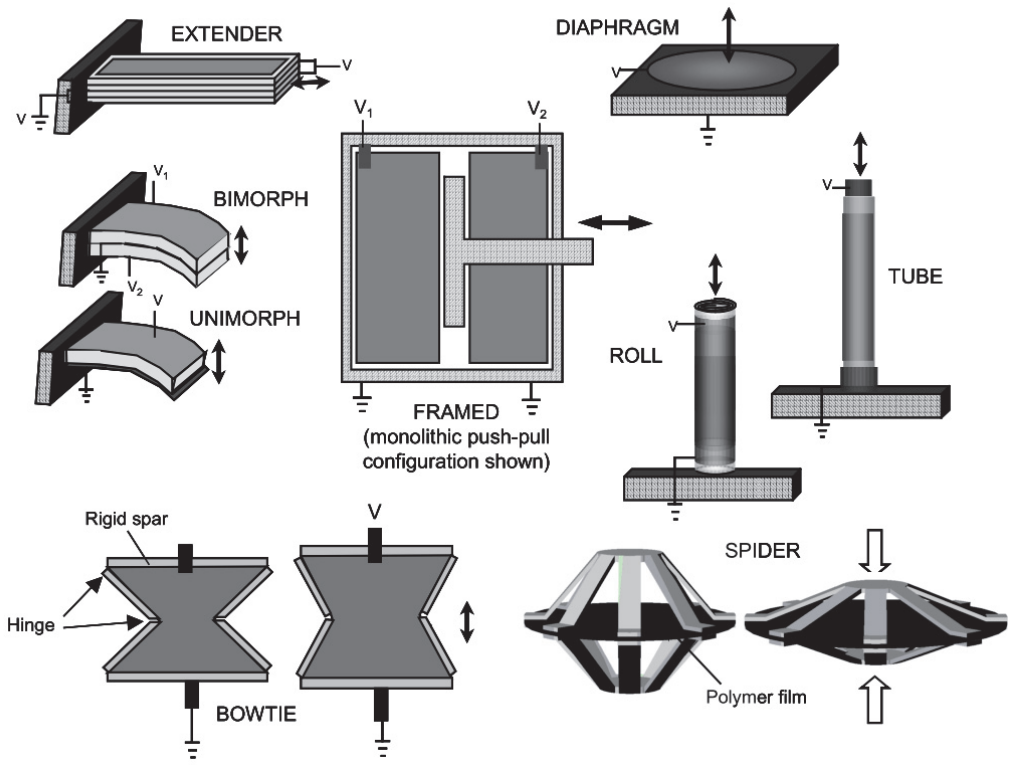


**Figure 1.45** Various DE configurations, including a stack extender, bimorph, unimorph, monolithic push-pull, bowtie, diaphragm, spring roll, tube, and spider architecture. [227]

## 1.6 Biomedical Applications of Dielectric Elastomers

To provide some context for the research that follows, it is worth giving some examples of the biomedical applications to which DEs have been applied in the recent past. Some such applications have included active microfluidic devices [234-240], cell bioreactors [241], anti-biofouling surfaces [195], diaphragm blood pumps [242], refreshable haptic displays [243-245], surgical robotics training [246], rehabilitation orthotics [247, 248], artificial limbs [106, 126, 233, 249, 250], and soft robots that can walk, crawl, hop, and fly. [1, 227, 251-253] Some of these and others are briefly discussed below.

### 1.6.1 Implantable Capacitive Pressure Sensors

Soft and viscoelastic, DEs have similar passive mechanical properties to living soft tissue, making them well-suited as implantable biological sensors. Chiang et al have designed an implantable DES for use with a neural prosthesis. [254] Neural prostheses typically employ a cuff electrode that wraps around a nerve trunk in order to stimulate a motor neuron, or to record a signal. Since the neuron can be damaged if the cuff is too tight (pressure > ~20 mmHg), the pressure at the cuff electrode/nerve trunk interface should be monitored. The DES used for this application consists of two gold electrodes sandwiching a polydimethylsiloxane (PDMS, Sylgard® 184) DE layer and encapsulated in a layer of insulating, biocompatible polyimide (PI, Durimide® 7320). While more rigid than the silicone (Young's modulus $Y$ = 750 kPa), the PI is still flexible ($Y$ = 2.5 GPa). Figure 1.46

illustrates the sensor design, whereby gaps have been placed around the sensor to allow for area expansion upon deformation in the thickness direction.

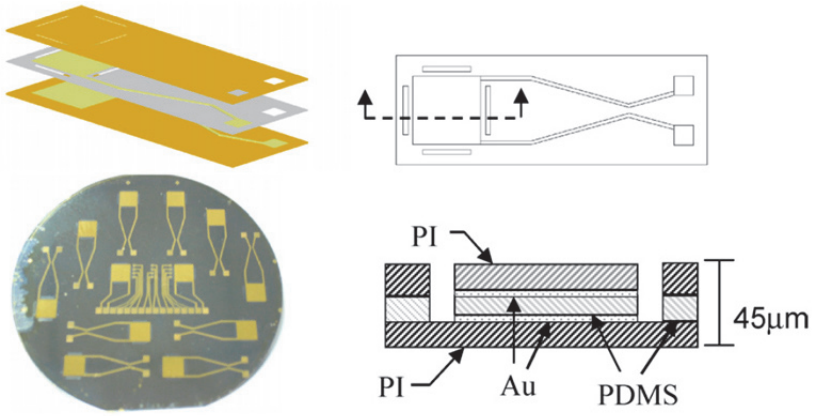


**Figure 1.46** A silicone-based DES for monitoring the cuff electrode pressure of a neural prosthesis on a neuron trunk. Flexible Au electrodes and passive PI layers sandwich the PDMS DE, and adequate margin is left for the incompressible expansion of the DES upon thickness deformation. [254]

### 1.6.2 Haptics: Refreshable Braille Displays and Active Touch-Screens

Haptics is the biomedically-related field concerned with the sense of touch. One promising area of research for the visually-impaired is the refreshable Braille display. The literate blind must rely on enormous books of printed raised-dot Braille characters to read (Figure 1.47(a)). [255] Fortunately, the DEA can be used to create a single refreshable page of Braille dots. Ultimately, the goal is to produce the equivalent of an Amazon.com® Kindle™ or Apple® iPad® for the blind: a lightweight, portable tablet consisting of an array of these "smart" Braille dots, effectively replacing the bulky tome alternatives. Past members of our group have

designed a refreshable Braille display (Figure 1.47(b)) based on the BSEP DEA described in Section 1.5.2. [243] Each BSEP dot is constrained by a circular rigid boundary so that it will bump up when actuated, as shown in Figure 1.47(c). Because voltage and heat need applied to the array of dots only when refreshing the page, the BSEP Braille display can exhibit the low power consumption necessary for a lightweight, portable tablet- or smartphone-sized device.

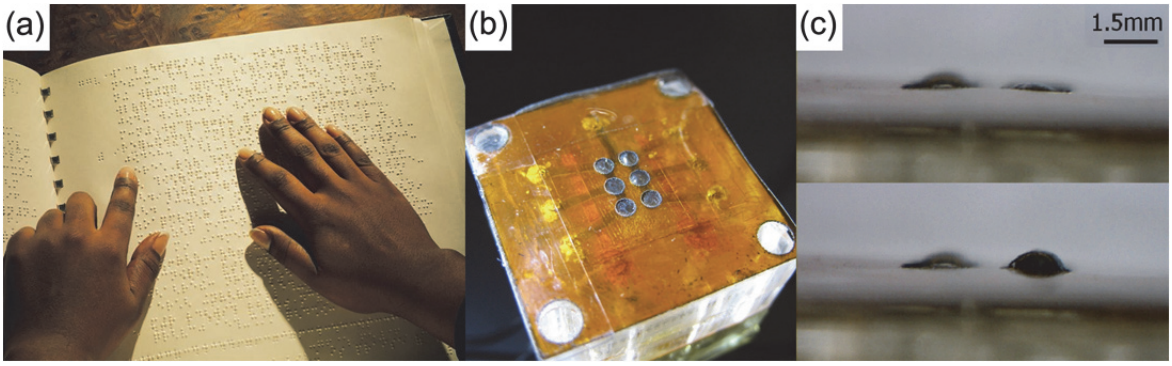


**Figure 1.47** (a) A typical Braille book for the blind. (b) Prototype refreshable BSEP Braille display for one character. (c) *Top:* BSEP Braille dot unactuated. *Bottom:* Heated, actuated, then cooled dot. [243, 255]

Figure 1.48 demonstrates the operating principle of enhanced thickness-mode actuation, which results in controllable surface textures. [256] Here, an acrylic DEA is sandwiched between two soft silicone passive layers. Upon actuation, the thickness of the active area decreases but bulges in the immediate periphery. The thick, soft silicone layer amplifies these bulges, creating a surface texture. This DEA technology can also be applied to a microfluidic device to form a peristaltic pump.

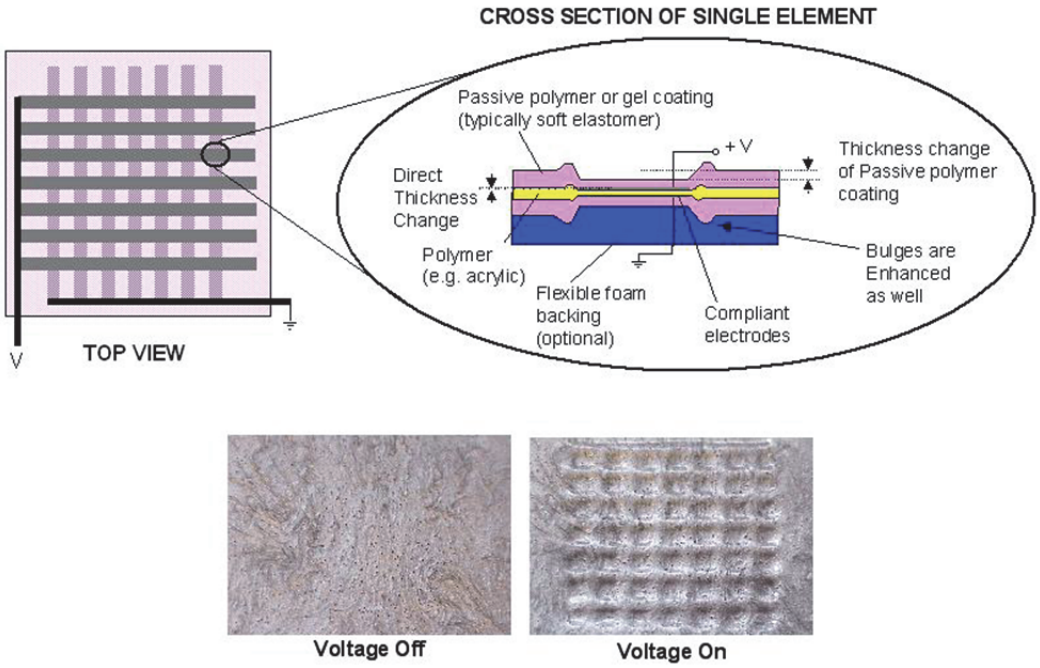


**Figure 1.48** General thickness-mode actuation scheme of a silicone-enhanced acrylic DEA to create a textured surface array. [256]

Flexible electronics, such as the bendable smart phone, are on the imminent technological horizon. [257-268] A perfect corollary to this technology would be DEA-based refreshable, flexible touch screens that can change topography or texture on a pixel-by-pixel area basis. [255] DEs of silicone or acrylic are normally transparent and can be patterned with flexible transparent electrodes. [113, 152, 170, 174, 269, 270] Furthermore, addition of capacitive self-sensing circuitry would enable a fully-integrated texture-active capacitive touch screen for smartphones, tablets, and personal computer monitors. [4]

### 1.6.3 DEA Cratering and Anti-Biofouling Surfaces

Another method of using the DE to reversibly modify surface textures is the formation of craters in DE films. The Zhao group has demonstrated this creasing to cratering instability in a unique DE configuration, as shown in Figure 1.49(a). [271] Rather than sandwich a DE polymer between two flexible electrodes, a 40 to 212 $\mu$m PDMS elastomer is instead fixed to a rigid PI (Kapton®, DuPont™) substrate, the reverse of which is coated with an electrode. The top of the polymer is submersed in a sodium chloride electrolyte solution, a potential difference of 7 to 15.6 kV is applied between the conductive solution and the substrate electrode, and creasing to cratering is observed in the PDMS (Figure 1.49(b)).

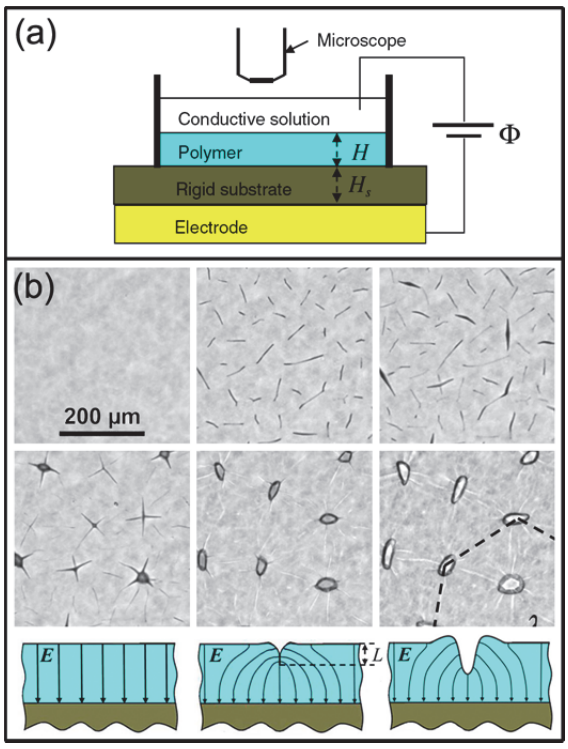


**Figure 1.49** (a) Experimental setup for observing the creasing-to-cratering instability in DE polymers. Cratering is most pronounced at 15.6 kV. (b) Optical micrographs and schematics of the phenomenon. [271]

An offshoot of controllable DE surface textures— whether by enhanced thickness mode or cratering— is the advent of smart anti-biofouling surfaces. As mentioned in Section 1.4.3.4, marine biofouling is a widespread problem in the maritime industry. Microorganisms, algae, plants, and other sea-borne biological entities inevitably adsorb themselves onto the submerged portions of sea vessels, thereby decreasing fluid dynamic efficiency and increasing fuel costs. Typical anti-biofouling regents are not environmentally-friendly, and anti-fouling microbes have been proposed as an eco-friendly alternative. [272] Still, an entire underside of a vessel could be inexpensively coated with a thin silicone film; a potential difference

applied periodically between the seawater and the conductive hull would cause the silicone to crater, thus safely freeing the surface from any adhered organisms.

### 1.6.4 DEA Bioreactors: Mechanostimulation of Cell Cultures

Tissue engineering is a subdiscipline of biomedical engineering that seeks to understand the mechanisms cells use to develop into living tissues and to take advantage of these mechanisms in order to promote the healing of damaged tissues in vivo, grow tissue transplants in vitro, and ultimately grow entire artificial organs in vitro for transplantation. Such cellular mechanisms include those underlying differentiation, growth, proliferation, and the formation of the extracellular matrix (ECM). Protein matrices already exist inside the cell, but cells may also secrete proteins outside themselves in order to encourage the growth of other cells into forming a tissue, and to additionally serve as the mechanical backbone of the tissue. For example, fibroblast cells produce the collagen protein fibers that give a tendon its mechanical properties. These collagen fibers form an anisotropic network aligned preferentially in the direction of loading for maximum tensile strength. However, the fibroblasts require mechanical stimulation to produce collagen, and loading in a given direction signals to the cells which direction to form the collagen networks. Tissue engineers have applied this knowledge to the growth of artificial tendons in vitro by using bioreactors to shake fibroblasts in a single direction. This large-scale mechanostimulation of collagen secretion produces the ECM of an artificial tendon.

Large-scale bioreactors are widespread, but the ability to study mechanostimulation of individual cells has been unfeasible with current bioreactor designs. However, with the use of DEAs, Shea et al. have created an array of 100 $\mu$m × 100 $\mu$m active surfaces capable of stimulating individual cells. [273] This efficient, precise design allows controlled studies of the effects of mechanostimulation on cellular gene expression, ECM formation, differentiation, and other behaviors. 100 $\mu$m-wide gold electrode lines were patterned onto both sides of a 30 $\mu$m-thick PDMS substrate using low-energy (< 5 keV) ion implantation. Electrode lines were aligned parallel on each side, but orthogonal to each other across the PDMS, creating a trellis-like pattern with each intersection serving as an active area (Figure 1.50(a)). The PDMS was pre-stretched to 175% uniaxially, resulting in a perpendicular active area strain of 56% under a 3.8 kV actuation bias. Any cell sitting atop one active area would thus feel a "stretch" (Figure 1.50(b)). An additional 20 $\mu$m-thick layer of PDMS was cast over the array to insulate the high voltage from the saline cell culture medium, resulting in a maximum in-plane strain of 37% at 3.8 kV.

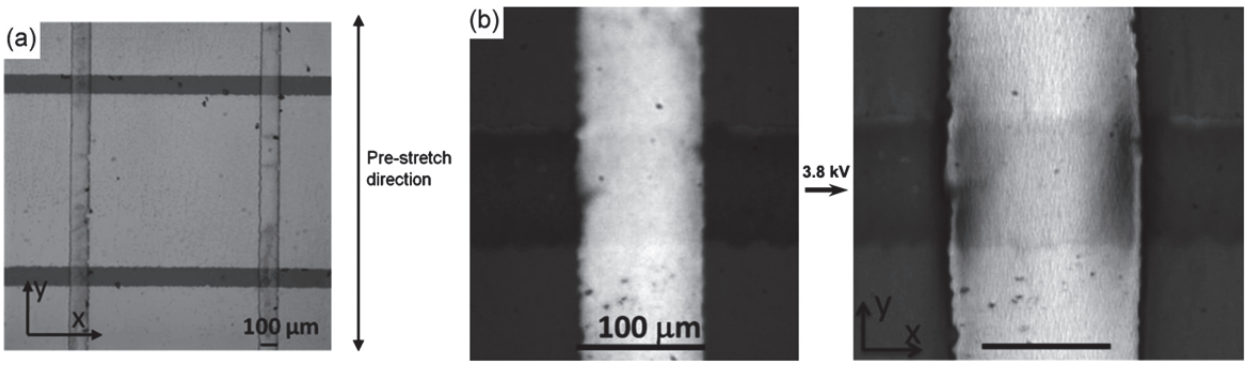


**Figure 1.50** (a) An array of four active areas, at the overlap of the 100 $\mu$m-wide Au electrodes. The PDMS DE was pre-strained to 175% uniaxially. (b) Upon application of a 3.8 kV actuation bias, strains of 56% were observed, and 37% with an additional passive PDMS layer. [273]

### 1.6.5 Labs-on-a-Chip: Microfluidic Pumps and Valves

Microfluidics concerns itself with the manipulation of very small volumes of fluid. Microactuators paired with microchannels can be used to mix reagents to perform chemical reactions and other laboratory functions at a very small scale. This results in a micro-electromechanical system (MEMS) known as a "lab-on-a-chip" (LOC) due to this miniaturization of lab processes to fit on a single millimeter-scale chip. Of biomedical interest is the use of microfluidics to model in vitro capillary flow in vivo, study cell behavior and transport, and even sort and trap cells. Size-exclusion sorting methods include "Weir-type" planar slits or pillar-type filters, while more complex methods involve the formation of microvortices to guide and sort cells. [274, 275] One application of cell sorting is to filter out circulating cancer cells from a patient's bloodstream to abate tumor metastasis.

An emerging trend in the MEMS arena is use of DEAs to control microfluidic systems. Maffli et al. in the Shea group at EPFL have developed a silicon/silicone-based "zipping" peristaltic pump. [236] The silicone DE is treated on one side only with gold ion implantation or another flexible electrode, while the other untreated side is electrostatically attracted to a doped silicon semiconductor or aluminum etched into a well once a potential difference is applied across the flexible electrode and the Si wafer (Figure 1.51(a)). [237] Zipping mode actuation is also possible with a rigid dielectric (Figure 1.51(b)), in which a dielectric membrane is coated on its inner face with a flexible electrode, and a rigid dielectric coats a rigid electrode. [239] A peristaltic pump can be constructed by placing several such DE zipping actuators in series, illustrated in Figure 1.51(c). In this configuration, fluid is drawn upward above the pillar when the first actuator in the series zips. Next, the first actuator zips down while the second zips up, both sealing the fluid from backflow and drawing the fluid forward. The process can then repeat for the desired length of linear pumping. [236] Although the compliant electrode side of the silicone membrane comes into contact with the liquid in the microchannel, the cured silicone-bound carbon black is unlikely to detach into the fluid. Also, the electric field is restricted to the region between the compliant and rigid electrodes, which does not intersect the microfluidic channel, allowing zipping microfluidic devices to be potentially biocompatible.

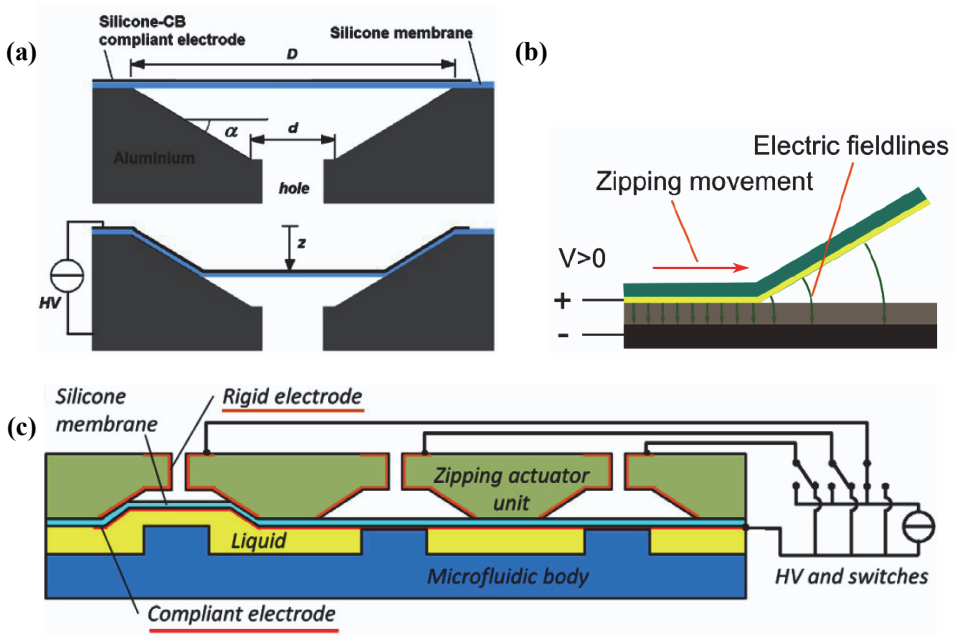


**Figure 1.51** **(a)** Cross-section of a conical zipping actuator consisting of a silicone elastomer coated on the outer surface with a silicone-bound carbon black compliant electrode and a rigid electrode of aluminum, which also serves as a structural component. Zipping mode actuation draws the silicone toward the aluminum, and a hole allows air to displace. [237] **(b)** Zipping actuation is also possible with a rigid dielectric. Pictured is a (green) silicone membrane coated on its inner surface with a (yellow) compliant electrode, which is drawn toward a (dark gray) rigid electrode coated with a (light gray) rigid dielectric. [239] **(c)** A microfluidic peristaltic pump concept with a series of zipping actuators. [236]

Price and Culbertson developed a simple EAP-based pump for hydrodynamically injecting samples for microchip electrophoresis. In this electroosmotic injection-mode actuation, standard DE actuation is combined with an electrophoretic microchip, depicted in Figure 1.52. First, a constant electric field was applied across the microchannels of the PDMS chip by applying a voltage to

sample reservoir 1 and buffer reservoir 2, and grounding the waste reservoirs 3 and 4. The same voltage applied to reservoirs 1 and 2 was also applied to the patterned electrode. To actuate the DE, the voltage applied to the patterned electrode was switched to zero, creating a potential difference between the patterned electrode and charged microchannel and compressing the EAP layer. Finally, an injection was performed by returning the patterned electrode voltage to its original nonzero value. Doing so switches off the DE, causing the EAP layer to quickly relax and pump fluid. These injections are faster than 200 ms, and the injection volume can be modified my altering the electric field across the EAP layer prior to discharging. [240] Other DEA designs are possible that can actively deform a microchannel to aid in mass transport. The novel research presented in Chapter 2 of this dissertation will discuss one such DE microfluidic device in detail.

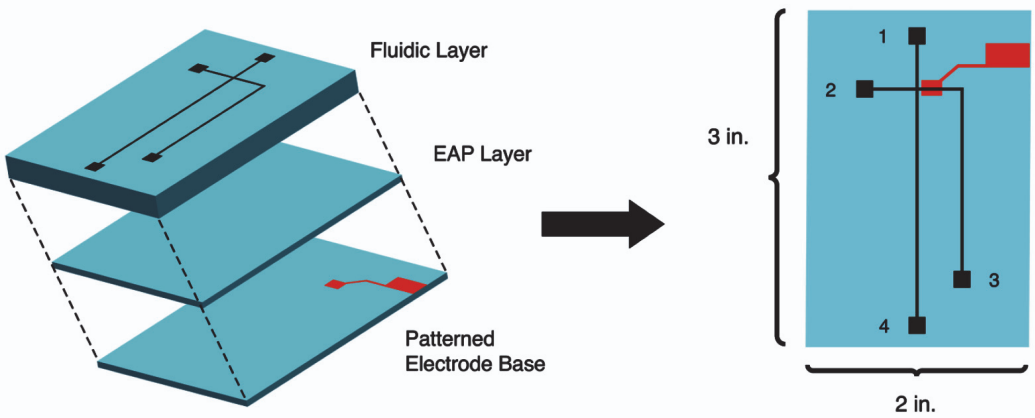


**Figure 1.52** The pictured EAM device consists of an electrophoretic PDMS microchannel system bonded to a ~40 um thick PDMS dielectric elastomer (EAP) layer. This layer is in turn bonded to a glass substrate with a lithographically patterned electrode. [240]

Moreover, SRI International has patented a fluidic pump actuated by electroactive polymers. In one embodiment of this design, such a device could consist of at least two opposing DE actuator membranes that surround a flexible orifice for fluid to pass through. The films are pushed inward by a passive force, potentially from cushioning, which would balance the tension in the unactuated DE films and keep the orifice open. During actuation, the tension in the DEs would relax and the now greater cushioning force would pinch the orifice shut. Cyclic actuation of the DE elements could create a pumping action. If the internal hydraulic pressure is greater than the inward passive pressure, outward expansion of the DEs may occur, but this mechanism can also create a pumping action when cycled between actuated and unactuated states. [276] Other DEA configurations are possible for fluid handling, and one such novel design is presented in Chapter 3.

### 1.6.6 Stacked and Folded Actuators for Prosthetic Limbs and Rehabilitation Robotics

The stacked or folded DEAs described in Section 1.5.4 are potentially promising for application to soft robotics, prosthetic limbs, and rehabilitation robotics and orthotics due to their shape, passive mechanical properties, and linear contraction. However, DEA stacks may possess several disadvantages. First, interlayer adhesion is strong during actuation due to Columbic attraction, but it tends to be poor in its passive state, leading to delamination. [106] Second, these stacks usually do not possess any prestrain, leading to low actuation performance;

interpenetrating polymer network (IPN) DEA stacks may exhibit better performance. [228] Third, because each layer is a thin film, thousands of layers may need stacked in this configuration, increasing the probability of failure. In this vein, automation may be necessary to make stack manufacture more feasible, and EMPA (Swiss Federal Laboratories for Materials Testing and Research) has been a key innovator in automated fabrication techniques of DEA stacks over the past decade. [277]

### 1.6.7 Compliant Surgical Robotics and Variable Stiffness Manipulators

Minimally-invasive surgical robotics has become increasingly widespread with the popularization of the da Vinci® Surgical System (Intuitive Surgical®, Inc.). Of concern when performing surgeries is the compliance of the surgical tool against soft tissue. If the surgeon's hand is too stiff, it may damage the tissue contacting the already rigid tool. Similarly, a surgical robot will also benefit from incorporating a compliant element. The da Vinci® Surgical System utilizes a spring and tuning gears to incorporate this compliant series elastic element in the tool shaft. [278] On the other hand, using DEAs as manipulators of the surgical instrument shafts is one natural alternative since DEs are compliant. In addition, a DEA-based manipulation scheme would provide noiseless operation; a lower cost of materials manufacture; and a lighter weight, less complex design. Promising work to this end

has been carried out by Wingert and colleagues at MIT with their DEA-driven hyper-redundant binary robotic manipulator prototype, shown in Figure 1.53. [279]

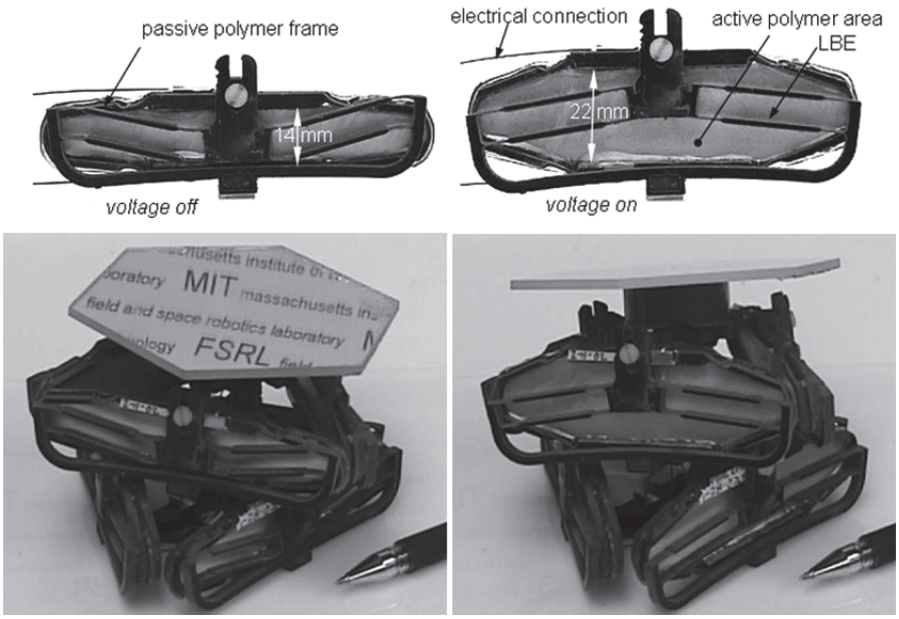


**Figure 1.53** The BRAID prototype for compliant binary robotic manipulation. *Top left:* When off, the prestretch of the DEA films balances the opposing upward force exerted by the passive linear bistable element (LBE) arms. *Top Right:* When a bias of 5.5 kV is applied, the DEA films relax, causing the post to expand upward. *Bottom:* When three such linear binary modules are fixed to a central post, selective actuation of each module will cause the post to tilt in the desired direction. [279]

This BRAID (Binary Robotic Articulated Intelligent Device) manipulator consists of three DEA frame modules arranged around a central post. Each frame module is binary, meaning they can translate a post either up or down. Each binary DEA frame module consists of passive, flexible frame arms that push up a center pole. This upward tension by the passive linear bistable element (LBE) arms is

balanced by the tension of prestretched VHB™ 4910 acrylic DE when in the off state so that the post is depressed. Under a 5.5 kV bias, the DE films relax, enabling the LBE arms to push up the post. When three such binary modules are arranged around a central post, degrees of freedom (DOFs) in the six primary directions can be achieved. However, by actuating each of the three modules partially and in tandem, the central post can be articulated through a virtually infinite number of DOFs along a complete circle. In addition, the polymer-built system has intrinsic compliance, something traditional robotic systems would need to incorporate extrinsically. While DEA stacks may need further development, the aforementioned manipulation system could show more short-term feasibility for use with compliant rehabilitation robotics used in physical therapy to help patients recover from injury, stroke, cerebral palsy, or other neuromuscular disorders.

On the operator side of the equation, the surgeon needs to be able to remotely feel the stiffness of the tissues the surgical instruments contact in order to prevent injury and perform surgeries correctly. This necessary tele-haptic feedback is delivered via servomotors in the remote laparoscopic da Vinci system, although DEAs are another suitable alternative due to their variable stiffness characteristics under actuation. [278, 280-282]

### 1.6.8 Foot Pressure Sensors for Gait Analysis

Of special interest to biomechanics studies of gait analysis, orthopedists, prosthetists, physical therapists, and podiatrists is a flat pressure sensor for

subjects and patients to walk across or stand upon. DE-based pressure sensors are widely being researched, and some are currently on the market, such as the Tactilus® Foot Plate Analysis System (Sensor Products, Inc.). [283] These polymer-based DES pads are lightweight, portable, foldable, and high-resolution. Figure 1.54 depicts the Tactilus® pressure measurement setup. [284]

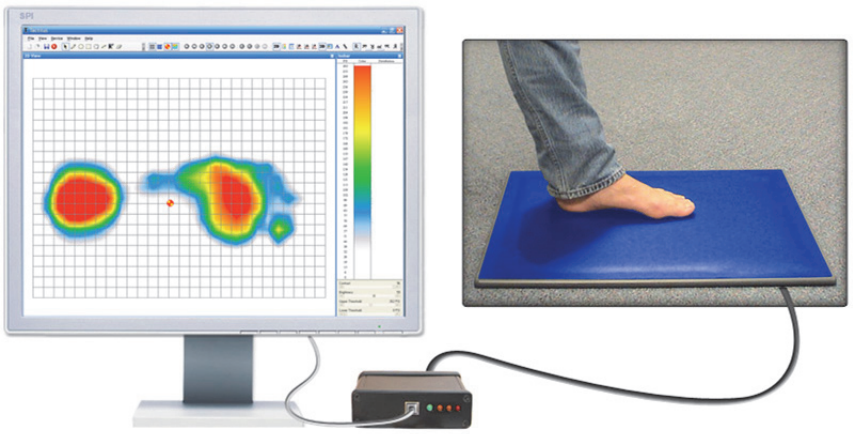

**Figure 1.54** A foot pressure measurement setup by the Tactilus® Foot Plate Analysis System, which utilizes DE-based sensing. This provides a lightweight, foldable system for prosthetists, physical therapists, and podiatrists for gait and posture analysis. [284]

### 1.6.9 Tile and Shoe Energy Harvesting

In the spirit of the previous topic, DE-based energy harvesting from the action of walking is under investigation by incorporating DEGs into pavement tiles or even inside the heels of shoes; Figure 1.55 illustrates the shoe heel concept. [285] Under this design, a DE film is stretched through a rigid honeycomb array from the compression of an underlying bellows chamber during a heelstrike. The mechanical deformation of a charged DE film results in the generation of electricity that can be

used to charge a battery, or be attached to the energy grid if this design were incorporated into sidewalk tiles and streets.

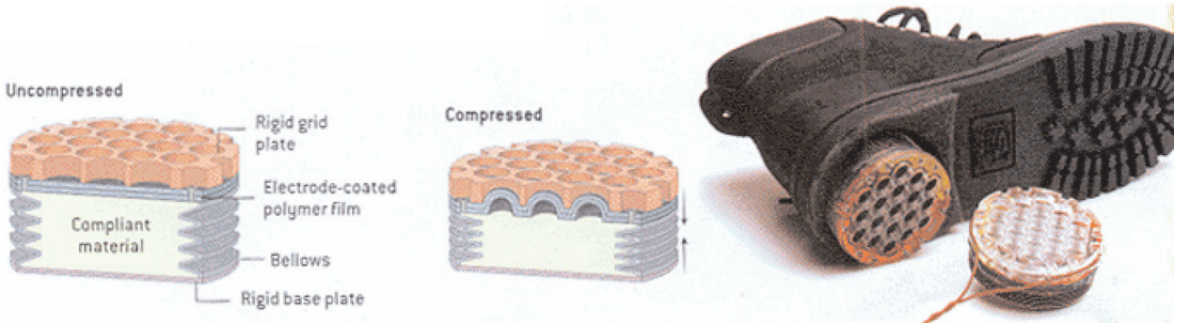


**Figure 1.55** A shoe-integrated DEG concept for personal energy harvesting. [285]

### 1.6.10 Summary

The dielectric elastomer is a highly versatile biomimetic smart material with an impressively wide girth of engineering applications due to its high strain, variable stiffness, and noiseless operation devoid of moving parts. Because it shares many of the same intrinsic mechanical properties of living muscle, it finds quite a natural niche in biomedical engineering technologies. Smart DE surfaces can help the blind to read, improve your touch screen sensory experience, or even cast barnacles off boats. Dielectric elastomer sensors can gently sense how tight neural prostheses clamp nerves; or help physical therapists, prosthetists, and researchers analyze gait and posture. DE generators can even harvest the bioenergy of the pedestrian masses. DEAs can also manipulate surgical equipment and provide a surgeon remote tactile feedback, find use in compliant rehabilitation robotics and

orthotics, and potentially give rise to the next generation of prosthetic limbs and artificial organs.

Over the past several decades, the field of microfluidics has blossomed into a highly interdisciplinary field, with applications in virtually every scientific discipline. Not surprisingly then, electroactive polymers is currently a growing field in microfluidics. The Shea group has demonstrated the ability to stretch single cells in soft DEA bioreactors. In addition, their group has recently created "zipping" mode actuation useful for pumping fluid by utilizing rigid sidewalls as one electrode and a silicone elastomer membrane coated with a flexible electrode. In perhaps one of the first attempts to integrate EAPs in a microfluidic device, Price and Culbertson created a sample injection microfluidic chip combining a dielectric elastomer with electroosmotic actuation. SRI International has further envisioned a device for controlling fluid flow utilizing a minimum energy configuration of DE actuators and passive elements. The novel research presented in the following chapters seeks to expand the field of dielectric elastomers in biomedical engineering, with a focus on those involving fluidic applications.

# CHAPTER 2

# Electroactive Bio-Microfluidic Device

## 2.1 Introduction

Dielectric elastomers with low modulus and large actuation strain have been investigated for applications in which they serve as active microfluidic channel walls. We present a novel application of DEAs in the arena of microfluidics in which we demonstrate a DEA-controlled microchannel capable of altering its geometry and of actively clearing channel blockages. A scale schematic of the microfluidic device is illustrated in Figure 2.1, generated using COMSOL Multiphysics®. This illustration depicts one of the four microchannel systems shown in Figure 2.2(d). DEAs are readily applicable to low-impact microfluidic devices because of their low power consumption, lack of needed encapsulation, and fast response times on the order of microseconds. [6, 286, 287] And while competing microfluidic actuation technologies may rely on pneumatics, shape memory alloys, piezoelectrics, magnetics, etc.; to our knowledge this is the first application of DEAs to microfluidics in a non-electroosmotic context. [286, 288-293]

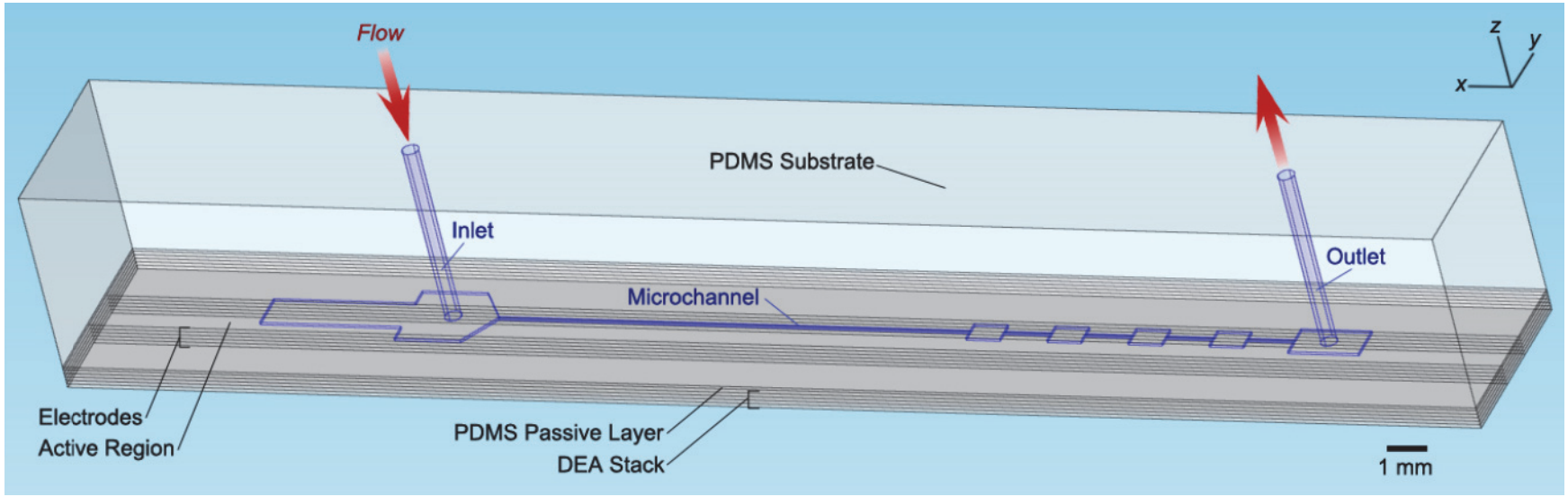


**Figure 2.1** DEA microchannel system concept schematic drawn to scale with COMSOL®. A DEA stack is interfaced with a soft microchannel system.

## 2.2 Materials and Methods

### 2.2.1 Device Fabrication and Architecture

The microfluidic device is comprised of an acrylic DEA bonded to a deformable silicone microchannel substrate. For the DEA, we employed a five-layer stack of 3M™ VHB™ 4910 acrylic industrial tape, each layer with a 500% × 100% anisotropic prestrain. With proper channel alignment, this prestrain choice favors actuation in the direction that increases channel width. Each layer is ~83.3 $\mu$m thick, and so the stack was ~417 $\mu$m thick in total. The prestrained stack was affixed to a rigid acrylic frame, which was shaped to fit easily into a fluorescence microscope stage for visualization experiments. Then, SWCNT electrodes were applied for short-tolerance by spray coating a SWCNT/chloroform solution over a CAD-designed, laser-cut mask. [115] The active area of electrode overlap for each channel was 0.5 mm wide. Copper tape leads were used as vias from the flexible SWCNT electrodes to the rigid frame, where they were soldered to insulated wires for easy operation. After the completion of an entire layer, the above procedure was repeated, stacking up to five layers. During stacking, special care was taken to avoid the capture of air bubbles by laminating each layer at an angle to the layer immediately below it.

A passive layer of polydimethylsiloxane (PDMS, Sylgard® 184, 1:10 crosslinker-to-polymer) was drop-cast directly atop the SWCNT-coated VHB™ and spread to a uniform thickness of ~60 $\mu$m, determined via microscopy. This passive layer isolates the electrodes from the aqueous channel environment. Next,

microchannels were imprinted in a PDMS substrate from a photolithographically-etched SU-8 wafer. [294] Specifically, a PDMS mix (1:10 crosslinker-to-polymer ratio) was cast over the master, placed in a desiccator for 2 hours, cured at 65°C for 3 hours, and finally cooled to room temperature. After cooling, channels were demolded from the wafer and trimmed. Inlets and outlets were formed by punching holes through the PDMS using a pin vise (Technical Innovations, Inc.). The resulting channels were 40 $\mu$m wide, 53 $\mu$m tall, ~2 cm long, and open on the top (Figure 2.2(d)).

Finally, the channels were bonded to the PDMS/VHB™ stack via air plasma activation (Plasma Cleaner, Harrick Plasma, 30 sec at 500 mTorr), with each channel aligned in the middle of its corresponding electrodes (Figure 2.2(c)). Following bonding, an additional layer of PDMS was poured over the entire device to a thickness of 2 mm to secure the channels in place. Additionally, short PDMS strips were cured in line with the inlets but on the side opposite to the inlet opening to reduce deformation at the inlet where the pressure is highest. The primary fabrication steps are outlined in Figure 2.2(a). The completed device photograph (Figure 2.2(b)) depicts four independent microchannel systems, each capable of actuation.

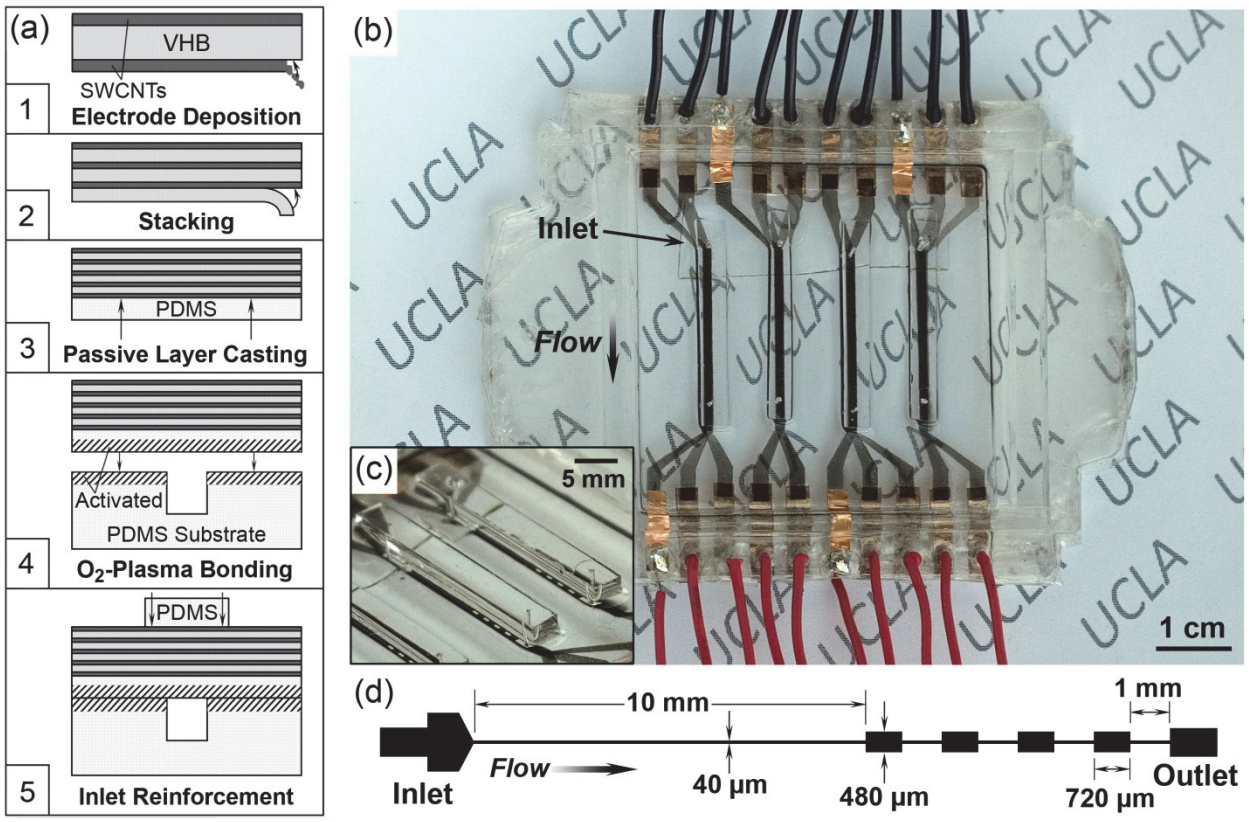


**Figure 2.2** Overview of the electro-adaptive microfluidic device. **(a)** Fabrication steps involved, including (1) electrode patterning and deposition onto the VHB acrylic elastomer, (2) stacking of these actuators, (3) casting a PDMS passive layer, (4) activating the PDMS substrate and passive layer, bonding them, and (5) reinforcing the inlet by casting a short PDMS strip over the inlet. **(b)** Photograph of the completed microfluidic device. Four independent channel systems have been fabricated in parallel. SWCNT electrodes, corresponding to dark regions, are in contact with strips of copper tape which are also adhered to the acrylic frame. Wires soldered to the copper tape supply the actuation voltage. **(c)** Profile view of the independent microchannel systems. As can be seen upon close examination, the DEA active area (in black) covers the entirety of each microfluidic channel. **(d)** Schematic of the microchannel, consisting of a straight channel 40 $\mu$m wide and 53 $\mu$m deep interfaced with 4 reservoirs spaced 1 mm apart downstream.

In order to achieve high actuation forces while still keeping voltages to a minimum, we stacked the dielectric elastomer into a multi-layered actuator. Such a stack can also passively withstand large externally-applied pressures more effectively than a single layer actuator, a design criterion which was desirable in this application. In general, two approaches would be possible to withstand these external fluidic pressures: (i) First, passive layers, with no electrodes, are stacked onto an active, electroded layer. In this regime, active actuation force would be severely diminished both due to the rigidity added by the passive layers and the lack of parallel activation of all layers that could occur. (ii) Alternatively, a thicker active layer could be used. However, impractically high voltages may be necessary to achieve the same actuation strain. The solution we employed in our device is stacking active layers, with each layer capable of actuating in parallel. [226] In this way, we could attain a higher passive film stiffness without sacrificing actuation force or requiring higher driving voltages.

### 2.2.2 Experimental Procedures

The DEA microfluidic device was interfaced to a syringe pump (Harvard Apparatus, PHD2000) using PEEK tubing (Upchurch Scientific, Product 1560) and electrically actuated using an in-house high voltage power supply (Figure 2.3(a)). The electrode closest to the channel interior was electrically grounded to safeguard against shorting through the channel. Channel geometry alterations were

characterized using a fluorescence microscope (Nikon Eclipse Ti, Photometrics CoolSNAP HQ2 CCD camera, Nikon NIS-Elements AR 3.0 software) and injecting a solution of fluorescein through the microchannel (Figure 2.3(b)). Pressure-flow (*P-Q*) measurements were carried out by perfusing an aqueous dye through each channel at constant flow rates ranging from 10 to 50 $\mu$L/min at 10 $\mu$L/min increments. Steady-state pressure measurements were recorded at each flow rate using a pressure transducer (Honeywell ASCX150AN) placed upstream and in parallel with the channel inlet. A LabVIEW™ (National Instruments™ Corp.) virtual instrument recorded the pressure signal at a sampling rate of 100 Hz. *P-Q* curves were developed for all four channels at 0 kV and at actuation voltages of 3 and 4 kV, and the results across channels were averaged.

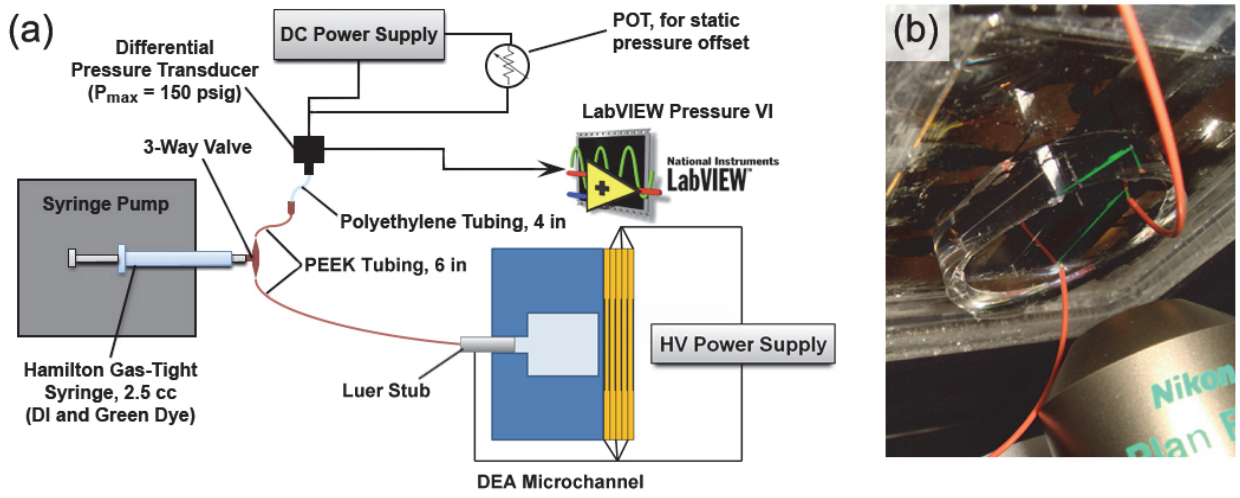


**Figure 2.3** **(a)** Constant-flow setup to measure DEA microchannel pressure as a function of actuation voltage. **(b)** Fluorescence microscope setup. Fluorescein can be seen filling the channel; the microscope objective is lower right.

Actuator dynamics were characterized by perfusing dye through each channel at a flow rate of 60 $\mu$L/min while recording channel pressure. When flow had reached steady state, bias voltages of 3 kV and 4 kV were applied, and the dynamic pressure response was recorded for one minute; these data were analyzed using MATLAB®. De-clogging a channel blockage was demonstrated using fluorescent ~50 $\mu$m diameter PDMS microbeads. The microbeads were prepared by emulsifying a mixture of PDMS (1:10 crosslinker-to-polymer ratio) containing Rhodamine B (10 mg/mL) in a solution of Tween 80. The emulsified suspension was then cured at 65°C for three hours and repeatedly centrifuged to eliminate particles greater than 50 $\mu$m. Finally, the microbeads were suspended in a solution of fluorescein for flow visualization. The bead solution was perfused at 20 $\mu$L/min while the inlet pressure was recorded. Flow was injected until the beads clogged the microchannel, at which a pressure rise was observed. 4.5 kV was supplied once the pressure reached 10 psi. Clogging and de-clogging events were observed under the fluorescence microscope with FITC and TRITC wavelengths to visualize beads and flow, respectively.

Finally, biocompatibility of our device was assessed. To do so, HeLa cells were cultured in RPMI medium 1640 with 10% FBS, then trypsinized and released in suspension before use. Cell suspension was injected at 10 $\mu$L/min through our active device with exposure to actuation voltages of 0, 3, and 4 kV, as well as through a passive control channel. At the EAM device outlet, the cell suspension was collected in a well plate, where live cells were stained with 2 mM Calcein AM

and dead cells with 2 mM EthD-1. Green (live) and red (dead) fluorescent cells were then counted using a hemocytometer.

## 2.3 Results and Discussion

### 2.3.1 Control of Steady-State Pressure-Flow Characteristics

Microscopy confirmed our ability to tune microchannel cross section with applied voltage at a constant flow rate (Figure 2.4(a)), and fluorescence measurements (Figure 2.4(b)) indicated both an increase in channel width (Figure 2.4(c)) and also channel height (Figure 2.4(d)). Compared to the 0 kV state, the increase in cross-sectional area was as much as 7.44 ± 0.49% at 4.0 kV. The ability to actively alter channel geometry allows for control of the pressure-flow characteristics of the microchannel system. At 0 kV, we measured the steady-state pressure at different constant flow rates. Actuation at 3 kV yielded a drop in fluidic resistance of ~16.8%, and 4 kV gave a drop of 18.1% (Figure 2.4(e)).

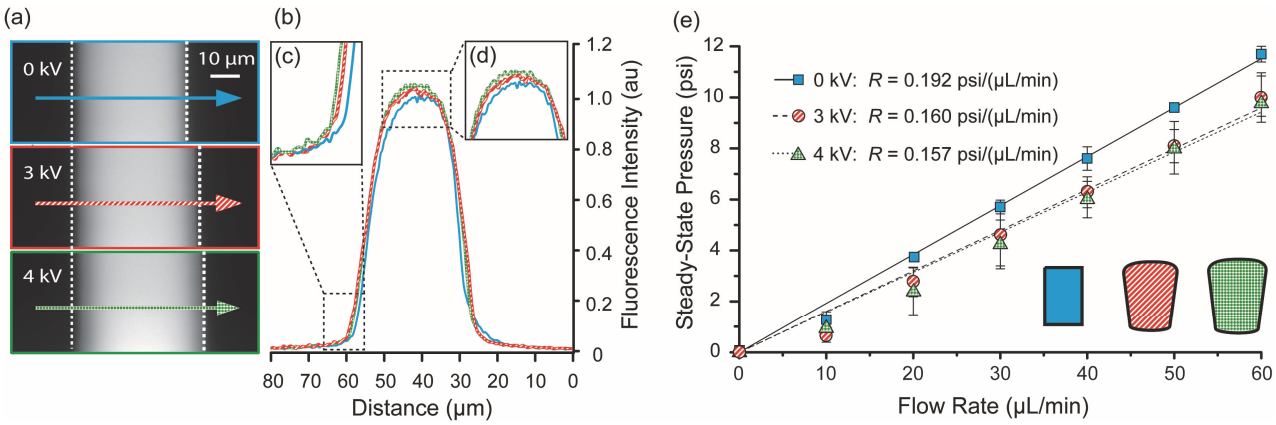


**Figure 2.4** **(a)** Micrograph depicting active increases in channel width at 3 and 4 kV. **(b)** Fluorescence measurements indicating an increase in channel **(c)** width and **(d)** height during actuation. Cross-sectional area strains of 2.89 ± 1.31% at 3 kV and 7.44 ± 0.49% at 4 kV were noted. **(e)** *P-Q* fluidic resistance was actively lowered, resulting in higher flows and lower pressures. Shown in the inset is a representation of how the cross-sectional geometry changes with actuation.

### 2.3.2 Dynamic Behavior

The DEA microchannel was also able to dynamically control microchannel pressure when 3 and 4 kV biases were applied, defining the operational pressure envelope (Figure 2.5). Water was injected at a constant 60 $\mu$L/min, and a steady-state pressure of 12.6 psi was reached. Then, the system was actuated first at 3 kV, resulting in a pressure drop of 0.89 ± 0.066 psi after 50 ± 3.5 seconds. The electric field was then removed, and steady-state pressure was again reached. At 4 kV, we observed a 1.4 ± 0.086 psi pressure drop after 60 ± 4.9 seconds, and once removed, pressure once again returned to its initial steady-state value. Since Maxwell pressure increases with the square of the applied voltage [7], we should observe

increasingly higher hydraulic pressure drops with increasing voltage. However for reasons given later, voltages above 4.5 kV were not explored.

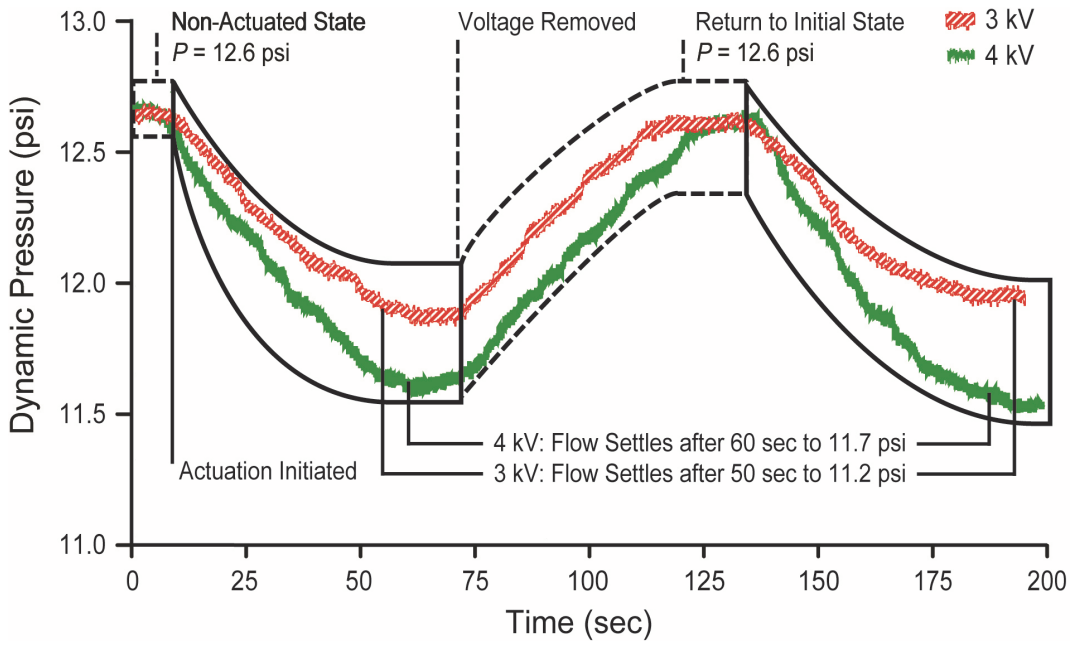


**Figure 2.5** Actuation at steady-state pressure results in decreases of 0.89 ± 0.066 psi after 50 ± 3.5 sec at 3 kV and 1.4 ± 0.086 psi after 60 ± 4.9 sec and 4 kV. Following removal of each voltage, pressures returned to their initial steady-state value of ~12.6 psi.

### 2.3.3 Active Clearing of Channel Blockages

Channel blockages are a common and persistent problem in the field of microfluidics. The consequences of clogging can be costly and time-consuming, often resulting in the abortion of tests and the discarding of microfluidic chips. [295, 296] Hence, the ability to actively clear channel blockages is a major strength of our DEA microchannel system. As depicted in Figure 2.6, a microbead blockage forms immediately (Event 1) and is eventually released (Event 7) after three actuation attempts at 4.5 kV (Event 6). Events (2)–(5) involve stopping the flow to confirm a

blockage, restarting the flow, and the microbead passively dislodging then re-clogging further downstream.

For our DEA, 4.5 kV corresponds to a nominal electric field of 54 V/$\mu$m. Hypothetically, higher voltages should be possible since breakdown fields above 200 V/$\mu$m have been reported for VHB™ 4910 at a similar prestrain. [7] However, for safety and also biocompatibility, voltages 4.5 kV and below were desirable. Although the electromechanical instability for this actuator configuration is not precisely known, in theory higher voltages could be applied for non-biological fluids, resulting in more drastic alterations in channel geometry and *P*-*Q* behavior.

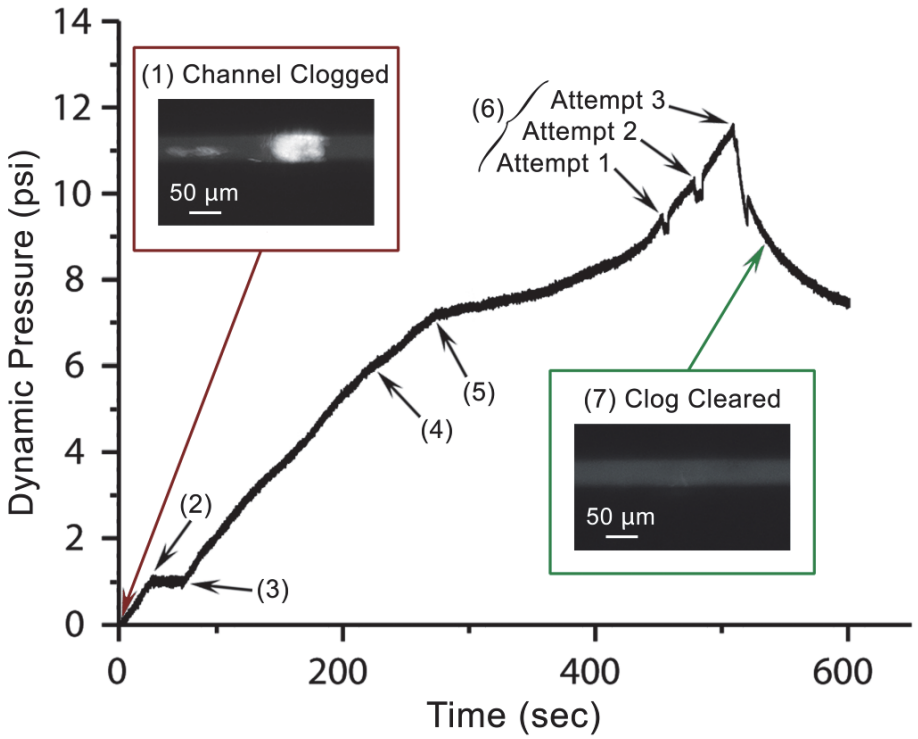


**Figure 2.6** Demonstration of de-clogging in situ by the DEA device. *Primary events:* (1) channel clogged, (6) channel actuated; (7) clog cleared. *Secondary events:* (2) flow is stopped to confirm a blockage, (3) flow is resumed, (4) blockage passively dislodged; (5) blockage re-lodges. (For MATLAB® processing, see Section 6.4.1.)

### 2.3.4 Biocompatibility

To ensure that the microfluidic system would not adversely affect biological samples, we used biocompatible materials such as PDMS for constructing the microfluidic components. PDMS is currently one of the most commonly used materials in bio-microfluidics research for several reasons, one being its permeability to oxygen and carbon dioxide, which is crucial for long term cell growth within the devices. [297, 298] We also cast a thin protective layer of PDMS over the acrylic VHB™ EAP in order to insulate biological samples from coming into

direct contact with the EAP or its SWCNT electrodes. In addition, efforts were made to separate the high electric fields needed for actuation from the fluidic samples within the channel. This is important since large electric fields can cause cell membrane poration [299], which could interfere with biochemical or cell biology assays. To address this, the electrode closest to the channel interior was grounded, eliminating any cross-channel potentials.

To validate the device biocompatibility of the DEA microchannel system, a dynamic viability assay was performed. HeLa cells were injected through the microchannel with actuation voltages of 0, 3, and 4 kV, as well as a standard Glass/PDMS microfluidic channel of the same geometry as a control (Figure 2.7). Cells were collected after injection, stained and counted for live and dead cells using a hemocytometer. The Glass/PDMS control demonstrated a viability of 83.5 ± 1.38%, while the 0, 3, and 4 kV states demonstrated viabilities of 82.1 ± 2.37 %, 91.9 ± 7.20%, and 41.4 ± 7.61%, respectively. While the 3 kV actuation state demonstrated negligible effect on cell viability, the 4 kV state appeared to reduce the viability by approximately 42% compared to the glass/PDMS control. Future designs may remedy this by utilizing thicker passive layers of PDMS or VHB™ to help insulate above 3 kV. Additionally, 3 kV does not appear to have any effect on cell viability, yet it causes channel deformation comparable to that at 4 kV (Figure 2.4(e)). Hence, a 3 kV actuation voltage may be optimal for biocompatible applications based on our system.

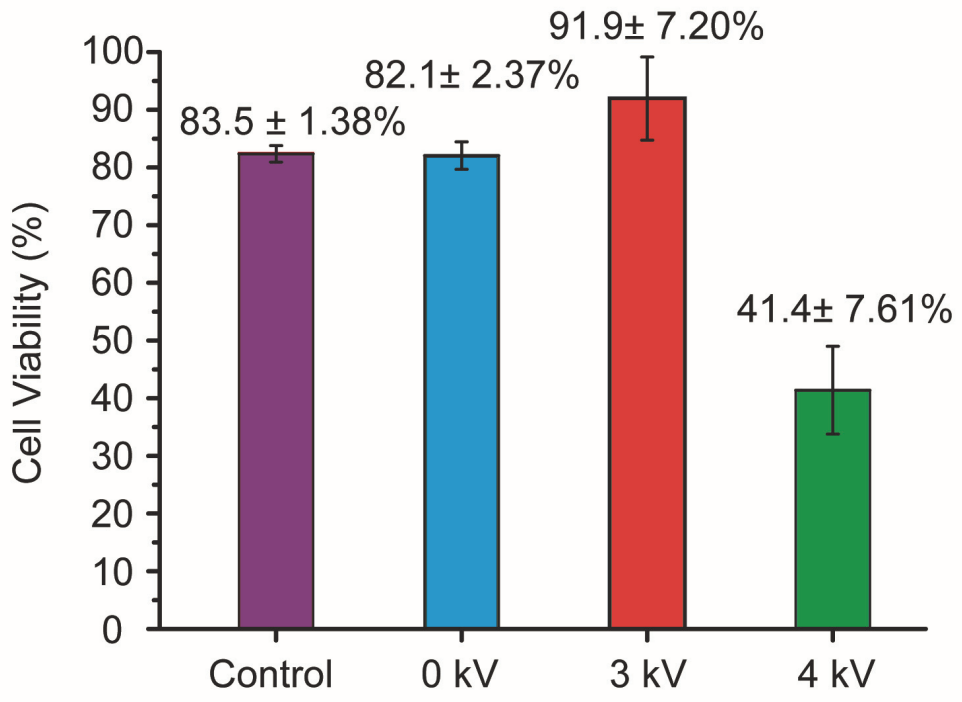


**Figure 2.7** Biocompatibility assessment for the DEA microfluidic device at 0 kV, actuated at 3 kV, actuated at 4 kV, and compared to a non-active control glass/PDMS chip with the same microchannel geometry. HeLa cell viability for the glass/PDMS control was 83.5 ± 1.38% while the viability for 0, 3, and 4 kV was 82.1 ± 2.37%, 91.9 ± 7.20%, and 41.4 ± 7.61%, respectively. Results shown are the average of three separate injections.

### 2.3.5 Actuation Mechanisms

Prior to actuation, the prestrain of the DEA membrane may pull the channel walls slightly inwards in the absence of a significant hydraulic pressure. To simplify the discussion, let us assume the PDMS channel walls deform with little resistance. As the hydraulic pressure increases, the channel walls may open slightly. Once equilibrium is reached, the force of the DEA membrane on the channel walls will balance the opposing hydraulic force on the channel walls. At this point, there are

two potential mechanisms of actuation at work in this system. The first is stress relaxation of the DEA membrane stack and a resulting expansion of the channel cross section by the intrachannel hydraulic pressure (Figure 2.8(a)). In this mode, when actuated, the DEA membrane will decrease in thickness and increase in area from the Maxwell pressure, releasing its tension on the channel walls. At this point, the force from the DEA membrane will be overtaken by the hydraulic pressure, which will increase the channel cross section.

The second possible mechanism is shear force transmission through extension-mode (planar) actuation. [227] In this regime, force from Maxwell pressure in the thickness direction is transmitted orthogonally into the planar direction due to incompressibility of the elastomer. Assuming a strong bond with the channel substrate, this force could shear open the channel, even in the absence of an intrachannel pressure (Figure 2.8(b)). Assuming few losses through each DEA layer, this shear force would ideally scale linearly with layer number when a stack is used. If outward buckling of the DEA stack occurs, this mode of force transmission may be hampered. Since the microchannel width (40 $\mu$m) is much less than the total thickness of the stack and passive layer (~477 $\mu$m), outward buckling, if any, occurs only close to the vicinity of the channel, and thus this mode of actuation force transmission is possible in our device configuration. In our system, it is not presently clear which actuation mechanism dominates. However, it is likely that both are factors that contribute to the observed alterations in channel geometry in our system (Figure 2.8(c)).

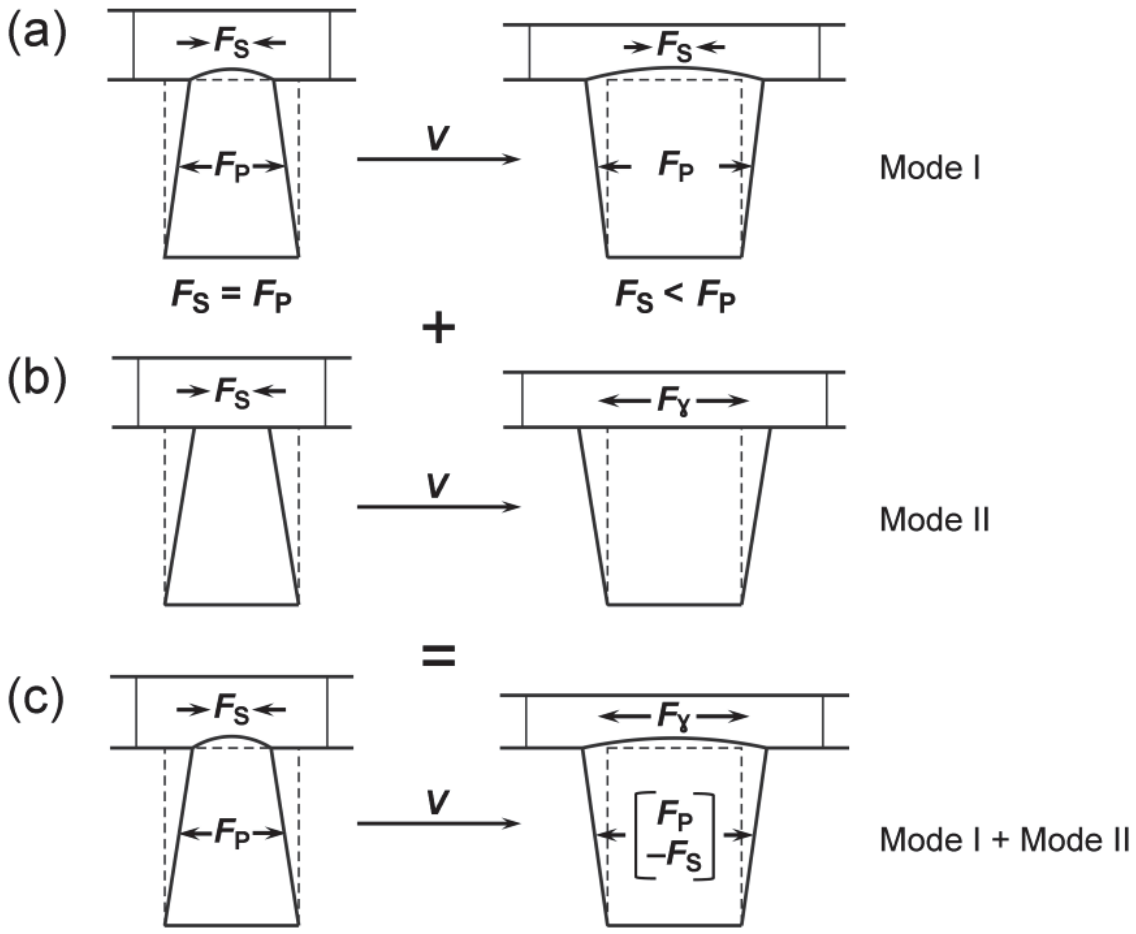


**Figure 2.8** Cross section of DEA microchannel system (not to scale), illustrating both possible actuation modes. Prior to actuation with voltage $V$ the prestrain force $F_S$ of the DEA stack may bow the channel walls inward slightly, and the force from the hydraulic pressure $F_P$ will balance $F_S$ at equilibrium. **(a)** In actuation mode I, Maxwell pressure causes an increase in planar area, decreasing the DEA membrane tension on the channel walls. This decrease in $F_S$ causes $F_P$ to dominate, and the channel cross-sectional area increases. **(b)** In mode II, the Maxwell pressure creates a shear force $F_Y$ that opens the channel, even in the absence of hydraulic pressure. **(c)** Increase in channel cross-sectional area is likely due to the sum of these two actuation modalities.

## 2.4 Concluding Remarks

Marriage of artificial muscle DEAs to deformable microfluidics is a logical one and holds future promise to the biomedical and microfluidic arenas. We have developed a novel DEA-microfluidic hybrid device capable of actively altering the geometry of a microchannel at actuation voltages between 3 and 4.5 kV. We hypothesize the actuation mechanism to consist of a combination of DEA in-plane shear stresses, DEA membrane stress relaxation, and hydraulic pressure. Further study is needed to characterize these actuation modalities. Consequences of this ability to actively tune channel cross-sectional area are active control of pressure-flow characteristics, as well as active clearing of channel blockages, both of which we have demonstrated while still maintaining good biocompatibility. Micro-peristaltic pumps and reduced-complexity lab-on-a-chip devices can readily be realized from this technology. DEAs can also act as capacitive pressure sensors, allowing our device to find further application as a programmable robotic microchannel, capable of sensing and responding to the samples it carries. [4] In this vein, adaptive microfilters and self-clearing channels are just a couple examples of the myriad applications that are possible.

# CHAPTER 3

# Biomimetic Fluidic Valve as an Artificial Sphincter

## 3.1 Introduction

The research in this section presents another DEA alternative to manipulate the pressure-flow characteristics of a fluidic system: a low-profile, biomimetic dielectric elastomer valve (DEV). The DEV is a novel minimum-energy tubular actuator consisting of a semi-rigid, flexible frame affixed to a prestrained dielectric elastomer. The DEV controls flow by generating a pinching force at its midline. Pinching force is achieved in part from the flexure of part of the frame, which acts as two opposing leaf springs. Because the prestrain is primarily isotropic, or equal in both directions, this pinching flexure is caused by tension in both the circumferential and axial directions. When actuated, the dielectric elastomer membranes increase in area due to Maxwell pressure, relieving this tension and resulting in movement in both directions. This motion mimics the function of the intestines, which contract both longitudinal and transverse muscle fibers during digestion. [300] Additionally, while several alternatives for controlling fluid flow using DEA MESs have been proposed, to date there has been no efficient design that allows the walls of a tube to directly control flow. [276]

## 3.2 Materials and Methods

### 3.2.1 Actuator Fabrication and Function

Figure 3.1(a) illustrates the fabrication steps of the tubular actuator. First, a 3M™ VHB™ 4905 acrylic elastomer is prestrained biaxially to 400% × 400% (Step 1). Second, single-walled carbon nanotube (SWCNT) electrodes are spray-deposited on both sides according to a specific pattern (Step 2). Another prestrained layer is then laminated to the first, and a top layer of SWCNT electrodes is spray deposited to form a two-layer DEA stack. Stacking multiple layers and actuating them in parallel allows the passive pinching force to be higher without increasing the actuation voltage. Third, the DEA stack is laminated to a 7 mil-thick PET frame and released from the surrounding VHB™ within one hour (Step 3). After releasing, the frame shown in Step 3 of Figure 3.1(a) folds into the minimum energy conformation shown in Figure 3.1(b), wherein the free edges are taped together to form a hoop of length 5 cm and long outer diameter 3 cm. In Figure 3.1(b), the upper left is a top view, upper right is the side, the lower left shows the view looking down the tube, and the lower right shows an inset with the DEV wrapped around the silicone tube.

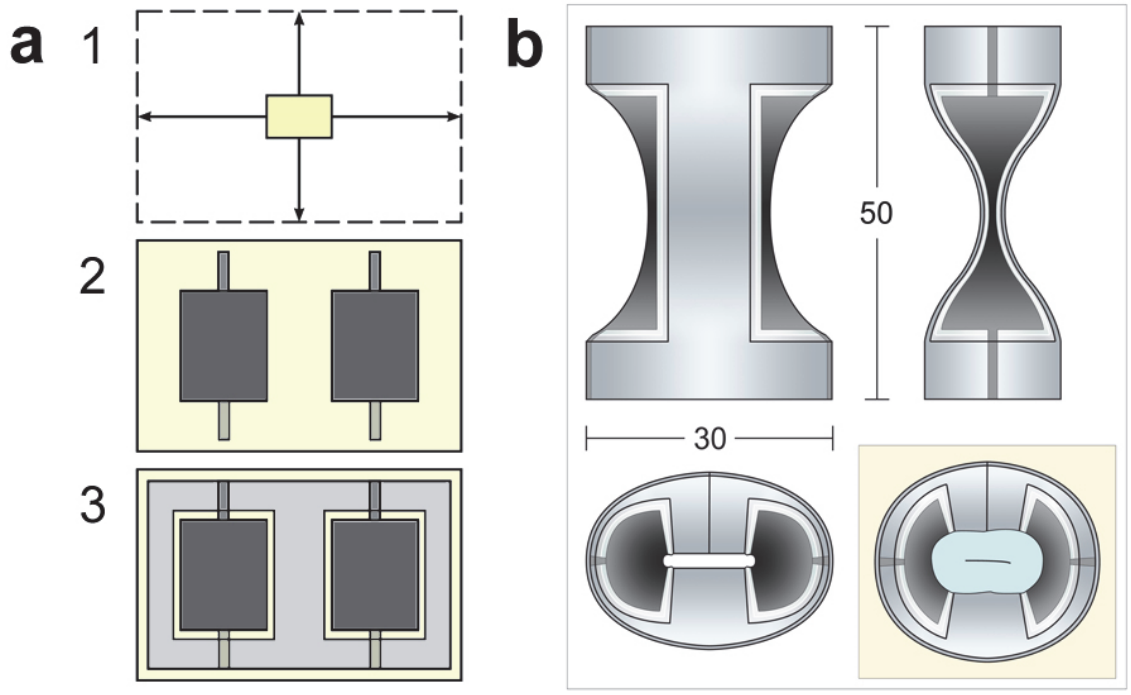


**Figure 3.1** **(a)** Fabrication steps of tubular actuator: *Step 1:* Prestrain VHB™ 4905 400% biaxially. *Step 2:* Spray deposit SWCNT electrodes on both sides by utilizing a shadow mask. Stack a second prestrained layer, and spray deposit an additional layer of SWCNTs. *Step 3:* Affix a semi-rigid, laser-cut PET frame to the DEA stack, and release the frame from the surrounding VHB™. **(b)** CAD illustration of the uncreased DEV tubular actuator, with three views shown as an orthographic projection. *Inset:* Shown wrapped around and pinching a custom silicone tube. Dimensions are in millimeters.

Actuation performance of the tubular actuator is shown in Figure 3.2(a) and (b), in which the actuator is depicted suspended in a vertical, freely hanging position. Figure 3.2(b) shows the deformation of the actuator at 2.7 kV. In this state, there is a ~108% increase in the diameter of the midline cross section. There is also a slight increase in the actuator length by about 4%. The longitudinal strips of the PET frame function as opposing leaf springs. In this configuration, the tubular

actuator exhibits high active strain but low passive pinching pressure. However, if these leaf springs are creased at the centerline, the passive pinching pressure increases, but at the expense of strain.

This design is biomimetic, mimicking the human lower esophageal sphincter (LES), pictured closed in Figure 3.2(c) and open in Figure 3.2(d). [301] In addition, the LES has muscle fibers oriented in both the longitudinal direction along the intestinal axis, as well as in the circumferential direction. This is visible in the cross section of the LES in Figure 3.2(e), which clearly shows muscle fibers oriented in plane and perpendicular to the plane. [300] The result of these two muscle fiber layers is contraction in both the circumferential and longitudinal directions during peristalsis, the name given to the muscular contractions responsible for moving matter through the intestines during digestion. By incorporating equibiaxial, isotropic prestrain in the DEV, both a circumferential and a longitudinal motion could be achieved simultaneously during actuation.

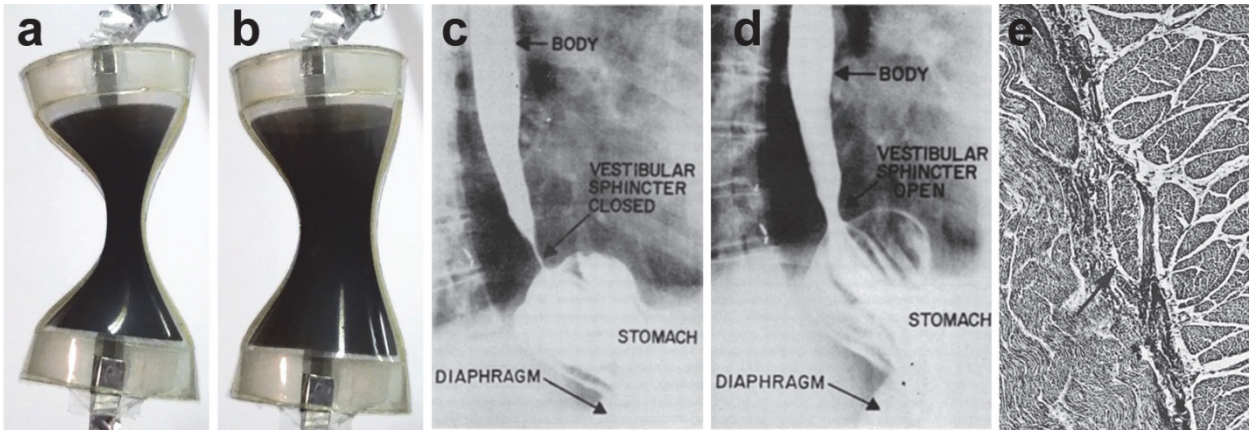


**Figure 3.2** **(a)** Tubular conformation after folding and taping the free edges of the frame together to form a hoop. The completed actuator is shown freely hanging at 0 V. **(b)** 2.7 kV applied, leading to a ~108% diameter strain and a length strain of ~4%. **(c)** Barium contrast radiology of the human lower esophageal sphincter in the closed position. [301] **(d)** Human LES in the opened position. [301] **(e)** Histological cross section of the wall of the human LES. In-plane circumferential muscle fibers are visible to the left, while longitudinal muscle fibers can be seen perpendicular to the image on the right. *Magnification:* 120× [300]

### 3.2.2 Fluidic Application

To control fluidic pressure, the DEV was interfaced with a custom silicone tube with an outer diameter of ~15 mm (Figure 3.3(c)), although much thinner tubing is possible. One purpose of the silicone tube is to avoid direct contact of the aqueous fluid with the DEV. However, with proper inner coating and sealing, the DEV could be used as an inline valve, replacing a segment of hose and coming into direct contact with the fluid. No lubricant is needed at the DEV-tube interface. The "hot" electrode is sandwiched between the DE layers, although encapsulation may

be needed due to moderately high voltages. Still, the DEV requires only low power. Moreover, with a wall thickness of less than 1 mm and a weight of less than 1.5 g, the DEV is relatively low-profile.

In order to apply adequate pinching stress to the silicone tubing, the longitudinal leaf springs were creased at the centerline to roughly 95°, and the completed DEV was wrapped around the custom silicone tube and joined into a hoop using polyimide (Kapton®) tape. Creasing greatly diminishes any restoring stresses in the PET leaf springs, increasing the effective pinching stress of the DEV. The DEV was left wrapped around the tube overnight in order to allow the actuator to stress relax sufficiently before testing, providing for a relatively flat baseline. After this time has elapsed, the average crease angle on the tube is about 120°. Figure 3.3(a) illustrates the unactuated DEV from three different angles, and wrapped around the tube. Figure 3.3(b) depicts a photograph of a freestanding DEV, and Figure 3.3(c) shows the DEV wrapped around the silicone tube.

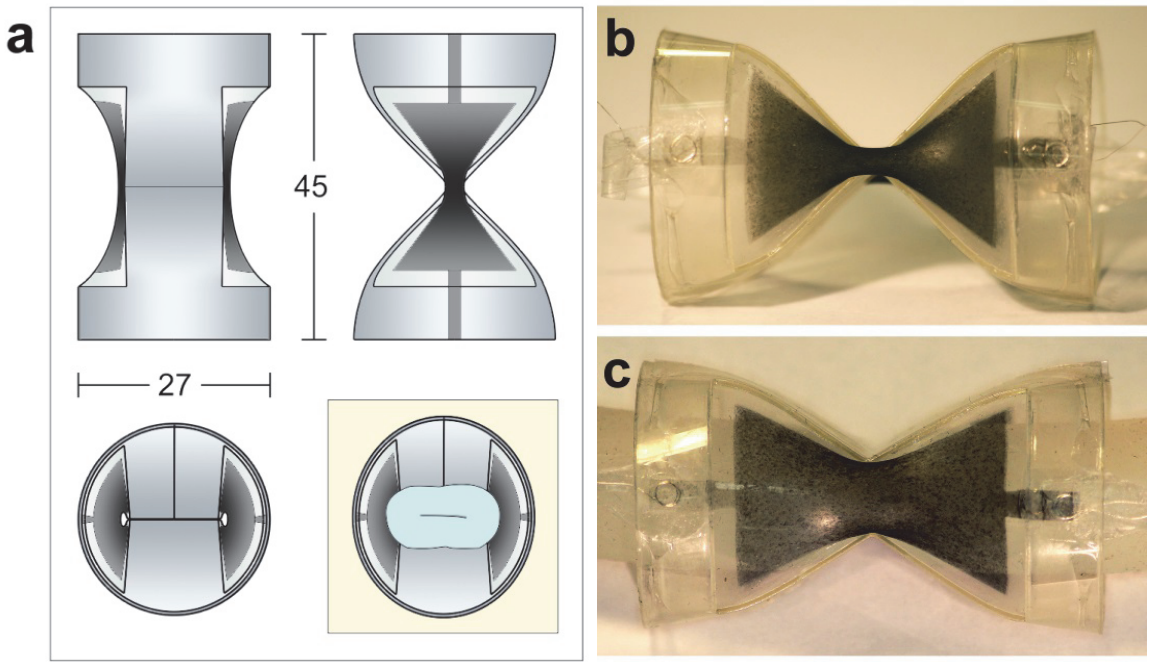


**Figure 3.3** **(a)** CAD illustration of the creased DEV tubular actuator, with three views shown as an orthographic projection. *Inset:* Shown wrapped around and pinching the silicone tube. Dimensions are in millimeters. **(b)** Photograph of the passive, free-standing DEV in profile. **(c)** Photograph of the passive DEV wrapped around the silicone tube.

### 3.2.3 Experimental Design

In order to measure the effectiveness of our device as a valve, the DEV and silicone tube were placed in series with a constant-flow fluidic system. This system, illustrated in Figure 3.4, consists of three primary components: a syringe pump to administer a hydraulic pressure (KD Scientific Model 100 Series), the DEV wrapped around a soft silicone tube (cast from Ecoflex® 00-10 with 20% silicone thinner by weight), and a pressure sensor (Honeywell NSCDANN005PGUNV). The syringe pump perfuses an aqueous dye through a plastic 60 cc syringe. Flow is divided by a three-way connector, and a gauge pressure transducer in parallel with the DEV

measures the upstream hydraulic pressure in a LabVIEW™ virtual instrument (VI) (via a National Instruments™ NI USB-9162 and NI 9219 interface system). The VI (see Appendix, Section 0) also outputs an actuation voltage command (National Instruments™ NI USB-6009), which controls an in-house high voltage power supply to actuate the DEV.

Three experiments were performed. In the first system characterization experiment, a red dye (food coloring, ~2.5 vol.%) was perfused at 400 mL/hr, and the DEV was actuated at 3.2 kV. The top and side of the DEV were illuminated through backlighting and photographed (i) before flow or voltage, (ii) during flow with no voltage, and (iii) during flow with voltage. In the second flow-pressure experiment, flow was driven at 8 flow rates between 50 and 400 mL/hr, inclusive, at 50 mL/hr increments. For each flow rate, the DEV was actuated at 11 voltages between 400 and 2,400 V, inclusive, at 200 V increments; this constitutes a single trial, which was repeated three times per flow rate. Three separate DEVs were tested; therefore, 72 trials were performed in total. For each trial, flow was initially started at the highest, or "fast-forward" (FF), setting of a fixed 420.9 mL/hr, then removed to create a maximum baseline pressure value for comparison across trials. Then, the DEV was actuated continuously for 15 seconds, discharged for 15 seconds, and repeated until 2.4 kV was reached. The upstream pressure was recorded in LabVIEW™ at a sampling rate of 100 Hz.

In the third reliability experiment, flow was perfused at 100 mL/hr, with 10 syringe changes in a 6 h period. The DEV was actuated via computer control at 600

V and 0.1 Hz, with a duty cycle of 50% for more than 2,000 actuation cycles. Next, flow was perfused at 400 mL/hr, with 40 syringe changes in 6 h, and a second DEV was actuated in the same manner as previously but at 2.2 kV. We observed faster settling times at higher flow rates; 400 mL/hr was sufficient to allow for a full pressure drop at the higher 2.2 kV during the cycle "on" time of 5 s. Additionally, a mathematical model was developed and fit to experimental data for DEVs with four different initial prestretch ratios (5 × 5, 4 × 4, 5 × 4, and 4 × 5). Initial pinching pressures for these four DEVs were measured, three trials per DEV, at the pressure maximum when the hydraulic pressure equaled the pinching pressure, before stress relaxation set in. The 5 × 5 model was also fit to data from the second experiment after being adjusted for stress relaxation over an average 8 hour period.

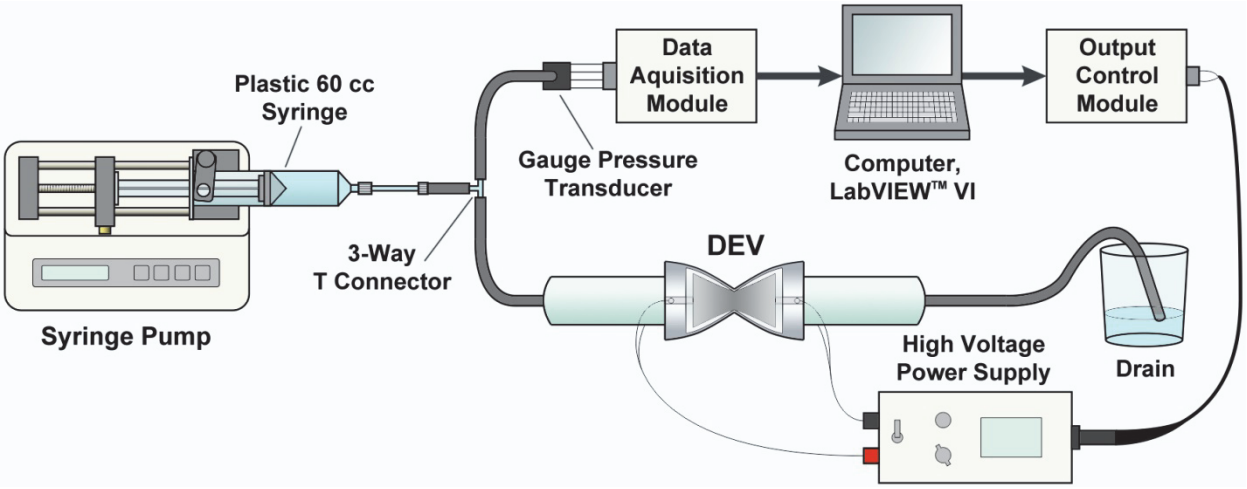


**Figure 3.4** Experimental setup to test the function of the DEV. A syringe pump perfuses an aqueous medium to the DEV wrapped around a custom silicone tube and a gauge pressure transducer in parallel. The upstream pressure is read in LabVIEW™, and output control is sent to a high voltage power supply to actuate the DEV.

### 3.2.4 Data Processing

Data were processed using MATLAB® and Excel for Experiment 2. Steady-state pressure data points were extracted from the dynamic data collected. To systematically extract the pressure drop from each actuated valley, 10 seconds were added to the point right before each actuation dip, and the following 2 seconds were then averaged. This was performed for each of the 11 actuation valleys (see Figure 3.7 and Figure 6.14). Next, there still appeared to be some baseline drift over the duration of each trial due to the viscoelasticity of the DEV. To eliminate this settling, baseline data points were extracted by averaging the 4 seconds before each actuation dip, which were then subtracted from the first 4 second average before 400 V. These differences were then added to the points extracted from each respective valley to eliminate drift. Afterwards, all baselines were shifted into alignment as follows. 4 seconds were added to the minimum before each FF plateau, and the following 1 second of data was averaged for each. Differences were found between the FF average of each trial and the highest FF value. These differences were then added to all drift-shifted data points, and the resulting data points were averaged across the 9 trials. Pressure-flow curves were plotted from these processed pressure averages, and least squares regression fit lines to each pressure-flow voltage trend. The MATLAB® code is provided in Section 6.4.2.1.

For Experiment 3, filtering was performed in MATLAB® to eliminate the baseline drift. A minimum order Butterworth low-pass filter was designed having a

normalized passband frequency of 0.001 Hz with a 6 dB attenuation, and a stopband frequency of 0.05 Hz with a 250 dB attenuation. This filter created a thin trace of the baseline, which was then subtracted from the initial data. Then, MATLAB® was used to quantify any change in actuation performance over 2,000 cycles (see Section 6.4.2.2). Maxima for the first 100 consecutive 10 second intervals were subtracted from the minima in these same intervals, and this difference data set was averaged. Subtracting the maxima from the minima gives the total pressure drop with actuation. The same was performed for the final 100 consecutive 10 second intervals, and the difference $D$ was taken between these two averages. Standard deviations $S_i$ and $S_f$ were taken for the initial and final difference data sets, and a comparison was made between $D$, $S_i$, and $S_f$ to asses any change in actuation pressure drop. These steps were performed for both 600 V and 2.2 kV reliability tests.

## 3.3 Results and Discussion

### 3.3.1 Experiment 1: System Characterization

In this characterization experiment, we demonstrate that the DEV pinches the silicone tube completely shut at 0 V and 0 mL/hr, as shown in Figure 3.5(a) and (d). After flow was started at 400 mL/hr, the DEV appeared to hold back much of the pressure at steady state, since the upstream inner diameter of the silicone tubing dilated by as much as two times (Figure 3.5(b) and (e)). Flow across the DEV in this state was thus highly encumbered. Finally, the DEV was actuated at 3.2 kV, allowing flow to proceed virtually unhindered (Figure 3.5(c) and (f)). During actuation, there was no significant pressure buildup upstream, as evidenced by the upstream inner diameter returning to its initial size as the pressure equalized on both sides of the DEV.

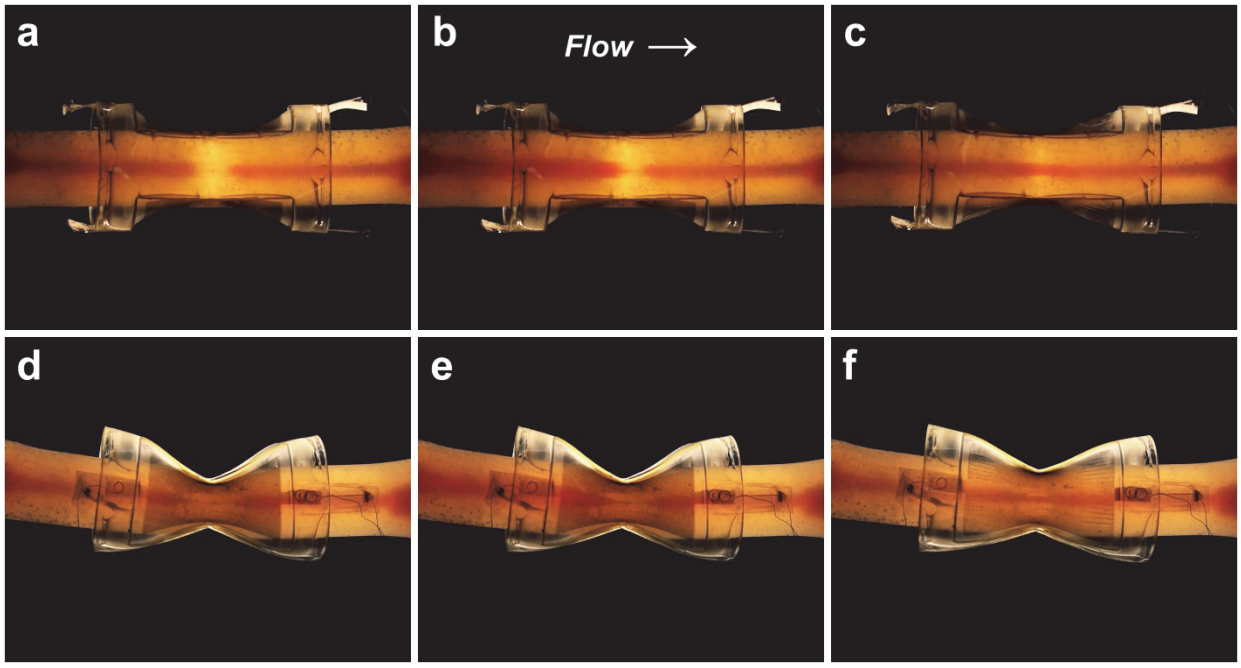


**Figure 3.5** Visual characterization of DEV function via backlight illumination. Aqueous dye in red; silicone tubing in yellow. Top views: **(a)** 0 V, 0 mL/hr, **(b)** 0 V, 400 mL/hr, **(c)** 3.2 kV, 400 mL/hr, **(d)–(f)** Side views of (a)–(c).

### 3.3.2 Actuation Mechanisms

The observations from the previous experiment can be explained by the following simple analysis of the underlying actuation mechanisms of the DEV. In the "off" state, the DE membranes are in a high stress state from the prestrain. At equilibrium, the resulting in-plane force exceeds the restoring force of the two opposing creased PET leaf springs at the centerline of the frame. As a result, the DEV pinches the silicone tubing shut completely, and pressure builds upstream with flow, causing the upstream tube to dilate. In the "on" state during actuation, a Maxwell pressure is generated in the thickness direction of the DE membranes,

causing them to stress relax. At equilibrium, the restoring force of the PET leaf springs is now larger by comparison than the stress in the DE membranes. Thus, the center of the DEV opens to allow fluid to flow freely. The upstream dilation vanishes as pressure equalizes on both sides of the tube. The illustration in Figure 3.6 shows side and front views of these two states.

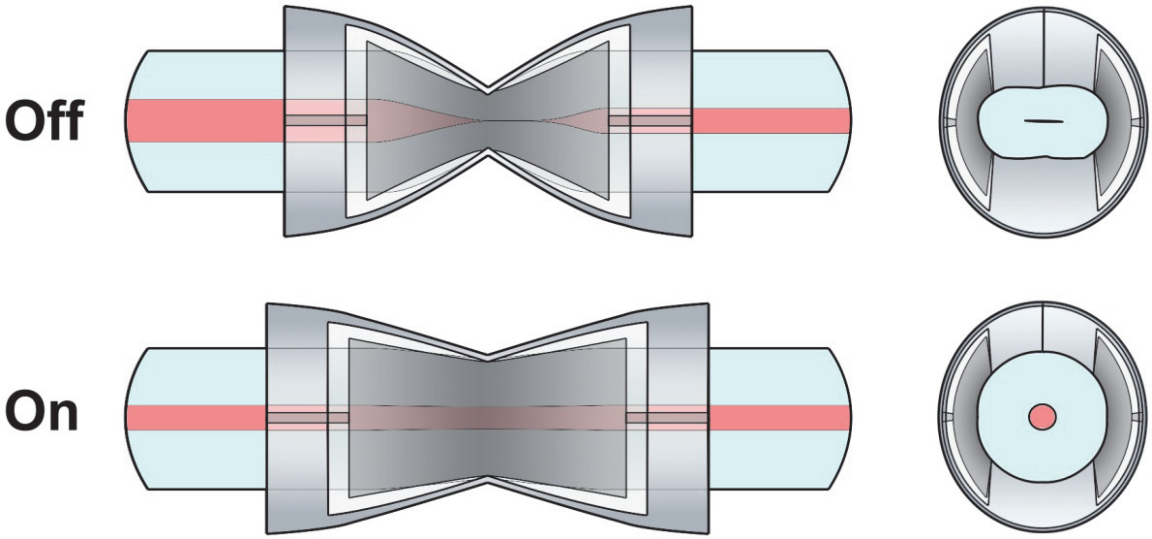


**Figure 3.6** Actuation of the DEV, as observed in Experiment 1. In the "Off" state, the DE membrane force exceeds the restoring force of the creased leaf springs, and the DEV is shut. In the "On" state, an actuation voltage causes the in-plane force in the DE membranes to decrease below that of the leaf springs, and the DEV opens. The hydraulic pressure may also play a role in opening the DEV during actuation.

### 3.3.3 Experiment 2: Pressure-Flow Performance

In the second experiment, the DEV was shown to increase the steady-state system pressure by 3 to 3.5 kPa in the off state (following stress relaxation

overnight) and reliably decrease this pinching pressure with the square of the applied voltage. As shown in Figure 3.7, the DEV increases the intrasystem pressure by ~3.3 kPa at 200 mL/hr and 0 V when the DEV is closed and the flow is most encumbered. Actuation at 400 V shows a noticeable drop in pinching pressure, and there appears to be a quadratic drop in this pressure with linearly increasing actuation voltage. By 2.4 kV, the DEV has completely relieved its pinching pressure, and the intrasystem pressure drops to 0 Pa. Any baseline drift is likely due to the passive viscoelasticity of the acrylic DE, which should be mostly avoidable with silicone DEs. This creep is not entirely visible in Figure 3.7, but a small amount was present. The settling time constant is not quantified, but it is observed to increase with decreasing flow rate and increasing voltage, indicated by the increase in slope of the actuation valleys with time. For example, if Figure 3.7 were replotted for 400 mL/hr data, the pressure drops would be more abrupt, especially at higher voltages.

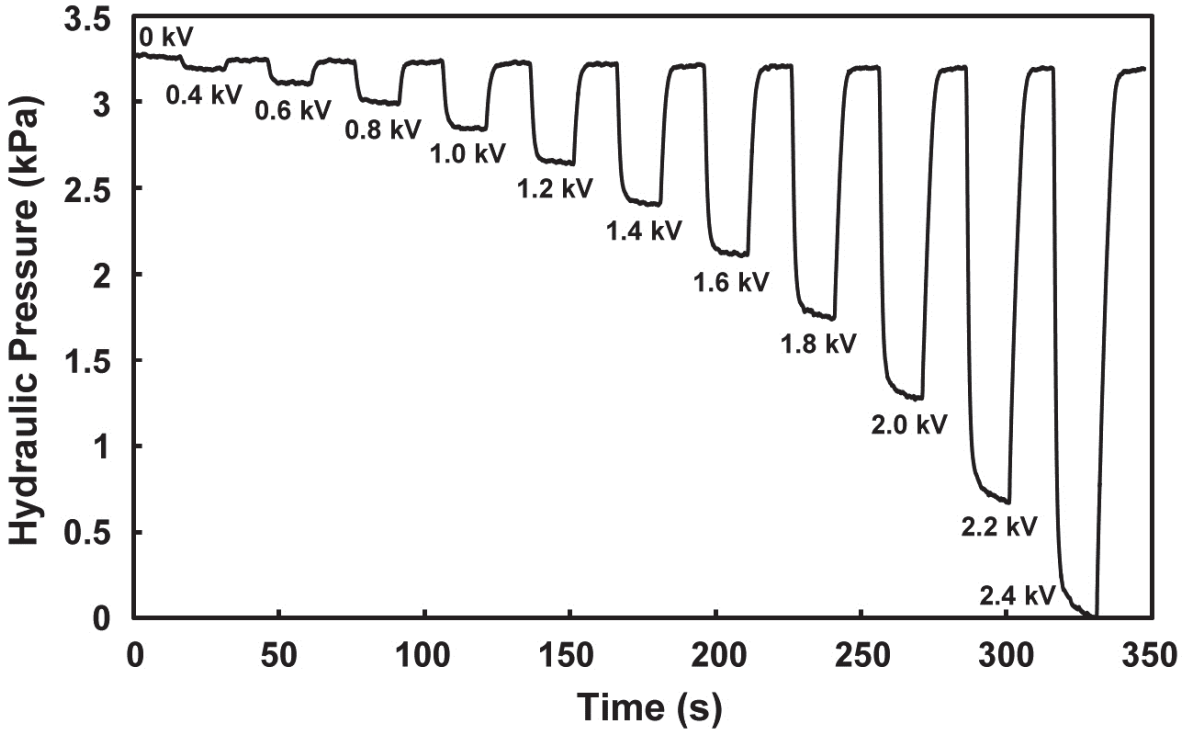


**Figure 3.7** Representative dynamic pressure drops with actuation voltage at 200 mL/hr for one trial. A quadratic fall in pressure is observed from ~3.3 kPa at 0 V to 0 Pa at 2.4 kV with linearly increasing actuation voltage, apparent with the constantly-spaced 30 s cycle intervals.

Dynamic pressure data similar to that in Figure 3.7 were obtained for several flow rates and voltages, and data points were extracted and averaged over several trials to produce the pressure-flow plot shown in Figure 3.8. The horizontal axis is the input flow rate controlled by the syringe pump, and the vertical axis is the upstream steady-state pressure resulting from passive pinching and active relaxation of the DEV. Linear regression was performed, and all $R^2$ values were between 96.7% and 97.4%. This suggests a primarily linear trend for the pressure-flow data sets at each voltage. Additionally, most of the lines are parallel, indicating

equal fluidic resistances. The slopes are all roughly 1.2 Pa-hr/mL, except for a slight decrease to ~0.8 Pa-hr/mL at 2.4 kV.

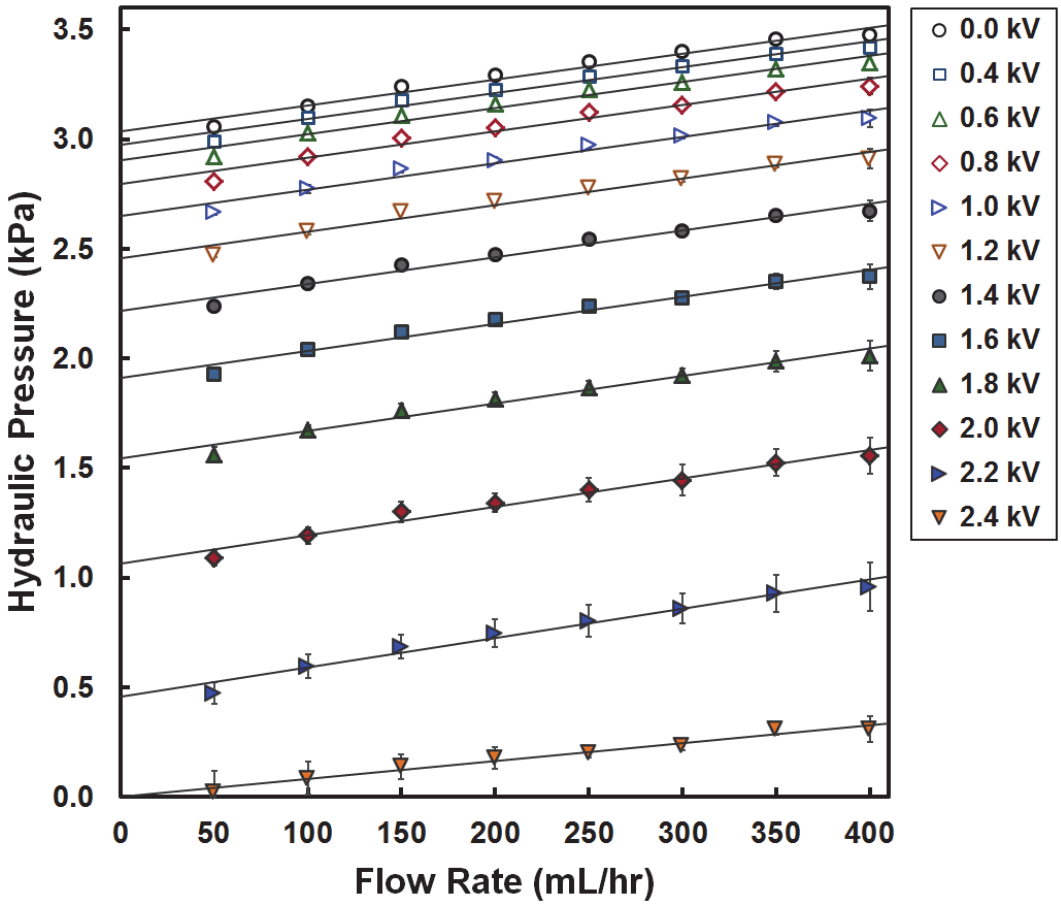


**Figure 3.8** System pressure as a function of syringe pump flow rate and DEV actuation voltage. Data points extracted from dynamic pressure plots and averaged across nine trials per flow rate: three trials per DEV, and three different DEVs. Linear regression fits data trends with an $R^2$ value of less than 97.4%. Some pressure changes occurred with varying flow rates, but the largest pressure changes resulted from active actuation of the DEV.

We hypothesize that there may be a slight change in fluidic resistance for every curve, which corresponds to the change in effective inner diameter of the tube.

However, it is possible that this effect was too small to measure with the current experimental setup. This would be especially true for the closer-spaced trends, in which the lower voltages cause only very small changes in the tube inner diameter as the DEV actuates. The fluidic resistance with the DEV at 0 V was $1.2 \times 10^{-3}$ kPa-hr/mL, over one order of magnitude higher than the resistance with no DEV wrapped around the tube, which was measured to be $9 \times 10^{-5}$ kPa-hr/mL (Figure 3.9).

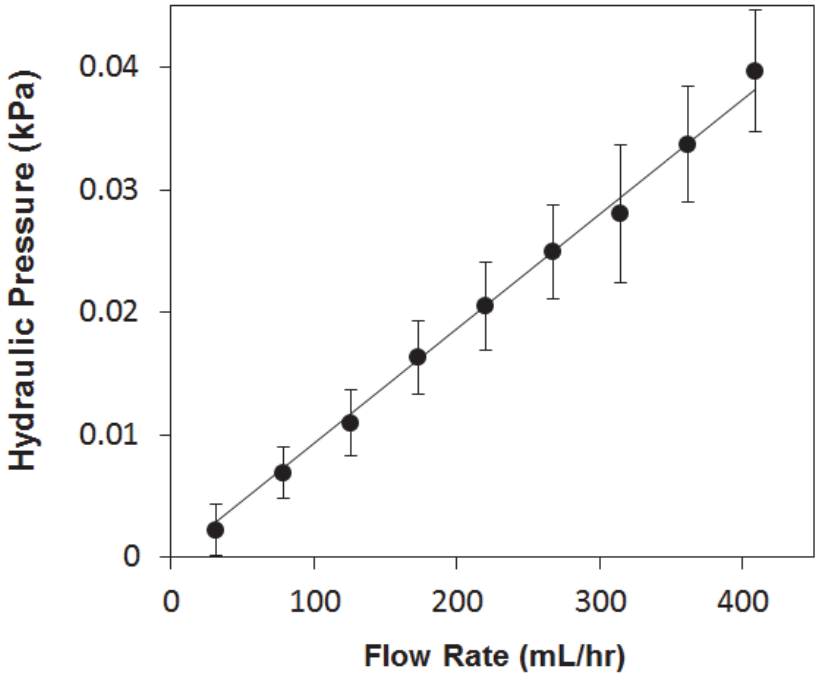


**Figure 3.9** Fluidic pressure versus flow rate for the system pictured in Figure 3.4 without the DEV wrapped around the silicone tube. Linear regression determined the fluidic resistance to be $9 \times 10^{-5}$ kPa-hr/mL, with an $R^2$ value of 0.9958. Error bars represent plus and minus one standard deviation of the measured hydraulic pressure data at each flowrate.

To better view the quadratic drop in intrasystem pressure with linearly increasing voltage, the pressure drop at each flow rate was plotted as a function of actuation voltage in Figure 3.10. As before, lower flow rates result in slightly lower pressures, but by no more than 0.5 kPa. By contrast, actuation voltage alters the system pressure by at least 3.0 kPa.

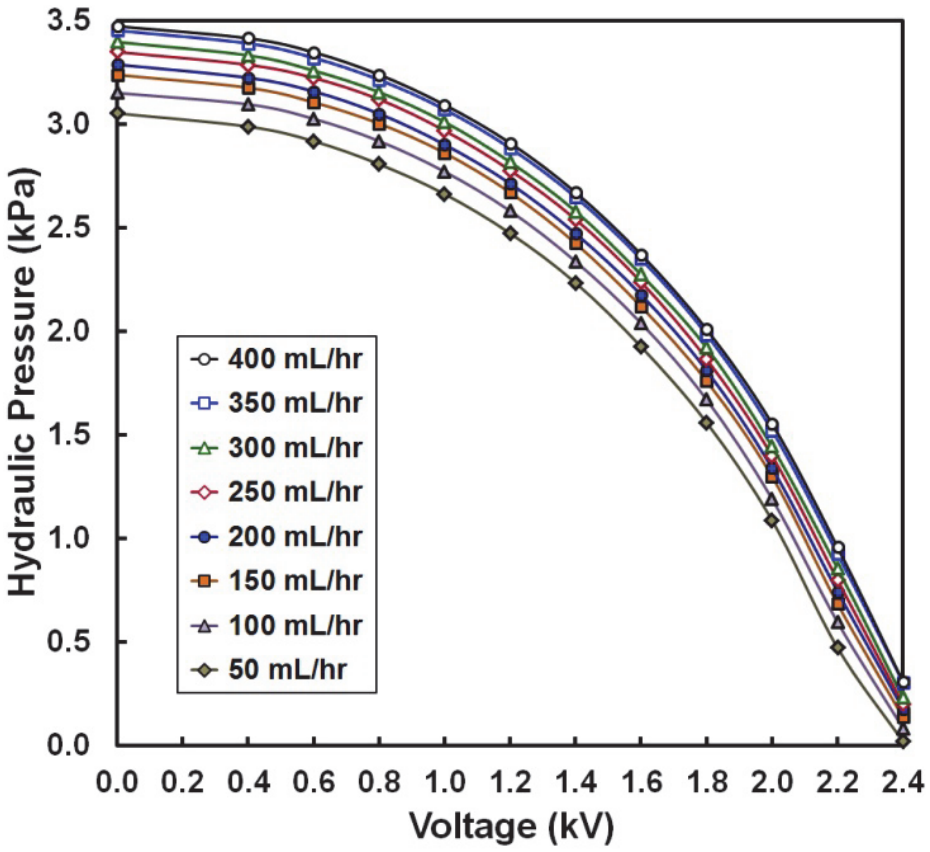


**Figure 3.10** Pressure as a function of actuation voltage, plotted to better visualize the quadratic fall in pressure with linearly increasing actuation voltage. At 50 mL/hr, the rise in system pressure at 0 V is ~3 kPa, dropping to 0 kPa at 2.4 kV. Higher flow rates result in higher pressures, but only by ~0.5 kPa. Smoothed curves are fitted to the data points to guide the eye.

### 3.3.4 Experiment 3: Reliability Testing

Reliability testing of the DEV was carried out over 2,000 actuation cycles using a computer controlled high voltage source. As shown in the top two quadrants of Figure 3.11, a square wave input voltage at 600 V actuated the DEV at 0.1 Hz, with a duty cycle of 50%. The bottom two plots show similar actuation but at 2.2 kV. The full 2,000 cycles are shown in the right column, while a representative 5 cycles are shown in the left column to clarify the shapes of the actuated pressure drop curves. Because of syringe changes, the 600 V plot (at 100 mL/hr) combines 10 consecutive trials in sequence, while the 2.2 kV plot (at 400 mL/hr) stitches together 40 successive trials.

For the 600 V reliability test, the difference in mean pressure drops $D$ between the beginning and end of the 2,000 cycles was only $5.6 \times 10^{-3}$ kPa. This value is less than the standard deviation $S_i$ of the data set sampled near the beginning, which was $6.8 \times 10^{-3}$ kPa, as well as less than the standard deviation $S_f$ of the data set sampled near the end, namely $9.0 \times 10^{-3}$ kPa. Similar results were demonstrated with the 2.2 kV test, in which $D$ was actually a pressure rise of $7.59 \times 10^{-2}$ kPa, but was less than one order of magnitude higher than $S_i$ and $S_f$ of $3.95 \times 10^{-2}$ kPa and $2.17 \times 10^{-2}$ kPa, respectively. $D$ was not significantly greater than random variability in the data as measured by $S_i$ and $S_f$. This is an indication that the DEV shows no significant degradation in electromechanical performance over 2,000 cycles at 600 V and virtually no degradation over 2,000 cycles at 2.2 kV.

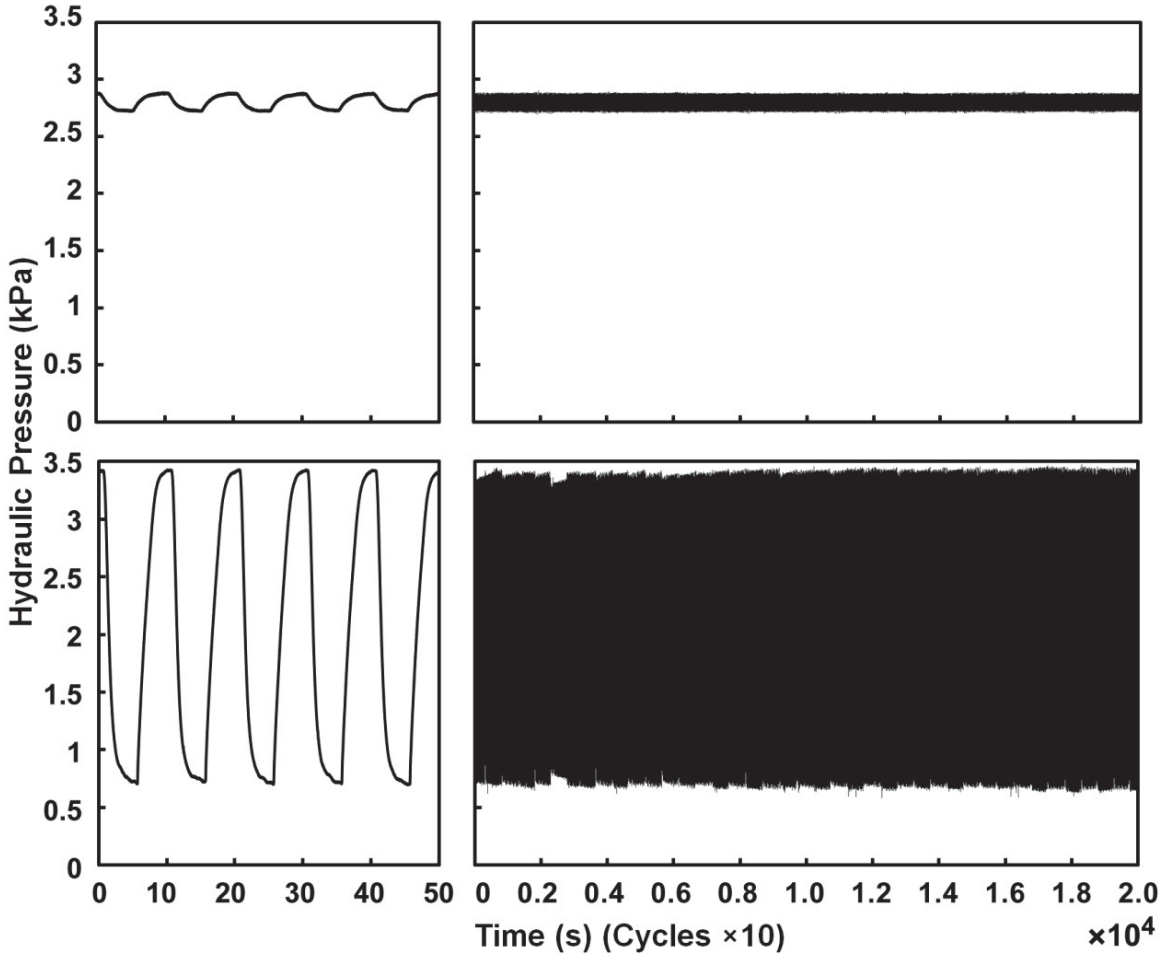


**Figure 3.11** Reliability testing of two separate DEV tubular actuators: The top row graphs the performance of a DEV actuated at 600 V for 2,000 cycles, while the bottom row plots a DEV actuated at 2.2 kV for 2,000 cycles. The right column shows the 2,000 actuation cycles, with several consecutive runs stitched together due to syringe changes. The left column shows a zoomed in view of each automated actuation pressure drop curve, chosen at random from the data in the right column.

### 3.3.5 Modeling

The DEV actuator was modeled as an equivalent actuator with the simplest possible geometry that performs the same function. Specifically, the complicated

"bowtie" pincher minimum energy DEV can be represented in its simplest form as an elastic band (Figure 3.12). While this is a drastic simplification of this complex system, it embodies the fundamental operating principles of the DEV. The stress within this band in the circumferential direction $\sigma_c$, or hoop stress, is related to the rise in intrasystem pressure $P$ by the following equation

$$P = \frac{\sigma_c T}{r} \tag{3.1}$$

where $T$ is the total thickness of the rubber band and $r$ is the outer radius of the cylinder the band encircles. Because of its importance to the research of this dissertation, a derivation of Equation 3.1 is provided in the Appendix. Since the silicone tube that the actuator encircles is incompressible, it is assumed that the pressure is transmitted to the fluid with no mechanical loss, and so the outer radius of this tube is used.

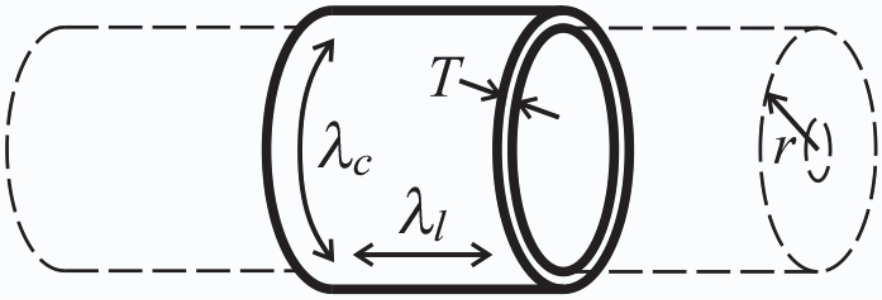


**Figure 3.12** Equivalent actuator to the DEV, depicted wrapped around the silicone tube. This is the simplest geometry that performs the same primary function as the DEV. The circumferential stretch $\lambda_c$, longitudinal stretch $\lambda_l$, total passive thickness $T$, and outer radius of the silicone tube $r$ are labeled.

The hoop stress $\sigma_c$ in the band is a function of the prestretch in the elastomer. To ensure the passive stress in this hoop is equivalent to the stress in the bowtie DEV actuator, equivalent stretches were estimated based on the geometry of the actual DEV. From Figure 3.13 one can see that the equivalent stretch in the longitudinal direction is

$$\lambda_l = (c/l_0)\lambda_{0,l} \tag{3.2}$$

where the initial longitudinal prestretch $\lambda_{0,l}$ is multiplied by the ratio of half the square hole length after folding and wrapping around the tube *c*, to half the hole length $l_0$ when the stretch equals $\lambda_{0,l}$, before the actuator frame is folded. This accounts for any compression in the longitudinal direction.

Stretch in the circumferential direction is further diminished due to the change in shape from a rectangle to pairs of triangles, with a slight opening in the center due to the tube (Figure 3.13). For one side of the actuator, the stress in each symmetric quadrant is identical, so only one triangular quadrant needs considered. The circumferential stretch is estimated to be

$$\lambda_c = \lambda_{0,c} - \lambda_{\text{lost},c} \tag{3.3}$$

where $\lambda_{\text{lost},c}$ is the average stretch that was lost from folding, and $\lambda_{0,c}$ is the initial circumferential prestretch. $\lambda_{\text{lost},c}$ was estimated by taking the average of the stretch lost in the center of the DEV $\left[(a-b)/a\right]\lambda_{0,c}$ with the stretch lost at the outside of the DEV $(0/a)\lambda_{0,c}$:

$$\lambda_{\text{lost},c} = \frac{1}{2}\left(\frac{0}{a}\lambda_{0,c} + \frac{a-b}{a}\lambda_{0,c}\right) = \frac{1}{2}\left(\frac{a-b}{a}\right)\lambda_{0,c} \tag{3.4}$$

Combining (3.3) and (3.4), we find that

$$\lambda_c = \left[1 - \frac{1}{2}\left(\frac{a-b}{a}\right)\right]\lambda_{0,c} \tag{3.5}$$

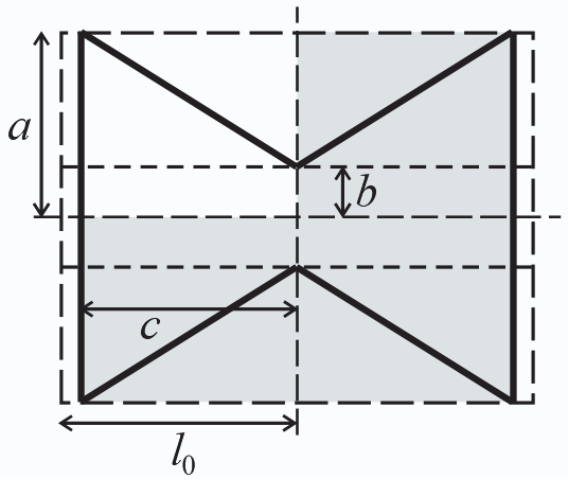


**Figure 3.13** Illustration representing a profile view of one side of the DEV, after wrapping around the silicone tube. By measuring the labeled lengths, the stretches of the equivalent system can be geometrically estimated. The equivalent circumferential stretch $\lambda_c$ is estimated by essentially averaging together the stretch at the edge and center of one of the quadrants, and multiplying this by the initial prestretch.

From the experimental data, it can be inferred that the system is described by the equation

$$P(Q,V,\lambda_l,\lambda_c) = P_{\text{R}}(Q) + P_0(\lambda_l,\lambda_c) - P_{\text{M}}(V,\lambda_l) \tag{3.6}$$

in which the measured hydraulic pressure $P$ results from three separate contributions: (i) the fluidic pressure $P_{\text{R}}$ as a function of flow $Q$ driven by the syringe pump, (ii) the pinching pressure of the DEV $P_0$, and (iii) the hydraulic

pressure due to the Maxwell actuation pressure $P_{\mathrm{M}}$. The pinching pressure $P_0$ is a function of the equivalent longitudinal stretch $\lambda_l$ and equivalent circumferential stretch $\lambda_c$ defined above, and the Maxwell hydraulic pressure $P_{\mathrm{M}}$ depends on the applied actuation voltage, as well as on the longitudinal stretch $\lambda_l$, which will be shown below.

Let us consider each of these three contributions separately. First, our DEA device controls the flow of a fluidic system. The governing equation for flow $Q$ in a tube is given by a basic form of the Hagen-Poiseuille equation, which is analogous to Ohm's law [302]:

$$\Delta P = \overline{R}Q \tag{3.7}$$

where $\Delta P$ is the hydraulic pressure drop between the tube inlet and outlet, and $\overline{R}$ is the equivalent fluidic resistance of the entire system, which can be measured empirically from the slopes of the pressure-flow curves. Because the measured upstream pressure $P$ is gauge pressure, and the pressure at the outlet is atmospheric pressure, $\Delta P = P_{\mathrm{inlet}} - P_{\mathrm{outlet}} = \left(P - P_{\mathrm{atm}}\right) - P_{\mathrm{atm}} = P$, and we can write

$$P_{\mathrm{R}}\left(Q\right) = \overline{R}Q \tag{3.8}$$

for our system. Because the slope remains roughly the same in Figure 3.8 across all applied voltages, we let  remain constant as a simplification in our model.

Second, we can write an expression for $P_0$ as a function of the equivalent stretches based on Equation 3.1 as

$$P_0(\lambda_l,\lambda_c)=\frac{\sigma_c(\lambda_l,\lambda_c)T}{r} \tag{3.9}$$

We can rewrite $T$ in terms of the stretches by recalling that for an incompressible solid, volume is constant and

$$\lambda_l\lambda_c\lambda_z=1 \tag{3.10}$$

where the stretch in the $z$-direction is defined as

$$\lambda_z=T/T_0 \tag{3.11}$$

Combining (3.10) and (3.11) we obtain

$$T=\frac{T_0}{\lambda_l\lambda_c}=\frac{nt_0}{\lambda_l\lambda_c} \tag{3.12}$$

where $n$ is the number of layers of VHB™ of equal initial thickness $t_0$. Equation 3.9 then becomes

$$P_0(\lambda_l,\lambda_c)=\frac{\sigma_c(\lambda_l,\lambda_c)nt_0}{r\lambda_l\lambda_c} \tag{3.13}$$

In order to write the circumferential stress as a function of the stretches we utilize the Gent hyperelastic model, a revised form of the Neo-Hookean model that takes into account elastomer stiffening at high strains. The strain energy function according to the Gent model is

$$W(\lambda_l,\lambda_c)=-\frac{G}{2}J\ln\left(1-\frac{\lambda_l^2+\lambda_c^2+\lambda_l^{-2}\lambda_c^{-2}-3}{J}\right) \tag{3.14}$$

Furthermore, the state equation for the circumferential stress in an ideal dielectric elastomer is

$$\sigma_c = \lambda_c \frac{\partial W}{\partial \lambda_c} - \varepsilon_r \varepsilon_0 \left( \frac{V}{t} \right)^2 \tag{3.15}$$

Substituting (3.14) into (3.15) and differentiating yields

$$\sigma_c = \frac{G\left(\lambda_c^2 - \lambda_l^{-2}\lambda_c^{-2}\right)}{1 - \left(\lambda_l^2 + \lambda_c^2 + \lambda_l^{-2}\lambda_c^{-2} - 3\right)J^{-1}} - \varepsilon_r \varepsilon_0 \left( \frac{V}{t} \right)^2 \tag{3.16}$$

where $G$ is the shear modulus, $J$ is the strain stiffening coefficient, $\varepsilon_0$ is the permittivity of free space, $\varepsilon_r$ is the dielectric constant of the elastomer, and $t$ is the thickness of the actuating region of one layer of VHB™, defined below in Equation 3.21. Values of $G$ = 50 kPa, $J$ = 120, and $\varepsilon_r = 4.5$ were used in this model, which have been shown by Bozlar et al. and Lu et al. to be a good fit for VHB™ 4910 (and 4905) acrylics. [10, 15]

For the second part of the model, we will temporarily ignore the Maxwell pressure term in (3.16), i.e., when $V = 0$. Substituting this result into (3.13) gives

$$P_0\left(\lambda_l, \lambda_c\right) = \frac{nt_0 G}{r\lambda_l \lambda_c}\left[\frac{\lambda_c^2 - \lambda_l^{-2}\lambda_c^{-2}}{1 - \left(\lambda_l^2 + \lambda_c^2 + \lambda_l^{-2}\lambda_c^{-2} - 3\right)J^{-1}}\right] \tag{3.17}$$

Third, let us consider $P_M$, the active contribution of Maxwell pressure on the hydraulic pressure during actuation. The regions of the DEV that experience the largest degree of Maxwell pressure are the regions with the smallest thickness and highest prestretch, near the edges. Here, the circumferential prestretch is assumed to be unchanged from its initial state before folding. Equation 3.12 becomes

$$T' = \frac{nt_0}{\lambda_l \lambda_{0,c}} \tag{3.18}$$

and we can thus write

$$P_{\mathrm{M}}\left(V,\lambda_l\right) = \frac{\sigma_{c,\mathrm{M}}\left(V,\lambda_l\right)T'}{r} = \frac{\sigma_{c,\mathrm{M}}\left(V,\lambda_l\right)nt_0}{r\lambda_l\lambda_{0,c}} \tag{3.19}$$

in which the hoop stress contributed by the Maxwell stress is given by the final term in (3.16) as

$$\sigma_{c,\mathrm{M}}\left(V,\lambda_l\right) = \varepsilon_r\varepsilon_0\left(\frac{V}{t}\right)^2 \tag{3.20}$$

wherein the thickness in the actuating region for one layer is

$$t = \frac{t_0}{\lambda_l\lambda_{0,c}} \tag{3.21}$$

Substituting Equation 3.21 into Equation 3.20, we obtain

$$\sigma_{c,\mathrm{M}}\left(V,\lambda_l\right) = \varepsilon_r\varepsilon_0\frac{V^2}{{t_0}^2}\lambda_l^2\lambda_{0,c}^2 \tag{3.22}$$

Finally, substituting (3.22) into (3.19) yields

$$P_{\mathrm{M}}\left(V,\lambda_l\right) = \frac{n\varepsilon_r\varepsilon_0\lambda_l\lambda_{0,c}}{rt_0}V^2 \tag{3.23}$$

In this portion of the derivation, we consider only the thickness near the edges as contributing to the decrease in hoop stress. Typically, actuation occurs at varying degrees throughout the DE membrane, especially when the actuator is not

creased and can experience higher strains of its narrowed opening. However, the creased pincher shape modeled here does not exhibit an appreciable amount of strain, and actuation is confined primarily to the outer edges, where prestretch remains the highest. Moreover, these regions of high actuation strain are not in direct contact with the tube, but the stress changes are transduced to the tube by the PET frame leaf springs, which have been slightly creased to bias this process.

The primary results for this model are given by Equations 3.8, 3.17, and 3.23. Substituting these equations into Equation 3.6 gives the model in its full form:

$$P\left(Q,V,\lambda_l,\lambda_c\right)=\overline{R}Q+\frac{nt_0G}{r\lambda_l\lambda_c}\left[\frac{\lambda_c^2-\lambda_l^{-2}\lambda_c^{-2}}{1-\left(\lambda_l^2+\lambda_c^2+\lambda_l^{-2}\lambda_c^{-2}-3\right)J^{-1}}\right]-\frac{n\varepsilon_r\varepsilon_0\lambda_l\lambda_{0,c}}{rt_0}V^2 \qquad (3.24)$$

$$\text{where } \lambda_l=\left(c/l_0\right)\lambda_{0,l}, \text{ and } \lambda_c=\left[1-\left(a-b\right)/\left(2a\right)\right]\lambda_{0,c}$$

In addition to the constants for $G$, $J$, and $\varepsilon_r$ given above: $\overline{R}=1.2\times10^{-3}$ kPa-hr/mL, $r$ = 7.75 mm, $l_0$ = 18 mm, $t_0$ = 0.5 mm, and $n$ = 2 layers were used in this model.

To verify the model, Equation 3.24 was used to generate curves plotted alongside experimental data, shown in Figure 3.15. In addition to the eight constants listed above, the model curves (solid lines) were obtained by using a ruler to carefully measure the values of $a$, $b$, and $c$ for each of four DEVs wrapped around the silicone tube. The DEVs each had different initial prestretches $\left(\lambda_{0,l},\lambda_{0,c}\right)$, and the values of $a$, $b$, and $c$ calculated the equivalent stretches needed by (3.24). After the syringe pump was started, the hydraulic pressure steeply rose until reaching a sharp maximum, after which flow began to cross the DEV and the dynamic pressure curve began to decay from viscoelasticity (Figure 3.14). At this pressure maximum,

we assume that the intrasystem hydraulic pressure equals the pinching hoop pressure, that is

$$P_{\text{hydraulic}} = P_0 \tag{3.25}$$

Therefore, this pressure peak was used to give the initial pressures of the model curves in Figure 3.15(a), before any viscoelastic creep set in. The four DEVs were then actuated and pressure drops were plotted.

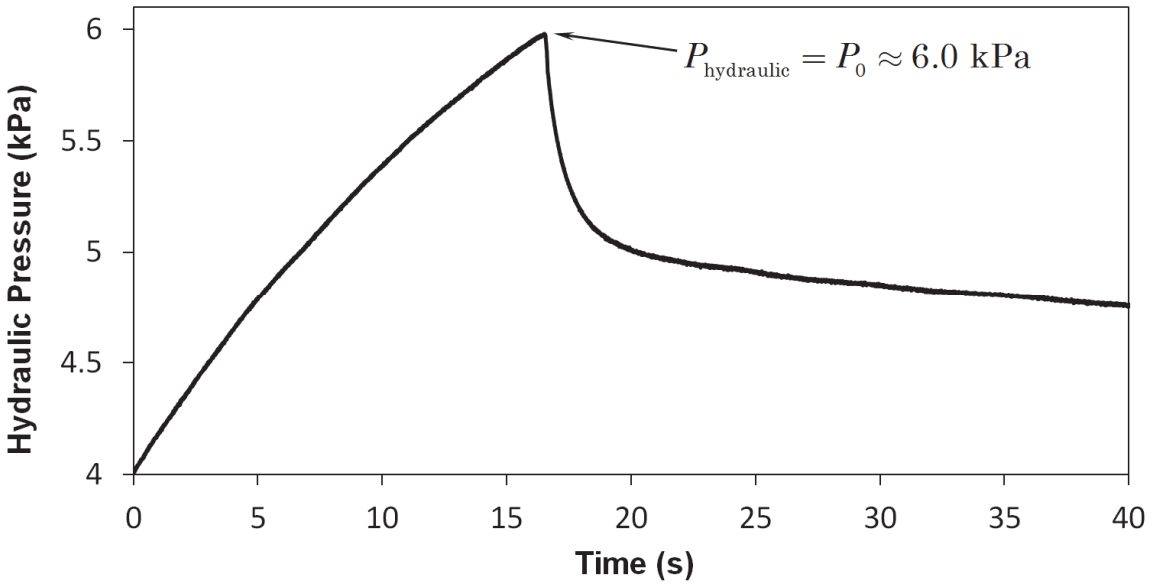


**Figure 3.14** Dynamic pressure behavior at 100 mL/hr for a DEV with prestretch 5 × 5. The $P_0$ peak of 6.0 kPa agrees with the model predictions. After this pressure maximum, the hydraulic pressure is greater than or equal to the pinching pressure, and viscoelastic creep of the VHB™/PET DEV sets in.

The experimental data fit the model well, exhibiting quadratic falls in intrasystem pressure with increasing actuation voltage, as well as following

different shapes dependent on the initial prestretches. These results confirm that the originally chosen stretch of 5 × 5 provides the highest initial pinching pressure with the largest active pressure drop at a given voltage. Higher prestretch in the circumferential direction results in a higher initial pinching pressure, but the active pressure drop is not quite as large. There is also a slight underestimation of the data for both $\lambda_{0,l} = 5$ curves, likely due to viscoelasticity of the VHB™ as a function of the applied Maxwell pressure, which was not included in this model.

The only creep adjustments made were performed in Figure 3.15(b) to allow the model, which does not take viscoelasticity into account, to be fit to the experimental data presented earlier. Passive creep data (not shown) for the 5 × 5 DEV, similar to that in Figure 3.14, were collected for several hours after wrapping around the silicone tube. After 8 hours, the hydraulic pressure had dropped from the initial ~6 kPa to only 2.9 kPa. This ~3 kPa pressure drop was subtracted from the 5 × 5 curve in (a) at four different flow rates. Once again, the model agrees reasonably well with experiment, with a slight underestimation of the pressure drop at higher voltages likely due to viscoelastic actuation behavior at higher Maxwell pressures. However, it should be noted that due to the high level of simplification made in modeling the DEV as a band, the accuracy of this model is limited. More sophisticated modeling techniques involving finite element analysis, such as with Abaqus FEA, may be helpful in furthering future theoretical understanding of the DEV actuator system.

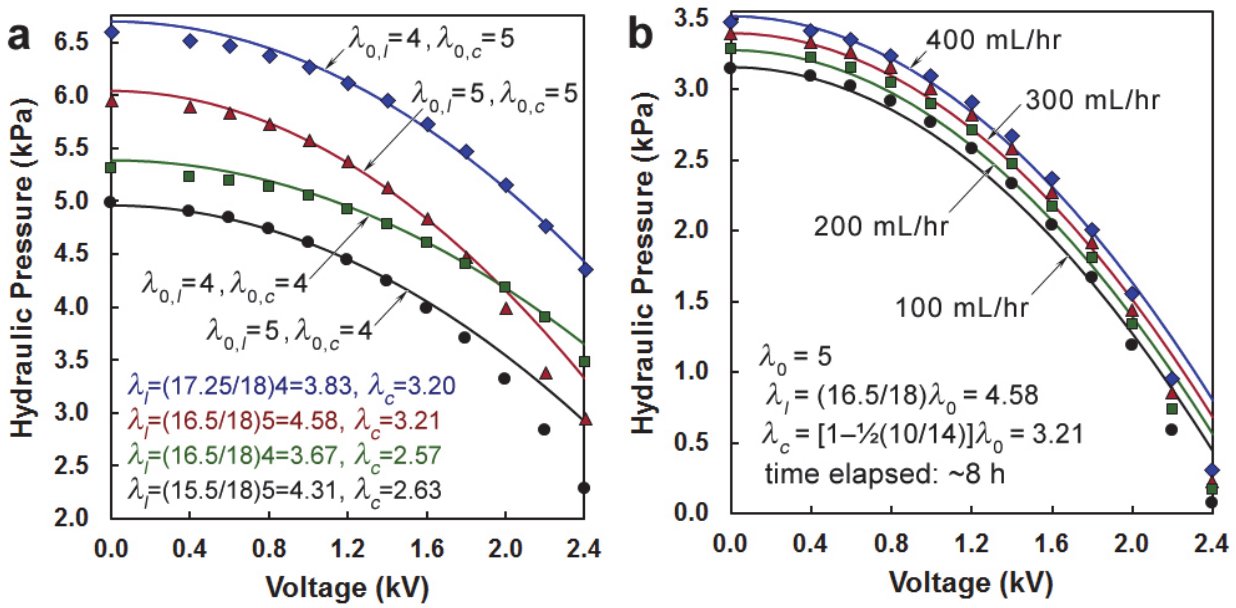


**Figure 3.15** Model curves plotted alongside experimental data points. Measurements for model equivalent stretches taken (in mm) for DEVs wrapped around a silicone tube. **(a)** Pressure-voltage behavior at 100 mL/hr for DEVs of four different initial prestretches, and initial data points taken immediately after wrapping on the tube at the pressure maximum when flow began.[1] Pre-creep measurements were taken to fit the model, which does not take into account creep. **(b)** Pressure-voltage behavior for DEV with initial biaxial prestretch of 5 at four flow rates. Data points were recorded the following day, and using relaxation data, model curves were corrected for the resulting stress relaxation over ~8 h after wrapping around the tube. Post-creep correction of the model was performed to fit the relaxed data, which are shown in the previous results sections.

[1] $\lambda_c$ calculations: 4 × 5: [1– (10.1/14)/2]5 = 3.20; 5 × 5: [1– (10/14)/2]5 = 3.21; 4 × 4: [1– (10/14)/2]4 = 2.57; and 5 × 4: [1– (9.6/14)/2]4 = 2.63.

## 3.4 Conclusions

Presented here was the design, testing, and modeling of a novel minimum energy tubular actuator that can find application as a dielectric elastomer valve for fluidic control. The DEV can pinch a silicone tube shut in the "off" state, preventing flow in a fluidic system when there is no external pressure bias such as from a syringe pump. In this state, the DEV is completely shut. If the syringe pump is activated, the passive DEV remains almost completely closed, highly restricting any flow. In the "on" state, the DEV allows increasingly less encumbered flow with voltage, exhibiting a quadratic decrease in upstream pressure with linearly increasing actuation voltage. At 2.4 kV and above, the DEV opens sufficiently to completely remove the passive ~3.0 kPa pinching pressure. The DEV has been shown to be reliable at 2.2 kV for at least 2,000 actuation cycles, with no significant change in performance.

Modeling of the DEV actuator was performed using the Gent hyperelastic model and Maxwell pressure equation to describe the stresses in an equivalent system. A simple hoop stress equation related these membrane stresses to observed hydraulic pressure changes. The stresses were calculated from equivalent stretches, which were obtained from length measurements taken of the DEVs. The resulting model curves agree well with experimental data, but more sophisticated FEA-based modeling techniques may be necessary for more accurate predictions to be made. One strength of the DEV is that it allows for a continuous gradient of fluidic control between 0 and ~3 kV. Specific, reliable pressure-flow behavior can be dialed in at

the discretion of the user, or by computer control. Future work may wish to explore the use of other DE materials, such as silicones, to eliminate any time-dependent behavior due to the viscoelasticity of VHB™. Potential applications for the DEV could lie in biomedicine as a biomimetic artificial sphincter, as part of a peristaltic pump, or as a valve for computerized fluidic or pneumatic control.

# CHAPTER 4

# Lower Esophageal Sphincter Dielectric Elastomer Band for the Treatment of Gastroesophageal Reflux Disorder

## 4.1 Introduction

Gastro-esophageal reflux disease (GERD) is a prevalent problem, affecting over 19 million Americans and costing them roughly $10 billion per year. [303] Not only is the quality of life of GERD sufferers severely diminished, but serious complications can result, such as swelling (esophagitis), ulcers and strictures, and even cancer (adenocarcinoma). [304] GERD has been traditionally addressed via surgery— primarily via Nissen, Belsey, and Hill fundoplications— but these often result in dysphagia (difficulty swallowing) and can be potentially lethal. [305, 306] Other modern surgical techniques include the Bard EndoCinch™ system and NDO Plicator, which strengthen the lower esophageal sphincter (LES) through stitching in pleats, as well as the Stretta® system, which burns the LES, strengthening it via scar tissue. [307] These latter methods are damaging to the LES, and negative complications are generally not reversible.

Non-surgical approaches have therefore garnered foothold as attractive alternatives to the treatment of GERD. While surgery is required for implantation of such alternatives, surgery via laparoscopic implantation is minimal, and the LES itself is left unaltered. One traditional alternative has been the Angelchik® prosthesis, silicone gel-filled cushion that wraps around the LES. [308-310]

However, the most widespread side effect of this implant is dysphagia, and subsequent surgeries for readjustment are were common. [305, 306, 311, 312] It has since been replaced by the LINX® Reflux Management System (Torax Medical), a band of Titanium-coated magnetic beads, but dysphagia soon after implantation has still been reported (Figure 4.1(a)). [313] A device with an actively tunable diameter would be ideal, as dysphagia can be avoided. Several such ideas have been patented, but the most elegant and space-efficient design may only be realized through the use of dielectric elastomer "artificial muscle" thin films. [314, 315] The design of a medical device such as this is highly interdisciplinary, requiring knowledge across many fields, such as materials science, applied mechanics, and medicine. The general form factor of such an active LES band is illustrated *in situ* in Figure 4.1(b).

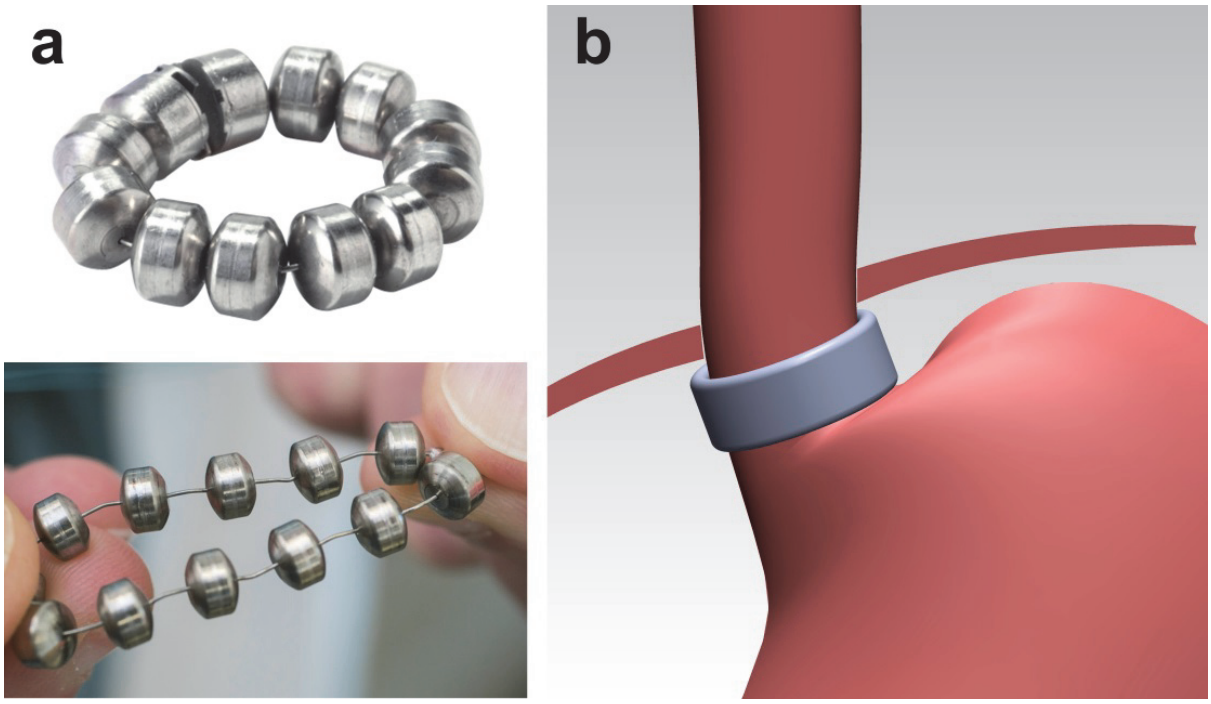


**Figure 4.1** **(a)** The LINX® system consists of a passive linkage of magnetic beads that pinches the LES shut when closed and which can be opened during swallowing. [316, 317] **(b)** SolidWorks® CAD illustration representing an embodiment of the target DE band device.

## 4.2 Materials and Methods

### 4.2.1 Actuator Design and Fabrication

The goal of this research effort was to design and fabricate a dielectric elastomer-driven band (DEB) to function comparably to the LINX® Reflux Management System in the treatment of GERD. The completed dielectric elastomer band is pictured in Figure 4.2(a), with a resting length of 30 mm, a width of ~11 mm, a thickness of just under 0.5 mm, and a weight of 0.2 grams. Like the LINX® system, the DEB is also highly stretchable, as shown in Figure 4.2(b). The DEB was designed: (i) to raise the internal pressure of a tube— i.e., exert a pinching pressure— when at rest by an amount sufficient to enclose stomach contents, (ii) to exert less pressure than will cause ischemia, in which blood circulation is cut off, (iii) to actively relieve this pressure as much as possible for small swallows, and (iv) to actively open as much as possible for larger swallows.

In the first case, the DEB was designed to exert a resting pinching pressure of 3.35 kPa when wrapped around the LES at a length of 45 mm. The average diameter of the human LES in the closed position as determined from computerized tomography measurements is 14.4 mm, which corresponds to a circumference of about 45 mm. [318] Next, 3.35 kPa is the average of the lower and upper required pinching pressures of 2.7 kPa and 4.0 kPa, respectively. These pressure requirements were arrived at as follows. From the hoop stress equation used previously (Equation 3.1), we have

$$\sigma = \frac{Pr}{t} = \frac{Pd}{2t} \tag{4.1}$$

where $\sigma$ is the stress in the DEB, $P$ is the hydraulic (or pinching) pressure, $d$ is the outer diameter of the LES, and $t$ is the thickness of the DE band. When wrapped around the LES, the stress in the band wall is equal to the force in the band divided by the cross-sectional area $ht$, in which $h$ is the height of the band and $t$ is the band thickness. We then find that

$$\frac{F}{h\cancel{t}} = \frac{Pd}{2\cancel{t}} \Rightarrow P = \frac{2F}{dh} \tag{4.2}$$

The LINX® system exerts a magnetically-generated force of 0.39 N in the closed position. [319] Additionally, the average length of the LES is 2 cm. [320] From this information, the required pinching pressure is calculated as

$$P = \frac{2F}{dh} = \frac{2\left(0.39\text{ N}\right)}{\left(14.4\times10^{-3}\text{ m}\right)\left(2\times10^{-2}\text{m}\right)} = 2.7\text{ kPa} \tag{4.3}$$

Furthermore, this agrees with a study assessing the efficacy of the LINX® system, in which the resting LES pressure after LINX® implantation was 19.7 mmHg as determined by clinical manometry; 19.7 mmHg equals ~2.63 kPa. [319]

Secondly, the maximum required pinching force was chosen to be 4.0 kPa since intestinal ischemia has been shown to occur between 0.6 psi and 0.7 psi, or roughly 4.1 kPa to 4.8 kPa. [321] In the third design requirement, the band should be capable of stress relaxation while maintaining roughly the same length, that is, in an isometric boundary condition. This operation would apply to swallowing liquids or saliva, or to belching. In the fourth design requirement, the DEB is

supplied an internal pressure, such as during larger swallows of food, which aids in the actuation strain of the band. This is equivalent to an isotonic boundary condition involving fixing an opened DEB on one end while lengthening the DEB at the other with an applied force during actuation.

It was assumed that isometric operation would follow if the DEB was designed to open as much as possible when given an internal force, so priority was given to satisfy the fourth design requirement. This fourth design requirement of obtaining the highest possible active strain under an applied load was accomplished through modeling. Specifically, the optimum circumferential and transverse prestretch values were determined to give a passive external pinching pressure of 3.35 kPa when lengthened to 45 mm, while simultaneously allowing for maximum active actuation strain at the same internal swallowing pressure of 3.35 kPa or higher. As a simplification, it was assumed that swallowing pressures higher than 3.35 kPa would result in higher active strains, and swallowing pressures below this would begin to function like the isometric case. As a result, maximum active strain was determined at only this single swallowing pressure of 3.35 kPa.

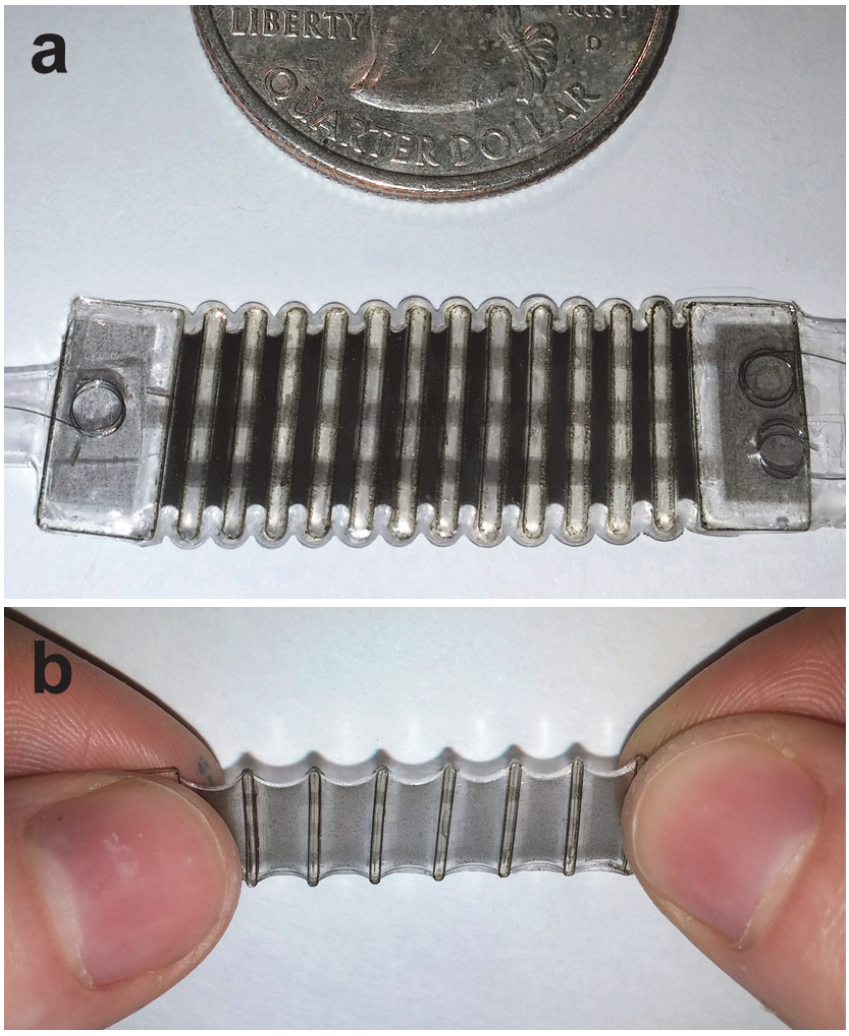


**Figure 4.2** **(a)** Completed DEB in the resting state, with a length of ~3 cm. **(b)** Like the LINX®, the DEB is highly extensible.

In order to maintain the necessary transverse prestretch, semi-rigid bars were incorporated into the DE band. A two-layer stack of prestretched VHB™ 4905 with single-walled carbon nanotube (SWCNT) electrodes was selectively rigidified by a solution-processable, UV-curable polymer: ethoxylated (4) bisphenol A dimethacrylate, also known by the trade name Sartomer SR-540 (Figure 4.3). This approach is similar to a combination of an interpenetrating polymer network— in

which a second uncured polymer network is incorporated into an initial polymer network and then cured— and a minimum energy structure, in which a DE is partially rigidified by adhesion to semi-rigid elements that aid in maintaining prestretch. The novelty of this method lies in selectively maintaining the prestretch of an actuator with a secondary polymer network. Because it is solution processable, the secondary rigidifying network can be patterned into virtually any shape with high resolution. In addition, because it is integrated into the DE actuator before curing, this rigidifying network adheres more strongly to the DE substrate than through simple surface adhesion alone of previously cured elements.

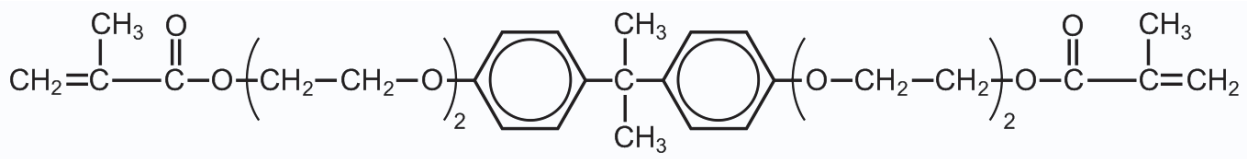

**Figure 4.3** Chemical structure of ethoxylated (4) bisphenol A dimethacrylate (Sartomer SR-540).

The fine structure of the DEB is shown in Figure 4.4, in which the rigidified elements are clearly visible. Figure 4.4(a) depicts a photograph of the DEB prior to releasing from the surrounding VHB™. Shown are three layers of SWCNT electrodes and patterned SR-540 elements with rounded edges on two layers of prestretched VHB™. SWCNTs were chosen for ease of deposition, high strains possible at low concentrations, and fault-tolerant properties. [115] The SR-540 is patterned on both sides, one element aligned directly atop another, sandwiching the

VHB™. Each SR-540 element is just under 1 mm wide, about 10.6 mm tall, and spaced at roughly 2 mm apart. End tabs arbitrarily chosen at 5 mm wide allow for easy interfacing with 1 mil-thick wires, and potentially additional embedded thin film electronics. The wires lead to a low power, high voltage supply with input voltage control.

Viewing the DEB at an angle, the height of the SR-540 elements on one side can be seen, which are ~7 mil (~178 $\mu$m) thick on each side (Figure 4.4(b)). Under the microscope, passive margins can clearly be seen between the SWCNT electrode and each rigid SR-540 bar (Figure 4.5(c)). These vertical margins prevent electromechanical instability by allowing the VHB™ to expand away from the rigid SR-540 boundaries. Patterning electrodes with no margin leads to premature wrinkling and breakdown. Due to manual alignment limitations, the width of the overlapping electrodes is only a little over 1 mm, which means the passive margin on each side is just under 0.5 mm. The margins may appear to be less than 0.5 mm in the micrograph due to the thick diffraction edges of the SR-540 elements, or any misalignment with the rigid elements on the reverse side. Ideally, these margins should be made as small as possible to maximize actuation strain, but accomplishing this may require automated or other microfabrication techniques. From inspection one can also see that after releasing, there will be additional margins between the top and bottom edges of each vertical electrode and the free edges of the VHB™. These secondary margins prevent short-circuiting between

adjacent electrode layers with opposite polarity, but again should be made as small as possible.

Last, Figure 4.4(d) depicts a micrograph of a cross section of the DEB. Although there are two layers of SR-540, only the top layer of SR-540 is shown. The sample was prepared by immersing a portion of the DEB in melted paraffin wax, cooling the wax, and creating a thin slice with a razor blade. The mechanical properties of each material can be inferred from the surface morphologies at the cut. The prominent striations of the 7 mil-thick SR-540 layer indicates its rigid but brittle nature, while the smooth, homogeneous VHB™ layer appears to be soft. IN addition, while this is not conclusive, there does appear to be some slight overlap at the interface between the SR-540 and the VHB™, indicating a strong adhesion.

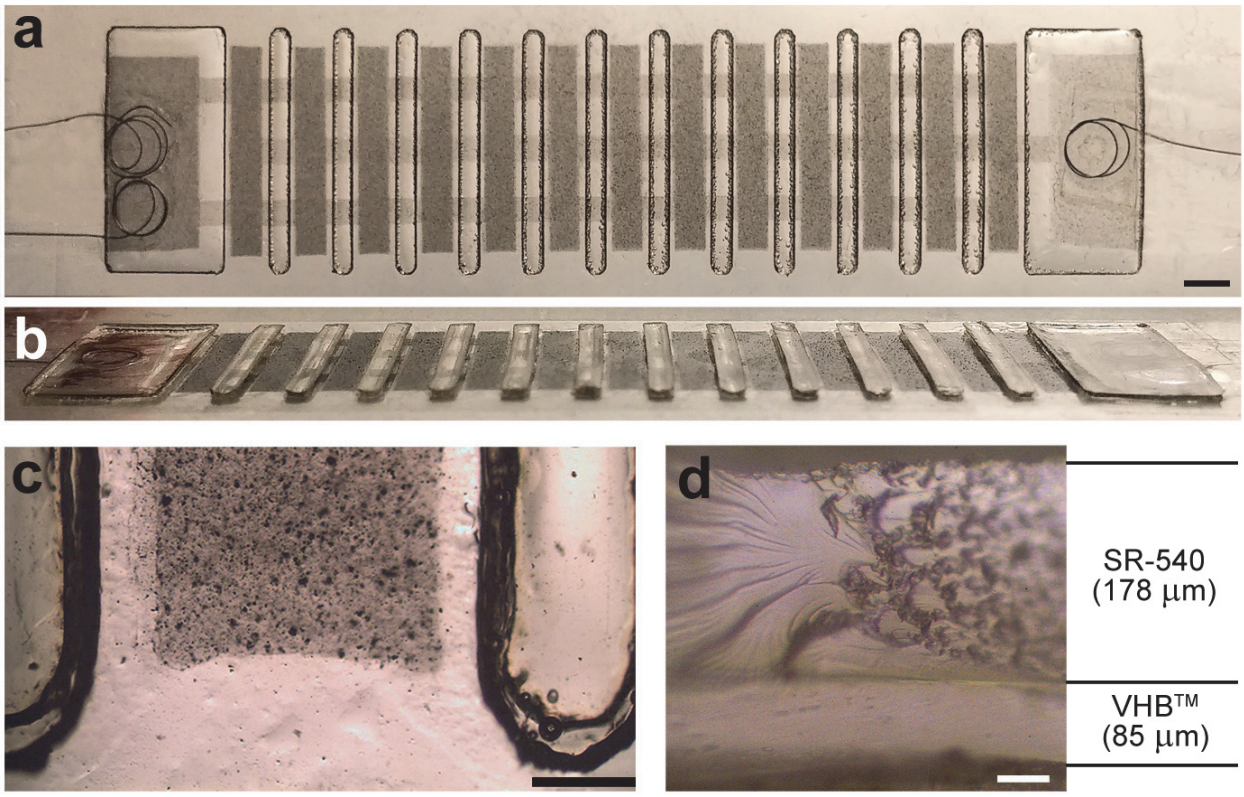


**Figure 4.4** **(a)** Photograph of completed DEB before releasing from the surrounding VHB™. Scale bar = 2 mm. **(b)** Profile view of (a) with height of SR-540 elements visible. **(c)** Micrograph of edge features in (a). Scale bar = 500 $\mu$m. **(d)** Micrograph of cross section of DEB. The prestretched VHB™ layer and top SR-540 layer are shown; the bottom SR-540 is not shown. Scale bar = 50 $\mu$m.

Figure 4.5 illustrates the primary fabrication steps involved in the manufacture of the DEB. First, a cut portion of VHB™ is prestretched anisotropically by 5.5 times vertically and 2.15 times horizontally (Figure 4.5(a)). These prestretch values were determined to be optimal in achieving the highest isotonic actuation strain while simultaneously having the required passive circumferential stress (see Section 4.3.3 for details). Second, SWCNTs in chloroform

are spray-deposited on both sides of the prestretched VHB™ through CAD-designed, laser-cut masks of silicone-lined paper. The chloroform swells and/or partially dissolves the surface of the VHB™, improving adhesion of the SWCNTs. Then, a second layer of identically-prestretched VHB™ is laminated to the first at an angle to avoid entrapping air bubbles, and a third layer of SWCNT electrodes are patterned on the remaining uncoated side (Figure 4.5(b)). Inner wire contacts are made prior to lamination, and outer wire contacts are made after spraying the third layer of SWCNTs.

Third, a laser-cut UV-opaque mask is placed over the SWCNT electrodes, as shown in Figure 4.5(c). The function of the mask is two-fold; the mask: (i) defines the pattern of the to-be-cast rigid elements, and (ii) protects the active regions of VHB™ from the UV curing process, which can damage the VHB™ and negatively affect performance. In addition to these features, the mask was designed to adhere well enough to the VHB™ surface to contain the drop-cast diluted SR-540 solution, yet not so much that it would prove difficult to remove after the curing process. The mask is placed as shown, and a solution of SR-540 diluted in ethyl acetate (1:1 by weight) is carefully drop cast into the well openings of the mask using a syringe with a dulled needle. Diluting the SR-540 has several benefits, allowing for: (i) precise drop casting using a syringe, (ii) more uniform film thicknesses, and (iii) potential swelling of the VHB™ surface, further improving adhesion to the SR-540. Next, it is passed through a UV conveyor (Dymax UVCS Light Curing Conveyor) twice at a higher speed of ~15 ft/min. This prevents overheating as compared to one

pass at half the speed. Due to the dilution, a second deposition and curing is needed to fully fill the wells with SR-540. The above is then repeated for the reverse side.

In the final step (Figure 4.5(d)), the actuator is carefully released from the surrounding VHB™ using two parallel razor blades that cleanly cut both sides simultaneously. The resulting DEB is shown in Figure 4.5(e), in which the free edges of the VHB™ sag into energy minima known as catenaries. Modeling these catenary structures will be explored in Section 4.3.3. Predicting the amount of prestretch loss due to the catenary sagging allowed for a determination of the optimal spacing between rigid elements.

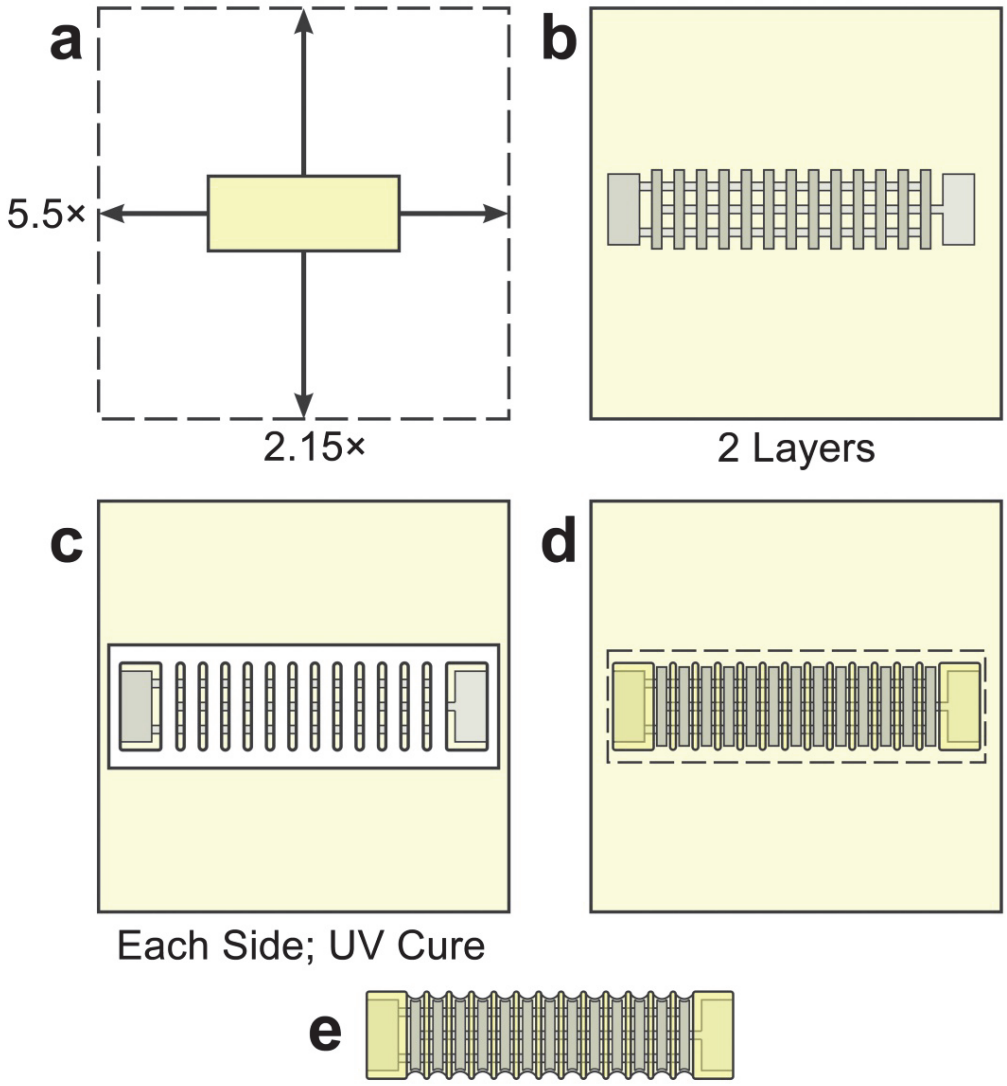


**Figure 4.5** **(a)** VHB™ 4905 is prestretched by 5.5× vertically and 2.15× horizontally. **(b)** SWCNT electrodes are patterned on both sides of the VHB™, wire contacts are made, and a second layer of prestretched VHB™ and SWCNT electrodes are laminated to the first layer. **(c)** For each side, a UV-opaque mask is aligned, SR-540 is cast in the holes with a modified syringe, and the SR-540 is cured with a UV conveyor. **(d)** The masks are removed, and the actuator is released from the residual VHB™ with two razor blades. This step illustrates the photograph in Figure 4.4. **(e)** The completed DEB actuator is shown here.

### 4.2.2 Experimental Design

As mentioned in the previous section, the two test conditions of interest for the DEB were isotonic, which corresponds to larger swallows, and isometric, which corresponds to smaller swallows. In Figure 4.6(a), the DEB is shown in an isotonic setup, fixed on the top by a clamp and freely hanging, extended by a constant force from a hanging weight. The weight was constructed of stacked VHB™, and weighs 24.5 g (0.24 N). The DEB was actuated from 1 kV to 3.6 kV nominal voltage at 200 V increments, the output voltage was monitored with a high voltage probe (B&K Precision® PR-28A 40kV) and a multimeter (Extech® EX470), and the displacement was recorded by high-definition video. Although passive creep behavior was salient as soon as the weight was hung, it was eliminated from the resulting data by subtracting the active final position from the initial position right before actuation.

Figure 4.6(b) shows the isometric test setup, in which the DEB was clamped to the sample holder of a dynamic mechanical analysis (DMA) testing apparatus (TA Instruments RSAIII). Before actuation, passive viscoelastic creep behavior was characterized. First, the DEB was fixed to the sample holder at a length of 30 mm. Then, the DEB was extended to 45 mm over 3 seconds (at rate of 5 mm/s), and the change in force with time was monitored. The resulting plot has a peak at the initial force, followed by an exponentially decaying force with time. After letting the DEB stress relax for several minutes, it was actuated from 0.4 kV to 3.6 kV nominal voltage at 100 V increments. Once again, the voltage was monitored using a high

voltage probe and a multimeter. Modeling and data analysis were performed using MATLAB® and Excel.

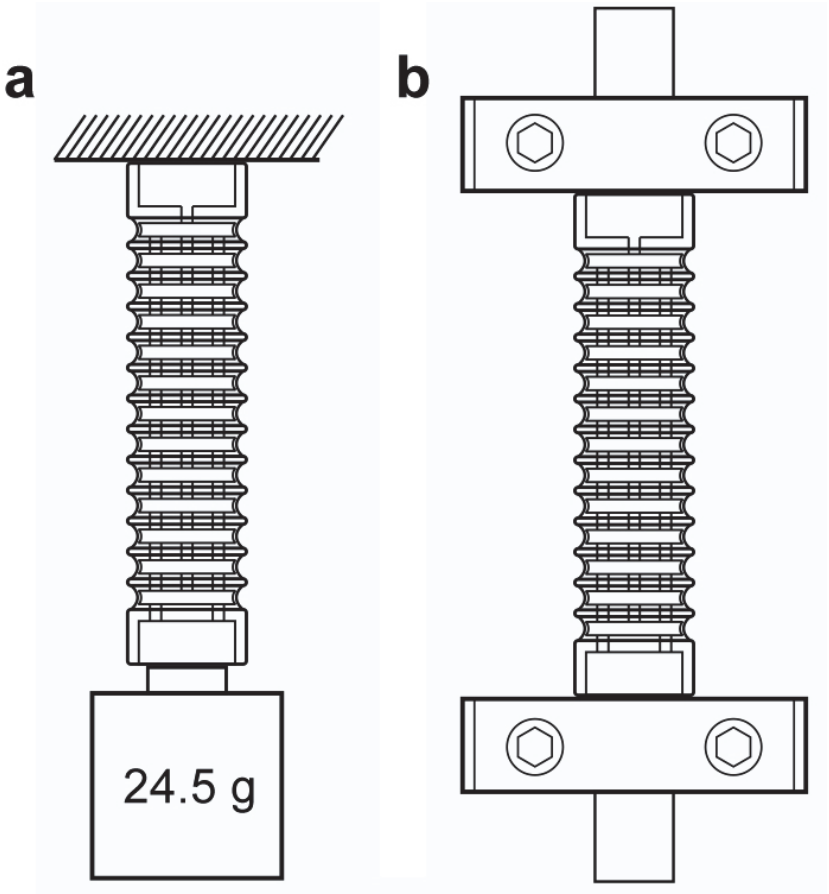


**Figure 4.6** **(a)** Isotonic experimental setup. The DEB is fixed at the top, and its other end suspends a freely-hanging 24.5 g weight. **(b)** Isometric experimental setup. The DEB is clamped into the sample holder of a dynamic mechanical analysis machine at an initial length of 3.0 cm and stretched to a resting length of 4.5 cm.

## 4.3 Results and Discussion

### 4.3.1 Isotonic Tests

The results of the isotonic tests of the DEB are given in Figure 4.7. The resting state (Figure 4.7(a)) had a length of about 64 mm, and at 3.6 kV nominal voltage (3.42 kV measured) the DEB lengthened to about 80 mm (Figure 4.7(b)). This maximum displacement of 16 mm is equivalent to an actuation strain of 25%, which is comparable to living muscle. The data points in Figure 4.7(c) are the average of four trials: two separate DEB devices, with two trials per device. The overlaid solid curve was generated from a model simulation of the DEB. Specifically, the DEB was modeled in a pure shear configuration, wherein the entire length is capable of contraction and has no loss of transverse prestretch. This ideal case was then scaled down by 21% of the original to account for margins and passive elements that needed to be included in the real design for practical reasons. This percentage was calculated based on photographic measurements of the DEB and is discussed in more detail in Section 4.3.3.

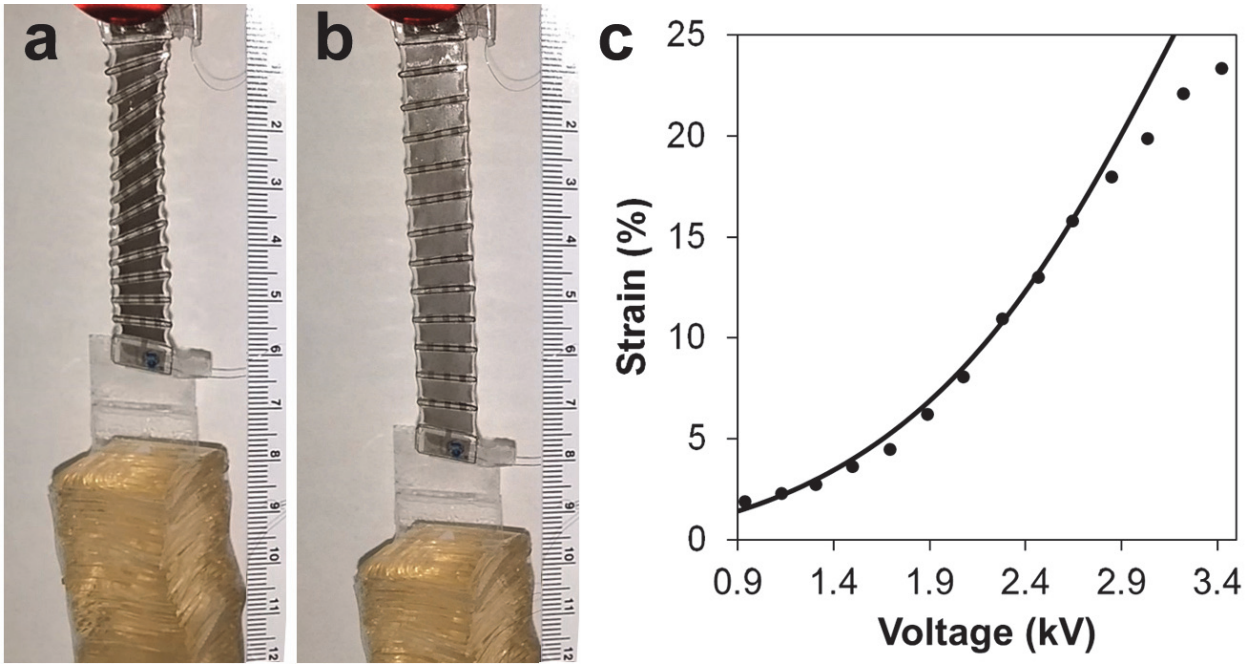


**Figure 4.7** **(a)** Resting length of DEB. Was 4.5 cm long when weight was first hung, but may be slightly longer due to creep. **(b)** The pictured DEB actuated at 3.6 kV nominal voltage (3.42 kV measured) exhibits a maximum strain of 25%. **(c)** Isotonic strain data points with voltage, overlaid with model (solid curve) scaled by 21% of the original. The data shown is the average of four trials: two devices, two trials per device.

### 4.3.2 Isometric Tests

The DEB was fixed in the sample holder of the RSAIII DMA, expanded from 30 mm to 45 mm over 3 seconds, and let to stress relax for about 10 minutes prior to actuation. The force drops were measured with applied actuation voltage, producing graphs like that shown in Figure 4.8. In this figure, nominal voltages from 1.5 kV to 2.9 kV were applied at 100 V increments over a 400 second time period. Data points were extracted from this figure, producing Figure 4.10. Passive viscoelastic creep behavior was eliminated by taking the difference between each force drop value and

its preceding baseline value immediately before actuation. Then, the baseline was shifted to match the measured peak in the creep curve depicted in Figure 4.9.

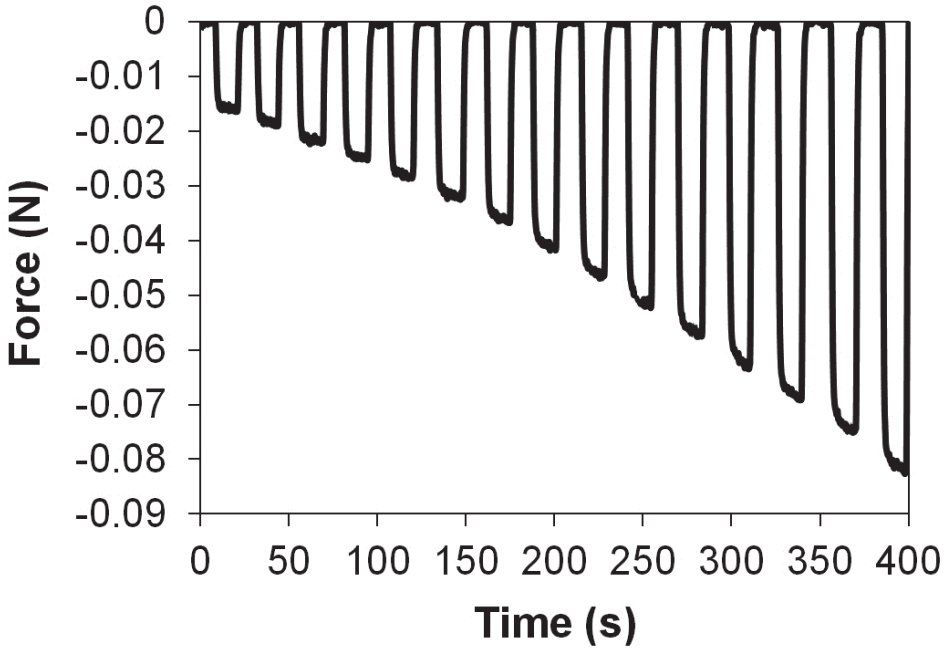


**Figure 4.8** Dynamic force drops from an isometric DEB test, corresponding to nominal actuation voltages from 1.5 kV to 2.9 kV nominal voltage at 100 V increments over 400 s.

The results of the isometric DEB tests are shown in Figure 4.10. Data points for one trial are shown for the DEB actuated at a fixed length of 4.5 cm from 1 kV to 3.6 kV nominal voltage. The maximum active force drop was from 0.25 N to 0.143 N at 3.32 kV. The solid overlaid curve was generated from modeling. An ideal DEB with two layers of VHB™ 4905, a transverse prestretch of 5.5, a circumferential prestretch of 2.15, and a width of 10.6 mm was predicted to exert a passive force of 0.253 N at a length of 4.5 cm, which is empirically confirmed here (Figure 4.9). The actuation force drops of the model were then scaled by 44% of the original to

account for the margins. The calculation of this percentage is given in Section 4.3.3. As was the case in Figure 3.15, the data points slightly underestimate the model, likely due to the active viscoelastic behavior of the VHB™.

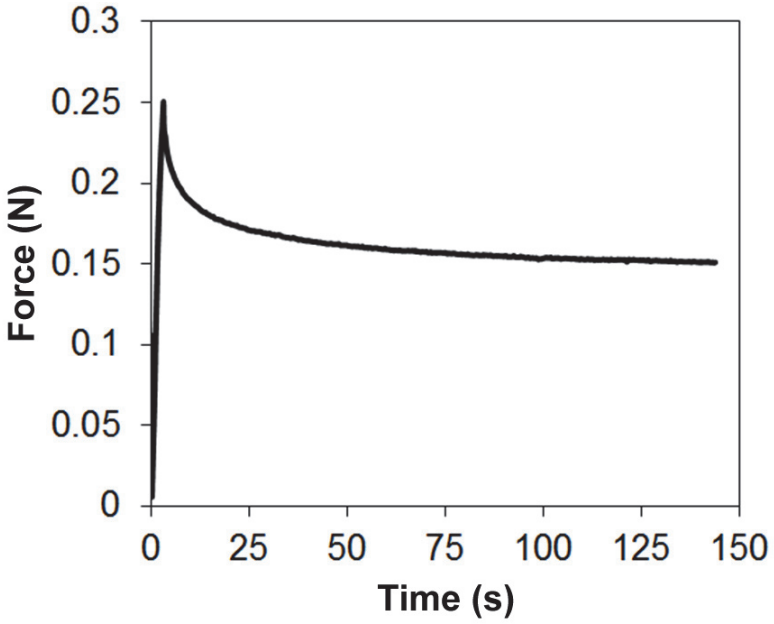


**Figure 4.9** DEB creep test. Confirms ~0.25 N initial circumferential (vertical) force when DEB is stretched from 30 mm to 45 mm over 3 seconds (a rate of 5 mm/s). Due to the viscoelasticity of VHB™, which was not considered in the DEB design, the force relaxes by almost 0.1 N over 150 s.

Because it is fabricated from VHB™, the DEB exhibits both passive and active viscoelasticity. Passive and active viscoelasticity were not considered in the modeling and design of the DEB. However, effort as made to eliminate the passive viscoelastic behavior of the DEB during data processing, as mentioned previously. Passive creep of the DEB was also studied, as shown Figure 4.9. As mentioned

above, the initial peak shows the force exerted by the DEB after having been lengthened to 4.5 cm, which is ~0.25 N, as predicted by the model. Over 150 seconds, this force drops by almost 0.1 N, approaching an asymptote around 0.15 N. Future designs may benefit from the use of silicone, or other DE materials that do not exhibit the same degree of creep behavior.

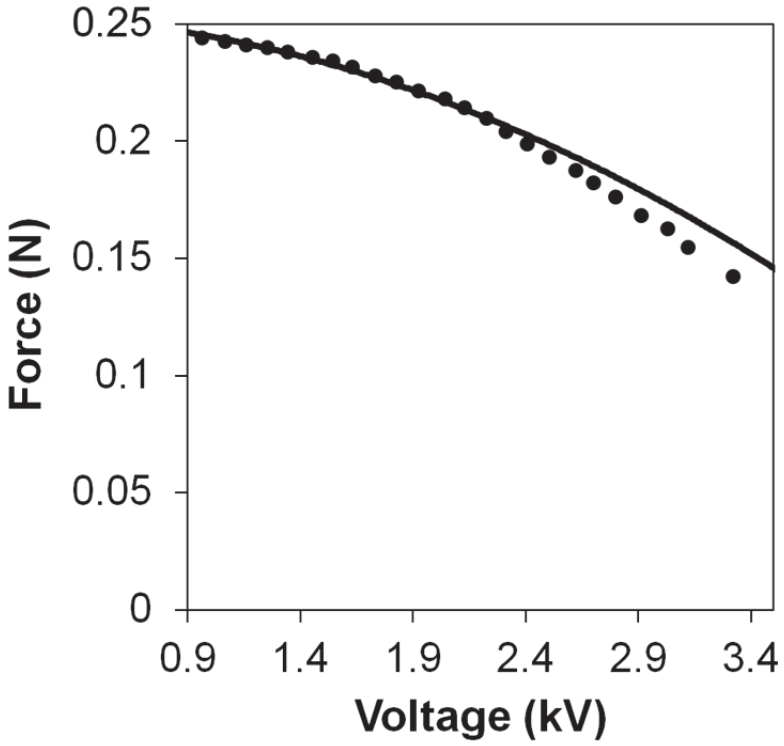


**Figure 4.10** Isometric actuation of the DEB at a length of 4.5 cm. Model (solid curve) scaled by 44% of the original. Data points were extracted from plots similar to that shown in Figure 4.8.

### 4.3.3 Modeling

#### 4.3.3.1 Prestretch Optimization

To design of the DEB relied heavily on mathematical modeling. Modeling was employed to determine the optimal prestretches necessary to obtain maximum circumferential strain at the required passive pinching pressure. Additional modeling was used to predict the transverse prestretch loss with spacing to determine the optimal spacing of the rigid elements. The modeling to determine the optimal prestretches employed a method similar to that utilized by Lu et al. [15] A pure shear case was considered, in which a prestretched dielectric elastomer actuator is suspended by a weight in an isotonic setup as shown in Figure 4.6(a). The vertical prestretch is maintained by the weight, and if wrapped around a tube, the DEA maintains its vertical prestretch by the tube. In this latter case, the vertical prestretch may also be referred to as the circumferential prestretch. The transverse prestretch (perpendicular to the vertical prestretch) is assumed to be maintained at every point along the vertical length of the DEA. Furthermore, this ideal model assumes that the entire length of the DEA is capable of actuation, with no break or margins.

In this configuration, the DEA may be described by the following equilibrium state equations, which describe the stress in the DEA in the circumferential and transverse directions, respectively:

$$\sigma_c = \frac{G\left(\lambda_c^2 - \lambda_c^{-2}\lambda_t^{-2}\right)}{1-\left(\lambda_c^2 + \lambda_t^2 + \lambda_c^{-2}\lambda_t^{-2} - 3\right)J^{-1}} - \varepsilon_r\varepsilon_0\left(\frac{V}{t}\right)^2 \tag{4.4}$$

$$\sigma_t = \frac{G\left(\lambda_t^2 - \lambda_c^{-2}\lambda_t^{-2}\right)}{1-\left(\lambda_c^2 + \lambda_t^2 + \lambda_c^{-2}\lambda_t^{-2} - 3\right)J^{-1}} - \varepsilon_r\varepsilon_0\left(\frac{V}{t}\right)^2 \tag{4.5}$$

where $G$ is the shear modulus, $J$ is the strain stiffening coefficient, $\varepsilon_0$ is the permittivity of free space, $\varepsilon_r$ is the dielectric constant of the elastomer, and $t$ is the thickness of the actuating region of one layer of VHB™. Values of $G$ = 45 kPa, $J$ = 120, and $\varepsilon_r = 4.5$ were used in this model, which have been shown by Bozlar et al. and Lu et al. to be a good fit for VHB™ 4910 (and 4905) acrylics. [10, 15] Note that Equation 4.4 is the same as Equation 3.16.

Next, from material incompressibility, the total thickness $t$ was written in terms of the initial thickness of one actuating layer $t_0$, the number of actuation layers $n$, and the principal stretches:

$$\lambda_t\lambda_c\lambda_z = \lambda_t\lambda_c\frac{t}{t_0 n} = 1 \tag{4.6}$$

and so

$$t = \frac{t_0 n}{\lambda_t\lambda_c} \tag{4.7}$$

where $\lambda_t$ and $\lambda_c$ are the stretches in the transverse and circumferential directions, respectively. This is essentially the same as Equation 3.12. By rearranging Equation 4.1 and using (4.7), the result is

$$\sigma_c = \frac{Pd\lambda_t\lambda_c}{2t_0 n} \tag{4.8}$$

in which $d$ is the average diameter of the LES ($14.4 \times 10^{-3}$ m). Substituting (4.8) and (4.7) into (4.4), we obtain

$$\frac{Pd\lambda_t\lambda_c}{2t_0 n} = \frac{G\left(\lambda_c^2 - \lambda_c^{-2}\lambda_t^{-2}\right)}{1-\left(\lambda_c^2 + \lambda_t^2 + \lambda_c^{-2}\lambda_t^{-2} - 3\right)J^{-1}} - \varepsilon_r\varepsilon_0\left(\lambda_t\lambda_c\frac{V}{t}\right)^2 \tag{4.9}$$

By solving this equation for $V$ and inputting values for $\lambda_c$ such as from 0.1 to 10, MATLAB® can plot the result. The values of $P$ = 2.7, 3.35, and 4.0 kPa were inputted as boundary conditions, and at least 9 different plots were generated from varying the transverse prestretch $\lambda_t$ from 1 to 9, shown in Figure 4.11. The leftmost blue curve corresponds to the boundary condition $P$ = 2.7 kPa, the rightmost blue curve corresponds to $P$ = 4.0 kPa, and the black dashed line corresponds to the mean of these two pressures: 3.35 kPa. The intersection of each curve with the $x$-axis indicates the circumferential prestretch $\lambda_{0,c}$ required to obtain the pinching pressure $P$ corresponding to that curve.

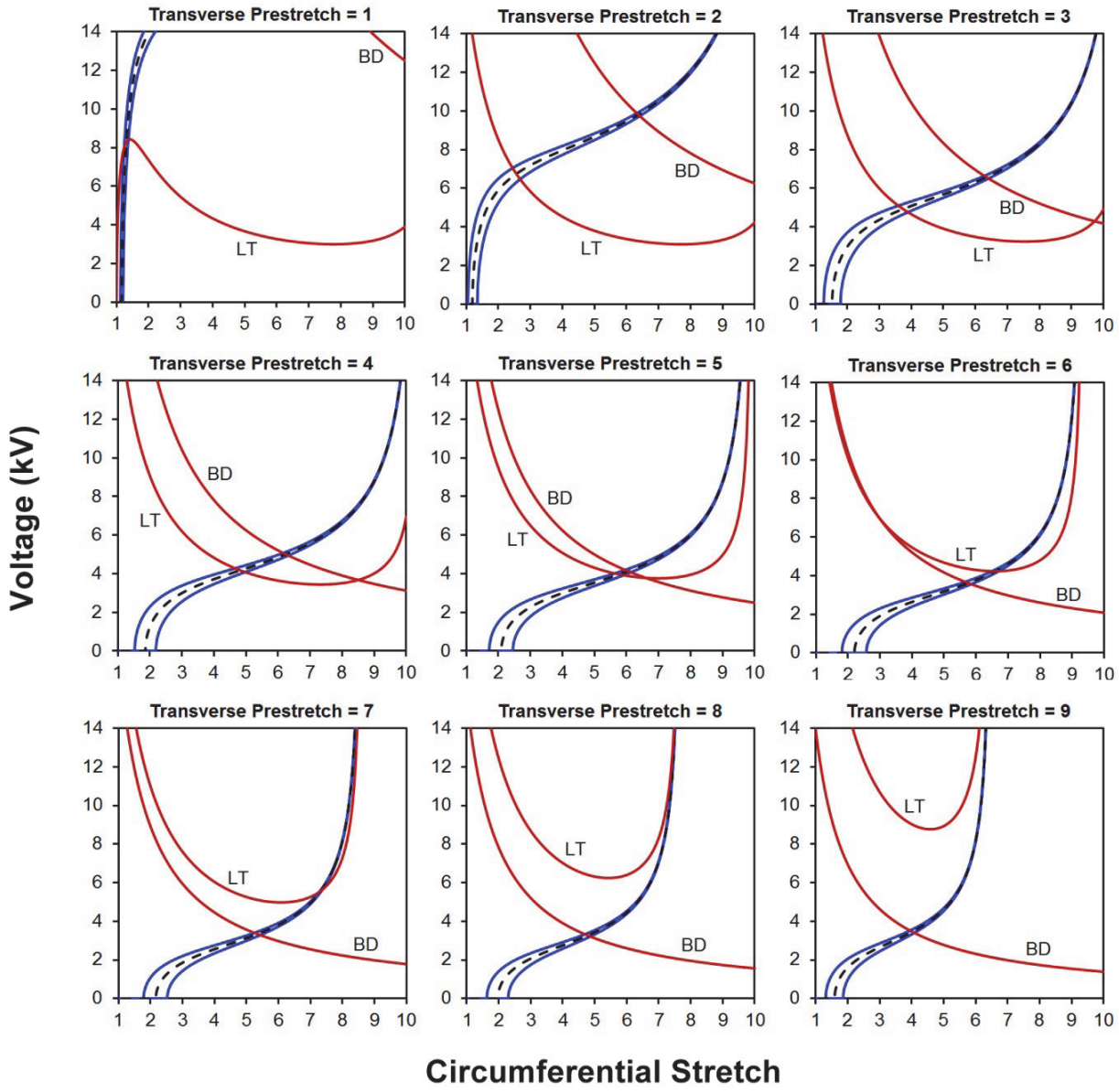


**Figure 4.11** Pure shear model simulations for two layers of VHB™ 4905, with electrodes across each layer of VHB™. Plotted are the circumferential stretches with actuation voltage for nine transverse prestretch integer values. The DE is assumed to be fixed on one end, suspended in the circumferential direction by a weight at the other end. This weight corresponds to a circumferential hoop stress value in the DE membrane, which in turn can be converted into a hydraulic pressure. The two blue curves show the actuation profiles corresponding to the minimum and maximum required hydraulic pressures of 2.7 and 4.0

kPa, respectively. The black dashed curve is the average of the two blue curves. The red curves represent the loss of tension (LT) and breakdown threshold (BD) for the DE. (See Section 6.4.3.1 for code.)

It can also be noted that there is a voltage at which tension is lost in the transverse direction, that is, when $\sigma_t = 0$. Equation 4.5 becomes

$$\frac{G\left(\lambda_t^2 - \lambda_c^{-2}\lambda_t^{-2}\right)}{1-\left(\lambda_c^2 + \lambda_t^2 + \lambda_c^{-2}\lambda_t^{-2} - 3\right)J^{-1}} = \varepsilon_r\varepsilon_0\left(\lambda_t\lambda_c\frac{V}{t}\right)^2 \tag{4.10}$$

The red loss of tension curves (LT) are labeled in Figure 4.11. This is a potentially unstable actuation regime since loss of transverse prestretch will result in wrinkling, after which EMI typically follows. Therefore, stretches beyond the intersection of the LT curves with the blue and black curves are not guaranteed to be stable. This considers mechanical instability that can occur.

Moreover, considering electrical instability, the DE will not be capable of stable operation above its dielectric breakdown strength of $E_{\mathrm{BD}}$ = 250 V/$\mu$m. This field varies with the stretches and can also be plotted. Hence

$$V_{\mathrm{BD}} = \frac{E_{\mathrm{BD}}t_0}{\lambda_t\lambda_c} \tag{4.11}$$

where $V_{\mathrm{BD}}$ is the breakdown voltage. The red breakdown curves (BD) are also plotted in Figure 4.11. As with the LT curves, strains on the blue or black curves above the intersection with the BD curve is electrically not stable. Therefore, maximum stretches are taken to be the intersection of the blue and black curves with either the LT or BD curve, whichever crosses at the lower value. Note that in

Figure 4.11, the LT and BD curves switch position slightly above a transverse prestretch of 5.

In order to convert the circumferential stretches to actuation stretches for each curve, we must divide by the circumferential prestretch $\lambda_{0,c}$ of each curve. This is because we define $\lambda_c$ in the plot as

$$\lambda_c = \frac{l_{f,a}}{l_i} \tag{4.12}$$

where $l_{f,a}$ is the final actuated circumferential (vertical) length, and $l_i$ is the initial length of the DE before prestretching. However, it is desired to obtain the actuation stretch

$$\lambda_{c,a} = \frac{l_{f,a}}{l_{0,c}} \tag{4.13}$$

where the actuated final length $l_{f,a}$ is divided by $l_{0,c}$, the initial length of the DE after prestretching. Note that

$$\lambda_{c,a} = \frac{l_{f,a}}{l_{0,c}} = \left(\frac{l_{f,a}}{l_i}\right)\left(\frac{l_i}{l_{0,c}}\right) = \frac{\lambda_c}{\lambda_{0,c}} \tag{4.14}$$

where the circumferential prestretch is defined as $\lambda_{0,c} = l_{0,c}/l_i$. Therefore, dividing by $\lambda_{0,c}$ converts the total circumferential stretch of each curve $\lambda_c$ into the circumferential actuation stretch $\lambda_{c,a}$.

The maximum circumferential actuation strain is defined as

$$s_{c,a,\max}(\%) = (\lambda_{c,a,\max} - 1) \times 100 = \left( \frac{\lambda_{c,\max}}{\lambda_{0,c}} - 1 \right) \times 100 \tag{4.15}$$

in which $\lambda_{c,\max}$ for each blue or black curve is its intersection with the red LT or BD curve, whichever comes first (left to right). Then, by plotting $s_{c,a,\max}$ against the transverse prestretch of each of the plots in Figure 4.11, the transverse prestretch corresponding to the highest $s_{c,a,\max}$ value can be chosen, illustrated in Figure 4.12. In this plot, the blue curve corresponds to the $s_{c,a,\max}$ values computed from the 2.7 kPa curves, the red curve corresponds to the 4.0 kPa curves, and the black dashed curve corresponds to the average 3.35 kPa curves. For each of these curves, it can be seen that the highest $s_{c,a,\max}$ values occur at a plateau between transverse prestretched of 5 and 5.5. For this design, a transverse prestretch of 5.5 was selected to allow for some prestretch loss that will occur when the rigid element spacing is maximized. As a general rule of thumb, prestretches larger than 5.5 in any direction are difficult to obtain for VHB™ 4905 and 4910, since a prestretch of 6 is close to the physical extension limit of VHB™.

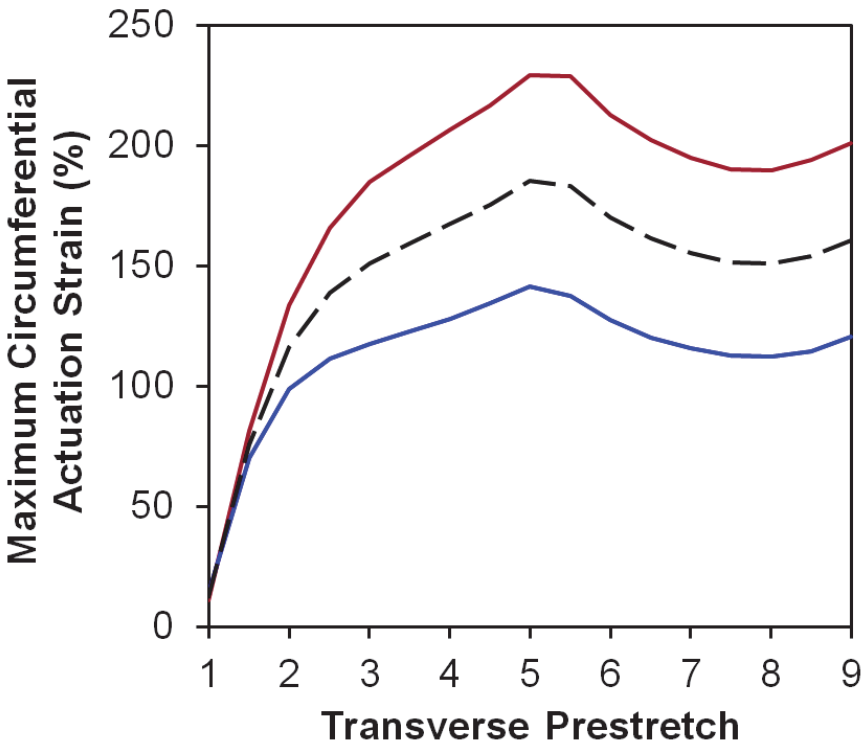


**Figure 4.12** Transverse prestretch versus the maximum circumferential actuation strain, which was determined by extracting the intersections of the blue and black curves with either the LT or BD red curves for transverse prestretch graphs from 1 to 9 at increments of 0.5. These intersections were then divided by the circumferential prestretches to obtain the actuation stretches, which were then converted to strains. The blue and red curves correspond to the minimum pinching pressure of 2.7 kPa and the maximum pinching pressure of 4.0 kPa, respectively. The dashed black curve is the mean of these two extremes, and was used in the design of the DEB. Note the maximum plateau between the transverse prestretches of 5 to 5.5. Maximum strain is possible at a transverse prestretch of 5, but a higher prestretch of 5.5 is chosen since it allows for a longer active area, shown later. (See 6.4.3.2 for code.)

Now that the optimal transverse prestretch value of 5.5 has been selected, the circumferential prestretch required to obtain the correct pinching pressure can

be found. Figure 4.13 plots the circumferential prestretches $\lambda_{0,c}$ for each pressure curve against the corresponding transverse prestretch value for that plot. For example, the black dashed line in the "Transverse Prestretch = 5" plot of Figure 4.11 intersects the $x$-axis at ~2. This results in the point (5, 2) on the black dashed line in Figure 4.13. As with Figure 4.12, the blue curve corresponds to the 2.7 kPa curves, the red curve corresponds to 4.0 kPa, and the black dashed curve corresponds to 3.35 kPa.

It was decided to use the black dashed curve, which is 0.65 kPa more pressure than the LINX® band exerts when fully closed. This will allow for potentially greater efficacy at addressing GERD, while not posing any dysphagia problems since the DEB can actively relieve this resting pressure, while the LINX® cannot. In addition, 3.35 kPa is still below the ischemia minimum of 4.1 kPa. By selecting the black dashed curve in Figure 4.13, it can be seen that a circumferential prestretch of 2.15 corresponds to a transverse prestretch of 5.5. The optimal prestretches are now selected: A 5.5× transverse prestretch ensures maximum circumferential actuation strain, and a 2.15× circumferential prestretch will allow the DEB to exert a pinching pressure of $P$ = 3.35 kPa.

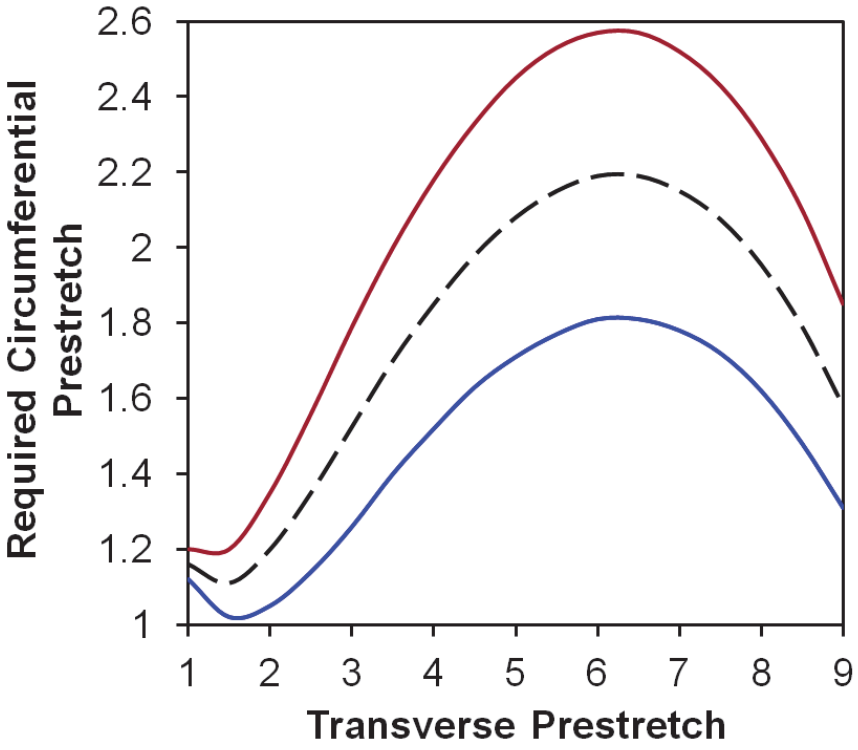


**Figure 4.13** As before, the blue curve corresponds to the minimum required pinching pressure of 2.7 kPa, the red curve corresponds to the maximum required pinching pressure of 4.0 kPa, and the black dashed curve corresponds to an average pinching pressure of 3.35 kPa. At a transverse prestretch of 5.5, the circumferential prestretch required to obtain a pinching pressure of 3.35 kPa is 2.15. (See Section 6.4.3.2 for code.)

#### 4.3.3.2 Geometric Optimization

The next part of the model was concerned with predicting the amount of transverse prestretch loss that will occur from the freely hanging VHB™ edge when the spacing between rigid elements is altered. Doing so will allow the maximum distance of separation possible that will preserve enough transverse prestretch to obtain optimal circumferential strain. For example, as can be seen in Figure 4.14(a)

and (c), an unconstrained prestretched VHB™ edge between two rigid boundaries will sag like a suspension cable of a bridge. This shape is known as a catenary. A suspension bridge cable sags between two post boundaries because the pull of gravity is equal along the entire length of the cable. Similarly, the VHB™ sags between the two rigid elements because the pull of the prestretch is equal along the entire length of the edge. An expression describing this catenary curve $Y(x)$ was derived (see Appendix, Section 6.3) and can be written as follows:

$$Y(x)=\frac{2l_0+l_0\left(\lambda_t-1\right)\left\{\exp\left[-\frac{\lambda_t x}{l_0\lambda_c\left(\lambda_t-1\right)}\right]+\exp\left[\frac{\lambda_t\left(x-l\right)}{l_0\lambda_c\left(\lambda_t-1\right)}\right]\right\}}{1+\frac{\lambda_t-1}{\lambda_t}\exp\left[-\frac{\lambda_t l}{l_0\lambda_c\left(\lambda_t-1\right)}\right]+\frac{1}{\lambda_t}},\ l_0=\frac{l_{t,f}}{\lambda_t} \tag{4.16}$$

where $\lambda_t=5.5$, $\lambda_c=2.15$, $l_{t,f}=5$ mm and is about half the width of the DEB, and $l$ is the spacing between rigid elements in the circumferential direction. Plotting this function atop Figure 4.14(a) and (c) is shown in (b) and (d) and is a near perfect match to the VHB™ edge profile. Also shown are the two constituent decaying exponentials, outlined in shorter dashes.

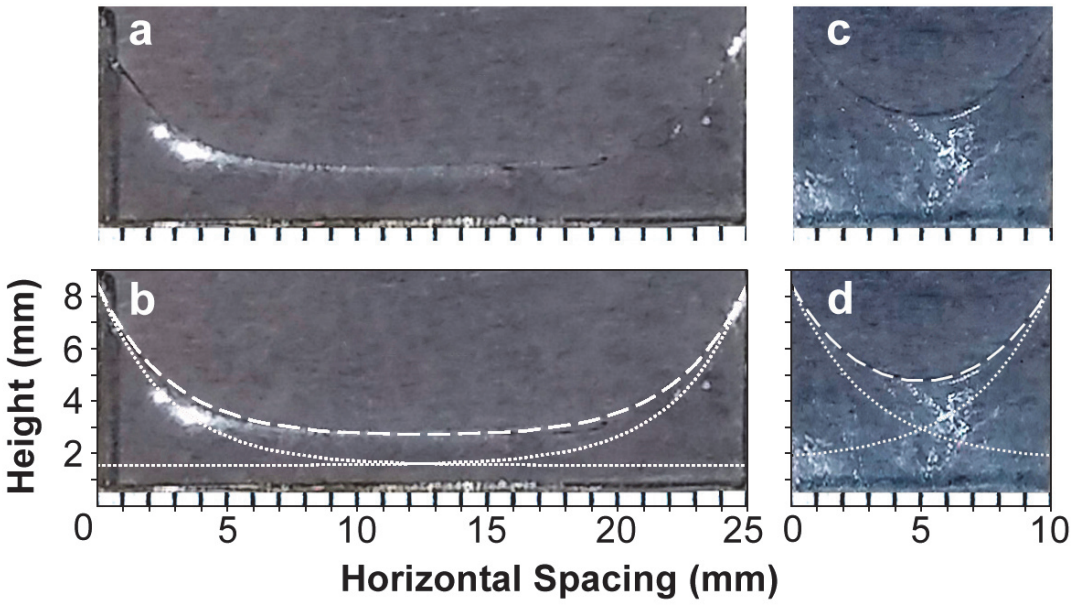


**Figure 4.14** **(a)** Free edge of VHB™ 4905 with a gap of 25 mm between vertical rigid elements. **(b)** Catenary model (long white dashed lines) overlaid on (a) predicts the profile of the VHB™ free edge. The catenary model is the sum of two decaying exponentials (short white dashed lines). **(c)** Free edge of VHB™ 4905 with a gap of 10 mm between vertical rigid elements. **(d)** Catenary model overlaid on (c) predicts the profile of the VHB™ free edge. The two constituent decaying exponentials are also shown.

Next, the transverse prestretch minimum $\lambda_{t,\min}$ was determined as a function of the spacing $l$. $\lambda_{t,\min}$ is the transverse prestretch at the VHB™ edge catenary minimum, which is located at $l/2$. Thus, the minimum height is $Y(l/2)$, the fraction of the original stretch is $(Y(l/2))/l_{t,f}$, and $\lambda_{t,\min}$ as a function of $l$ is

$$\lambda_{t,\min}(l) = \frac{Y(l/2)}{l_{t,f}}\lambda_t = 1.1Y\left(\frac{l}{2}\right) \tag{4.17}$$

It was then useful to determine how the maximum actuation strain $s_{c,a,\max}$ changes with the spacing $l$. To design in a factor of safety, it was assumed that the minimum prestretch $\lambda_{t,\min}$ was constant across the length of $l$, rather than $\lambda_{t,\min}$ simply being a minimum. Once $\lambda_{t,\min}$ was determined at a given $l$, linear interpolation was used on Figure 4.12 to approximate the maximum actuation strain $s_{c,a,\max}$. Specifically:

$$\frac{s_{c,a,\max} - s_1}{\lambda_{t,\min} - \lambda_1} = \frac{s_2 - s_1}{\lambda_2 - \lambda_1} \tag{4.18}$$

in which $\lambda_1 < \lambda_{t,\min} < \lambda_2$ and $s_1 < s_{c,a,\max} < s_2$, and the following points are found on the dashed black curve of Figure 4.12: $(\lambda_1, s_1), (\lambda_{t,\min}, s_{c,a,\max})$, and $(\lambda_2, s_2)$. Solving for $s_{c,a,\max}$ as a function of $l$:

$$s_{c,a,\max}(l) = \frac{s_2 - s_1}{\lambda_2 - \lambda_1}\left[\lambda_{t,\min}(l) - \lambda_1\right] + s_1 \tag{4.19}$$

and substituting in Equation 4.17:

$$s_{c,a,\max}(l) = \frac{s_2 - s_1}{\lambda_2 - \lambda_1}\left[\frac{\lambda_t}{l_{t,f}} Y(l/2) - \lambda_1\right] + s_1 \tag{4.20}$$

Now that $s_{c,a,\max}(l)$ is known, the following expression was plotted versus $l$ in Figure 4.15:

$$\frac{s_{c,a,\max}(l)}{s_{c,a}(0.2)} \times 100 \tag{4.21}$$

Here, a comparison is made between the maximum actuation strain $s_{c,a,\max}$ at several values of $l$ and the actuation strain $s_{c,a}$ at $l$ = 0.2 mm, the minimum spacing value considered. It was assumed that at this spacing of 0.2 mm the prestretch loss

was minimal, and that the original transverse prestretch of $\lambda_t = 5.5$ is about equal to $\lambda_{t,\min}$ at $l$ = 0.2 mm. In fact, $\lambda_{t,\min}(0.2) = 5.49$. To generate Figure 4.15, values of $l$ ranging from 0.2 mm to 3.4 mm at 0.2 mm increments were inputted into Expression 4.21 and Equation 4.20, which depends on Equation 4.16.

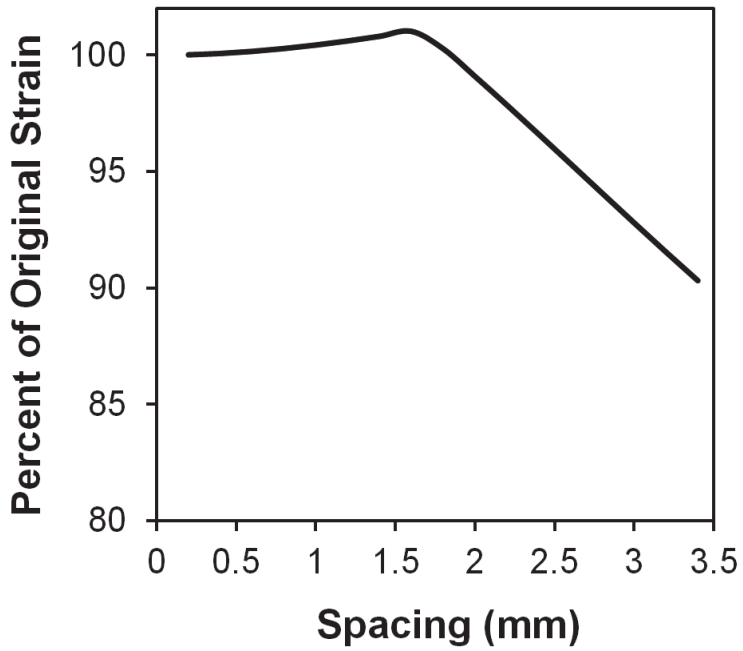


**Figure 4.15** Percent of original theoretical circumferential actuation strains at various transverse prestretches, which change with active area spacing as predicted by the catenary model. Due to the plateau in Figure 4.12 between 5 and 5.5 transverse prestretch, the catenary model predicts a slight increase in actuation strain up to a spacing of ~2 mm, after which the maximum actuation strain decreases linearly.

From Figure 4.15, the percent of the original strain actually increases slightly at 1.6 mm to 101%. This is due to a slightly higher predicted strain at a transverse prestretch of 5. In addition, the roughly flat shape of the plot from $l$ = 0.2

mm to 1.6 mm is a direct result of the predicted strain plateau between the transverse stretches of 5 and 5.5 in Figure 4.12. Between $l$ = 1.6 mm and 2.0 mm, the curve dips back down to ~100%, and above 2.0 mm the amount of achievable circumferential strain decreases linearly to roughly 90% at a spacing of $l$ = 3.5. Larger spacing is ideal since it maximizes the active area and minimizes the number of required rigid elements. Therefore, from this analysis it was concluded that a spacing of $l$ = 2.0 mm between rigid elements would be ideal since this is the maximum spacing possible without losing any predicted maximum circumferential actuation strain.

To determine the number of required rigid elements $n$ – 1, the following expression was derived, based on Figure 4.16:

$$L - 2w_e = nl + (n-1)w_r \quad \Rightarrow \quad n = \frac{L - 2w_e + w_r}{l + w_r} \tag{4.22}$$

where the width of the rigid end tabs is $w_e$, the width of the intermediary rigid elements is $w_r$, the length of the spacing between rigid elements is $l$, the total length is $L$, and the number of active areas of length $l$ is $n$.

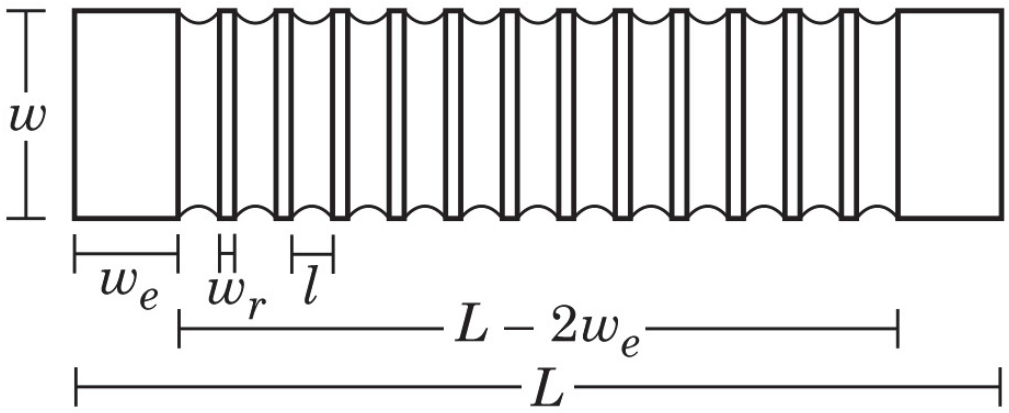


**Figure 4.16** Theoretical geometry of the DEB. Labeled in the figure are the width of the band $w$, the width of the rigid end tabs $w_e$, the width of the intermediary rigid elements $w_r$, the length of the spacing between rigid elements $l$, the total length $L$, and the length minus the end tabs $L - 2w_e$.

The end tab width $w_e$ was arbitrarily chosen to be 5 mm for easy handling and wire interfacing. Although they would ideally be as narrow as possible, the width of the other rigid bars $w_r$ was chosen to be 0.75 mm because this is the practical lower limit the current fabrication procedure could reliably support. Substituting in these values, as well as $L$ = 45 mm and $l$ = 2.0 mm, a value of $n$ = 13 is obtained. This means that there should be 13 active areas and 12 rigid bars.

#### 4.3.3.3 Practical Model Adjustments

In order to fit the model predictions to the performance data for the real DEB, ideal model plots of circumferential strain or force relaxation with voltage were first generated, then these plots were scaled using percentages derived from

photographic measurements taken of the real DEB. First, to generate a plot of isotonic circumferential actuation strain with voltage for an ideal DEB, the circumferential stretch versus voltage was plotted for a transverse prestretch of 5.5 using the same conventions as in Figure 4.11. This resulted in Figure 4.17(a). Figure 4.17(b) depicts a zoomed in view of (a). Plotted are blue curves for 2.7 and 4.0 kPa, a black dashed curve for 3.35 kPa, and the red breakdown (BD) and loss of tension (LT) curves.

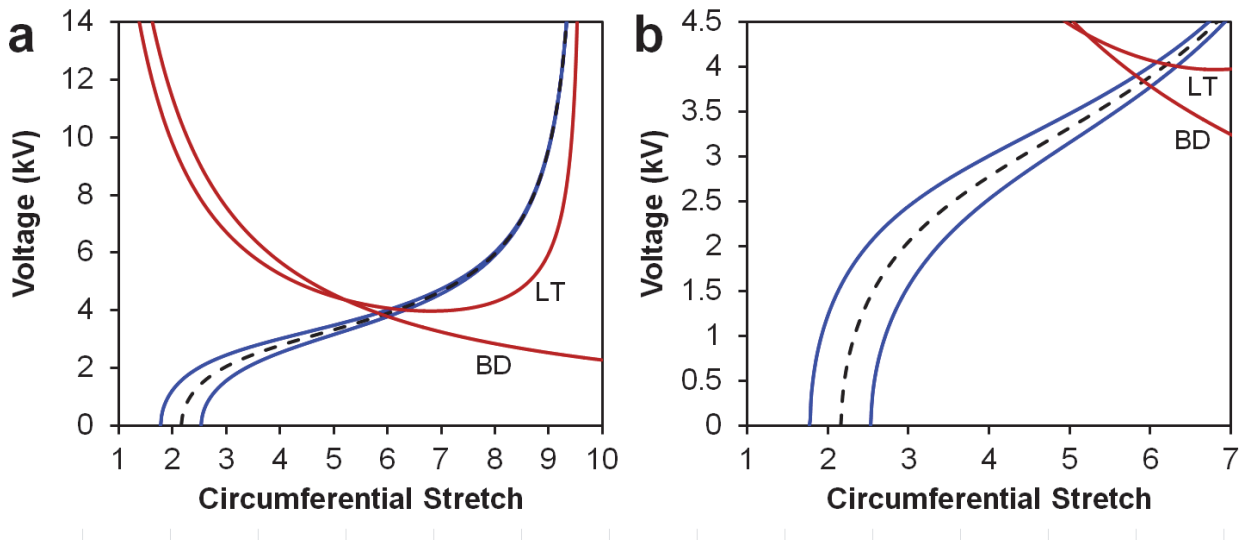


**Figure 4.17** **(a)** Circumferential stretch versus voltage for pure shear DE under the same conditions as in Figure 4.11, with a transverse stretch of 5.5. The blue curves correspond to the boundary conditions 2.7 kPa and 4.0 kPa, and the black dashed curve is the average. The breakdown voltage with stretch (BD) and loss of transverse tension (LT) are plotted in red. **(b)** Zoomed in view of (a), with the portions of interest of the curves more visible. (See Section 6.4.3.3 for code.)

The blue curve in Figure 4.18 was easily created by replotting the dashed black curve in terms of the strain and swapping the horizontal and vertical axes. Similar adjustments were also made for the red BT and LT curves. Next, the scaling percentage was calculated using the measurements shown in Figure 4.19. As shown in the illustration, passive margins between the active areas and the rigid elements were added to minimize wrinkling and EMI that would occur with no margins. As a result, the total amount of active actuation due to these margins is

$$\frac{1.05\text{ mm}}{1.95\text{ mm}}\times 100 = 53.8\% \tag{4.23}$$

in which the circumferential length of electrode overlap (1.05 mm) is divided by the spacing between rigid elements (1.95 mm). Passive margins were also added between the active areas and the VHB™ free edges to prevent short circuiting across layers. The remaining amount of active length in the transverse direction was measured to be roughly

$$\frac{8.79\text{ mm}}{10.65\text{ mm}}\times 100 = 82.5\% \tag{4.24}$$

in which the transverse electrode length (8.79 mm) is divided by the total length of the passive rigid elements (10.65 mm). Finally, these passive rigid elements are unable to actuate, so considering them, the remaining circumferential active length is given by

$$\left[1-\frac{2(5.22\text{ mm})+13(1\text{ mm})}{45.25\text{ mm}}\right]\times 100 = 48.2\% \tag{4.25}$$

Multiplying these percentages yields the following:

$$(0.538)(0.825)(0.482)\times 100 = 21.4\% \tag{4.26}$$

Therefore, the blue curve in Figure 4.18 was scaled by 21.4% of the original values, creating the black curve, which fits the real data points well. The red BD and LT curves were also scaled down by 21.4%, replotted as the dashed lines BD′ and LT′.

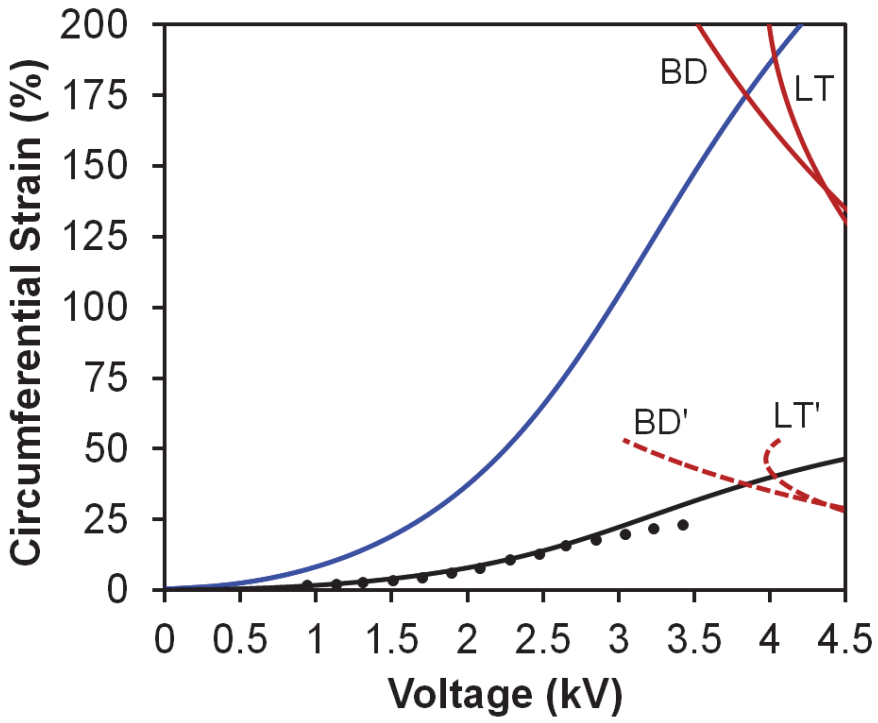


**Figure 4.18** Isotonic circumferential actuation strain of the DEB with voltage. Ideal model in blue and 21% scaled model in black, overlaid with experimental data points. The ideal breakdown (BD) and transverse loss of tension (LT) curves are shown in solid red, and the scaled breakdown (BD′) and loss of tension (LT′) curves are plotted in dashed red. (See Section 6.4.3.4 for code.)

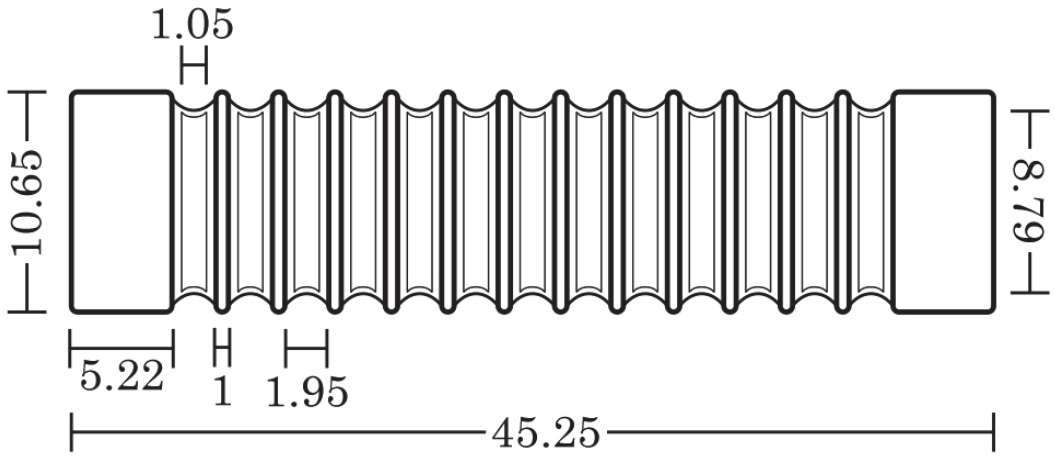


**Figure 4.19** Real DEB geometry, with horizontal and vertical passive margins added for practical actuation concerns. The passive elements were lengthened slightly, end the edges were rounded to minimize stress localization at the soft joints. Measurements shown are in millimeters.

To plot the ideal isometric tests, $\sigma_c$ in Equation 4.4 was substituted for the following equation:

$$\sigma_c = \frac{F_c}{wt} = \frac{F_c \lambda_t \lambda_c}{wt_0 n} \tag{4.27}$$

in which $F_c$ is the force in the circumferential direction, $w$ = 10.6 mm is the width of the DEB, $t_0$ = 0.5 mm is the initial thickness of one DE layer, $n$ = 2 is the number of DE layers, $t$ is the total thickness, $\lambda_t = 5.5$, and $\lambda_c = 2.15$. Following the substitution, the state equation becomes

$$\frac{F_c \lambda_t \lambda_c}{wt_0 n} = \frac{G\left(\lambda_c^2 - \lambda_c^{-2}\lambda_t^{-2}\right)}{1 - \left(\lambda_c^2 + \lambda_t^2 + \lambda_c^{-2}\lambda_t^{-2} - 3\right)J^{-1}} - \varepsilon_r \varepsilon_0 \left(\frac{V}{t}\right)^2 \tag{4.28}$$

Solving for $F_c$ and plotting with voltages from 10 V to 4,000 V at 10 V increments yields the blue curve in Figure 4.20.

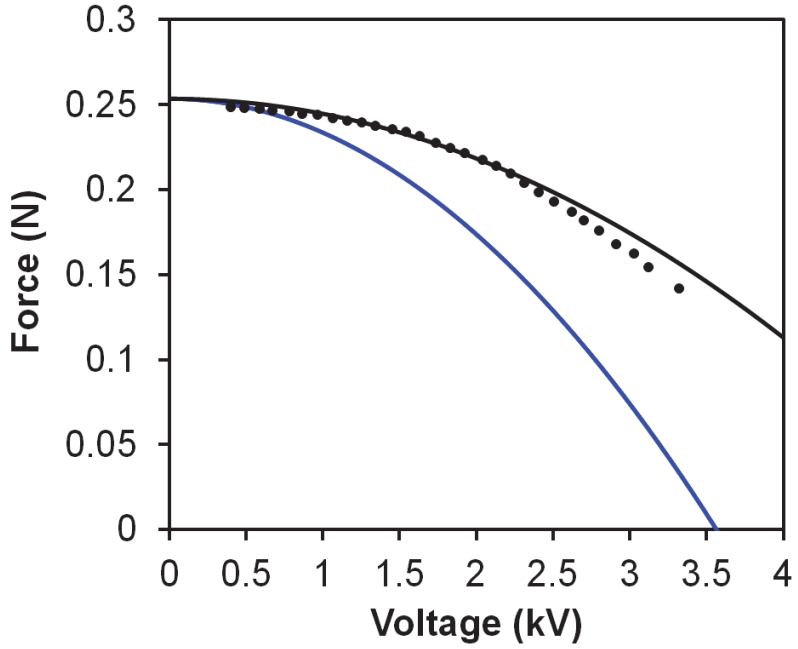


**Figure 4.20** Isometric actuation of DEB with voltage. Ideal model in blue and 44% scaled model in black, overlaid with experimental data points. (See Section 6.4.3.5 for code.)

To scale the blue curve, only Percentages 4.23 and 4.24 were multiplied. This is because the rigid passive elements considered in Percentage 4.25 do not diminish the force relaxation in under isometric test conditions. As a result

$$(0.538)(0.825)\times 100 = 44.4\% \tag{4.29}$$

The blue ideal model curve was therefore scaled by 44% of the original, followed by a baseline shift so its initial force at 0 V coincides with the blue curve at ~0.25 N. The scaling was necessary to adjust the actuation performance, while the baseline shift rectified the initial force. The resulting black curve in Figure 4.20 also agrees

with the experimental data well. Finally, by solving Equation 4.9 for $P$ and inputting a range of voltages from 10 V to 4,000 V at 10 V increments, the blue ideal model curve was plotted in Figure 4.21. Note that the theoretical curve intersects the $y$-axis at ~3.35 kPa. If a DEB was wrapped around the LES, or a tube of diameter $d$ = 14.4 mm, it would likely actuate following the profile shown in black, in which the blue curve was scaled by 44% and baseline shifted. This is because the DEB wrapped around the tube is essentially an isometric setup, assuming no internal pressure is felt. In the case of an internal pressure, if constant in an isobaric condition, the actuation would be similar to that shown under isotonic conditions.

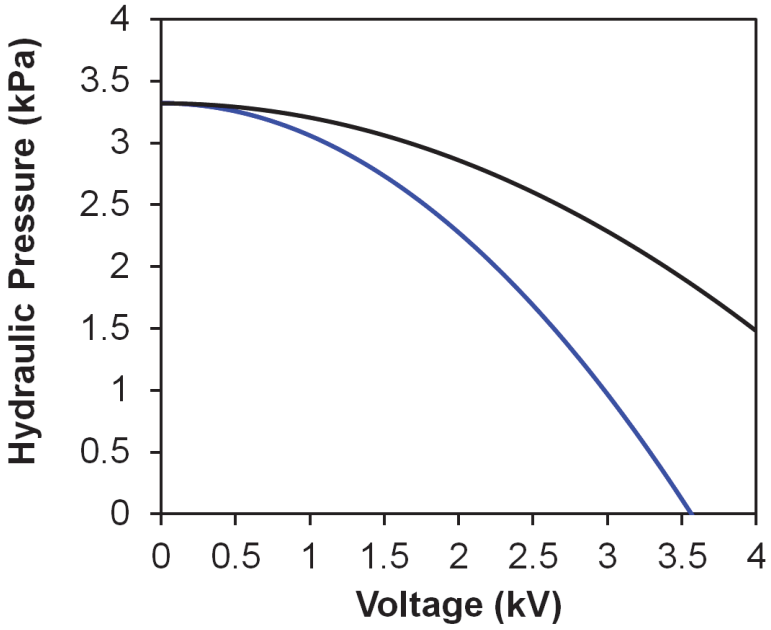


**Figure 4.21** Theoretical hydraulic pressure drops of DEB wrapped in an isometric configuration around the LES. The blue curve shows an ideal DEB, and the black curve is the ideal DEB scaled by 44%. (See Section 6.4.3.5 for code.)

## 4.4 Summary and Conclusions

The research presented in this chapter introduced a novel dielectric elastomer based alternative to the treatment of GERD. This dielectric elastomer band consists of a two-layer stack of prestretched VHB™ 4905 with three layers of SWCNT electrodes. Its transverse prestretch was maintained by an innovative process involving the selective rigidification of the DE band using a UV-curable, solution-processable polymer network. The resulting actuator exhibited a maximum vertical actuation strain of 25% at 3.4 kV in an isotonic setup with a 24.5 g weight. Isometric tests fixed at a 4.5 cm length showed a maximum force drop of 0.11 N, from 0.25 N to 0.143 N at 3.32 kV. In addition, the passive band force of 0.25 N was confirmed by the maximum of the stress relaxation curve prior to isometric actuation.

Mathematical modeling was performed to ascertain the prestretches necessary to achieve the maximum strain while simultaneously exerting the required force of 0.25 N, which corresponds to a required pinching pressure of 3.35 kPa. Modeling was also utilized to optimize the DE band geometry, such as the spacing distance of the rigid elements. Practical considerations such as adding margins reduced the amount of actuation strain or force drops as compared to the model predictions. The model curves were scaled using photographic measurements of the band, which show a reasonable fit with the empirical data. Future progress could involve computerized fabrication or other microfabrication techniques to reduce features sizes and margins, or may employ the use of silicone DEs to

eliminate passive viscoelastic creep or BSEP DEs to minimize power consumption. Although the DE band could be improved to achieve higher strains or force drops, the current performance is comparable to that of living muscle, and the DE band is a noteworthy first step toward the use of dielectric elastomers for the treatment of GERD. In addition, an offshoot of this technology could offer a highly low-profile alternative to a linear peristaltic pump, and potentially the development of artificial intestines or blood vessels.

# CHAPTER 5

# Summary and Future Directions of This Work

## 5.1 Conclusions

The focus of the original research presented in this dissertation is the application of soft actuators, specifically VHB™ acrylic dielectric elastomers, to biomimetic designs capable of fluid handling and with potential biomedical engineering significance. The first such device was a dielectric elastomer-driven microfluidic system pairing a 5-layer, anisotropically prestretched DE stack to a PDMS microchannel. This system exhibited dynamic and steady-state alteration of channel geometry, as well as active alteration of the system pressure-flow characteristics. The DE microchannel also demonstrated active clearing of microchannel blockages, which is a common problem in microfluidic systems.

The second novel device was a biomimetic dielectric elastomer valve inspired by intestinal anatomy. This tubular minimum energy actuator consisted of a two-layer, biaxially prestretched DE paired with a flexible PET frame, which could function as two opposing leaf springs to pinch a tube shut. This opening could be actively tuned with voltage to control the pressure-flow characteristics of a fluidic system. This DE valve was also shown to be reliable for 2,000 cycles at low and high voltages, and simple modeling was performed to mathematically describe the system performance.

The final contribution discussed was a dielectric elastomer band designed to wrap around the lower esophageal sphincter in the treatment of chronic acid reflux. This ring actuator consists of a DE with an anisotropic prestretch designed specifically to maximize strain while meeting the required passive pinching pressure. The transverse prestretch was maintained by selectively incorporating a solution-processed, UV-curable polymer into the band. The spacing between rigid elements was also optimized. Practical limitations with margins and alignment slightly limited performance, but the maximum strains were comparable to those of living muscle, and the actuation was stable and repeatable.

## 5.2 Future Work

### 5.2.1 Alternative Dielectric Elastomer Materials

The three novel explorations summarized above are seminal in the subfields of microfluidics, soft robotics, and medical devices, demonstrating the first such DE-based device of its kind in each area. Further work is therefore merited in many facets, including in the study of new and improved materials for application to all of the biomedical and biomimetic devices presented herein. One critical improvement that can be made to all of these devices is to replace the VHB™ dielectric elastomer with silicone elastomers. Although silicones may not be capable of outputting passive pressures as high as VHB™ due to their lower prestrains by comparison, they mostly lack one of the most salient and often problematic features of acrylic DEs like VHB™: viscoelasticity. [7]

As mentioned previously, the time-dependent nature of viscoelasticity: (i) potentially interferes with device reliability since the DE stress state varies as a function of time; (ii) reduces performance lifetimes as this creep phenomenon can lead to delamination, crack propagation, and time-drifting of prestretch; and (iii) restricts shelf life due to delamination, crack propagation, and prestretch drift in the resting state. As an industrial-strength adhesive, the high viscoelasticity of VHB™ is beneficial in the joining of two surfaces because it: (i) provides resistance to motion from moderate to fast transient forces, maintaining bond stability and providing shock absorption; and (ii) creeps into the pores of the two joining surfaces, thereby increasing the bond surface area and improving bond strength with time.

Indeed, 3M™ had originally engineered VHB™ to serve as a weld-alternative adhesive with said properties. [322] However, as the field of dielectric elastomer transducers has matured, new research efforts have overwhelmingly adopted the use of silicone DEs in lieu of VHB™. [76, 82-85, 124, 132, 241, 273] Because many silicones lack any appreciable extent of viscoelastic behavior, they can greatly improve device reliability, lifetime, and shelf-life, and will help pave the way toward the commercialization of mass-produced DE-based products.

The original fluidic and biomedical devices presented in this dissertation may also benefit from fabrication using BSEP materials, especially where low power consumption is beneficial. In the DE microchannel and DEV, portability may be desired, and as a potential medical implant the power supply of the DEB would likely need to be self-contained. In both cases, power consumption management is a requirement. For example, a BSEP-actuated microchannel could deform to the desired channel geometry and then lock in this shape without needing to continue supplying power. A BSEP DEV could be actively tuned to the desired pinching pressure and then passively set into that state. And, a BSEP-based DEB could be heated, actuated to the desired opening or level of tightness, and cooled to "freeze" in this state without consuming any power; heating again can allow it to return to its initial stress state. As such, a BSEP DEB could be opened before a meal and closed afterwards, potentially reducing the number of required actuation cycles and required power. For all these cases, the BSEP material would likely need sufficient

crosslinking to support prestretch, although these devices could be reenvisioned to operate with prestretch-free DE materials.

Finally, these fluidic and biomedical devices would potentially benefit from higher dielectric constant DE materials, such as those surveyed in Section 1.3.2, in order to reduce the required actuation voltage. Because they are low power, biomedical DE devices do not pose a substantial safety concern to the biological systems with which they interface. However, lower actuation voltages would still be ideal, increasing safety even further such as where cell viability in a DE microfluidic device or voltage isolation in a DE implant are concerned. Alternatively, voltages can be lowered by manufacturing thinner DE layers. In this vein, higher precision and potentially automated microfabrication techniques could help increase electrode patterning precision and device performance even further.

### 5.2.2 Reliability Testing

Once the appropriate new materials are chosen, the reliability of these devices should be tested by performing cyclic actuation tests over as many cycles as possible. Cycles on the order of $10^5$ or $10^6$ are ideal for most commercially viable devices. For example, the dielectric elastomer band in Chapter 4 should be capable of roughly 500,000 actuation cycles in its lifetime if it is to be used as an implant. A BSEP band may require fewer cycles, but should still be capable of the same magnitude of cycles. From U.S. census food and beverage consumption data and swallowing volume research, it can be calculated that the average American

swallows roughly 50,000 times per year for eating and drinking. [323, 324] As a benchmark, the average pacemaker lifetime is 10 years. [325, 326] Hence in 10 years, the DE band should be capable of actuating 500,000 times. Other applications may require similar longevities to be commercially useful.

Testing on this scale will likely need accelerated, but devices driven by silicone-based DE actuators should be testable at higher frequencies than VHB™ since silicones are much less viscoelastic. For example, the VHB™-based DEV in Chapter 3 could be actuated no more quickly than 0.1 Hz at 400 mL/hr in order to reach full strain, which would require about 3,000 hours (~120 days) of continuous testing to reach $10^6$ cycles. However, actuation of silicone-based devices could be carried out at 1 Hz or even 10 Hz, cutting the total testing time to only 300 h or 30 h. Moreover, parallel actuation of devices is also encouraged, as it (i) accounts for the possibility of premature failure of some devices, (ii) allows a "competition" among devices to yield a percentage of total devices able to undergo the full number of cycles, and (iii) gives more data points to average when plotting performance evolution (such as of force, pressure, strain, or electrode resistance) with time.

### 5.2.3 *In Vitro*, *In Vivo*, and Clinical Trials

The prototype devices presented in this work form an exciting new collection of approaches to solving a variety of biomedical problems. Further exploration is therefore merited in biomedical testing. The DE microchannel has been shown to be biocompatible and able to handle PDMS microbeads, but a variety of *in vitro*

microfluidic studies should be explored that involve fluid handling containing live cells. Following further material refinement and adequate reliability testing, the DE band would be one step closer to becoming a viable medical implant. As a primer for this, *in vivo* implantation of the DEB into vertebrate animals should be performed, with a focus on acid reflux and safety studies. Finally, with good *in vivo* results, human clinical trials could be performed, and FDA approval sought. With the necessary refinements, the DEB has the potential to offer a reasonably natural cure to GERD.

### 5.2.4 Related Applications

Future applications of the novel DE technology presented in this dissertation need not be limited solely to microchannels, valves, or bands. As mentioned previously, the DE microchannel could be readily adapted to function as a microperistaltic pump or an artificial capillary. When paired with sensing ability, the DE microchannel could also function as an adaptive microfilter, potentially reducing the complexity of lab-on-a-chip devices. Secondly, one offshoot of the DEV is an artificial sphincter, designed with more layers to replace the LES, or to be used in conjunction with an ileostomy pouch for continent ileostomy patients. Another related application is a low profile linear peristaltic pump or artificial intestine when a series linkage of DEV-like devices is created. The DEV can also be adapted for pneumatic control in HVAC systems, both able to control the amount of flow as well as steer the air flow in a specific direction.

Thirdly, the DEB could not only function as a band for the LES, but could be adapted for use as a gastric band, wrapping around the entire stomach to aid in caloric restriction in the treatment of obesity. The DEB could also find use external to the body as an orthotic device, functioning as a variable stiffness ankle or wrist brace. In addition, as with the DEV, when a series of DEBs are linked together, an efficient linear peristaltic pump could be designed. With the proper modifications, this design could be adapted to function as an artificial intestine (small intestine, large intestine, or esophagus), as an artificial urethra, or as an artificial vein or artery (e.g., aorta or carotid artery). Indeed, the myriad of DE applications that can be envisioned is quite substantial, and the application of dielectric elastomer transducers to biology, medicine, and engineering holds great promise. This research work is just the beginning of an accelerating field, and there remains much more to be explored.

# CHAPTER 6

# Appendices

## 6.1 Unconventional Electrode Materials for Dielectric Elastomers

### 6.1.1 Opaque Compliant Conductors

#### 6.1.1.1 Metals

##### *6.1.1.1.1 Nickel Microparticle Composites*

Exciting recent advances utilizing magnetic templating have created anisotropic composites of nickel in PDMS that actually exhibit an increase in conductivity with increasing strain. Kim and colleagues fabricated these stretchable conductors by first mixing a nickel powder with ~5 $\mu$m particle size at up to 18.3% by volume in an uncured matrix of Sylgard® 184. [327] Then, the mixture was drop cast on an aluminum mold and sandwiched between two iron-neodymium permanent magnetic structures (4,000 G). Because nickel is ferromagnetic, it aligns in the uncured PDMS matrix along the magnetic field lines normal to the plane of the film being cast. Thermal curing crosslinks the PDMS matrix, locking in this alignment of Ni microparticles. By the incompressibility of the composite, uniaxial stretching causes a decrease in length in the perpendicular in-plane direction. This in turn brings the lines of Ni particles, magnetically aligned normal to the plane, into closer proximity with one another, thereby increasing conductivity with strain.

The increase in conductivity saturated at about 40% tensile strain, and was about 115 S/cm at 100% strain. To lower the initial resistance from over ~100 Ω at no strain, silver ink was inkjet printed atop the Ni/PDMS composite. Because the initial resistance of Ag thin films on PDMS is low but increases steeply at higher strains, it was thought that it would help lower the initial resistance of the Ni/PDMS composite until the Ni/PDMS is able to decrease the resistance at higher strains. This was in fact observed, and the Ag/Ni/PDMS composite exhibited a resistance of less than 20 Ω from 0 to 100% strain (sample at 0% strain measured 10 mm long × 1 mm wide × 1 mm thick).

In a slightly different direction, Ni/polymer composites have been shown to possess self-healing properties as well. To this end, Tee et al. doped a hydrogen-bonded elastomer matrix with nanostructured nickel microparticles. [328] The Ni increased the tensile strength of the composite to 1 MPa at 31 vol.% Ni, but failed at less than 30% tensile strain; at 15 vol.% Ni, the tensile strength was roughly 40 kPa and was capable of at least 100% strain. More importantly, the hydrogen bond-linked polymer network is capable of breaking and easily reforming its bonds under slight applied pressure at room temperature, making self-healing possible. Cutting the composite increased the resistance from ~30 Ω to $10^8$ Ω, but pressing the separated ends together for only 15 seconds completely restored the ~30 Ω resistance. Moreover, by nanostructuring, that is, roughening the surface of the Ni microparticles, percolation can be reached at about 15 vol.% Ni, above which conductivities of ~40 S/cm were reached. Although the ferromagnetic properties of

the Ni particles were not used to their advantage in this study, it would be interesting to see a combination of both this method and the magnetically-aligned Ni composites above. Doing so could create a highly conductive, highly stretchable, and self-healing composite.

#### *6.1.1.1.2 Liquid EGaIn Alloys*

Although not a conventional DE electrode material, liquid metal alloys could potentially find application in microfluidic-integrated DE systems, or any other DE system with encapsulation that requires among the highest conductivities and strains possible. In this novel direction, a liquid metal alloy is injected into fluidic channels, such as of PDMS. One good liquid metal candidate is eutectic gallium-indium (EGaIn). With a melting point of only ~15.5°C, EGaIn (75 wt.% Ga, 25 wt.% In) is a liquid at room temperature, so no heating or cooling steps are required for most applications. [329, 330] This is clearly an advantage over molten solders of eutectic lead-tin (EPbSn), whose high melting point of 183°C is incompatible with untreated organic elastomers. [331] EGaIn is also advantageous over indium or indium-tin alloys, which have been injected into silanized PDMS channels, but which have melting points of 158°C and 118°C, respectively, allowing for only moderately flexible but not extensible conductors at room temperature. [332] Moreover, EGaIn possesses a high conductivity of ~$3.4 \times 10^6$ S/m (resistivity of 29.4 $\pm 1.3 \times 10^{-6}$ Ω·cm). [333] For these reasons, EGaIn appears poised as a promising candidate for stretchable conductors of eutectic metallic alloys in elastomers.

To enable EGaIn to flow into a 20 × 40 $\mu$m PDMS microchannel, a gauge injection pressure greater than 85 kPa needed to be applied. When compared to liquid mercury, any gauge pressure greater than 54 kPa would suffice. However, when returned to ambient pressure, the mercury flowed almost completely out of the microchannel to minimize interfacial free energy, whereas the EGaIn remained stable, continuing to occupy the microchannel. This can be attributed to the formation of a surface oxide layer "skin" with unique properties. This skin encapsulates and contains the liquid Ga and additionally exhibits elastic behavior below a critical stress, above which the Ga flows easily. Figure 6.1 shows the influence of this skin on the stable moldability of the alloy, as well as the relationship between required injection pressure and inverse channel width to enable EGaIn to flow into a microchannel, as compared to Hg. [333, 334]

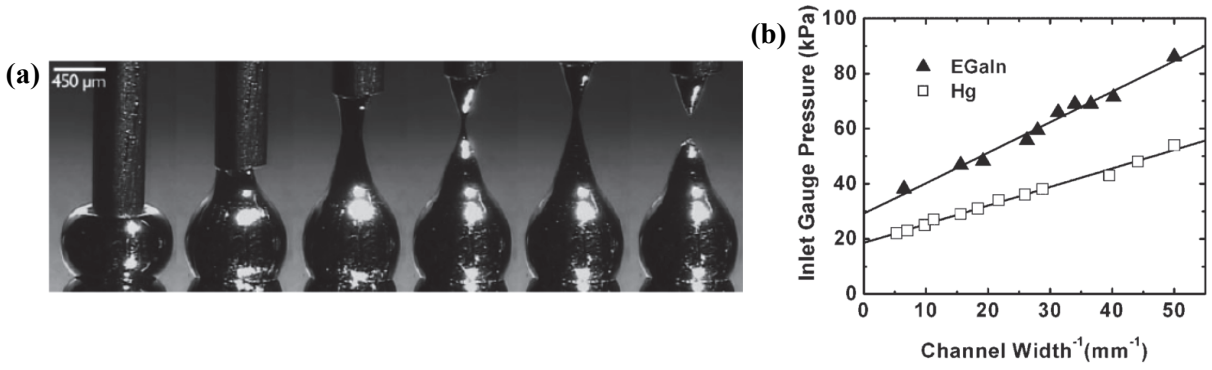


**Figure 6.1** **(a)** Series of photographs showing the progression of the 5 second formation of a conical tip on a drop of EGaIn, made possible by surface oxide formation. [334] **(b)** Inlet gauge pressure required for EGaIn and Hg to flow into a 20 × 40 $\mu$m PDMS microchannel. The narrower the channel (or the larger the inverse channel width), the higher the required

pressure. The slope of the linear fit is proportional to the surface tension, in which EGaIn is clearly higher than Hg. [333]

Feasible EGaIn/PDMS systems have been demonstrated, consisting of three layers: PDMS containing the microchannel, a middle layer with inlet and outlet holes, and a top capping layer. The bottom of the microchannel contains an evaporated layer of gold for easy wetting of the EGaIn. The microchannels are 100 $\mu$m high, with varying widths of 30, 70, or 100 $\mu$m. A diamond-shaped lattice with 100 $\mu$m-wide channels was also fabricated, which exhibited a maximum stretchability of 100% and only a 0.24 Ω change in resistance. Also, 180° bending caused less than a 0.02 Ω change in resistance. [335]

In another slightly different application, Zhu et al. fabricated stretchable wires of hollow-core SEBS triblock copolymer fibers filled with EGaIn. The poly(styrene-*b*-(ethylene-*co*-butylene)-*b*-styrene), or SEBS, resin utilized was Kraton G1643 for its high failure strain of over 900%. The hollow fibers were manufactured by melt extruding the SEBS through a die with a circular slit divided into three equal segments; upon exiting the dye, the SEBS segments melted together to form hollow fibers. The spinning rate of the collection roller was varied from 25 to 1,000 m/min to create hollow fibers of inner diameters ranging from 360 to 1,030 $\mu$m. These remarkable stretchable wires can stretch up to 700% strain while still maintaining metallic conductivity. As a proof of utility, these stretchable EGaIn wires were incorporated into a functional stretchable earphone and iPod charging cables. [26] However, these fibers could be surrounded by an additional layer of

EGaIn and a thin outer layer of SEBS encapsulant to form DEA artificial muscle fibers with high strains possible. Such would be a simple variant of the work by Kofod and Stoyanov, in which SEBS was used to form "co-axial" DEAs. [336, 337]

#### 6.1.1.2 Carbons

##### *6.1.1.2.1 Carbon/Polymer Nanocomposites*

More recent advances utilize carbon nanotubes in an elastomer matrix in lieu of carbon powders or microscale fibers. As with metal filler/polymer composites, the conductivity of carbon filler/polymer composites generally follows percolation theory. In a model proposed by Kirkpatrick and Zallen, the percolation threshold for randomly-distributed spherical conductors such as carbon black is 16% by volume, unless agglomerates are formed as in carbon black/epoxy resins. [71, 338, 339] However, due to their high aspect ratio geometry, SWCNTs typically have a percolation threshold less than 0.1 vol.%, assuming good dispersion in the host matrix. [340, 341] Because of the low percolation threshold of polymer/CNT nanocomposites, high conductivity can theoretically be obtained without high CNT loading, leading to greater mechanical compliance. Good results have also been demonstrated with graphene; Kujawski et al. in the Smela group filled PDMS with exfoliated graphene, creating a compliant conductor with conductivities up to 0.4 S/cm. They reached percolation at 3 wt.% graphene, and notably, were able to keep the modulus at only 1.4 MPa when loaded with up to 25 wt.% graphene. [342]

Other work with MWCNTs shows noteworthy progress, demonstrating both high conductivity and high strain at relatively high filler loadings. To this end, Li and Shimizu report a stretchable nanocomposite conductor of SEBS triblock copolymer loaded with 15 wt.% MWCNTs. A processing technique was utilized in which high shear stress is exerted on the SEBS/MWCNT mixture by extruding at a screw rotation speed of 1,000 rpm during melt compounding. While this shear stress may exfoliate the MWCNTs, it ensures a high degree of MWCNT homogeneity in the SEBS matrix. Conductivity increased asymptotically with increasing MWCNT loading, reaching 5.16 S/cm at 15 wt.%. Dynamic mechanical tests of the composite at this loading exhibited stretchability up to 600% strain, and electrical tests showed conductivity stability at strains below 50%. [110]

#### *6.1.1.2.2 Ionic Dispersion*

While shear extrusion does ensure homogenous nanocomposites with high loading, another more common approach involves utilizing an ionic liquid to homogeneously disperse CNTs into a polymer matrix. The ionic liquid also augments the electrical conductivity of the composite. Sekitani et al. utilized an ionic liquid to prepare millimeter-long SWCNTs for doping into a flexible fluorinated copolymer matrix. Specifically, the nanotubes were mixed with 1-butyl-3-methylimidazolium bis(trifluoromethanesulfonyl)imide (BMITFSI) before being uniformly dispersed into a vinylidene fluoride-hexafluoropropylene copolymer matrix, drop cast on glass, and dried overnight at room temperature. Using this

method, 99% of the ionic liquid can be recovered by Soxhlet extraction and recycled. Although the extraction lowers conductivity, it does not do so appreciably, and the composite conductivity after extraction is as high as 10 S/cm. Nevertheless, the stretchable conductors under test were left to retain the ionic liquid, enabling conductivities as high as 57 S/cm.

Although the resulting nanocomposite conductor is flexible, it has low elasticity. To improve stretchability, holes were punched into the conductor to form a grid, after which it was encapsulated in PDMS. This elastic conductor does not show notable changes in its conductivity of 57 S/cm or any mechanical damage below 38% uniaxial strain, and at 134% uniaxial strain, the conductor exhibited a moderately high conductivity of 6 S/cm. This is in contrast with conventional carbon black-loaded rubbers, which can strain up to 150% but that have a conductivity of only 0.1 S/cm for all strains. The stretchable conductor proved reliable with no change in conductance after 4,000 cycles at 25% strain and 500 cycles at 50% strain. The group also fabricated a soft transistor array with this stretchable conductor nanocomposite as the bit-line and word-line interconnects. The flexible transistor array could stretch biaxially up to 70% strain without degrading in electrical performance. [36]

In later improvements, Sekitani and colleagues incorporated a jet milling process into the fabrication of their SWCNT/fluorinated copolymer composite. This process not only ensures a more uniform dispersion of longer and finer nanotube bundles, but also increases the viscosity of the composite to a level appropriate for a

printing process. As was seen with metal inks, printable CNT/elastomer conductors are another exciting development in the realm of stretchable conductors because printing allows for intuitive, high-resolution electrode patterning and deposition of these conductors. Because it could be printed onto flexible substrates such as PDMS, their new jet-milled conductor also did not require additional encapsulation as before. The printed conductor had an even higher conductivity of 102 S/cm at 29% strain and 15.8 wt.% SWCNTs, as well as a maximum stretchability of 118% at 9.7 S/cm and 1.4 wt.% SWCNTs. Additionally, no change in conductivity was observed for conductors with 1.4 wt.% or 2.8 wt.% SWCNTs after 1,000 cycles at 70% strain. [37]

Along similar lines, Chun et al. have developed a printable stretchable conductor of Ag-functionalized MWCNTs dispersed in a polyvinylidenefluoride (PVDF) copolymer using an ionic liquid. Although this conductor was not printed, the materials utilized are hypothetically printable. Silver nanoparticles with phenyl rings were manufactured via a self-assembly process and subsequently conjugated with the MWCNTs via π-π interactions. The resulting "decorated" MWCNTs (nAg-MWNTs) were mixed with the ionic fluid 1-butyl-4-methylpyridinium tetrafluoroborate to form a gel. Following this step, the gel was mixed and sonicated with the PVDF solution, drop cast, and cured at 160°C. Instead of jet milling, the resulting composite was then hot-rolled, leading to densification and a ~5% reduction in thickness. After hot-rolling, the initial conductivity was increased by 190% and stretchability was increased by as much as 342%. The hot-rolled nAg-

MWNT/PVDF composite had a conductivity of 5,710 S/cm at 0% strain and 20 S/cm at the maximum 140% strain. [224] Another stretchable conductor fabricated with the aid of a similar ionic liquid (1-butyl-3-methylimidazolium chloride) was a MWNT/polyurethane nanocomposite, with a conductivity of 5.3 S/cm and a stretchability of more than 100%. [41]

To increase conductivity even further, one of these ionic liquid-prepared CNT/elastomer composites was exposed to a nitric acid vapor, effectively hole-doping the CNTs. Specifically, Kim et al. ground SWCNTs with BMITFS to form a gel (with 4 wt.% SWCNT), dissolved it in toluene, mixed it with a silicone rubber, and sprayed the conducting electrodes on acrylic elastomer substrates. After drying on a hot plate and in a vacuum, the composite was saturated in a nitric acid environment at 70°C for 30 minutes, followed by drying in a vacuum oven at 25°C for one day. At 0% strain, the treated samples exhibited a sevenfold decrease in sheet resistance, from 350 to 50 Ω/sq.; at 200% strain, the sheet resistance for the treated composite was 320 Ω/sq., versus 1600 Ω/sq. Moreover, the treated composite could maintain its conductivity of ~18 S/cm at 200% strain after 20 stretch cycles. [208] These efforts to fabricate conducting SWCNT/elastomer composites using an ionic liquid are cost-effective and scalable to an industrial scale. However, further improvement is necessary in order to compete with the high conductivity of stretchable metallic conductors, except for applications where high conductivity is not a requirement.

### 6.1.2 Transparent Compliant Conductors

#### 6.1.2.1 Metals

##### *6.1.2.1.1 AgNW/Polymer Composites*

In an alternative approach, Akter et al. explored the use of biologically-inspired adhesion layers to form a highly stretchable AgNW/PDMS composite conductor. Typically, silicone substrates are highly hydrophobic, limiting the adhesion of AgNWs in fabricating stretchable AgNW/silicone composites. In this method, dopamine was utilized as an adhesion layer between a PDMS substrate and a Ag nanowire network. Dopamine contains 3,4-dihydroxy-L-phenylalanine (DOPA) and lysine peptides, which are the source of the adhesive properties in foot protein 5 of the mussel *Mytilus edulis*. PDMS substrates were cured, then soaked in dopamine hydrochloride solutions. Afterwards, the prepared substrates were spray coated with a AgNW dispersion, followed by heat treatment at 200°C for 20 minutes. The resulting transparent composites showed a transmittance of 80% and had an average sheet resistance of only 35 Ω/sq. Moreover, conductivity was maintained up to 20% mechanical elongation. [52, 343]

Other efforts to improve the conductivity at high strains of silver nanowire composites have involved utilizing very long nanowires. While typical AgNWs (100–150 nm diameter) are less than 20 $\mu$m long, these high-aspect-ratio AgNWs have lengths up to 200 $\mu$m after seven cycles of a successive multistep growth method. Using these very long AgNW, high conductivity can be attained without needing to increase AgNW density and compromise mechanical compliance. After formation of

the AgNWs, a “nano-welded” network was formed via the uniform suction pressure of a vacuum filtration process. Lee et al. tested the electromechanical properties of long AgNW networks on silicone Ecoflex substrates. Their AgNW/Ecoflex composites with 300% prestrain could be stretched to and additional ~200% strain with no increase in sheet resistance, and over 460% strain with less than a 10 times increase in sheet resistance. [33] Later work by the same group resulted in hybrid networks of small CNTs grafted to larger AgNW meshes, resulting in a transparent (80–93%) and highly stretchable (> 460%) conductor when transferred to 150% prestrained Ecoflex substrates. [225]

#### *6.1.2.1.2 Copper Nanowires*

Copper has been researched as an alternative material for the fabrication of nanowires for transparent, flexible conductors because it is 100 times less expensive and 1,000 times more abundant than silver. Rathmell et al. have proposed a scalable synthesis for copper nanowires (CuNWs), and demonstrated their use as transparent conductors with a transmittance of 85% and a sheet resistance of 30 Ω/sq. This was attainable via a new synthesis route that produces longer, thinner, better-dispersed CuNWs. The synthesis involves heating a reaction mixture of $Cu(NO_3)_2$ with hydrazine in NaOH and ethylenediamine (EDA) to 80°C for only 3 minutes to reduce the Cu ions, followed by the addition of polyvinylpyrrolidone (PVP) to prevent aggregation, then cooling in an ice bath to allow for longer, thinner nanowires to form at a lower temperature. A CuNW ink was then formulated by

dissolving nitrocellulose, which allows the formation of uniform CuNW films, in acetone, followed by the addition of the CuNWs with isopropyl alcohol and ethanol to improve the dispersion. Before depositing the ink on PET substrates, ethyl acetate and pentyl acetate were added to improve the ink spreading, followed by toluene to reduce the evaporation rate. After deposition, the ink on PET was dried in air for 5 minutes, plasma cleaned in a 5% hydrogen, 95% nitrogen atmosphere to remove the nitrocellulose, PVP, and other solvents, and finally annealed at 175°C in a hydrogen atmosphere. After 1,000 bending cycles from a radius of curvature of 10 mm to 2.5 mm, the CuNW conductor on PET experienced a change in sheet resistance of only 10 Ω/sq., from 30 to 40 Ω/sq. [28, 29]

Wu et al. demonstrate another interesting approach to fabricating transparent CuNW electrodes. Using an inexpensive, scalable electrospinning process, ultra-high aspect ratio (up to 100,000:1) CuNWs were grown. First, precursors with copper acetate are dissolved in poly(vinyl acetate) (PVA) and are electrospun onto a glass substrate. Next, heating at 500°C for 2 hours in air removes the polymer components, and subsequent annealing at 300°C for 1 h in and $H_2$ atmosphere completes the CuO nanofiber synthesis. During this procedure, roughly three-fourths of the junctions at overlapping points are fused together, thereby greatly reducing any junction resistances. This property of the CuNW network allows for very high conductivities such as 50 Ω/sq. at reasonably low CuNW concentrations, resulting in a corresponding transmittance of ~90% from 300 to 1,100 nm. Other figures of merit include 200 Ω/sq. at ~96% transmittance and 12

Ω/sq. at ~80% transmittance. Additionally, the CuNW films show virtually no change in sheet resistance at 10% strain on a PDMS substrate, while the resistance of copper thin films sputtered on PDMS increases by 100 times. [206]

More recent advances by Hu et al have enabled even more stretchable conductors of CuNWs in a polyurethane matrix. The CuNW/PU composite as fabricated using a similar transfer method to that used to create AgNW composite conductors: The CuNWs are first deposited on glass and treated with 6-aminohexanoic acid, followed by the drop casting of a two-part PU elastomer atop the CuNWs. After curing at room temperature for 24 hours, the PU was peeled off, transferring the CuNWs from the glass to the polymer. The treatment of the CuNWs with 6-aminohexanoic acid is thought to improve the adhesion of the CuNWs to the PU, both during the transfer process, as well as during mechanical deformation. The resulting CuNW/PU composite conductor exhibited low sheet resistances under $10^2$ Ω/sq. at tensile strains up to 60%. [207]

#### *6.1.2.1.3 Metal Rubber™*

Alternate electrode materials have been explored by companies such as Nanosonic, who have developed Metal Rubber™ (MR™), a transparent, low modulus Au-polymer nanocomposite with a bulk resistivity as low as $10^{-5}$ Ω-cm and the ability to withstand elongations of up to 1,000% without mechanical failure. These electrodes have tailorable moduli (1 to 100 MPa) and can be used either as a free-standing material or as a conformal coating on active polymer substrates, such

as conductive backplanes for flexible displays or electrodes for actuators. Moreover, free-standing MR™ films with 30 Ω resistance show resistance recovery to the initial value after cycling at 30% elongation for 150 cycles and at 10% elongation for 1,500 cycles. [214]

Metal Rubber™ is a multilayer structure fabricated via electrostatic self-assembly (ESA). In this procedure, alternating polyanion and polycation polymer monolayers are deposited onto a substrate functionalized with a charged release layer. As shown in Figure 6.2, ESA is driven by electrostatic attraction, whereby each successive layer is attracted to the oppositely-charged layer below, as well as protected from like-charged repulsive layers that have been completely covered. In this way, thin films of excellent thickness uniformity can be fabricated at room temperature and pressure using non-volatile compounds. [213, 344]

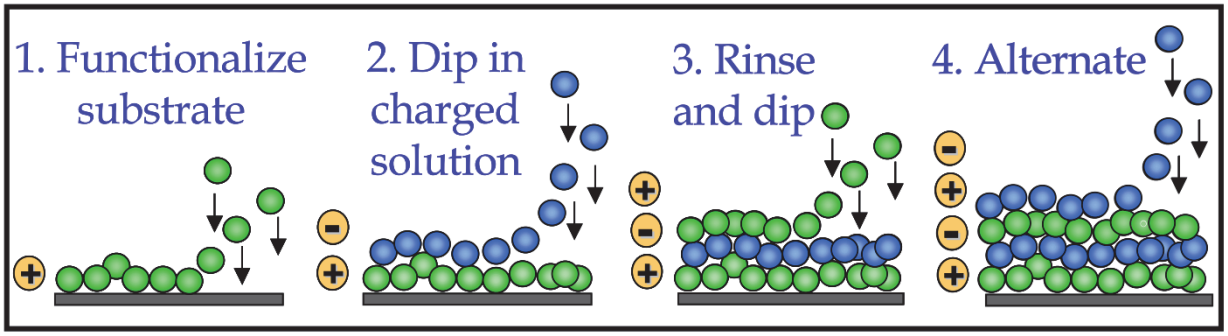


**Figure 6.2** Electrostatic self-assembly process. A charged, functionalized substrate is dipped in a charged polymer solution, rinsed with ultrapure deionized water, then dipped in a bath of oppositely-charged polymer solution. The process is repeated, until the desired MR™ thickness is achieved. [214]

#### 6.1.2.2 Aligned Carbon Nanotubes

In an alternative approach, Zhang et al. demonstrated the usefulness of aligned carbon nanotube ribbons embedded in PDMS as a stretchable, transparent conductor. The CNT ribbons were drawn from a continuous forest ~0.6 mm high. The resulting conductor exhibited a transmittance of ~60% at 400–800 nm and a stable resistance of 35.5 kΩ, obtained after the first six stretching cycles. [209] Generally, high strain and reliability after thousands of stretching cycles is possible with conductors fabricated from aligned SWCNTs because stretching can create fissures in such a way that bridges of SWCNTs are formed across the fissures, thereby maintaining conductivity (Figure 6.3(b)). Yamada and colleagues fabricated such a conductor, which was shown to withstand a 280% maximum strain and 10,000 stretching cycles at 150% strain. Although not tested for transparency as did Zhang and others, this conductor demonstrates the potential utility of aligned SWCNTs in stretchable electronic systems. [345]

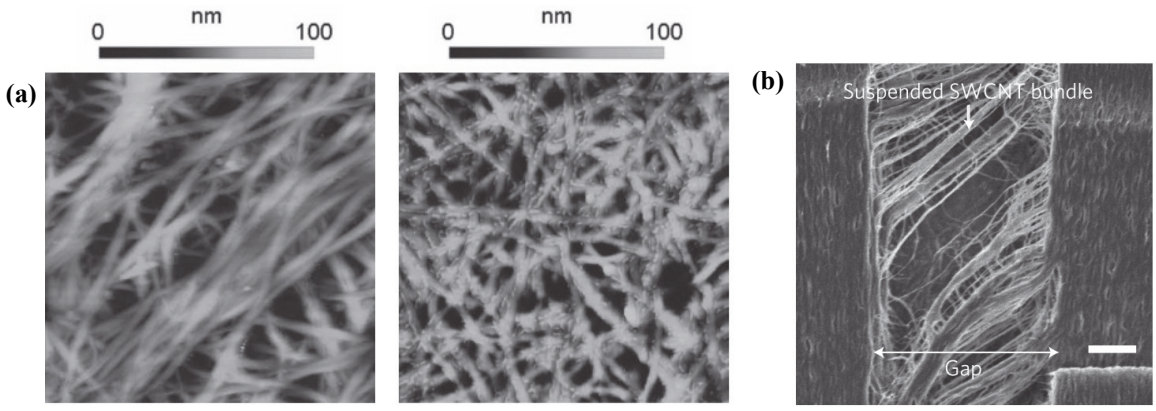


**Figure 6.3** **(a)** Atomic force micrographs of SWCNTs on glass with a surface roughness of > 60 nm (*left*) and the SWCNT/P*t*BA composite with surface roughness < 10 nm (*right*). [179] **(b)** Scanning electron micrograph of a fissure in an aligned SWCNT film, bridged by suspended SWCNT bundles. *Scale bar:* 1 $\mu$m. [345]

Furthermore, aligned carbon nanotubes hold promise for industrial scalability of transparent, stretchable conductors. Feng et al. propose a roll-to-roll process of fabricating films of super-aligned carbon nanotubes (SACNTs) formed from MWCNTs, shown in Figure 6.4(a). Since nanometer-thick ribbons of MWCNTs joined end-to-end can be drawn directly from a SACNT array, a ~6–20 m$^2$ SACNT film can be drawn from a mere 0.01 m$^2$ SACNT array via a roll-to-roll technique that additionally joins the film to a PET substrate. This dry, high-yield process is in contrast with solution-processed SWCNT powders, in which large agglomerations are often filtered out and wasted to produce better quality films. At 24 Ω/sq. and 83.4% transmittance at 550 nm, these SACNT films possess excellent figures of merit. In addition, the SACNT/PET composite demonstrated reversible stretchability up to 60% strain, at which maximum the sheet resistance increased to

1.6 Ωsq. [346] Along similar lines, Liu et al. produced stretchable, semi-transparent conductors of alternating, cross-stacked SACNT films in PDMS and PVA (Figure 6.4(b)). SACNT films with 45° stacking alignment showed an increase in resistance of only 8% and SACNT/PDMS composite films with 45° stacking alignment showed an increase of 35% resistance under 30% strain. [211]

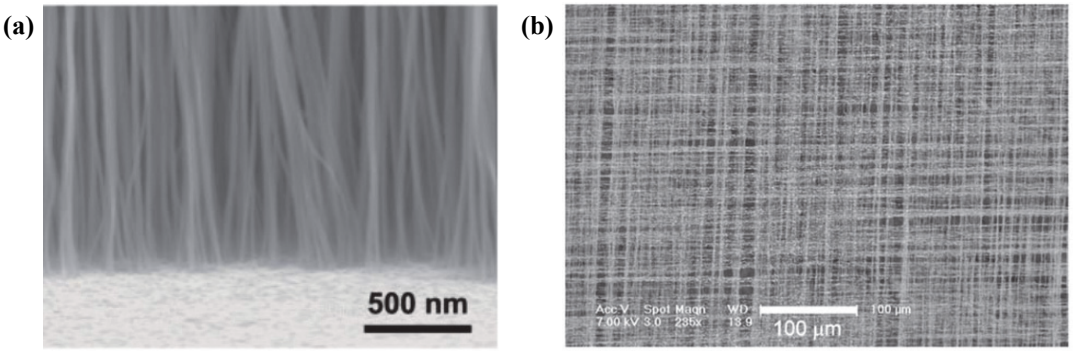


**Figure 6.4** **(a)** SEM profile of SACNT film on silicon wafer. [346] **(b)** SEM of a two-layer cross-stacked SACNT film. [211]

Another method employs the use of SWCNT aerogels, which are highly porous 3D networks of SWCNTs formed from drying SWCNTs dispersed in an aqueous elastic gel. Kim et al. backfilled SWCNT aerogels with PDMS to form a conducting, stretchable composite. Elastic conductors formed from a 3 $\mu$m-thick SWCNT aerogel had an initial conductivity of 83 S/cm and a transmittance of 93%. At a tensile strain of 100%, the elastic conductor resistance increased only slightly, by 14%. In addition, repeated cyclic stretching under 100% strain did not degrade the electrical conductivity of the SWCNT aerogel/PDMS composite. The maximum

reported tensile strain that the composite remained electrically conductive was 250%, which was limited by the deformability of the PDMS matrix. [210]

### 6.1.3 Opaque Compliant Conductor Architectures

#### 6.1.3.1 Microcracking

Freestanding metal thin films rupture at strains of only 1–2%, while a thin metal film bonded to an elastomeric substrate can remain conductive up to strains of about 50%. [347-349] The rupture of freestanding metal films under stretch is caused by strain localization at the weakest cross section, causing necking within the space available for local elongation. However, when adhered to an elastomer, this space is unavailable, preventing necking and allowing the polymer substrate to delocalize the strain field in the metal. [350-352] This results in strains over ten times that of freestanding metal thin films. However, once the metal film starts to debond from the substrate in one region, the strain localizes and the metal film begins to neck, propagate cracks, and rupture. [353-357] Larger strains can be achieved if the metal film is bonded more strongly to the elastomeric substrate, in which case the substrate can delocalize the stress, spreading it over a larger area. Thus, improving the adhesion of film to substrate can be a critical component in stretchable thin film metallization of elastomeric substrates. [358]

Attempts have been made to improve the adhesion between metal and polymer by utilizing adhesion layers. PET substrates were coated with an acrylic primer before depositing evaporated silver. Using a tensile test machine, the

resulting Ag/PET films could be stretched beyond even 70% without fracture of the Ag layer. Once failure does occur, the mechanism is believed to be similar to that of a ductile metal film on an elastomer, wherein metal film debonding coevolves with strain localization. [358] Figure 6.5 depicts this mechanism via cross-sectional SEM. Other researchers have improved the adhesion of Ti/Au electrode arrays to PDMS by utilizing an intermediate parylene layer in order to prevent microcracking. [359]

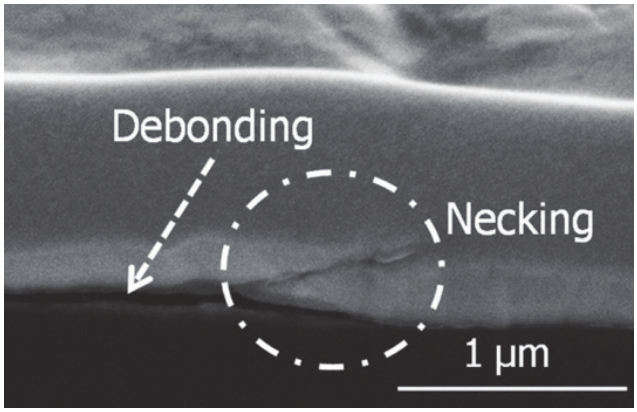


**Figure 6.5** Strain localization resulting in necking and crack propagation in the metallic film layer, accompanying debonding from the polymer substrate. [358]

Alternately, rather than suppress the formation of microcracks, some have realized that microcracking can actually aid in the stretchability of metal thin films on elastomers, without drastically decreasing conductivity within a certain operational range. Texturing and adhesion layers are still useful in achieving even higher strains by preventing crack propagation, but may be unnecessary if only small strains are required. During elongation of a PDMS substrate, disconnected tribranched ("Y"-shaped) microcracks will form, whose lobes can twist and deflect

out of plane. Because little to no plastic deformation occurs in this process, conductivity is unaltered below ~32%. Hence, although counterintuitive, a large applied elongation can produce only a small elastic strain in the metal thin film, leading to reliable conductivity over many cycles. [349] Microcracks may also form spontaneously when evaporating metals on relaxed substrates, detailed in the next section. [360]

For evaporated metals on smooth PDMS substrates, electrical conduction is still possible even after 1,000 cycles at 20% strain. After 1,000 cycles, cracks are free to propagate to the point where the metal surface resembles a network of touching islands that are still able to form a continuous conducting path. Rather than become more separated upon uniaxial loading, the islands can actually remain in contact as Poisson stresses compress the islands together in the transverse direction. The islands are capable of reversibly moving in this fashion, allowing up to 250,000 cycles at 20% strain without loss of electrical continuity. That said, while resistance is ~$3R_0$ at 20% strain below 1,000 cycles, above this the resistance at 20% strain increases to ~$10R_0$. [215] Although Robinson et al. did not test past 1,000 cycles, due to the lower percentage of cracking it is implied that microstructuring the surface might result in higher conductances beyond 1,000 cycles compared to a flat elastomer surface.

In addition, microcracking of nanoporous gold embedded in silicone elastomers leads to a significant reduction in elastic modulus while still retaining electrical conductivity. When $Au_{35}Ag_{65}$ white gold leaf is dissolved in nitric acid, the

Au atoms rearrange and solidify into a porous network, which is then placed atop a carrier wafer coated with photoresist as a release layer. PDMS then is spun coat atop the nanoporous gold film, allowing the Au to mechanically interlock with the elastomer by penetrating its nanoscale pores. Because of this interlocking, the gold demonstrates excellent adhesion with the PDMS. When stretched, the gold layer cracks, leading to an elastic modulus on the order of the elastomer. The resulting resistivity varies from only ~$1 \times 10^{-6}$ to ~$3 \times 10^{-5}$ Ω-m when elongated to ~25% strain. [217]

#### 6.1.3.2 Buckled Metallic Thin Films

Buckling has been researched as an alternative to microcracking for stretchable metal thin films. In this regime, a wave-like, folded surface morphology allows for mechanical elongation without the formation of cracks. Some of these patterns are isotropic, allowing area expansions, while other corrugated topologies offer anisotropic stretchability, along a preferred direction. Buckling surface architectures can be manufactured thermally, mechanically, or via corrugated surface patterning. Several different fabrication techniques have been developed that take advantage of the mismatch of the thermal expansion coefficients of metal and elastomer in order to form buckled metal thin films on relaxed elastomer substrates. Other methods first mechanically prestretch the substrate in one or two directions, deposit the metal, and then relax the substrate. Finally, corrugated

substrate topologies can be patterned via photolithographically-etched molds, then sputtered with an evaporated metal to form a thin film.

#### *6.1.3.2.1 Buckling on Relaxed Substrates*

Lacour et al. made stretchable, buckled interconnects by exploiting the built-in compressive thin films of gold evaporated via electron beam onto room-temperature elastomeric membranes of PDMS. The conductors consisted of roughly 1 mm-thick strips of PDMS topped with 100 nm × 250 $\mu$m gold strips and a 5 nm-wide adhesive interlayer of chromium. Compressive stress in the gold films causes spontaneous wrinkling, which can shrink the total length of the conductors by several tenths of one percent. The compressive stress in the film is thought to be the result of built-in stress, as well as thermal expansion mismatch. This conductor exhibited a linear increase in resistance below ~8%, in which small cracks form at the edges perpendicular to the stretch direction. Above 15% transverse strain, the cracks begin to propagate and cause film rupture. [361]

It is important to note that the evaporation of metals on smooth, relaxed elastomeric substrates at room temperature results in the spontaneous formation of either a buckled structure or of a microcracked structure, and that the precise factors deciding which structure dominates are not fully understood. [360] Figure 6.6 shows the microstructure and nanostructure of the two possible species: a spontaneously-buckled surface with no microcracking, or an unbuckled surface with microcracking. Additionally, the spontaneous buckling structure can also look like

that depicted in Figure 6.7(a), although the structure in that micrograph was produced by slightly different means.

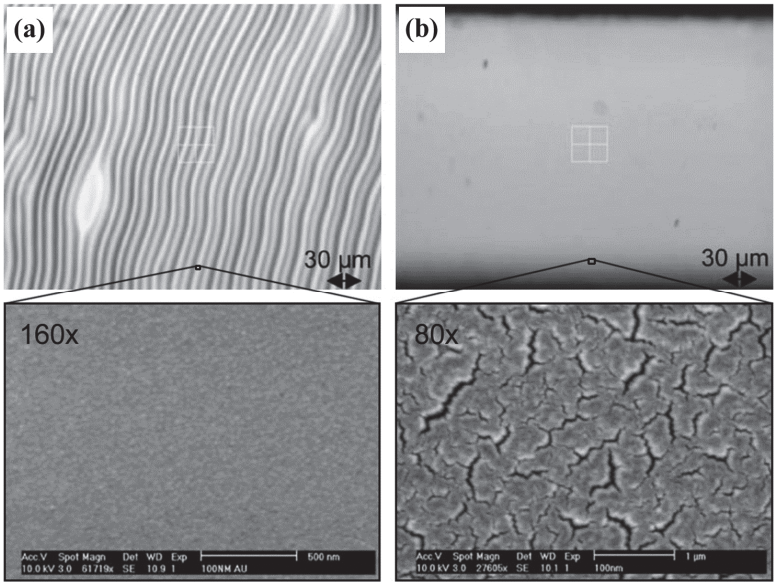


**Figure 6.6** The two types of specimens possible when depositing Au on room-temperature, relaxed, smooth PDMS. Optical micrographs shown above, with corresponding SEM micrographs below. **(a)** Buckled architecture with no microcracking, and **(b)** Smooth surface but with microcracking. [360]

Specifically, in this case the silicone substrate is first heated, then deposited with a metal thin film; buckles in the film form once the substrate cools to room temperature. Bowden et al. demonstrated this when depositing Ti or Cr followed by Au on a PDMS substrate heated to roughly 110°C; following cooling, a surface pattern like the ridges and fissures (gyri and sulci) of the brain developed (Figure 6.7). When the silicone cools, the gold layer compresses due to the larger coefficient of thermal expansion of the PDMS, causing buckling. An isotropic tessellation-like

pattern results on a smooth PDMS surface, while different wave patterns are possible depending on the boundary conditions applied by prefabricated surface features, such as rectangular ridges and pillars. [362, 363]

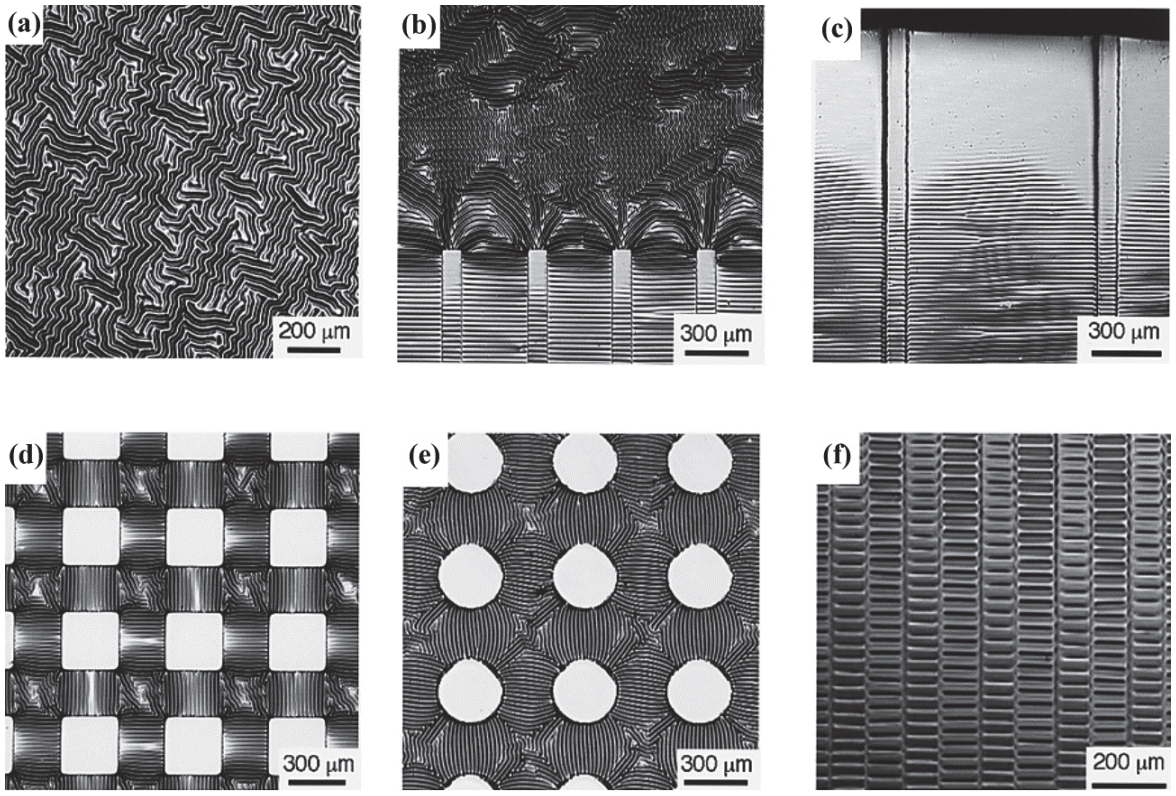


**Figure 6.7** Optical micrographs of the buckled, "wavy" surface morphology formed by evaporating metals onto heated (~110°C) PDMS, then allowing to cool to room temperature. Buckled topologies with **(a)** initially flat PDMS, **(b)** PDMS showing a wave transition with rectangular ridges (100 $\mu$m wide, 10–20 $\mu$m high, separated by 200 $\mu$m), **(c)** PDMS with the same rectangular ridges, separated by 800 $\mu$m, **(d)** PDMS with square pillars, 300 $\mu$m on each side, elevated by 10–20 $\mu$m, **(e)** PDMS with circular pillars, 150 $\mu$m radius, elevated by 10–20 $\mu$m, and **(f)** rectangular ridges as in (c) with 100 $\mu$m spacing. PDMS was coated with 5 nm of Cr or Ti, followed by 50 nm of Au. [362]

#### *6.1.3.2.2 Buckling on Prestretched Substrates*

While the preferred formation of buckles over microcracks on relaxed substrates is not well-understood, buckles can be reliably manufactured using mechanical prestretch. Higher functional strains are possible when buckling metal thin films are created from prestretching a PDMS substrate, depositing an evaporated metal, and then relaxing the film. The elastomer is typically prestretched uniaxially by 10 to 25%. Upon relaxation from prestretch, the deposited metal forms buckles since it experiences compression from the contracting substrate (Figure 6.8). Buckling is even observed in brittle semiconductors and metals, as thin films of these materials behave differently than in bulk. For anisotropically-prestrained films, stretching and relaxing the substrate can be performed uniaxially, in the prestretch direction, without altering the electronic properties of the metal thin film. For gold deposited on PDMS prestrained to ~15%, the highest strain achieved before electrical failure was 100%. [364] Similarly, Jones et al. have made buckled electrodes by depositing Cr then Au onto a 25% prestrained PDMS substrate. The stretchable conductor remains electrically conductive up to 100% strain and maintains low electrical resistance (< 100 Ω) under repeated mechanical deformation. [218] While functional strains beyond the prestrain are possible, strains well beyond the prestrain of the substrate are typically not reliable. For example, Wagner et al. found that for prestretched, buckled metal films, resistance actually decreases with increasing strain up to ~25%, which is beyond the value of the prestretch (15%). However, above ~25%

strain, the resistance becomes infinite, suggesting the rupture of the gold thin film. [360]

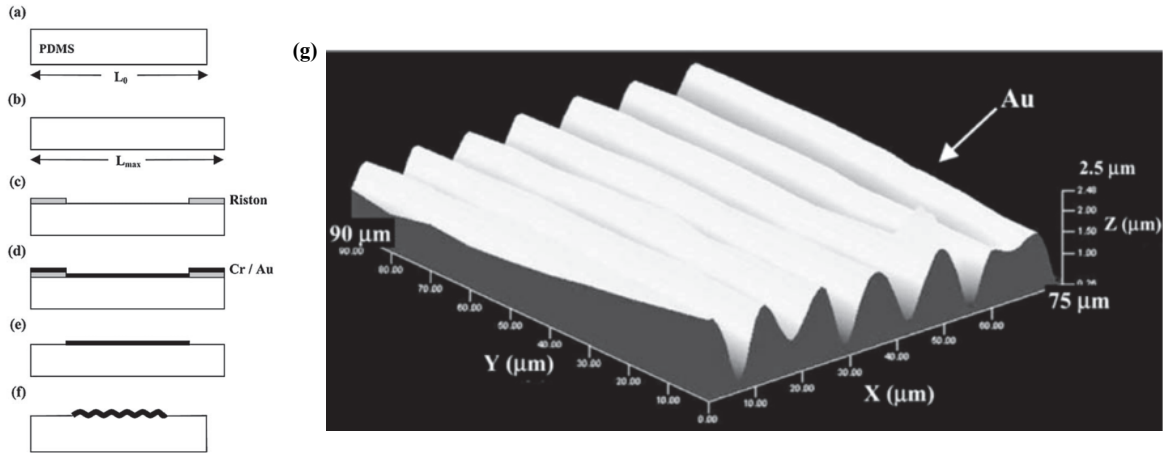


**Figure 6.8** Fabrication steps involved in the formation of a buckled Au electrode structure by prestretching the PDMS substrate. **(a)** The PDMS substrate first at the initial length $L_0$, **(b**) is then stretched to $L_{max}$, **(c)** a Riston photoresist mask is deposited, **(d)** followed by the evaporated metal films. **(e)** Lift-off removes the mask and excess metal, and **(f)** the substrate is relaxed to form a buckled structure, **(g)** whose structure is shown via optical microscopy. [364]

Fabrication of metal thin films with buckled architectures can be an expensive process, usually requiring costly metal evaporation technologies and other microfabrication techniques. Moreover, these stretchable conductors are capable of strains mostly below ~70% due to delamination of metal from substrate. In a cost-effective alternative, Wang et al. proposed a novel solution-processing approach to fabricate stretchable conductors capable of tensile strains larger than 300% and stable metallic conductivities of $1 \times 10^5$ S/cm. By adding a silicone

polyelectrolyte nanoplatform layer to the surface of a silicone elastomer, the subsequent deposition of a metal could be performed via solution-processing, and much greater adhesion between metal and elastomer could also be achieved for high strains. Specifically, the surface of a PDMS elastomer is oxygen plasma treated and functionalized, and a 30 nm-thick layer of poly(2-(methacryloyloxy)ethyltrimethylammonium chloride) (PMETAC) is grown on the surface via surface-initiated atom transfer radical polymerization (SI-ATRP). Following additional steps, the PDMS is prestretched by 30% and then immersed in a copper electroless deposition (ELD) bath to form the top Cu layer. After relaxation, buckles form on the surface. Thus, the addition of a specialized intermediate layer can improve both the performance and the manufacturing cost of buckled metallic interconnect technology. [219]

In addition, metals need not be the only material under study for the formation of opaque buckled conductors. Dense, 2D networks— or "macrofilms"— of SWCNTs have been investigated as a buckled electrode in stretchable supercapacitors. To form such a stretchable architecture, a PDMS substrate is prestrained, UV-treated to render the surface hydrophilic, laminated to an OH-group-rich SWCNT macrofilm to form –C–O–Si– crosslinks, and then relaxed to form a buckled, wavy surface topology. Under tensile testing, the resistance remains unchanged up to the prestrain (40%), and even up to 60% tensile strain. This is because the SWCNT overlap length remains unchanged during stretching up to these strains, in which the buckling wavelength merely increases under

stretch. Within the prestrain range, this process can be repeated through many cycles, similar to the contraction and expansion of an accordion bellows. [365] Similar structures that are additionally transparent will be discussed in the following Buckled CNT Ribbons section.

### 6.1.4 Transparent Compliant Conductor Architectures

#### 6.1.4.1 Ultrathin Metal Films

Interestingly, metallic thin films can be rendered transparent if the metal is made sufficiently thin, namely, less than 10 nanometers in thickness. In a recent report, Leosson et al. demonstrated a 75% transmittance at 530 nm for a 4.2 nm-thick metal film of gold. The same metal film had a sheet resistance of only 86 Ω/sq. [221] By comparison, thin films of Au on PDMS are typically greater than 25 nm thick— often 100 to 500 nm thick— and sometimes additionally utilize one or two 5 nm-thick layers of Cr to improve bonding. [349, 351, 361, 364, 366] The transparent ultrathin metal thin film (UTMF) was fabricated using standard vacuum electron beam deposition methods without the need for seeding layers.

In another study, Ghosh et al. created transparent electrodes of Ni and Cr that were 2–10 nm-thick via DC sputtering on UV grade silica and silicon substrates. [367] Their Ni films showed the best performance, with visible transmittance of ~65% and a sheet resistance of ~120 Ω/sq. for 5 nm-thick Ni; these metrics are almost as high as those for Au of the same thickness as shown by Leosson. In general, the Ni films of Ghosh et al. showed a visible transmittance of

~40–80% and a sheet resistance of 30–1200 Ω/sq. There does appear to be a limitation to this approach: Resistivity sharply increases with decreasing film thickness below 20 nm due to the nanoscale effects of surface and grain boundary scattering becoming more pronounced. [368, 369] Nevertheless, these effects may be counteracted by utilizing high conductivity metals such as silver or gold in lieu of nickel or chromium.

To date, the exploration of UTMFs as a transparent electrode material has been confined to non-compliant contexts. For example, while silica, silicon, and transparent polymers such as Cyclotene and Ormoclear were used as substrates, elastomers like PDMS or softer were not. To our knowledge, the behavior of UTMFs as a stretchable or flexible electrode material lay largely unknown. Future research of interest may wish to explore deposition and cyclic testing of ultrathin Au and Ag on PDMS and other transparent elastomers. Other research may benefit from exploring the use of adhesion layers, surface texturing, and any of the other previously described methods to improve the performance of ultrathin metals as potential stretchable conductors.

#### 6.1.4.2 Buckled CNT Ribbons

Carbon nanotubes have traditionally been used as a transparent stretchable conductor when deposited on planar substrates. [115] However, creating continuous buckled ribbons of carbon nanotubes— and further sputtering them with conductors such as gold and palladium— offers much lower sheet resistances, lower increases

in sheet resistance with stretch, high stretchability, and transparency. Xu and coworkers created buckled CNT nanoribbons with a sheet resistance of 72 Ω/sq., capable of 100% strain and only a 4.1% change in sheet resistance. This is in contrast with SWCNTs deposited on a flat substrate, or even composites of aligned CNTs in PDMS, whose sheet resistance is typically > 200 Ω/sq. and has a higher increase in this resistance under the same stretch. To form these buckled CNT nanoribbons, they grew and spun CNT ribbons, aligned them on a Teflon film, sputtered the surface with a Au/Pd alloy, transferred to prestrained PDMS, and relaxed to form buckles. This method of transferring a material to prestrained PDMS to create buckles appears to be standard protocol for creating buckled nanoribbons of various materials. [211, 370] Figure 6.9 shows the buckled microstructure of this transparent stretchable conductor. [222]

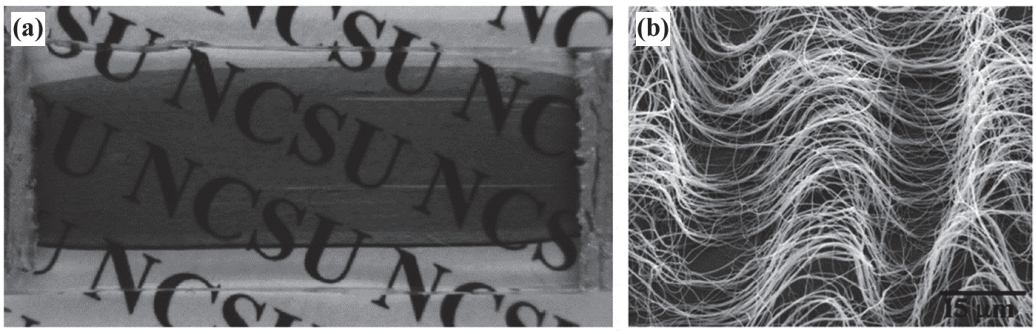


**Figure 6.9** **(a)** The optical macroscopic appearance of the PDMS/CNT nanoribbon composite is semi-transparent. **(b)** Scanning electron micrograph of the CNT nanoribbons reveals the buckling structure. [222]

In a similar effort, Lipomi et al. fabricated transparent conductors of buckled SWCNTs (2–3 $\mu$m in length) on PDMS. Their methods were perhaps slightly simpler than those of Xu since Lipomi spray-deposited the nanotubes in a solution of *N*-methylpyrrolidone directly onto the oxygen-plasma treated PDMS substrate. Lower resistance values were achieved following spin-coating with the charge-transfer dopant tetrafluoro-tetracyanoquinodimethane (F4-TCNQ) in chloroform. The PDMS substrate was then stretched biaxially and relaxed to form a buckled SWCNT morphology with isotropic electromechanical properties. The resulting stretchable conductors had a resistance of 328 Ω/sq., and a 550 nm transmittance of 79% at 0% strain. A maximum conductivity of 1,100 S/cm was obtained for a 100 nm film with 68% transmittance. A maximum reversible strain of 150% was achieved, with a corresponding conductivity of 2,200 S/cm. At double the conductivity in the stretched state than initially, this is notably different from most bulk conductors that experience the opposite effect. The authors attribute this phenomenon to increased CNT alignment in the current direction as a result of the stretch. Moreover, after 1,500 stretching cycles at 50% strain, the resistance of the conductor decreased by 22% before actually increasing again. It is speculated that during these stretching cycles, the nanotube bundles adopt their optimum buckling morphology and alignment, after which the conductive junctions between bundles begin to fracture. [283]

While the above method of prestraining is commonly employed to create buckles, it may pose scalability problems in large-scale manufacturing, such as with

roll-to-roll processing. As an alternative, "post-straining" can be utilized, whereby an already manufactured device is stretched, then released to form buckles. This "interface-mediated" buckling occurs when interfacial friction causes the deposited material to buckle upon relaxation rather than sliding back into its original, flat conformation. Aligned CNT ribbons were grown and deposited onto a PDMS substrate, which was then stretched to 80% and relaxed. Bundles of buckles form, evident in Figure 6.10. The exact mechanism of buckle formation remains to be researched. The resulting buckled CNT nanoribbons on PDMS exhibited optical transmittance of ~40%, stretchability greater than 100%, and unchanged resistance below 100% strain. [371]

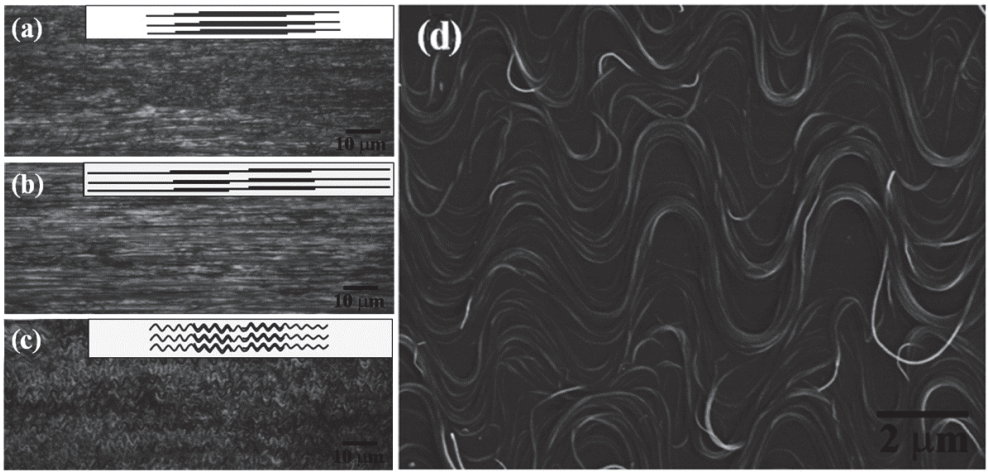


**Figure 6.10** Microstructure of CNT ribbons on PDMS during buckling procedure. Optical micrographs of a sample **(a)** unaltered, **(b)** stretched to 80%, then **(c)** relaxed to 0% strain to form buckles. **(d)** Scanning electron micrograph of the buckle structure from **(c)**. [371]

#### 6.1.4.3 Zigzag PEG/Ag Composites

This stretchable, transparent conductor consists of ~140 nm-thick zigzag ridges of a poly(ethylene oxide) (PEO or PEG) and Ag nanoparticle composite on PDMS, which was formed from a buckled template of polystyrene-coated PDMS (Figure 6.11(a)). Specifically, a PDMS substrate was biaxially prestrained, coated with polystyrene, and relaxed either biaxially (Figure 6.11(b)) or sequentially in each direction (Figure 6.11(c)) to form different types of buckling structures. The researchers do not specify the order of polystyrene deposition, but it seems likely that this deposition occurred after first prestraining the PDMS. The trenches of the resulting buckled template were then filled with UV-curable PEG-diacrylate and Ag trifluoroacetate nanoparticle precursor, and UV gelation and reduction formed the PEG-Ag composite conductor. The conducting composite lines were then transferred from the buckled template to another PDMS substrate with a surface modified with 3-(trichlorosilyl) propyl methacrylate, and further UV exposure bonded the PEG-Ag to the functionalized PDMS.

Composites with isotropic zigzag patterns experienced electrical failure at 23% strain, while the ordered anisotropic zigzag patterned samples could withstand strains up to 55%. Metallic percolation was achieved at a weight fraction of 67% Ag nanoparticles, at which the conductivity of the composite was ~$2 \times 10^6$ S/m. Remarkably, for strains less than 20%, this conductivity remained constant over 900 stretching cycles. Additionally, the composite exhibited a high transparency of ~70% in the visible spectrum from 400–800 nm. This unique transparent,

stretchable architecture may find application as a conductor in stretchable displays or light-emitting devices. [223]

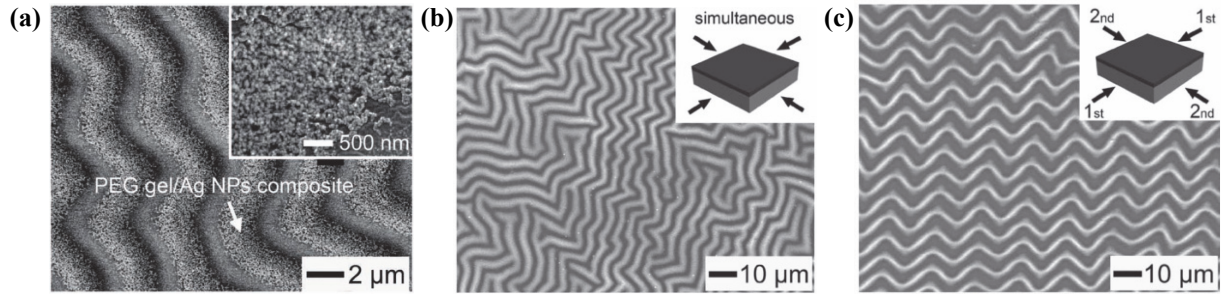


**Figure 6.11** **(a)** Scanning electron micrograph of the transparent, stretchable PEG-Ag nanoparticle composite conductor with a zigzag morphology. **(b)** Isotropic buckling pattern from simultaneous relaxation of the polystyrene-PDMS substrate. **(c)** Anisotropic buckling zigzag patterns from sequential relaxation, as shown in the inset. [223]

## 6.2 Derivation of Hoop Stress Equation

Throughout this dissertation, the so-called hoop stress equation has been utilized to convert the hydraulic pressure (stress) inside a flexible tube into the stress inside the wall of a prestretched DE membrane wrapped around this tube. The derivation is straightforward. Consider the free body diagram involving half of the hoop, as shown below in Figure 6.12.

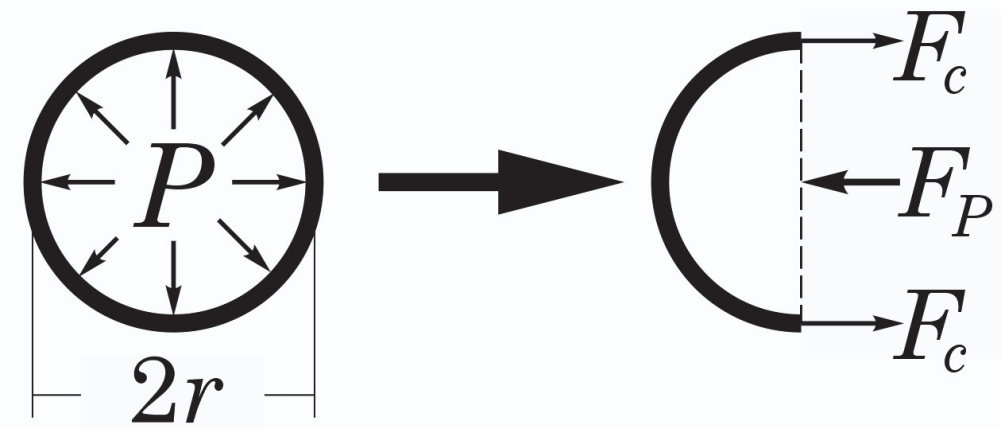


**Figure 6.12** A cross section of a tube with a DE membrane in tension at left can be represented by the free body diagram at right.

At equilibrium, the internal pressure $P$ exerts an equivalent force $F_P$ that balances the hoop stress forces $F_c$ in the wall of the DE:

$$F_P = 2F_c \tag{6.1}$$

By definition, pressure $P$ (or stress $\sigma$) equals force $F$ divided by the cross-sectional area $A$:

$$P = \frac{F_P}{A_P} \text{ and } \sigma_c = \frac{F_c}{A_c} \tag{6.2}$$

in which $P$ is the hydraulic pressure, $F_P$ is the force the hydraulic pressure exerts on the cross-sectional boundary area $A_P$ (dashed line in profile), $F_c$ is the force in the walls of the DE hoop acting on the cross-sectional area $A_c$. Equation 6.1 becomes

$$PA_P = 2\sigma_c A_c \tag{6.3}$$

The pressure acts on the cross-sectional boundary area indicated by the dashed line, which has area

$$A_P = 2rl \tag{6.4}$$

where $l$ is the length of tube over which the pressure $P$ acts. Likewise, the circumferential stress $\sigma_c$ acts on the cross-sectional area of the DE wall:

$$A_c = tl \tag{6.5}$$

where $t$ is the thickness of the wall. Substituting Equations 6.4 and 6.5 into Equation 6.3 gives

$$2lrP = 2l\sigma_c t \tag{6.6}$$

Eliminating $2l$ from both sides:

$$rP = \sigma_c t \tag{6.7}$$

This final equation can now be written as

$$P = \frac{\sigma_c t}{r} \text{ or } \sigma_c = \frac{Pr}{t} \tag{6.8}$$

This equation is useful only for thin-walled cases, where $t$ is thin. This equation proved useful in this research since the thin film DE membranes under study had

almost negligible thicknesses. In cases where the wall thickness is not negligible, calculus can be utilized in the so-called Lamé equation to describe the stress distribution in the thick walls of pressure vessels. [372]

## 6.3 Derivation of Catenary Equation

In Chapter 4, Section 4.3.3.2, Equation 4.16 was presented to model the outline of the freely-hanging DE edge between rigid elements on the DEB, which is known as a catenary. This then allowed a prediction to be made regarding the maximum amount of transverse prestretch that would be lost (at the center of the catenary) as a function of spacing between rigid elements. This equation was derived as a function of the stretches and other relevant geometric parameters as follows.

Let the discussion first start with considering the decaying exponential

$$y_1(x) = C_0 \exp(-bx) + a \tag{6.9}$$

as shown in Figure 6.13. $a$ is assumed to be proportional to the initial DE length $l_0$:

$$a = Al_0 \tag{6.10}$$

where $A$ is a constant. Since the transverse stretch $\lambda_t$ equals the final transverse length $l_{t,f}$ divided by the initial length $l_0$, or

$$\lambda_t = \frac{l_{t,f}}{l_0} \tag{6.11}$$

then (6.10) is also

$$a = A\frac{l_{t,f}}{\lambda_t} \tag{6.12}$$

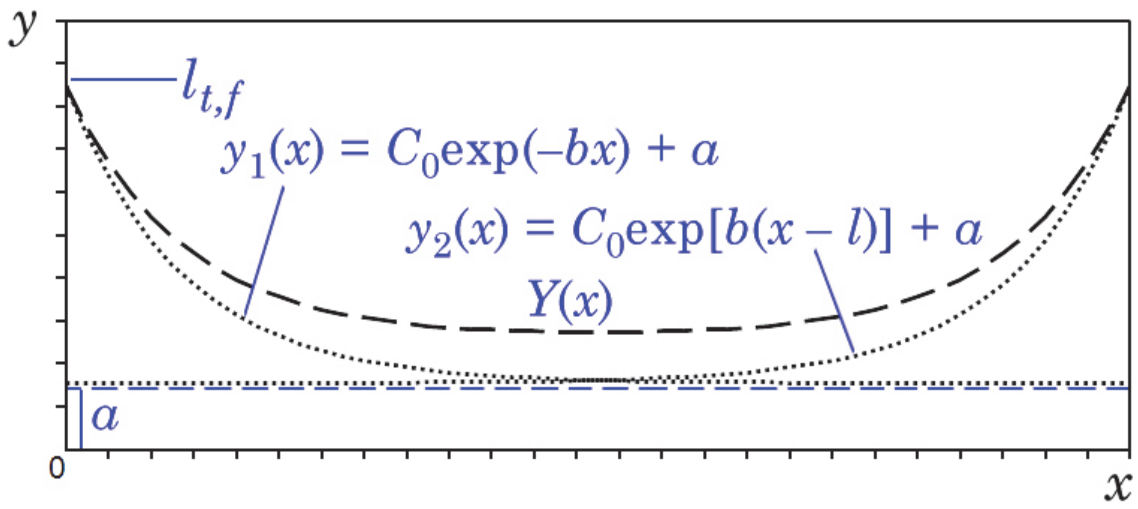


**Figure 6.13** Exponential functions $y_1(x)$ and $y_2(x)$ plotted as dotted lines. They are shifted up from the origin by a constant value $a$, and $y = a$ is the asymptote shown as the blue dashed line. $l_{t,f}$ is defined as $y$-intercept of $y_1$, and $Y(x)$ is the final Equation 6.32.

Next, the pre-exponential $C_0$ is defined as the $y$-intercept of $y$ since

$$y(0) = C_0 \exp(0) = C_0 \tag{6.13}$$

This applies to the decaying exponential where $a = 0$. So,

$$C_0 \propto l_f - l_0 \tag{6.14}$$

in which the actual exponential has a $y$-intercept of $l_f$, but the $C_0$ here is defined only when $a = 0$. Thus, $a$ is subtracted as $l_0$ since $a \propto l_0$. By Equation 6.11,

$$C_0 = B(l_f - l_0) = B(\lambda_t l_0 - l_0) = Bl_0(\lambda_t - 1) \tag{6.15}$$

Regarding $b$ in Equation 6.9, the observation was made that the slope at $x = 0$ is proportional to the ratio of the final transverse length $l_{t,f}$ to the final circumferential length $l_{c,f}$, or

$$\left.\frac{dy_1}{dx}\right|_{x=0} \propto \frac{l_{t,f}}{l_{c,f}} \tag{6.16}$$

This is equivalent to

$$-C_0 b \exp(0) = C\frac{l_{t,f}}{l_{c,f}} \tag{6.17}$$

where $C$ is an arbitrary constant. Then, from Equations 6.15 and 6.11,

$$b = -\frac{C}{C_0}\frac{l_{t,f}}{l_{c,f}} = -\frac{C}{B\frac{\cancel{l_{t,f}}}{\lambda_t}(\lambda_t - 1)}\frac{\cancel{l_{t,f}}}{l_0\lambda_c} = -\frac{C\lambda_t}{Bl_0\lambda_c(\lambda_t - 1)} \tag{6.18}$$

From determining $C_0$, $b$ and $a$, Equation 6.9 becomes

$$y_1(x) = Bl_0(\lambda_t - 1)\exp\left(-\frac{C\lambda_t}{Bl_0\lambda_c(\lambda_t - 1)}x\right) + Al_0 \tag{6.19}$$

From fitting to empirical data, it was determined that $A = B = C = 1$, so the above becomes

$$y_1(x) = l_0(\lambda_t - 1)\exp\left(-\frac{\lambda_t}{l_0\lambda_c(\lambda_t - 1)}x\right) + l_0 \tag{6.20}$$

It can be easily seen, then, that the exponential $y_2$ going the other direction in Figure 6.13 can be written as

$$y_2(x) = l_0(\lambda_t - 1)\exp\left[\frac{\lambda_t}{l_0\lambda_c(\lambda_t - 1)}(x - l)\right] + l_0 \tag{6.21}$$

At this point, it was observed that the desired function $Y(x)$ involves the sum of $y_1$ and $y_2$, with some vertical shifting necessary. Specifically, it was seen that

$$Y(x) = \frac{y_1(0)}{y_1(0) + y_2(0)}\left[y_1(x) + y_2(x)\right] \tag{6.22}$$

This is because

$$Y(0) = \frac{y_1(0)}{\cancel{y_1(0) + y_2(0)}}\cancel{\left[y_1(0) + y_2(0)\right]} = y_1(0) \tag{6.23}$$

where $y_1(0)$ is the $y_1$-intercept. This means that Equation 6.22 will shift $Y(x)$ down so that $Y(0)$ coincides with $y_1(0)$ as desired. From Equation 6.20,

$$y_1(0) = l_0(\lambda_t - 1)\exp(0) + l_0 = l_0(\lambda_t - 1) + l_0 = l_0\lambda_t - l_0 + l_0 = l_0\lambda_t = l_{t,f} \tag{6.24}$$

And from Equation 6.21,

$$y_2(0) = l_0(\lambda_t - 1)\exp\left[-\frac{\lambda_t l}{l_0\lambda_c(\lambda_t - 1)}\right] + l_0 \tag{6.25}$$

Substituting Equations 6.24, 6.25, and 6.11 into Equation 6.22 gives

$$Y(x) = \frac{l_{t,f}\left[y_1(x) + y_2(x)\right]}{l_{t,f} + \frac{l_{t,f}}{\lambda_t}(\lambda_t - 1)\exp\left[-\frac{\lambda_t l}{l_0\lambda_c(\lambda_t - 1)}\right] + \frac{l_{t,f}}{\lambda_t}} \tag{6.26}$$

and simplifying yields

$$Y(x) = \frac{y_1(x) + y_2(x)}{1 + \frac{\lambda_t - 1}{\lambda_t}\exp\left[-\frac{\lambda_t l}{l_0\lambda_c(\lambda_t - 1)}\right] + \frac{1}{\lambda_t}} \tag{6.27}$$

Finally, evaluating the numerator of Equation 6.27 is simplified by the following variable substitutions:

$$\text{Let } Q = l_0(\lambda_t - 1),\ R = \frac{\lambda_t}{l_0\lambda_c(\lambda_t - 1)},\ \text{and } S = l_0 \tag{6.28}$$

Then we have

$$y_1(x)+y_2(x)=\left[Q\exp(-Rx)+S\right]+\left\{Q\exp\left[R(x-l)\right]+S\right\} \tag{6.29}$$

which simplifies to

$$y_1(x)+y_2(x)=2S+Q\left\{\exp(-Rx)+\exp\left[R(x-l)\right]\right\} \tag{6.30}$$

or

$$y_1(x)+y_2(x)=2l_0+l_0(\lambda_t-1)\left\{\exp\left(-\frac{\lambda_t x}{l_0\lambda_c(\lambda_t-1)}\right)+\exp\left[\frac{\lambda_t(x-l)}{l_0\lambda_c(\lambda_t-1)}\right]\right\} \tag{6.31}$$

Substituting Equation 6.31 into Equation 6.27 gives the final form

$$Y(x)=\frac{2l_0+l_0(\lambda_t-1)\left\{\exp\left[-\frac{\lambda_t x}{l_0\lambda_c(\lambda_t-1)}\right]+\exp\left[\frac{\lambda_t(x-l)}{l_0\lambda_c(\lambda_t-1)}\right]\right\}}{1+\frac{\lambda_t-1}{\lambda_t}\exp\left[-\frac{\lambda_t l}{l_0\lambda_c(\lambda_t-1)}\right]+\frac{1}{\lambda_t}},\ l_0=\frac{l_{t,f}}{\lambda_t} \tag{6.32}$$

As a footnote, catenary functions are typically written in terms of the hyperbolic cosine, in which

$$\cosh(x)=\frac{\exp(-x)+\exp(x)}{2} \tag{6.33}$$

Equation 6.32 is similar, primarily involving the sum of two exponential functions, one decaying and one growing. Equation 6.32 could potentially be re-written in terms of cosh($x$), but its current form may better suit the geometric parameters of interest.

## 6.4 Sample MATLAB® Code

### 6.4.1 Data Processing for Figure 2.6 in Chapter 2

The following simple code was used to process the data for declogging Figure 2.6. The experimental data was imported into the workspace, and the code removed some background noise and exported a plot as an EPS file. This file was then imported into Photoshop at roughly 1200 dpi and completed:

```
% Convert the imported data "Declog" from Pa to psi and rename:
Declog_psi(:,2) = Declog(:,2).*0.000145037738;
Declog_psi(:,1) = Declog(:,1);

% Apply some smoothing to remove high frequency noise, and plot the figure:
plot(Declog_psi(:,1),smooth(Declog_psi(:,2),5),'k')

% Format the plot:
axis([0 650 0 14])
grid off;
set(gca, 'FontName', 'Arial Narrow','Box','off','TickDir','out',...
    'TickLength',[.02 .02],'XMinorTick','on','YMinorTick','on','XColor'...
    ,[0 0 0],'YColor',[0 0 0],'LineWidth',1);

% Print the above plot to an EPS file for completion in Photoshop:
set(gcf, 'PaperPositionMode', 'auto');
print -depsc2 Declog.eps
```

### 6.4.2 Data Processing for Chapter 3

#### 6.4.2.1 Data Processing of *P-Q* Data

The following code opens all the LabVIEW™ measurement files (*.lvm) in the current directory as variables with the same names as the file names. Then, one of these files is set to 'A' and plotted. From this plot, 12 *x*-coordinate (time) values are extracted manually using the Data Cursor tool in the Figure window, specifically those shown in Figure 6.14. Once the 'x' vector is built, 4 seconds (400 samples at

100 Hz) are added to x(1), and the mean is evaluated for all pressure values from the one corresponding to x(1) to that corresponding to the time point 1 second later. This gives the fast-forward (FF) value used later for baseline drifting in Excel, which is placed in the first row and first column of the P matrix. Next, 10 seconds (1,000 samples at 100 Hz) are added to x(2), and the average is taken of all corresponding pressure values from this time point to a time point 2 seconds later. This gives the pressure actuation drop at 400 V. This is then repeated for the remaining 10 pressure drops from x(3) through x(12). The 11 pressure drop values are placed in the second column of P. Finally, 4 s are subtracted from x(2) through x(12), and the corresponding pressure values from 4 s back to the first time point are averaged. This gives the 0 V baseline values before each actuation drop, which are used in Excel to correct for creep.

P is then copied to Excel. The first value in the third column of P is used as the first 0 V point, and column 2, rows 2 through 11 are used for the remaining actuation drop values. Next, each value from column 3, rows 2 through 11 are subtracted from the first entry in column 3. This calculates 11 unique drift values, which are then added to each entry in column 2. Lastly, the difference was taken between each FF average value and the highest FF value at 400 mL/hr. These differences were added to all data points to shift the baselines into alignment; the highest FF value, which happens to be at 400 mL/hr, was used to ensure all values are above 0. The 9 processed trials were then averaged and plotted in Figure 3.8 and Figure 3.10:

```
% Open all *.lvm files in the current directory as variables:
files = dir('*.lvm');
for i=1:length(files)
    eval(['load ' files(i).name ' -ascii']);
end

% Specify file to analyze. Change file name to open the next plot:
A=A_200_2;
plot(A(:,1),A(:,2));

% Input extracted values from the graph here. Change x for each graph:
x=[9.06 44.14 74.15 104.1 134.2 164.4 194.2 224.2 254.2 284.4 314.1 344];

clear P;  P=zeros(length(x)-1,3);
for i=1:(length(x)-1)
    % Extract the FF baseline from x(1):
    P(1,1)=mean(A((find(A==x(1))+400):(find(A==x(1))+500),2));
    % Extract P drops at 0.4 to 2.4 kV from x(2) to x(12):
    P(i,2)=mean(A((find(A==x(i+1))+1000):(find(A==x(i+1))+1200),2));
    % Extract P baselines at 0 V before all 11 actuation P drops:
    P(i,3)=mean(A((find(A==x(i+1))-400):find(A==x(i+1)),2));
end
```

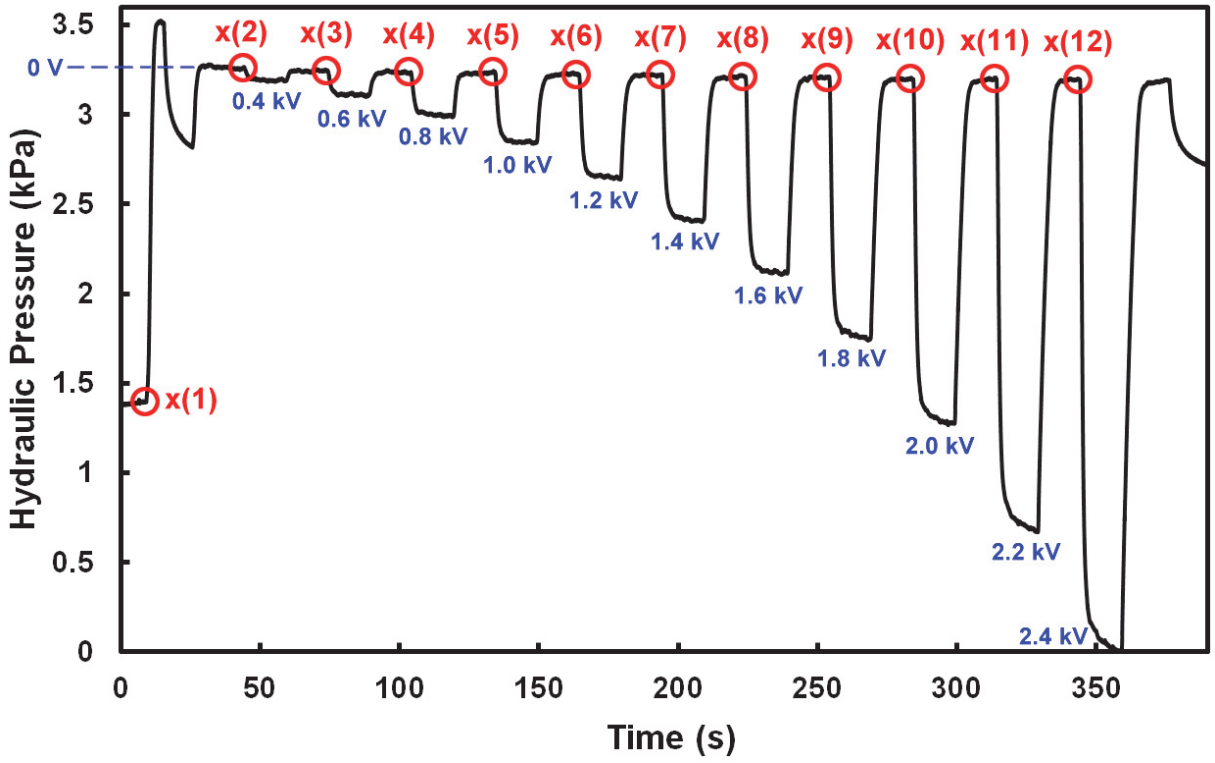


**Figure 6.14** Uncropped version of Figure 3.7 highlighting the data points manually extracted from each data plot using the Data Cursor tool in the MATLAB® Figure window. These points were then used to extract the pressure data that were exported to Excel for baseline shifting and plotting.

### 6.4.2.2 Reliability Data Processing

The following code can be divided into three parts: (i) cropping, stitching together, and aligning all trial segments, (ii) Performing simple statistics to determine any change in performance, and (iii) Using filtering to eliminate any low frequency noise and make the baseline flat. Processing was performed for both the 600 V and 2200 V trials simultaneously. This first part of code performs the processing depicted in Figure 6.15(a) and (b):

```
% Open all *.lvm files in the current directory as variables:
files = dir('*.lvm');
for i=1:length(files)
    eval(['load ' files(i).name ' -ascii']);
end


%%%%   Baseline Shifting:   %%%%

% Clear variables utilized below from memory:
clear a a2 x x2 r r2 rr2 A A2 M M2 R R2 RR RR2 i j k;

% Assign opened data matrices to cell arrays A (for 600 V) and A2 (2200 V):
A{1}=R1_100_600V_1;                 A{2}=R1_100_600V_2;
A{3}=R1_100_600V_3;                 A{4}=R1_100_600V_4;
A{5}=R1_100_600V_5;                 A{6}=R1_100_600V_6;
A{7}=R1_100_600V_7;                 A{8}=R1_100_600V_8;
A{9}=R1_100_600V_9;                 A{10}=R1_100_600V_10;

A2{1}=R1_400_2200V_1;               A2{2}=R1_400_2200V_2;
A2{3}=R1_400_2200V_3;               A2{4}=R1_400_2200V_4;
A2{5}=R1_400_2200V_5;               A2{6}=R1_400_2200V_6;
A2{7}=R1_400_2200V_7;               A2{8}=R1_400_2200V_8;
A2{9}=R1_400_2200V_9;               A2{10}=R1_400_2200V_10;
A2{11}=R1_400_2200V_11;             A2{12}=R1_400_2200V_12;
A2{13}=R1_400_2200V_13;             A2{14}=R1_400_2200V_14;
A2{15}=R1_400_2200V_15;             A2{16}=R1_400_2200V_16;
A2{17}=R1_400_2200V_17;             A2{18}=R1_400_2200V_18;
A2{19}=R1_400_2200V_19;             A2{20}=R1_400_2200V_20;
A2{21}=R1_400_2200V_21;             A2{22}=R1_400_2200V_22;
A2{23}=R1_400_2200V_23;             A2{24}=R1_400_2200V_24;
A2{25}=R1_400_2200V_25;             A2{26}=R1_400_2200V_26;
A2{27}=R1_400_2200V_27;             A2{28}=R1_400_2200V_28;
A2{29}=R1_400_2200V_29;             A2{30}=R1_400_2200V_30;
A2{31}=R1_400_2200V_31;             A2{32}=R1_400_2200V_32;
A2{33}=R1_400_2200V_33;             A2{34}=R1_400_2200V_34;
A2{35}=R1_400_2200V_35;             A2{36}=R1_400_2200V_36;
A2{37}=R1_400_2200V_37;             A2{38}=R1_400_2200V_38;
A2{39}=R1_400_2200V_39;             A2{40}=R1_400_2200V_40;
A2{41}=R1_400_2200V_41;

% x values are left and right x bounds of the desired data, from both 600 V
% (x) and 2200 V (x2) tests:
x=[278.2 2369 61.02 2141 41.22 2161 61.26 2141 61.06 2181 0.02 2059 ...
    0.02 2079 41.21 2101 71.04 2191 41.12 2171];
x2=[20.14 380.8 40.85 550.7 30.88 530.7 30.82 530.7 30.82 500.7 40.84 ...
    530.8 30.82 420.7 30.81 520.7 30.85 540.8 30.83 510.8 20.81 530.8 ...
    30.86 530.7 30.85 540.7 30.83 540.8 40.81 540.7 40.81 550.7 30.82 ...
    540.8 30.8 550.7 30.81 540.8 30.84 550.8 30.85 540.7 40.83 540.7 ...
    30.83 540.7 30.83 540.7 30.87 530.7 30.8 540.7 40.83 540.7 30.85 ...
    530.7 30.89 530.7 50.82 550.7 40.85 550.7 60.86 560.8 50.82 570.7 ...
    30.85 550.7 50.82 550.7 50.85 580.7 40.83 540.7 30.8 500.7 30.83 ...
    540.7 30.83 500.7 40.83 460.7];
```

```
% Preallocate variables, matrices, and cell arrays used in the following
% loop for the 600 V test:
j=1; k=0;
a=cell(1,(length(x))/2); M=zeros(1,(length(x))/2-1);
r=[]; rr=[];

for i=1:((length(x))/2)
    % Extract data from A per the endpoints in x and store to a:
    a{i}=A{i}(find(A{i}==x(j)):find(A{i}==x(j+1)),2);
    j=j+2;

    % Find baseline shift values by subtracting segment mean from 1st mean:
    M(k+1)=mean(a{1})-mean(a{k+1});
    k=k+1;

    % Shift all baselines into alignment (divided trials from syringe
    % changes):
    r=[r; a{i}+M(i)];

    % Build rr with non-shifted baselines for comparison:
    rr=[rr; a{i}];
end

% 2200 V test:
j=1; k=0;
a2=cell(1,(length(x2))/2); M2=zeros(1,(length(x2))/2-1);
r2=[]; rr2=[];

for i=1:((length(x2))/2)
    a2{i}=A2{i}(find(A2{i}==x2(j)):find(A2{i}==x2(j+1)),2);
    M2(k+1)=mean(a2{1})-mean(a2{k+1});
    j=j+2;
    k=k+1;
    r2=[r2; a2{i}+M2(i)];
    rr2=[rr2; a2{i}];
end

% Build R, remapping the time in column 1 and assigning r to column 2;
% repeat for R2 as well:
R(:,2)=r;
R2(:,2)=r2;
R(:,1)=0:(length(R(:,2))-1);
R2(:,1)=0:(length(R2(:,2))-1);
R(:,1)=R(:,1)*0.01;
R2(:,1)=R2(:,1)*0.01;

% Build RR and RR2 with non-shifted baselines:
RR(:,2)=rr;
RR2(:,2)=rr2;
RR(:,1)=0:(length(RR(:,2))-1);
RR2(:,1)=0:(length(RR2(:,2))-1);
RR(:,1)=RR(:,1)*0.01;
RR2(:,1)=RR2(:,1)*0.01;
```

```
% Plot uncorrected and corrected data for comparison:
figure(1); plot(RR(:,1),RR(:,2))
figure(2); plot(R(:,1),R(:,2))
figure(3); plot(RR2(:,1),RR2(:,2))
figure(4); plot(R2(:,1),R2(:,2))
```

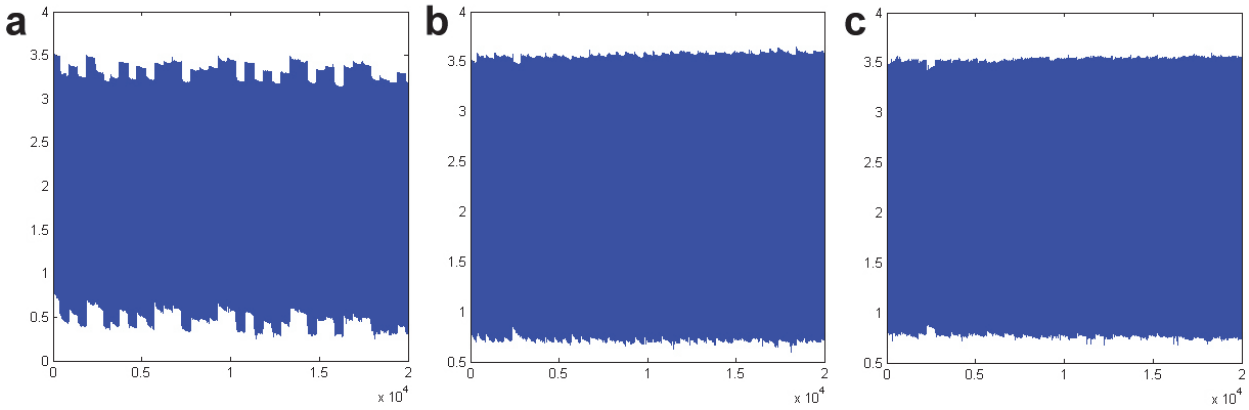


**Figure 6.15** 2,200 V reliability test data processing. **(a)** Raw data, manually cropped and stitched together. Each segment represents a separate syringe change, where flow had to be stopped and restarted between each one. The resulted in slightly different baseline pressures. **(b)** All baselines were aligned. **(c)** Filtering was performed to remove any low frequency baseline drift. Statistics were performed before filtering.

Part (ii) performs the simple statistics:

```
%%%%   Statistical Analysis:   %%%%

% Preallocate drop (600 V) and drop2 (2200 V) vectors:
drop=zeros(1,200); drop2=zeros(1,200);

for i=1:100
    % Find the pressure differences between the maximum and minimum of each
    % of 100 consecutive 10-second intervals at the beginning of the data:
    drop(i)=max(R((i*1000):((i+1)*1000),2))-min(R((i*1000):((i+1)*1000)...
        ,2));
    drop2(i)=max(R2((i*1000):((i+1)*1000),2))-min(R2((i*1000):((i+1)*...
        1000),2));

    % Find the pressure differences between the maximum and minimum of each
    % of 100 consecutive 10-second intervals at the end of the data:
```

```
    drop(i+100)=max(R((length(R(:,2))-(i*1000)):((length(R(:,2))-(i-1)*...
        1000)),2))-min(R((length(R(:,2))-(i*1000)):((length(R(:,2))-(i-...
        1)*1000)),2));
    drop2(i+100)=max(R2((length(R2(:,2))-(i*1000)):((length(R2(:,2))-...
        (i-1)*1000)),2))-min(R2((length(R2(:,2))-(i*1000)):((length(...
        R2(:,2))-(i-1)*1000)),2));
end

% Average these 100 pressure differences at the beginning and end:
beg=mean(drop(1:100)); beg2=mean(drop2(1:100));
en=mean(drop(101:200)); en2=mean(drop2(101:200));

% Find the pressure difference between the beginning and the end, as well
% as the standard deviations of the beginning and end data for 600 V:
beg-en
std(drop(1:100))
std(drop(101:200))

% Do the same for 2200 V:
beg2-en2
std(drop2(1:100))
std(drop2(101:200))
```

Finally, Part (iii) performs the final filtering, as shown in Figure 6.15, and generates the data used to plot Figure 3.11:

```
%%%%   Filtering Out Low-Frequency Baseline Noise:   %%%%

% Design a minimum-order Butterworth filter:
h=fdesign.lowpass('Fp,Fst,Ap,Ast',0.001,0.05,1,6,250);
d=design(h,'butter');
fvtool(d);
y=filter(d,R);
y2=filter(d,R2);

% Perform baseline filtering for R (600 V) and R2 (2200 V):
R_filt(:,1)=R(:,1);
R_filt(:,2)=R(:,2)-y(:,2)+mean(R(:,2));
R2_filt(:,1)=R2(:,1);
R2_filt(:,2)=R2(:,2)-y2(:,2)+mean(R2(:,2));

% Crop both filtered data sets from 100 seconds (10 cycles, 10,000 samples)
% to 20,100 seconds (2,010 cycles, 2,010,000 samples):
R_filt_crop(:,1)=R_filt(10000:2010000,1)-99.9;
R_filt_crop(:,2)=R_filt(10000:2010000,2)+0.084;
R2_filt_crop(:,1)=R2_filt(10000:2010000,1)-99.9;
R2_filt_crop(:,2)=R2_filt(10000:2010000,2)+0.221;

% Plot filtered data as a check; Filter Visualization Tool may appear as
```

```
% Figure 5, and the plot below as Figure 6:
figure(5);plot(R2_filt_crop(:,1),R2_filt_crop(:,2),'-b',R_filt_crop(:,1)...
    ,R_filt_crop(:,2),'-r')

% Final figures with intended scaling, plotted here as a check. Copy
% R_filt_crop and R2_filt_crop to Excel for plotting:
figure(7);plot(R_filt_crop(:,1),R_filt_crop(:,2)-.29,'-k');
axis([0 20000 0 3.5]);
figure(8);plot(R2_filt_crop(:,1),R2_filt_crop(:,2)-.29,'-k');
axis([0 20000 0 3.5]);

% Cropping for insets:
R_inset(:,1)=R(1:(699901-694900),1);
R_inset(:,2)=R(694900:699900,2)+0.0840;
R2_inset(:,1)=R2(1:(14991-9920),1);
R2_inset(:,2)=R2(9920:14990,2)+0.2208;

% Plot as a check, and copy R_inset and R2_inset to Excel for plotting:
figure(9);plot(R_inset(:,1),R_inset(:,2),'-r',R2_inset(:,1),R2_inset...
    (:,2),'-b')
```

### 6.4.3 Modeling in Chapter 4

#### 6.4.3.1 Modeling to Generate Figure 4.11

The following code was used to generate the model computations used to plot Figure 4.11. This figure plots the circumferential stretch versus voltage Gent model results for two layers of VHB™ 4905 and 18 different transverse prestretch values, in order to next evaluate the optimal transverse prestretch. However, only 9 representative plots of the total 18 were graphed in this figure. Twice as many plots were generated than were plotted in Figure 4.11 in order to provide more data to extract in generating Figure 4.12. The final plots were graphed and formatted in Excel after importing data from the voltage matrices generated below:

```
% Initialize model parameters:
clear

% Electronic material constants:
eps=3.98*10^(-11);    % Vacuum permittivity times VHB(TM) dielectric
```

```
                    %     constant (4.5). Units: F/m = N-m/(V^2-m) = N/V^2
E_BD=250*10^6;      % Dielectric breakdown field for VHB(TM). Units: V/m

% Mechanical material constants:
G=45000;            % Shear modulus for VHB(TM). Units: Pa = N/m
J=120;              % Strain stiffening coefficient for VHB(TM) (Unitless)

% Geometric constants:
t0=0.5*10^(-3);     % Initial thickness of one DE layer in meters
d=14.4*10^(-3);     % Average diameter of closed human lower esophagus
                    %     in meters

% Boundary conditions:
P=[2700/2 4000/2];  % Lower and upper bounds of required passive pressure
                    %     in Pa. t = 0.5 mm, so P = P/2 to account for
                    %     2 layers.
P2=(2700+4000)/4;   % Average required pinching pressure in Pa
                    %     (black dashed line)

% Stretch variables:
l_c=0.01:.01:10;    % Circumferential stretch ("l" = "lambda") input as
                    %     independent variable for plotting
l_t_pre=0.5:0.5:9;  % Transverse prestretch input to create different
                    %     plots

% Initialize matrices to preallocate memory:
V_1=zeros(length(l_c),length(l_t_pre)); % V_1 = Voltage curve at 2.7 kPa
V_2=zeros(length(l_c),length(l_t_pre)); % V_2 = Voltage curve at 4.0 kPa
V_A=zeros(length(l_c),length(l_t_pre)); % V_A = Voltage curve at 3.35 kPa
V_BD=zeros(length(l_c),length(l_t_pre));% V_BD = Breakdown voltage curve
V_LT=zeros(length(l_c),length(l_t_pre));% V_LT = Loss of transverse tension
                                        %     voltage curve

% Model computations. For each variable, evaluate voltage vectors using l_c
% and l_t_pre, and build matrices such that each column contains a voltage
% vector corresponding to a different l_t_pre:
for j=1:length(l_t_pre)
    for k=1:length(l_c)
        V_1(k,j) = real(sqrt((G.*(l_c(k).^2-(l_c(k).*l_t_pre(j)).^(-2))...
            ./(1-(l_c(k).^2+l_t_pre(j).^2+(l_c(k).*l_t_pre(j)).^(-2)-3)...
            ./J) - P(1).*d.*l_t_pre(j).*l_c(k)./(2.*t0)).*(t0./(l_t_pre...
            (j).*l_c(k))).^2./eps)./1000);
        V_2(k,j) = real(sqrt((G.*(l_c(k).^2-(l_c(k).*l_t_pre(j)).^(-2))...
            ./(1-(l_c(k).^2+l_t_pre(j).^2+(l_c(k).*l_t_pre(j)).^(-2)-3)...
            ./J) - P(2).*d.*l_t_pre(j).*l_c(k)./(2.*t0)).*(t0./(l_t_pre...
            (j).*l_c(k))).^2./eps)./1000);
        V_A(k,j) = real(sqrt((G.*(l_c(k).^2-(l_c(k).*l_t_pre(j)).^(-2))...
            ./(1-(l_c(k).^2+l_t_pre(j).^2+(l_c(k).*l_t_pre(j)).^(-2)-3)...
            ./J) - P2.*d.*l_t_pre(j).*l_c(k)./(2.*t0)).*(t0./(l_t_pre(j...
            ).*l_c(k))).^2./eps)./1000);
        V_BD(k,j) = t0.*E_BD./(1000*l_t_pre(j).*l_c(k));
        V_LT(k,j) = real(sqrt((G.*(l_t_pre(j).^2-(l_c(k).*l_t_pre(j)).^...
            (-2))./(1-(l_c(k).^2+l_t_pre(j).^2+(l_c(k).*l_t_pre(j)).^(-...
            2)-3)./J)).*(t0./(l_t_pre(j).*l_c(k))).^2./eps)./1000);
    end
```

```
    % Plot model in a 3x6 grid as a check, and copy V_1, V_2, V_A, V_BD,
    % and V_LT matrices into Excel for final plotting:
    subplot(3,6,j)
    plot(l_c,V_1(:,j),'-b',l_c,V_2(:,j),'-b',l_c,V_A(:,j),'--k',l_c,V_BD...
        (:,j),'-r',l_c,V_LT(:,j),'--r')

    % Set axis bounds and label plots:
    xlim([1 9.5])
    ylim([0.1 15])
    title(['Transverse Prestretch = ' num2str(l_t_pre(j))])
    axes('position',[0 0 1 1],'Visible','off');
    text(0.1,.5,'Voltage (kV)','VerticalAlignment','bottom',...
        'HorizontalAlignment','left','Rotation', 90, 'FontSize',14)
    axes('position',[0 0 1 1],'Visible','off');
    text(0.5,.05,'Circumferential Stretch','VerticalAlignment',...
        'bottom','HorizontalAlignment','left','FontSize',14)
end
```

#### 6.4.3.2 Generation of Figure 4.12 and Figure 4.13

The following code contains data extracted from the previous 18 plots, which was then manipulated to plot Figure 4.12 and Figure 4.13. Figure 4.12 plots the maximum attainable theoretical actuation strains for various transverse prestretches, and Figure 4.13 plots the circumferential prestretches needed to accompany a given transverse prestretch in order to give the required passive pinching pressure. The blue curves contain points extracted from the 2.7 kPa voltage-stretch curves, the red curves are extracted from the 4.0 kPa voltage-stretch curves, and the black dashed curves are the average of these two extremes:

```
clear
% Transverse prestretch values. 0.5 is excluded because it did not provide
% a solution:
l_t_pre=[1:0.5:9];

% Circumferential prestretches when V = 0, extracted from plots. L_c_low
% corresponds to 2.7 kPa, L_c_hi corresponds to 4.0 kPa, and L_c_mean
% corresponds to 3.35 kPa:
L_c_low=[1.12 1.02 1.05 1.14 1.26 1.4 1.52 1.63 1.71 1.77 1.81 1.81 ...
```

```
    1.78 1.72 1.62 1.48 1.31];
L_c_hi=[1.2 1.2 1.35 1.56 1.79 2 2.18 2.33 2.45 2.53 2.57 2.57 2.52 ...
    2.43 2.29 2.1 1.85];
L_c_mean=0.5.*(L_c_low+L_c_hi);

% Maximum circumferential stretches, at intersection of blue curves with
% either red LT or BD curve, whichever intersection has the smaller stretch
% value. L_c_low_max corresponds to 2.7 kPa, and L_c_hi_max corresponds to
% 4.0 kPa:
L_c_low_max=[1.24 1.85 2.45 3.03 3.59 4.14 4.66 5.16 5.63 5.82 5.66 ...
    5.47 5.25 4.99 4.69 4.35 3.94];
L_c_hi_max=[1.37 2.04 2.68 3.3 3.89 4.45 4.97 5.46 5.91 6.01 5.85 5.66 ...
    5.43 5.17 4.86 4.5 4.08];

% Preallocate memory for variable in loop:
L_c_low_astretch=zeros(length(l_t_pre));
L_c_hi_astretch=zeros(length(l_t_pre));

% Compute the maximum actuation stretches. L_c_low_astretch corresponds to
% 2.7 kPa, while L_c_hi_astretch corresponds to 4.0 kPa:
for i=1:length(l_t_pre)
    L_c_low_astretch(i)=L_c_low_max(i)./L_c_low(i);
    L_c_hi_astretch(i)=L_c_hi_max(i)./L_c_hi(i);
end

% Compute the mean maximum actuation stretch, corresponding to 3.35 kPa:
L_c_astretch_mean=0.5.*(L_c_low_astretch+L_c_hi_astretch);

% Plot as a check:
figure(1)
plot(l_t_pre,L_c_low,'-b',l_t_pre,L_c_hi,'-r',l_t_pre,L_c_mean,'--k')
xlabel('Transverse Prestretch');
ylabel('Required Circumferential Prestretch');

figure(2)
plot(l_t_pre,100*(L_c_low_astretch-1),'-b',l_t_pre,100*(L_c_hi_astretch...
    -1),'-r',l_t_pre,100*(L_c_astretch_mean-1),'--k')
xlim([1 9]);
ylim([0 240]);
xlabel('Transverse Prestretch');
ylabel('Maximum Vertical Actuation Strain (%)');

% Format generated vectors for plotting in Excel:
    l_t_pre=l_t_pre';
    L_c_low=L_c_low';
    L_c_hi=L_c_hi';
    L_c_mean=L_c_mean';

    % Convert stretches to strains:
    L_c_low_astretch=100*(L_c_low_astretch'-1);
    L_c_hi_astretch=100*(L_c_hi_astretch'-1);
    L_c_astretch_mean=100*(L_c_astretch_mean'-1);
```

#### 6.4.3.3 Generation of Figure 4.17

The following code plots a Gent voltage-stretch curve for two layers of VHB™ 4905 with a chosen transverse prestretch of 5.5:

```
% Initialize model parameters:
clear

% Electronic material constants:
eps=3.98*10^(-11);    % Vacuum permittivity times VHB(TM) dielectric
                      %     constant (4.5). Units: F/m = N-m/(V^2-m) = N/V^2
E_BD=250*10^6;        % Dielectric breakdown field for VHB(TM). Units: V/m

% Mechanical material constants:
G=45000;              % Shear modulus for VHB(TM). Units: Pa = N/m
J=120;                % Strain stiffening coefficient for VHB(TM) (Unitless)

% Geometric constants:
t0=0.5*10^(-3);       % Initial thickness of one DE layer in meters
d=14.4*10^(-3);       % Average diameter of closed human lower esophagus
                      %     in meters

% Boundary conditions:
P=[2700/2 4000/2];    % Lower and upper bounds of required passive pressure
                      %     in Pa. t = 0.5 mm, so P = P/2 to account for
                      %     2 layers.
P2=(2700+4000)/4;     % Average required pinching pressure in Pa
                      %     (black dashed line)

% Stretch variables:
l_c=0.01:.01:10;      % Circumferential stretch ("l" = "lambda") input as
                      %     independent variable for plotting
l_t_pre = 5.5;        % Optimized transverse prestretch value

% Initialize matrices to preallocate memory:
V_1=zeros(1,length(l_c)); % V_1 = Voltage curve at 2.7 kPa
V_2=zeros(1,length(l_c)); % V_2 = Voltage curve at 4.0 kPa
V_A=zeros(1,length(l_c)); % V_A = Voltage curve at 3.35 kPa
V_BD=zeros(1,length(l_c));% V_BD = Breakdown voltage curve
V_LT=zeros(1,length(l_c));% V_LT = Loss of transverse tension
                          %     voltage curve

% Model computations. For each variable, evaluate voltage vectors using l_c
% and l_t_pre = 5.5:
for i = 1:length(l_c)
    V_1(i) = real(sqrt((G.*(l_c(i).^2-(l_c(i).*l_t_pre).^(-2))./(1-(l_c...
        (i).^2+l_t_pre.^2+(l_c(i).*l_t_pre).^(-2)-3)./J) - P(1).*d.*...
        l_t_pre.*l_c(i)./(2.*t0)).*(t0./(l_t_pre.*l_c(i))).^2./eps)./1000);
    V_2(i) = real(sqrt((G.*(l_c(i).^2-(l_c(i).*l_t_pre).^(-2))./(1-(l_c...
        (i).^2+l_t_pre.^2+(l_c(i).*l_t_pre).^(-2)-3)./J) - P(2).*d.*...
```

```
        l_t_pre.*l_c(i)./(2.*t0)).*(t0./(l_t_pre.*l_c(i))).^2./eps)./1000);
    V_A(i) = real(sqrt((G.*(l_c(i).^2-(l_c(i).*l_t_pre).^(-2))./(1-(l_c...
        (i).^2+l_t_pre.^2+(l_c(i).*l_t_pre).^(-2)-3)./J) - P2.*d.*...
        l_t_pre.*l_c(i)./(2.*t0)).*(t0./(l_t_pre.*l_c(i))).^2./eps)./1000);
    V_BD(i) = t0.*E_BD./(1000*l_t_pre.*l_c(i));
    V_LT(i) = real(sqrt((G.*(l_t_pre.^2-(l_c(i).*l_t_pre).^(-2))./(1-(...
        l_c(i).^2+l_t_pre.^2+(l_c(i).*l_t_pre).^(-2)-3)./J)).*(t0./(...
        l_t_pre.*l_c(i))).^2./eps)./1000);
end

% Plot as a check:
figure
plot(l_c,V_1,'-b',l_c,V_2,'-b',l_c,V_A,'--k',l_c,V_BD,'-r',l_c,V_LT,'-r')
xlim([1 7.5])
ylim([0.1 15])
xlabel('Vertical (Circumferential) Stretch')
ylabel('Voltage (kV)')
title('Transverse Prestrain = 450%, 2 Layers of VHB 4905')

% Format for Excel to export the matrix V and the vector l_c for plotting:
V=[V_1' V_2' V_A' V_BD' V_LT'];
l_c=l_c';
```

#### 6.4.3.4 Generation of Figure 4.18

Here follows the code to generate Figure 4.18, which converts the previous figure into the theoretical maximum circumferential actuation strain. It also plots the scaled version of this maximum strain curve as a result of passive practical passive elements that were added:

```
% Initialize model parameters:
clear

% Electronic material constants:
eps=3.98*10^(-11);    % Vacuum permittivity times VHB(TM) dielectric
                      %     constant (4.5). Units: F/m = N-m/(V^2-m) = N/V^2
E_BD=250*10^6;        % Dielectric breakdown field for VHB(TM). Units: V/m

% Mechanical material constants:
G=45000;              % Shear modulus for VHB(TM). Units: Pa = N/m
J=120;                % Strain stiffening coefficient for VHB(TM) (Unitless)

% Geometric constants:
t0=0.5*10^(-3);       % Initial thickness of one DE layer in meters
d=14.4*10^(-3);       % Average diameter of closed human lower esophagus
                      %     in meters
```

```
% Boundary condition:
P=(2700+4000)/4;     % Average required pinching pressure in Pa

% Stretch variables:
l_c=0.01:.01:7.5;    % Circumferential stretch ("l" = "lambda") input as
                     %     independent variable for plotting
l_t_pre = 5.5;       % Optimized transverse prestretch value

% Initialize matrices to preallocate memory:
V=zeros(1,length(l_c));   % V = Voltage curve at 3.35 kPa
V_BD=zeros(1,length(l_c));% V_BD = Breakdown voltage curve
V_LT=zeros(1,length(l_c));% V_LT = Loss of transverse tension
                          %     voltage curve

% Model computations. For each variable, evaluate voltage vectors using l_c
% and l_t_pre = 5.5:
for i = 1:length(l_c)
    V(i) = real(sqrt((G.*(l_c(i).^2-(l_c(i).*l_t_pre).^(-2))./(1-(l_c(i)...
        .^2+l_t_pre.^2+(l_c(i).*l_t_pre).^(-2)-3)./J) - P.*d.*l_t_pre.*...
        l_c(i)./(2.*t0)).*(t0./(l_t_pre.*l_c(i))).^2./eps)./1000);
    V_BD(i) = t0.*E_BD./(1000*l_t_pre.*l_c(i));
    V_LT(i) = real(sqrt((G.*(l_t_pre.^2-(l_c(i).*l_t_pre).^(-2))./(1-(...
        l_c(i).^2+l_t_pre.^2+(l_c(i).*l_t_pre).^(-2)-3)./J)).*(t0./(...
        l_t_pre.*l_c(i))).^2./eps)./1000);
end

% Plot as a check, converting circumferential stretch to actuation strain.
% Includes curves scaled down by 21.4%:
figure
plot(V,100*((l_c/2.15)-1),'-b',V_BD,100*((l_c/2.15)-1),'-r',V_LT,100*((...
    l_c/2.15)-1),'-r',V_BD,.214*100*((l_c/2.15)-1),'-r',V_LT,.214*100*(...
    (l_c/2.15)-1),'-r',V,.214*100*((l_c/2.15)-1),'-k')
xlim([0.1 4])
ylim([0 200])
xlabel('Voltage (kV)')
ylabel('Circumferential Strain')
title('Isotonic Actuation Strain, 2 Layers, Transverse Prestrain = 450%')

% Format for Excel to export the matrix Vs and the vector l_cs to plot:
Vs=[V' V_BD' V_LT'];
l_cs=[100*((l_c'/2.15)-1) .214*100*((l_c'/2.15)-1)];
```

#### 6.4.3.5 Generation of Figure 4.20 and Figure 4.21

This code was used to plot the isometric force and pressure drops with voltage. Here, the predetermined transverse prestretch of 5.5 and circumferential prestretch of 2.15 are input into the model, causing the term containing $G$ and $J$ to

reduce to the desired stress in the DE, which equals 3.35 kPa or 0.25 N. Assuming the length does not change (and therefore, the circumferential prestretch also does not change), we can predict the amount of force or pressure drop from the magnitude of the Maxwell pressure term, which is a function of the input voltage. Plotted are the theoretical ideal models alongside the scaled (and baseline shifted) models, one of which fits the isometric experimental data well:

```
% Initialize model parameters:
clear

% Electronic material constants:
eps=3.98*10^(-11);    % Vacuum permittivity times VHB(TM) dielectric
                      %     constant (4.5). Units: F/m = N-m/(V^2-m) = N/V^2

% Mechanical material constants:
G=45000;              % Shear modulus for VHB(TM). Units: Pa = N/m
J=120;                % Strain stiffening coefficient for VHB(TM) (Unitless)

% Geometric constants:
n=2;                  % Number of DE layers
w = 1.06*10^(-2);     % Width of band in meters
t0=0.5*10^(-3);       % Initial thickness of one DE layer in meters
d=14.4*10^(-3);       % Average diameter of closed human lower esophagus
                      %     in meters

% Stretch constants:
l_c=2.15;             % Optimized circumferential prestretch ("l"="lambda")
l_t_pre = 5.5;        % Optimized transverse prestretch

% Input actuation voltage:
V =[10:10:4000];

% Initialize matrices to preallocate memory:
P=zeros(1,length(V));    % V = Voltage curve at 3.35 kPa
F=zeros(1,length(V));% V_BD = Breakdown voltage curve

% Model computations for force and hydraulic pressure in isometric case
% when voltage is input:
for i = 1:length(V)
     P(i) = (G.*(l_c.^2-(l_c.*l_t_pre).^(-2))./(1-(l_c.^2+l_t_pre.^2+(...
         l_c.*l_t_pre).^(-2)-3)./J) - eps.*(V(i)).^2./(t0./(l_t_pre.*...
         l_c)).^2)./(d.*l_t_pre.*l_c./(2.*n.*t0))./1000;
     F(i) = ((G.*(l_c.^2-(l_c.*l_t_pre).^(-2))./(1-(l_c.^2+l_t_pre.^2+(...
         l_c.*l_t_pre).^(-2)-3)./J) - eps.*((V(i)).^2)./(t0./(l_t_pre.*...
```

```
        l_c)).^2)./(l_t_pre.*l_c./(n.*t0.*w)));
end

% As a check, plot the models and corrected, baseline-shifted models:
figure(1)
plot(V/1000,P,'-b',V/1000,.44*P+(3.5-1.641),'--k')
xlim([0.1 4])
ylim([0 4])
xlabel('Voltage (kV)')
ylabel('Hydraulic Pressure (kPa)')
title('Isometric Pressure, 2 Layers, Transverse Prestrain = 450%')

figure(2)
plot(V/1000,F,'-b',V/1000,.44*F+(.25-.1081),'--k')
xlim([0.1 4])
ylim([0 .3])
xlabel('Voltage (kV)')
ylabel('Force (N)')
title('Isometric Force, 2 Layers, Transverse Prestrain = 450%')

% Format for Excel to export the matrices P and F and the vector V to plot:
V=V'/1000;
P=[P' .44*P'+(3.5-1.641)];
F=[F' .44*F'+(.25-.1081)];
```

## 6.5 Sample LabVIEW™ Virtual Instrument

This LabVIEW™ VI was written to perform the pressure-flow experiments in Chapter 3 and was the software utilized in the Figure 3.4 Experimental Setup. Specifically, it was used to collect the analog pressure sensor data plotted in Figure 3.7, and subsequently Figure 3.8, Figure 3.9, and Figure 3.10. It was also used to output an actuation signal to the high voltage power supply during reliability testing, producing the plots in Figure 3.11. The Block Diagram is pictured below in Figure 6.16.

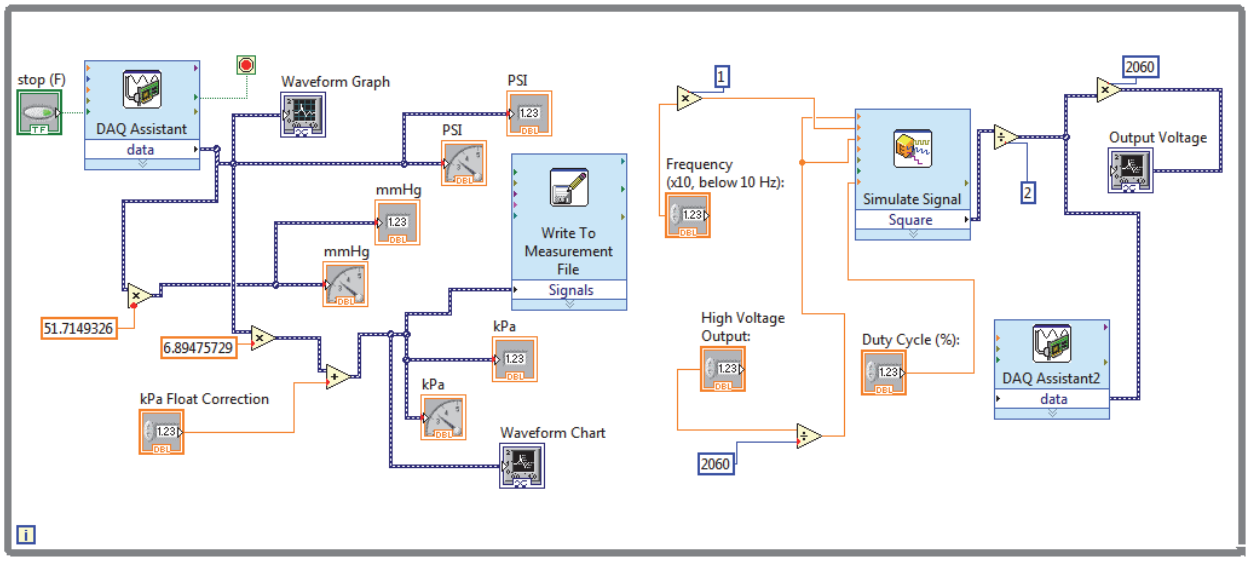


**Figure 6.16** Block diagram of custom LabVIEW™ VI.

The graphical code tree on the left measures the pressure signal, and the code on the right generates a square wave output to the high voltage supply. On the left, a DAQ Assistant Sub-VI reads the digitized analog input signal from the pressure transducer. This particular sensor has a signal input range of ±15 psi, a full bridge,

an internal “Vex” source with “Vex” value of 2.5 V, and a bridge resistance of 350. Data were sampled continuously at 100 Hz, and 100 samples were read. The input signal is read as pounds per square inch (psi), which is displayed on the leftmost Waveform Graph (see Front Panel, Figure 6.17 below), as well as on dial and numerical indicators. The psi signal is converted to millimeters of mercury (mmHg) and displayed. The psi signal is also converted to kilopascals (kPa), displayed on the primary Waveform Chart, dial indicator, and numerical indicator, and is finally output to the Write to Measurement File Sub-VI for processing and plotting. There is also a numerical input for adding any baseline drift in real time.

On the right of the Block Diagram, the Simulate Signal Sub-VI receives the input arguments of frequency, duty cycle, and voltage. The input voltage is divided by 2,060 in order for the custom high voltage box to output the intended voltage. Specifically, this converts the input voltage to a specific value that is under 5 V (since input voltages are less than ~10 kV), which is then output to the voltage supply. The Simulate Signal Sub-VI then outputs a square wave signal, which is divided by half since the output amplitude is normally doubled to create peaks and valleys. This digital signal is then output through the DAQ Assistant2 Sub-VI, as well as displayed on the Output Voltage Waveform Chart following conversion back into kilovolts.

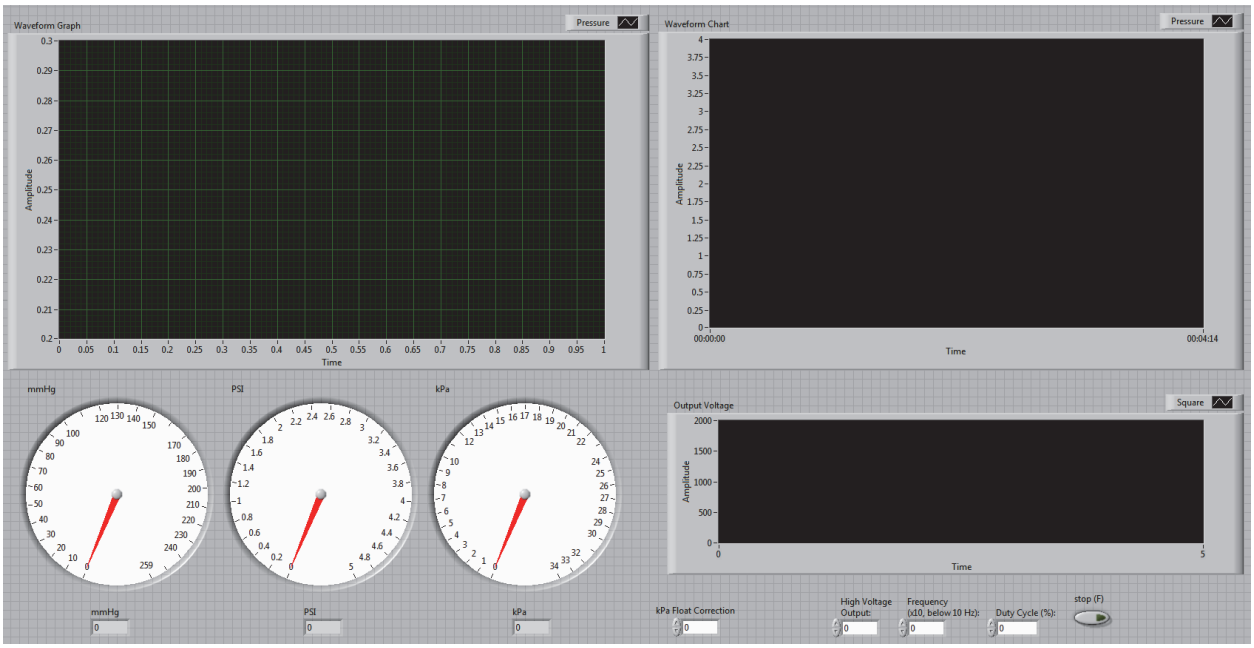


**Figure 6.17** Front Panel of custom LabVIEW™ VI.

# REFERENCES


[1] Pelrine, R., Kornbluh, R.D., Pei, Q., Stanford, S., Oh, S., Eckerle, J., Full, R.J., Rosenthal, M.A., and Meijer, K. *Dielectric elastomer artificial muscle actuators: toward biomimetic motion*. 2002.

[2] Brochu, P., Li, H., Niu, X., and Pei, Q. *Factors influencing the performance of dielectric elastomer energy harvesters*. 2010.

[3] Chiba, S., Waki, M., Kornbluh, R., and Pelrine, R., Current status and future prospects of power generators using dielectric elastomers. *Smart Materials and Structures*. **20**(12), 124006 (2011)

[4] Jung, K., Kim, K.J., and Choi, H.R., A self-sensing dielectric elastomer actuator. *Sensors and Actuators A: Physical*. **143**(2), 343-351 (2008)

[5] Brochu, P. and Pei, Q., Advances in Dielectric Elastomers for Actuators and Artificial Muscles. *Macromolecular Rapid Communications*. **31**(1), 10-36 (2010)

[6] Bar-Cohen, Y., Xue, T., Shahinpoor, M., Simpson, J.O., and Smith, J., Low-mass muscle actuators using electroactive polymers (EAP). *Proc. SPIE*. **3324**, 218–223 (1998)

[7] Pelrine, R., Kornbluh, R., Pei, Q., and Joseph, J., High-Speed Electrically Actuated Elastomers with Strain Greater Than 100%. *Science*. **287**(5454), 4 (2000)

[8] Pelrine, R.E., Kornbluh, R.D., and Joseph, J.P., Electrostriction of polymer dielectrics with compliant electrodes as a means of actuation. *Sensors and Actuators A: Physical*. **64**(1), 77-85 (1998)

[9] Pelrine, R., Kornbluh, R., Joseph, J., Heydt, R., Pei, Q., and Chiba, S., High-field deformation of elastomeric dielectrics for actuators. *Materials Science and Engineering C*. **11**(2), 12 (2000)

[10] Bozlar, M., Punckt, C., Korkut, S., Zhu, J., Foo, C.C., Suo, Z., and Aksay, I.A., Dielectric elastomer actuators with elastomeric electrodes. *Applied Physics Letters*. **101**(9), 091907 (2012)

[11] Kofod, G., Sommer-Larsen, P., Kornbluh, R., and Pelrin, R., Actuation Response of Polyacrylate Dielectric Elastomers. *Journal of Intelligent Material Systems and Structures*. **14**(12), 7 (2003)

[12] Zhang, Z., Liu, L., Fan, J., Yu, K., Liu, Y., Shi, L., and Leng, J. *New silicone dielectric elastomers with a high dielectric constant*. in *The 15th International Symposium on: Smart Structures and Materials & Nondestructive Evaluation and Health Monitoring*. 2008. International Society for Optics and Photonics.

[13] Zhao, X. and Suo, Z., Theory of Dielectric Elastomers Capable of Giant Deformation of Actuation. *Physical Review Letters*. **104**(17), 178302 (2010)

[14] Koh, S.J.A., Li, T., Zhou, J., Zhao, X., Hong, W., Zhu, J., and Suo, Z., Mechanisms of large actuation strain in dielectric elastomers. *Journal of Polymer Science Part B: Polymer Physics*. **49**(7), 504-515 (2011)

[15] Lu, T., Huang, J., Jordi, C., Kovacs, G., Huang, R., Clarke, D.R., and Suo, Z., Dielectric elastomer actuators under equal-biaxial forces, uniaxial forces, and uniaxial constraint of stiff fibers. *Soft Matter*. **8**(22), 6167-6173 (2012)

[16] Keplinger, C., Li, T., Baumgartner, R., Suo, Z., and Bauer, S., Harnessing snap-through instability in soft dielectrics to achieve giant voltage-triggered deformation. *Soft Matter*. **8**(2), 285-288 (2012)

[17] Röntgen, W.C., Ueber die durch Electricität bewirkten Form- und Volumenänderungen von dielectrischen Körpern. *Annalen der Physik*. **247**(13), 771-786 (1880)

[18] Li, B., Zhou, J., and Chen, H., Electromechanical stability in charge-controlled dielectric elastomer actuation. *Applied Physics Leters*. **99**(24), 244101-1-3 (2011)

[19] Keplinger, C., Kaltenbrunner, M., Arnold, N., and Bauer, S., Röntgen's electrode-free elastomer actuators without electromechanical pull-in instability. *Proceedings of the National Academy of Sciences*. **107**(10), 4505-4510 (2010)

[20] Gallone, G., Carpi, F., De Rossi, D., Levita, G., and Marchetti, A., Dielectric constant enhancement in a silicone elastomer filled with lead magnesium niobate–lead titanate. *Materials Science and Engineering: C*. **27**(1), 110-116 (2007)

[21] Stoyanov, H., Kollosche, M., Risse, S., McCarthy, D.N., and Kofod, G., Elastic block copolymer nanocomposites with controlled interfacial interactions for artificial muscles with direct voltage control. *Soft Matter*. **7**(1), 194-202 (2011)

[22] Romasanta, L.J., Hernández, M., López-Manchado, M.A., and Verdejo, R., Functionalised graphene sheets as effective high dielectric constant fillers. *Nanoscale research letters*. **6**(1), 1-6 (2011)

[23] Molberg, M., Crespy, D., Rupper, P., Nüesch, F., Månson, J., Löwe, C., and Opris, D., High Breakdown Field Dielectric Elastomer Actuators Using Encapsulated Polyaniline as High Dielectric Constant Filler. *Advanced Functional Materials*. **20**(19), 3280-3291 (2010)

[24] Stoyanov, H., Kollosche, M., McCarthy, D.N., and Kofod, G., Molecular composites with enhanced energy density for electroactive polymers. *Journal of Materials Chemistry*. **20**(35), 7558-7564 (2010)

[25] Kussmaul, B., Risse, S., Kofod, G., Waché, R., Wegener, M., McCarthy, D.N., Krüger, H., and Gerhard, R., Enhancement of dielectric permittivity and electromechanical response in silicone elastomers: molecular grafting of organic dipoles to the macromolecular network. *Advanced Functional Materials*. **21**(23), 4589-4594 (2011)

[26] Zhu, S., So, J.H., Mays, R., Desai, S., Barnes, W.R., Pourdeyhimi, B., and Dickey, M.D., Ultrastretchable Fibers with Metallic Conductivity Using a Liquid Metal Alloy Core. *Advanced Functional Materials*. **23**(18), 2308-2314 (2013)

[27] Lide, D.R., Editor, *Section 12, Properties of Solids; Electrical Resistivity of Pure Metals*, in *CRC Handbook of Chemistry and Physics, 84th Edition*. 2003, CRC Press: Boca Ranton, FL.

[28] Rathmell, A.R., Bergin, S.M., Hua, Y.L., Li, Z.Y., and Wiley, B.J., The Growth Mechanism of Copper Nanowires and Their Properties in Flexible, Transparent Conducting Films. *Advanced Materials*. **22**(32), 3558-3563 (2010)

[29] Rathmell, A.R. and Wiley, B.J., The Synthesis and Coating of Long, Thin Copper Nanowires to Make Flexible, Transparent Conducting Films on Plastic Substrates. *Advanced Materials*. **23**(41), 4798-4803 (2011)

[30] Cheng, Y., Wang, S., Wang, R., Sun, J., and Gao, L., Copper nanowire based transparent conductive films with high stability and superior stretchability. *Journal of Materials Chemistry C*. **2**(27), 5309-5316 (2014)

[31] Yun, S., Niu, X.F., Yu, Z.B., Hu, W.L., Brochu, P., and Pei, Q., Compliant Silver Nanowire-Polymer Composite Electrodes for Bistable Large Strain Actuation. *Advanced Materials*. **24**(10), 1321-1327 (2012)

[32] Li, L., Yu, Z., Chang, C.-h., Hu, W., Niu, X., Chen, Q., and Pei, Q., Efficient white polymer light-emitting diodes employing a silver nanowire–polymer composite electrode. *Phys. Chem. Chem. Phys.* **14**(41), 14249-14254 (2012)

[33] Lee, P., Lee, J., Lee, H., Yeo, J., Hong, S., Nam, K.H., Lee, D., Lee, S.S., and Ko, S.H., Highly Stretchable and Highly Conductive Metal Electrode by Very Long Metal Nanowire Percolation Network. *Advanced Materials*. **24**(25), 3326-3332 (2012)

[34] Dean, J.A. and Lange, N.A., *Section 4, Table 4.1 Electronic Configuration and Properties of the Elements*, in *Lange's Handbook of Chemistry*. 1999, McGraw-Hill.

[35] Granqvist, C.G. and Hultåker, A., Transparent and conducting ITO films: new developments and applications. *Thin Solid Films*. **411**(1), 1-5 (2002)

[36] Sekitani, T., Noguchi, Y., Hata, K., Fukushima, T., Aida, T., and Someya, T., A rubberlike stretchable active matrix using elastic conductors. *Science*. **321**(5895), 1468-1472 (2008)

[37] Sekitani, T., Nakajima, H., Maeda, H., Fukushima, T., Aida, T., Hata, K., and Someya, T., Stretchable active-matrix organic light-emitting diode display using printable elastic conductors. *Nature Materials*. **8**(6), 494-499 (2009)

[38] McEuen, P.L., Fuhrer, M.S., and Park, H., Single-walled carbon nanotube electronics. *IEEE transactions on nanotechnology*. **1**(1), 78-85 (2002)

[39] Nemes-Incze, P., Osváth, Z., Kamarás, K., and Biró, L., Anomalies in thickness measurements of graphene and few layer graphite crystals by tapping mode atomic force microscopy. *Carbon*. **46**(11), 1435-1442 (2008)

[40] Geim, A.K. and Novoselov, K.S., The rise of graphene. *Nat Mater*. **6**(3), 183-191 (2007)

[41] Shang, S., Zeng, W., and Tao, X.M., High stretchable MWNTs/polyurethane conductive nanocomposites. *Journal of Materials Chemistry*. **21**(20), 7274-7280 (2011)

[42] Sahoo, N.G., Jung, Y.C., Yoo, H.J., and Cho, J.W., Influence of carbon nanotubes and polypyrrole on the thermal, mechanical and electroactive shape-memory properties of polyurethane nanocomposites. *Composites Science and Technology*. **67**(9), 1920-1929 (2007)

[43] Ebbesen, T.W., Lezec, H.J., Hiura, H., Bennett, J.W., Ghaemi, H.F., and Thio, T., Electrical conductivity of individual carbon nanotubes. *Nature*. **382**(6586), 54-56 (1996)

[44] Choudhary, V., Singh, B., and Mathur, R., Carbon nanotubes and their composites. *Carbon Nanotubes and Their Composites, Syntheses and Applications of Carbon Nanotubes and Their Composites, ed. Dr S. Suzuki, ISBN*. 978-953 (2013)

[45] Primak, W. and Fuchs, L.H., Electrical Conductivities of Natural Graphite Crystals. *Physical Review*. **95**(1), 22-30 (1954)

[46] Tsukamoto, J., Takahashi, A., and Kawasaki, K., Structure and Electrical Properties of Polyacetylene Yielding a Conductivity of 10 5 S/cm. *Japanese Journal of Applied Physics*. **29**(1R), 125 (1990)

[47] Machida, S., Miyata, S., and Techagumpuch, A., Chemical synthesis of highly electrically conductive polypyrrole. *Synthetic Metals*. **31**(3), 311-318 (1989)

[48] MacDiarmid, A.G. and Epstein, A.J., Polyanilines: a novel class of conducting polymers. *Faraday Discussions of the Chemical Society*. **88**, 317-332 (1989)

[49] Groenendaal, L., Jonas, F., Freitag, D., Pielartzik, H., and Reynolds, J.R., Poly(3,4-ethylenedioxythiophene) and Its Derivatives: Past, Present, and Future. *Advanced Materials*. **12**(7), 481-494 (2000)

[50] Rosset, S. and Shea, H.R., Flexible and stretchable electrodes for dielectric elastomer actuators. *Applied Physics A*. **110**(2), 281-307 (2013)

[51] Tekin, E., de Gans, B.-J., and Schubert, U.S., Ink-jet printing of polymers - from single dots to thin film libraries. *Journal of Materials Chemistry*. **14**(17), 2627-2632 (2004)

[52] Akter, T. and Kim, W.S., Reversibly Stretchable Transparent Conductive Coatings of Spray-Deposited Silver Nanowires. *ACS Applied Materials & Interfaces*. **4**(4), 1855-1859 (2012)

[53] Ikeno, S., Yokoyama, M., and Mikawa, H., Electrically Conductive Elastomeric TCNQ Complexes *Journal of Polymer Science*. **16**(4), 717-723 (1978)

[54] Madaria, A.R., Kumar, A., and Zhou, C., Large scale, highly conductive and patterned transparent films of silver nanowires on arbitrary substrates and their application in touch screens. *Nanotechnology*. **22**(24), 245201-1-7 (2011)

[55] Holcomb, R.E., Kraly, J.R., and Henry, C.S., Electrode array detector for microchip capillary electrophoresis. *Analyst* **134**(3), 486-492 (2009)

[56] Chung, S., Lee, J., Song, H., Kim, S., Jeong, J., and Hong, Y., Inkjet-printed stretchable silver electrode on wave structured elastomeric substrate. *Applied Physics Letters*. **98**(15), 153110-153110 (2011)

[57] Mamunya, Y.P., Davydenko, V.V., Pissis, P., and Lebedev, E.V., Electrical and thermal conductivity of polymers filled with metal powders. *European Polymer Journal*. **38**(9), 1887-1897 (2002)

[58] Vinod, V.S., Varghese, S., and Kuriakose, B., Degradation behaviour of natural rubber–aluminium powder composites: effect of heat, ozone and high energy radiation. *Polymer Degradation and Stability*. **75**(3), 405-412 (2002)

[59] Boiteux, G., Fournier, J., Issotier, D., Scytre, G., and Marichy, G., Conductive thermoset composites: PTC effect. *Synthetic Metals*. **102**(1–3), 1234-1235 (1999)

[60] Kusy, R.P. and Corneliussen, R.D., The thermal conductivity of nickel and copper dispersed in poly(vinyl chloride). *Polymer Engineering & Science*. **15**(2), 107-112 (1975)

[61] Tamai, T., Electrical Properties of Conductive Elastomer as Electrical Contact Material. *Components, Hybrids, and Manufacturing Technology, IEEE Transactions on*. **5**(1), 56-61 (1982)

[62] Bigg, D.M., Mechanical properties of particulate filled polymers. *Polymer Composites*. **8**(2), 115-122 (1987)

[63] Bigg, D.M., Mechanical, thermal, and electrical properties of metal fiber-filled polymer composites. *Polymer Engineering & Science*. **19**(16), 1188-1192 (1979)

[64] Bridge, B., Folkes, M.J., and Wood, B.R., Investigation into the DC conductivity of colloidally dispersed gold/polymer composites. *Journal of Applied Physics D: Applied Physics*. **23**(7), 890-898 (1990)

[65] Corbierre, M.K., Cameron, N.S., Sutton, M., Mochrie, S.G.J., Lurio, L.B., Rühm, A., and Lennox, R.B., Polymer-Stabilized Gold Nanoparticles and Their Incorporation into Polymer Matrices. *Journal of the American Chemical Society*. **123**(42), 10411-10412 (2001)

[66] Goyal, A., Kumar, A., Patra, P., Mahendra, S., Tabatabaei, S., Alvarez, P., John, G., and Ajayan, P., In situ Synthesis of Metal Nanoparticle Embedded Free Standing Multifunctional PDMS Films. *Macromolecular Rapid Communications*. **30**(13), 1116-1122 (2009)

[67] Zhang, Z., Zhang, L., Wang, S., Chen, W., and Lei, Y., A convenient route to polyacrylonitrile/silver nanoparticle composite by simultaneous polymerization–reduction approach. *Polymer*. **42**(19), 8315-8318 (2001)

[68] Zhang, Q., Xu, J., Liu, Y., and Chen, H., In-situ synthesis of poly(dimethylsiloxane)-gold nanoparticles composite films and its application in microfluidic systems. *Lab on a Chip*. **8**(2), 352-357 (2008)

[69] Kofod, G. and Sommer-Larsen, P., Compliant electrodes: solutions, materials, and technologies. *Dielectric Elastomers as Electromechanical Transducers*. 69-76 (2011)

[70] Kofod, G., Dielectric elastomer actuators. *Ph.D. Thesis, The Technical University of Denmark*. (2001)

[71] Kirkpatrick, S., Percolation and Conduction. *Reviews of Modern Physics*. **45**(4), 574-588 (1973)

[72] Genetti, W.B., Yuan, W.L., Grady, B.P., O'Rear, E.A., Lai, C.L., and Glatzhofer, D.T., Polymer matrix composites: Conductivity enhancement through polypyrrole coating of nickel flake. *Journal of Materials Science*. **33**(12), 3085-3093 (1998)

[73] Lux, F., Models proposed to explain the electrical conductivity of mixtures made of conductive and insulating materials. *Journal of Materials Science*. **28**(2), 285-301 (1993)

[74] Salvadori, M.C., Cattani, M., Teixeira, F.S., and Brown, I.G., Conducting polymer formed by low energy gold ion implantation. *Applied Physics Letters*. **93**(7), 073102 (2008)

[75] Niklaus, M., Metal-Ion Implanted Elastomers: Analysis of Microstructures and Characterization and Modeling of Electrical and Mechanical Properties. *Doctoral Dissertation, École Polytechnique Fédérale de Lausanne*. (2010)

[76] Rosset, S., Niklaus, M., Dubois, P., and Shea, H.R., Large-Stroke Dielectric Elastomer Actuators With Ion-Implanted Electrodes. *Microelectromechanical Systems, Journal of*. **18**(6), 1300-1308 (2009)

[77] Brown, I.G., Vacuum arc metal plasma production and the transition of processing mode from metal ion beam to dc metal plasma immersion. *Surface and Coatings Technology*. **136**(1–3), 16-22 (2001)

[78] Rosset, S., Niklaus, M., Dubois, P., and Shea, H.R., Mechanical characterization of a dielectric elastomer microactuator with ion-implanted electrodes. *Sensors and Actuators A: Physical*. **144**, 185-193 (2008)

[79] Wegner, K., Piseri, P., Tafreshi, H.V., and Milani, P., Cluster beam deposition: a tool for nanoscale science and technology. *Journal of Physics D: Applied Physics*. **39**(22), R439-R459 (2006)

[80] Ghisleri, C., Borghi, F., Ravagnan, L., Podestà, A., Melis, C., Colombo, L., and Milani, P., Patterning of gold–polydimethylsiloxane (Au–PDMS) nanocomposites by supersonic cluster beam implantation. *Journal of Physics D: Applied Physics*. **47**, 015301 (2014)

[81] Corbelli, G., Ghisleri, C., Marelli, M., Milani, P., and Ravagnan, L., Highly deformable nanostructured elastomeric electrodes with improving conductivity upon cyclical stretching. *Advanced Materials*. **23**(39), 4504-4508 (2011)

[82] Rosset, S., Niklaus, M., Stojanov, V., Felber, A., Dubois, P., and Shea, H.R. *Ion-implanted compliant and patternable electrodes for miniaturized dielectric elastomer actuators*. 2008.

[83] Rosset, S., Niklaus, M., Dubois, P., and Shea, H.R. *Performance characterization of miniaturized dielectric elastomer actuators fabricated using metal ion implantation*. in *Micro Electro Mechanical Systems, 2008. MEMS 2008. IEEE 21st International Conference on*. 2008.

[84] Rosset, S., Niklaus, M., Dubois, P., and Shea, H.R., Metal ion implantation for the fabrication of stretchable electrodes on elastomers. *Advanced Functional Materials*. **19**(3), 470-478 (2009)

[85] Niklaus, M., Rosset, S., Dadras, M., Dubois, P., and Shea, H.R., Microstructure of 5 keV gold-implanted polydimethylsiloxane. *Scripta Materialia*. **59**(8), 893-896 (2008)

[86] Renau, A. and Scheuer, J.T. *Comparison of plasma doping and beamline technologies for low energy ion implantation*. in *Ion Implantation Technology. 2002. Proceedings of the 14th International Conference on*. 2002.

[87] Watanabe, H., Takahashi, K., and Iwaki, M., Raman spectroscpic study of Ag-, W- and Pd-ions implanted polymide films. *Materials Research Society Symposium*. **354**, 5 (1995)

[88] Wu, Y., Zhang, T., Zhang, H., Zhang, X., Deng, Z., and Zhou, G., Electrical properties of polymer modified by metal ion implantation. *Nuclear Instruments and Methods in Physics Research B*. **169**, 5 (2000)

[89] Wu, Y., Zhang, T., Zhang, Y., Zhang, H., Zhang, X., and Zhou, G., Behavior of PET implanted by Ti, Ag, Si and C ion using MEVVA implantation. *Nuclear Instruments and Methods in Physics Research Section B: Beam Interactions with Materials and Atoms*. **173**(3), 292-298 (2001)

[90] Seo, H.W., Chen, Q.Y., Rusakova, I.A., Zhang, Z.H., Wijesundera, D., Yeh, S.W., Wang, X.M., Tu, L.W., Ho, N.J., Wu, Y.G., Zhang, H.X., and Chu, W.K., Formation of silver nanoparticles in silicon by metal vapor vacuum arc ion implantation. *Nuclear Instruments and Methods in Physics Research Section B: Beam Interactions with Materials and Atoms*. **292**(0), 50-54 (2012)

[91] Zhang, H.X., Zhang, X.J., Zhou, F.S., Li, Q., Liu, F.H., Han, Z.E., and Lin, W.L., Mevva ion source for the application of material surface modification. *Review of Scientific Instruments*. **65**(4), 1295-1297 (1994)

[92] Choi, J.Y., Rosset, S., Niklaus, M., Adleman, J., Shea, H.R., and Psaltis, D., 3-dimensional electrode patterning within a microfluidic channel using metal ion implantation. *Lab on a Chip*. **10**(6), 783-788 (2010)

[93] Niklaus, M. and Shea, H.R., Electrical conductivity and Young's modulus of flexible nanocomposites made by metal-ion implantation of polydimethylsiloxane: The relationship between nanostructure and macroscopic properties. *Acta Materialia*. **59**(2), 830-840 (2011)

[94] Shahinpoor, M. and Kim, K.J., Ionic polymer-metal composites: I. Fundamentals *Smart Mater. Struct.* **10**, 819-833 (2001)

[95] Shahinpoor, M., Bar-Cohen, Y., Simpson, J.O., and Smith, J., Ionic polymer-metal composites (IPMCs) as biomimetic sensors, actuators and artificial muscles - a review. *Smart Materials and Structures*. **7**(6), R15 (1998)

[96] Mojarrad, M. and Shahinpoor, M., *Soft actuators and artificial muscles*. 2000, Google Patents.

[97] Urdaneta, M.G., Delille, R., and Smela, E., Stretchable electrodes with high conductivity and photo-patternability. *Advanced Materials*. **19**(18), 2629-2633 (2007)

[98] Delille, R., Urdaneta, M., Hsieh, K., and Smela, E., Novel compliant electrodes based on platinum salt reduction. *Proc. SPIE*. **6168**, 61681Q (2006)

[99] Delille, R., Urdaneta, M., Hsieh, K., and Smela, E., Compliant electrodes based on platinum salt reduction in a urethane matrix. *Smart Materials and Structures*. **16**(2), S272 (2007)

[100] Donnet, J.B., *Carbon Black: Science and Technology, Second Edition*. 1993: Taylor & Francis.

[101] Rwei, S.P., Ku, F.H., and Cheng, K.C., Dispersion of carbon black in a continuous phase: electrical, rheological, and morphological studies. *Colloid Polymer Science*. **280**(12), 6 (2002)

[102] O'Brien, B., Thode, J., Anderson, I., Calius, E., Haemmerle, E., and Xie, S. *Integrated extension sensor based on resistance and voltage measurement for a dielectric elastomer*. in *Electroactive Polymer Actuators and Devices (EAPAD)*. 2007. San Diego, California.

[103] Carpi, F., Chiarelli, P., Mazzoldi, A., and Dossi, D.D., Electromechanical characterisation of dielectric elastomer planar actuators: comparative evaluation of different electrode materials and different counterloads. *Sensors and Actuators A: Physical*. **107**(1), 11 (2003)

[104] Gorton, L., Carbon paste electrodes modified with enzymes, tissues, and cells. *Electroanalysis*. **7**(1), 23 (2005)

[105] O'Halloran, A., O'Malley, F., and McHugh, P., A review on dielectric elastomer actuators, technology, applications, and challenges. *Journal of Applied Physics*. **104**(071101), 10 (2008)

[106] Biddiss, E. and Chau, T., Dielectric elastomers as actuators for upper limb prosthetics: Challenges and opportunities. *Medical Engineering & Physics*. **30**, 16 (2008)

[107] Heydt, R., Kornbluh, R., Pelrine, R., and Mason, V., DESIGN AND PERFORMANCE OF AN ELECTROSTRICTIVE-POLYMER-FILM ACOUSTIC ACTUATOR. *Journal of Sound and Vibration*. **215**(2), 297-311 (1998)

[108] Schlaak, H.F., Jungmann, M., Matysek, M., and Lotz, P., Novel multilayer electrostatic solid state actuators with elastic dielectric. *Smart Structures and Materials 2005: Electroactive Polymer Actuators and Devices (EAPAD).* **5759**, 13 (2005)

[109] Matysek, M., Lotz, P., Winterstein, T., and Schlaak, H.F. *Dielectric elastomer actuators for tactile displays*. in *EuroHaptics conference, 2009 and Symposium on Haptic Interfaces for Virtual Environment and Teleoperator Systems. World Haptics 2009. Third Joint*. 2009.

[110] Li, Y. and Shimizu, H., Toward a stretchable, elastic, and electrically conductive nanocomposite: Morphology and properties of poly[styrene-b-(ethylene-co-butylene)-b-styrene] multiwalled carbon nanotube composites fabricated by high-shear. *Macromolecules*. **42**(7), 2587-2593 (2009)

[111] Baughman, R.H., Zakhidov, A.A., and de Heer, W.A., Carbon nanotubes - the route toward applications. *Science*. **297**(5582), 787-792 (2002)

[112] Avouris, P., Carbon nanotube electronics and photonics. *Physics Today*. **62**(1), 34-40 (2009)

[113] Hu, L., Yuan, W., Brochu, P., Grüner, G., and Pei, Q., Highly stretchable, conductive, and transparent nanotube thin films. *Applied Physics Leters*. **94**(16), 161108 (2009)

[114] Yuan, W., Lam, T., Biggs, J., Hu, L., Yu, Z., Ha, S., Xi, D., Senesky, M.K., Grüner, G., and Q., P., New electrode materials for dielectric elastomer actuators. *Proc. SPIE*. **6524**, 65240N (2007)

[115] Yuan, W., Hu, L.B., Yu, Z.B., Lam, T., Biggs, J., Ha, S.M., Xi, D., Chen, B., Senesky, M.K., Grüner, G., and Pei, Q., Fault-Tolerant Dielectric Elastomer Actuators using Single-Walled Carbon Nanotube Electrodes. *Advanced Materials*. **20**(3), 621-625 (2008)

[116] Yuan, W., Brochu, P., Zhang, H., Jan, A., and Pei, Q., Long lifetime dielectric elastomer actuators under continuous high strain actuation. *Proc. SPIE*. **7287**, 72870O (2009)

[117] Chua, S., Neo, X., and Lau, G., Multi-walled carbon nanotubes (MWCNT) as compliant electrodes for dielectric elastomer actuators. *Proc. SPIE*. **7976**, 79760V-1-11 (2011)

[118] Lau, G.K., Chua, S.L., Shiau, L.L., and Tan, A.W.Y., Self-clearing dielectric elastomer actuators using charcoal-powder electrodes. *Proc. SPIE*. **8340**, 834016 (2012)

[119] Kaempgen, M., Chan, C.K., Ma, J., Cui, Y., and Grüner, G., Printable thin film supercapacitors using single-walled carbon nanotubes. *Nano Letters*. **9**(5), 1872-1876 (2009)

[120] Yuan, W., Hu, L., Ha, S., Lam, T., Grüner, G., and Pei, Q., Self-clearable carbon nanotube electrodes for improved performance of dielectric elastomer actuators. *Proc. SPIE*. **6927**, 69270P (2008)

[121] Yuan, W., Li, H., Brochu, P., Niu, X., and Pei, Q., Fault-tolerant silicone dielectric elastomers. *International Journal of Smart and Nano Materials*. **1**(1), 40-52 (2010)

[122] Stoyanov, H., Brochu, P., Niu, X., Lai, C., Yun, S., and Pei, Q., Long lifetime, fault-tolerant freestanding actuators based on a silicone dielectric elastomer and self-clearing carbon nanotube compliant electrodes. *RSC Advances*. **3**(7), 2272-2278 (2013)

[123] Yuan, W., Brochu, P., Ha, S.M., and Pei, Q., Dielectric oil coated single-walled carbon nanotube electrodes for stable, large-strain actuation with dielectric elastomers. *Sensors and Actuators A: Physical*. **155**(2), 278-284 (2009)

[124] Araromi, O.A., Gavrilovich, I., Shintake, J., Rosset, S., Richard, M., Gass, V., and Shea, H.R., Rollable Multisegment Dielectric Elastomer Minimum Energy Structures for a Deployable Microsatellite Gripper. *IEEE/ASME Transactions on Mechatronics*. **PP**(99), 1-9 (2014)

[125] Bekyarova, E., Itkis, M.E., Cabrera, N., Zhao, B., Yu, A., Gao, J., and Haddon, R.C., Electronic Properties of Single-Walled Carbon Nanotube Networks. *Journal of the American Chemical Society*. **127**(16), 5990-5995 (2005)

[126] Carpi, F., Migliore, A., Serra, G., and De Rossi, D., Helical dielectric elastomer actuators. *Smart Materials and Structures*. **14**(6), 1210-1216 (2005)

[127] Sau, K.P., Chaki, T.K., and Khastgir, D., Carbon fibre filled conductive composites based on nitrile rubber (NBR), ethylene propylene diene rubber (EPDM) and their blend. *Polymer*. **39**(25), 6461-6471 (1998)

[128] Pramanik, P.K., Khastgir, D., and Saha, T.N., Conductive nitrile rubber composite containing carbon fillers: Studies on mechanical properties and electrical conductivity. *Composites*. **23**(3), 183-191 (1992)

[129] Bigg, D.M. and Stutz, D.E., Plastic composites for electromagnetic interference shielding applications. *Polymer Composites*. **4**(1), 40-46 (1983)

[130] Park, S.I., Xiong, Y.J., Kim, R.H., Elvikis, P., Meitl, M., Kim, D.H., Wu, J., Yoon, J., Yu, C.J., Liu, Z.J., Huang, Y.G., Hwang, K., Ferreira, P., Li, X.L., Choquette, K., and Rogers, J.A., Printed Assemblies of Inorganic Light-Emitting Diodes for Deformable and Semitransparent Displays. *Science*. **325**(5943), 977-981 (2009)

[131] Aschwanden, M. and Stemmer, A., Low voltage, highly tunable diffraction grating based on dielectric elastomer actuators. *Proc. of SPIE*. **6524**(65241N), 1-9 (2007)

[132] Dubois, P., Rosset, S., Koster, S., Stauffer, J., Mikhaïlov, S., Dadras, M., Rooij, N., and Shea, H.R., Microactuators based on ion implanted dielectric electroactive polymer (EAP) membranes. *Sensors and Actuators A: Physical*. **130–131**(0), 147-154 (2006)

[133] Liu, C., Bar-Cohen, Y., and Leary, S.P. *Electrostatically stricted polymers (ESSP)*. 1999.

[134] Pei, Q. and Inganläs, O., Conjugated polymers and the bending cantilever method: Electrical muscles and smart devices. *Advanced Materials*. **4**(4), 277-278 (1992)

[135] Pei, Q., Inganläs, O., and Lundstrom, I., Bending bilayer strips built from polyaniline for artificial electrochemical muscles. *Smart Materials and Structures*. **2**(1), 1-6 (1993)

[136] Lam, T., Tran, H., Yuan, W., Yu, Z., Ha, S., Kaner, R., and Pei, Q., Polyaniline nanofibers as a novel electrode material for fault-tolerant dielectric elastomer actuators. *Proc. SPIE*. **6927**, 69270O (2008)

[137] Baughman, R.H., Conducting polymer artificial muscles. *Synthetic Metals*. **78**(3), 339-353 (1996)

[138] Madden, J., Cush, R., Kanigan, T., Brenan, C., and Hunter, I., Encapsulated polypyrrole actuators. *Synthetic Metals*. **105**(1), 61-64 (1999)

[139] Su, J., Zhang, Q., Wang, P.-C., MacDiarmid, A.G., and Wynne, K.J., Preparation and characterization of electrostrictive polyurethane films with conductive polymer electrodes. *Polymers for Advanced Technologies*. **9**(6), 317-321 (1998)

[140] Watanabe, H., Shirai, H., and Hirai, T., Wrinkled polypyrrole electrode for electroactive polymer actuators. *Journal of Applied Physics*. **92**(8), 4631-4637 (2002)

[141] Fournier, J., Boiteux, G., Seytre, G., and Marichy, G., Percolation network of polypyrrole in conducting polymer composites. *Synthetic Metals*. **84**(1–3), 839-840 (1997)

[142] Fournier, J.m., Boiteux, G., and Seytre, G., Fractal analysis of the percolation network in epoxy-polypyrrole composites. *Physical Review B*. **56**(9), 5207-5212 (1997)

[143] MacDiarmid, A.G., "Synthetic Metals": A Novel Role for Organic Polymers (Nobel Lecture). *Angewandte Chemie International Edition*. **40**(14), 2581-2590 (2001)

[144] Fu, Y., Weiss, R.A., Gan, P.P., and Bessette, M.D., Conductive elastomeric foams prepared by in situ vapor phase polymerization of pyrrole and copolymerization of pyrrole and N-methylpyrrole. *Polymer Engineering & Science*. **38**(5), 857-862 (1998)

[145] He, F., Omoto, M., Yamamoto, T., and Kise, H., Preparation of polypyrrole–polyurethane composite foam by vapor phase oxidative polymerization. *Journal of Applied Polymer Science*. **55**(2), 283-287 (1995)

[146] Shenoy, S.L., Cohen, D., Erkey, C., and Weiss, R.A., A Solvent-Free Process for Preparing Conductive Elastomers by an In Situ Polymerization of Pyrrole. *Industrial & Engineering Chemistry Research*. **41**(6), 1484-1488 (2002)

[147] Hecht, D.S., Hu, L.B., and Irvin, G., Emerging Transparent Electrodes Based on Thin Films of Carbon Nanotubes, Graphene, and Metallic Nanostructures. *Advanced Materials*. **23**(13), 1482-1513 (2011)

[148] Granqvist, C.G., Transparent conductors as solar energy materials: A panoramic review. *Solar Energy Materials and Solar Cells*. **91**(17), 1529-1598 (2007)

[149] De, S. and Coleman, J.N., The effects of percolation in nanostructured transparent conductors. *Mrs Bulletin*. **36**(10), 774-781 (2011)

[150] Gong, C., Liang, J., Hu, W., Niu, X., Ma, S., Hahn, H.T., and Pei, Q., A Healable, Semitransparent Silver Nanowire-Polymer Composite Conductor. *Advanced Materials*. **15**(30), 4186-4191 (2013)

[151] Lee, J.Y., Connor, S.T., Cui, Y., and Peumans, P., Solution-processed metal nanowire mesh transparent electrodes. *Nano Letters*. **8**(2), 689-692 (2008)

[152] Yu, Z.B., Zhang, Q.W., Li, L., Chen, Q., Niu, X.F., Liu, J., and Pei, Q.B., Highly Flexible Silver Nanowire Electrodes for Shape-Memory Polymer Light-Emitting Diodes. *Advanced Materials*. **23**(5), 664-668 (2011)

[153] Yu, Z.B., Li, L., Zhang, Q.W., Hu, W.L., and Pei, Q.B., Silver Nanowire-Polymer Composite Electrodes for Efficient Polymer Solar Cells. *Advanced Materials*. **23**(38), 4453-4457 (2011)

[154] Hu, W., Niu, X., Li, L., Yun, S., Yu, Z., and Pei, Q., Intrinsically stretchable transparent electrodes based on silver-nanowire–crosslinked-polyacrylate composites. *Nanotechnology*. **23**(34), 344002 (2012)

[155] Cho, J.W., Kim, J.W., Jung, Y.C., and Goo, N.S., Electroactive shape-memory polyurethane composites incorporating carbon nanotubes. *Macromolecular Rapid Communications*. **26**(5), 412-416 (2005)

[156] Viry, L., Mercader, C., Miaudet, P., Zakri, C., Derre, A., Kuhn, A., Maugey, M., and Poulin, P., Nanotube fibers for electromechanical and shape memory actuators. *Journal of Materials Chemistry*. **20**(17), 3487-3495 (2010)

[157] Leng, J., Lv, H., Liu, Y., and Du, S., Electroactivate shape-memory polymer filled with nanocarbon particles and short carbon fibers. *Applied Physics Letters*. **91**(14), - (2007)

[158] Leng, J., Lan, X., Liu, Y., and Du, S., Electroactive thermoset shape memory polymer nanocomposite filled with nanocarbon powders. *Smart Materials and Structures*. **18**(7), 074003 (2009)

[159] Leng, J.S., Huang, W.M., Lan, X., Liu, Y.J., and Du, S.Y., Significantly reducing electrical resistivity by forming conductive Ni chains in a polyurethane shape-memory polymer/carbon-black composite. *Applied Physics Letters*. **92**(20), - (2008)

[160] Yu, K., Zhang, Z., Liu, Y., and Leng, J., Carbon nanotube chains in a shape memory polymer/carbon black composite: To significantly reduce the electrical resistivity. *Applied Physics Letters*. **98**(7), - (2011)

[161] Kim, R.H., Bae, M.H., Kim, D.G., Cheng, H., Kim, B.H., Kim, D.H., Li, M., Wu, J., Du, F., Kim, H.S., Kim, S., Estrada, D., Hong, S.W., Huang, Y., Pop, E., and Rogers, J.A., Stretchable, transparent graphene interconnects for arrays of microscale inorganic light emitting diodes on rubber substrates. *Nano Letters*. **11**(9), 3881-3886 (2011)

[162] Wu, J.B., Agrawal, M., Becerril, H.A., Bao, Z.N., Liu, Z.F., Chen, Y.S., and Peumans, P., Organic Light-Emitting Diodes on Solution-Processed Graphene Transparent Electrodes. *Acs Nano*. **4**(1), 43-48 (2010)

[163] Kim, B.J., Mastro, M.A., Hite, J., Eddy, C.R., and Kim, J., Transparent conductive graphene electrode in GaN-based ultra-violet light emitting diodes. *Optics Express*. **18**(22), 23030-23034 (2010)

[164] Jo, G., Choe, M., Cho, C.Y., Kim, J.H., Park, W., Lee, S., Hong, W.K., Kim, T.W., Park, S.J., Hong, B.H., Kahng, Y.H., and Lee, T., Large-scale patterned multi-layer graphene films as transparent conducting electrodes for GaN light-emitting diodes. *Nanotechnology*. **21**(17), 175201 (2010)

[165] Chung, K., Lee, C.H., and Yi, G.C., Transferable GaN Layers Grown on ZnO-Coated Graphene Layers for Optoelectronic Devices. *Science*. **330**(6004), 655-657 (2010)

[166] Wang, X., Zhi, L., Tsao, N., Tomović, Ž., Li, J., and Müllen, K., Transparent Carbon Films as Electrodes in Organic Solar Cells. *Angewandte Chemie*. **120**(16), 3032-3034 (2008)

[167] Novoselov, K.S., Geim, A.K., Morozov, S., Jiang, D., Zhang, Y., Dubonos, S., Grigorieva, I., and Firsov, A., Electric field effect in atomically thin carbon films. *science*. **306**(5696), 666-669 (2004)

[168] Liang, X., Chang, A.S.P., Zhang, Y., Harteneck, B.D., Choo, H., Olynick, D.L., and Cabrini, S., Electrostatic Force Assisted Exfoliation of Prepatterned Few-Layer Graphenes into Device Sites. *Nano Letters*. **9**(1), 467-472 (2008)

[169] Balandin, A.A., Ghosh, S., Bao, W., Calizo, I., Teweldebrhan, D., Miao, F., and Lau, C.N., Superior Thermal Conductivity of Single-Layer Graphene. *Nano Letters*. **8**(3), 902-907 (2008)

[170] Gomez De Arco, L., Zhang, Y., Schlenker, C.W., Ryu, K., Thompson, M.E., and Zhou, C., Continuous, Highly Flexible, and Transparent Graphene Films by Chemical Vapor Deposition for Organic Photovoltaics. *ACS Nano*. **4**(5), 2865-2873 (2010)

[171] Nair, R.R., Blake, P., Grigorenko, A.N., Novoselov, K.S., Booth, T.J., Stauber, T., Peres, N.M.R., and Geim, A.K., Fine Structure Constant Defines Visual Transparency of Graphene. *Science*. **320**(5881), 1308 (2008)

[172] Rao, C.N.R., Subrahmanyam, K.S., Matte, H.S.S.R., Abdulhakeem, B., Govindaraj, A., Das, B., Kumar, P., Ghosh, A., and Late, D.J., A study of the synthetic methods and properties of graphenes. *Science and Technology of Advanced Materials*. **11**(5), 054502 (2010)

[173] De, S., King, P.J., Lotya, M., O'Neill, A., Doherty, E.M., Hernandez, Y., Duesberg, G.S., and Coleman, J.N., Flexible, Transparent, Conducting Films of Randomly Stacked Graphene from Surfactant-Stabilized, Oxide-Free Graphene Dispersions. *Small*. **6**(3), 458-464 (2010)

[174] Kim, K.S., Zhao, Y., Jang, H., Lee, S.Y., Kim, J.M., Ahn, J.H., Kim, P., Choi, J.Y., and Hong, B.H., Large-scale pattern growth of graphene films for stretchable transparent electrodes. *Nature*. **457**(7230), 706-710 (2009)

[175] Aguirre, C.M., Auvray, S., Pigeon, S., Izquierdo, R., Desjardins, P., and Martel, R., Carbon nanotube sheets as electrodes in organic light-emitting diodes. *Applied Physics Letters*. **88**(18), - (2006)

[176] Rowell, M.W., Topinka, M.A., McGehee, M.D., Prall, H.-J., Dennler, G., Sariciftci, N.S., Hu, L., and Gruner, G., Organic solar cells with carbon nanotube network electrodes. *Applied Physics Letters*. **88**(23), - (2006)

[177] Scardaci, V., Coull, R., and Coleman, J.N., Very thin transparent, conductive carbon nanotube films on flexible substrates. *Applied Physics Letters*. **97**(2), - (2010)

[178] Zhang, D., Ryu, K., Liu, X., Polikarpov, E., Ly, J., Tompson, M.E., and Zhou, C., Transparent, Conductive, and Flexible Carbon Nanotube Films and Their Application in Organic Light-Emitting Diodes. *Nano Letters*. **6**(9), 1880-1886 (2006)

[179] Yu, Z., Niu, X., Liu, Z., and Pei, Q., Intrinsically stretchable polymer light-emitting devices using carbon nanotube-polymer composite electrodes. *Advanced Materials*. **23**(34), 3989-3994 (2011)

[180] Ouyang, J.X., Qianfei, Chu, C., Yang, Y., Li, G., and Shinar, J., On the mechanism of conductivity enhancement in poly(3,4-ethylenedioxythiophene):poly(styrene sulfonate) film through solvent treatment. *Polymer*. **45**(25), 8443-8450 (2004)

[181] Aasmundtveit, K.E., Samuelsen, E.J., Pettersson, L.A.A., Inganäs, O., Johansson, T., and Feidenhans'l, R., Structure of thin films of poly(3,4-ethylenedioxythiophene). *Synthetic Metals*. **101**(1–3), 561-564 (1999)

[182] Crispin, X., Jakobsson, F.L.E., Crispin, A., Grim, P.C.M., Andersson, P., Volodin, A., van Haesendonck, C., Van der Auweraer, M., Salaneck, W.R., and Berggren, M., The origin of the high conductivity of poly(3,4-ethylenedioxythiophene)-poly(styrenesulfonate) (PEDOT- PSS) plastic electrodes. *Chemistry of Materials*. **18**(18), 4354-4360 (2006)

[183] Levermore, P.A., Chen, L., Wang, X., Das, R., and Bradley, D.C., Highly Conductive Poly(3,4-ethylenedioxythiophene) Films by Vapor Phase Polymerization for Application in Efficient Organic Light-Emitting Diodes. *Advanced Materials*. **19**(17), 2379-2385 (2007)

[184] Ha, Y.H., Nikolov, N., Pollack, S.K., Mastrangelo, J., Martin, B.D., and Shashidhar, R., Towards a Transparent, Highly Conductive Poly(3,4-ethylenedioxythiophene). *Advanced Functional Materials*. **14**(6), 615-622 (2004)

[185] Kim, D., Lu, N., Ma, R., Kim, Y., Kim, R., Wang, S., Wu, J., Won, S.M., Tao, H., Islam, A., Yu, K.J., Kim, T., Chowdhury, R., Ying, M., Xu, L., Li, M., Chung, H., Keum, H., McCormick, M., Liu, P., Zhang, Y., Omenetto, F.G., Huang, Y., Coleman, T., and Rogers, J.A., Epidermal Electronics. *Science*. **333**(6044), 838-843 (2011)

[186] Lee, Y.Y., Lee, J.H., Cho, J.Y., Kim, N.R., Nam, D.H., Choi, I.S., Nam, K.T., and Joo, Y.C., Stretching-Induced Growth of PEDOT-Rich Cores: A New Mechanism for Strain-Dependent Resistivity Change in PEDOT:PSS Films. *Advanced Functional Materials*. **23**(32), 4020-4027 (2013)

[187] Hansen, T.S., West, K., Hassager, O., and Larsen, N.B., Highly stretchable and conductive polymer material made from poly (3,4-ethylenedioxythiophene) and polyurethane elastomers. *Advanced Functional Materials*. **17**(16), 3069-3073 (2007)

[188] Kwon, S.J., Kim, T.Y., Lee, B.S., Lee, T.H., Kim, J.E., and Suh, K.S., Elastomeric conducting polymer nano-composites derived from ionic liquid polymer stabilized-poly(3,4-ethylenedioxythiophene). *Synthetic Metals*. **160**(9), 1092-1096 (2010)

[189] Lipomi, D.J., Lee, J.A., Vosgueritchian, M., Tee, B.C.K., Bolander, J.A., and Bao, Z., Electronic properties of transparent conductive films of PEDOT:PSS on stretchable substrates. *Chemistry of Materials*. **24**(2), 373-382 (2012)

[190] Vosgueritchian, M., Lipomi, D.J., and Bao, Z., Highly conductive and transparent PEDOT:PSS films with a fluorosurfactant for stretchable and flexible transparent electrodes. *Advanced Functional Materials*. **22**(2), 421-428 (2012)

[191] Shi, C., Yao, Y., Yang, Y., and Pei, Q., Regioregular Copolymers of 3-Alkoxythiophene and Their Photovoltaic Application. *Journal of the American Chemical Society*. **128**(27), 8980-8986 (2006)

[192] Gustafsson, G., Treacy, G.M., Cao, Y., Klavetter, F., Colaneri, N., and Heeger, A.J., The "plastic" led: A flexible light-emitting device using a polyaniline transparent electrode. *Synthetic Metals*. **57**(1), 4123-4127 (1993)

[193] Yang, Y. and Heeger, A.J., Polyaniline as a transparent electrode for polymer light-emitting diodes: Lower operating voltage and higher efficiency. *Applied Physics Letters*. **64**(10), 1245-1247 (1994)

[194] Ha, S.M., New Electroelastomers for High Performance Actuators. *Doctoral Dissertation, University of California, Los Angeles*. (2007)

[195] Shivapooja, P., Qang, Q., Orihuela, B., Rittschof, D., López, G.P., and Zhao, X., Bioinspired Surfaces with Dynamic Topography for Active Control of Biofouling *Advanced Materials*. **25**(10), 1430-1434 (2013)

[196] Keplinger, C., Sun, J., Foo, C.C., Rothemund, P., Whitesides, G.M., and Suo, Z., Stretchable, Transparent, Ionic Conductors. *Science*. **341**(6149), 984-987 (2013)

[197] Chen, B., Bai, Y., Xiang, F., Sun, J.-Y., Mei Chen, Y., Wang, H., Zhou, J., and Suo, Z., Stretchable and transparent hydrogels as soft conductors for dielectric elastomer actuators. *Journal of Polymer Science Part B: Polymer Physics*. **52**(16), 1055-1060 (2014)

[198] Sun, J.Y., Keplinger, C., Whitesides, G.M., and Suo, Z., Ionic skin. *Advanced Materials*. **26**(45), 7608-7614 (2014)

[199] Bai, Y., Chen, B., Xiang, F., Zhou, J., Wang, H., and Suo, Z., Transparent hydrogel with enhanced water retention capacity by introducing highly hydratable salt. *Applied Physics Letters*. **105**(15), 151903 (2014)

[200] 3M(TM), *VHB(TM) Tapes: Technical Data*. September, 2010, St. Paul, MN.: Industrial Adhesives and Tapes Division, 3M(TM) Center.

[201] Huang, J., Shian, S., Diebold, R.M., Suo, Z., and Clarke, D.R., The thickness and stretch dependence of the electrical breakdown strength of an acrylic dielectric elastomer. *Applied Physics Letters*. **101**(12), 122905 (2012)

[202] Benslimane, M., Gravesen, P., and Sommer-Larsen, P., Mechanical properties of dielectric elastomer actuators with smart metallic compliant electrodes. *Proc. SPIE*. **4695**, 150 (2002)

[203] Xiao, J., Carlson, A., Liu, Z.J., Huang, Y., Jiang, H., and Rogers, J.A., Stretchable and compressible thin films of stiff materials on compliant wavy substrates. *Applied Physics Letters*. **93**(1), - (2008)

[204] Bay, L., West, K., Sommer-Larsen, P., Skaarup, S., and Benslimane, M., A Conducting Polymer Artificial Muscle with 12% Linear Strain. *Advanced Materials*. **15**(3), 310-313 (2003)

[205] Jeong, J., Kim, S., Cho, J., and Hong, Y., Stable stretchable silver electrode directly deposited on wavy elastomeric substrate. *IEEE Electron Device Letters*. **30**(12), 1284-1286 (2009)

[206] Wu, H., Hu, L.B., Rowell, M.W., Kong, D.S., Cha, J.J., McDonough, J.R., Zhu, J., Yang, Y.A., McGehee, M.D., and Cui, Y., Electrospun Metal Nanofiber Webs as High-Performance Transparent Electrode. *Nano Letters*. **10**(10), 4242-4248 (2010)

[207] Hu, W., Wang, R., Lu, Y., and Pei, Q., An elastomeric transparent composite electrode based on copper nanowires and polyurethane. *Journal of Materials Chemistry C*. **2**(7), 1298-1305 (2014)

[208] Kim, T.A., Kim, H.S., Lee, S.S., and Park, M., Single-walled carbon nanotube/silicone rubber composites for compliant electrodes. *Carbon*. **50**(2), 444-449 (2012)

[209] Zhang, Y., Sheehan, C.J., Zhai, J., Zou, G., Luo, H., Xiong, J., Zhu, Y.T., and Jia, Q.X., Polymer-embedded carbon nanotube ribbons for stretchable conductors. *Advanced Materials*. **22**(28), 3027-3031 (2010)

[210] Kim, K.H., Vural, M., and Islam, M.F., Single-walled carbon nanotube aerogel-based elastic conductors. *Advanced Materials*. **23**(25), 2865-2869 (2011)

[211] Liu, K., Sun, Y., Liu, P., Lin, X., Fan, S., and Jiang, K., Cross-stacked superaligned carbon nanotube films for transparent and stretchable conductors. *Advanced Functional Materials*. **21**(14), 2721-2728 (2011)

[212] Kim, Y.H., Sachse, C., Machala, M.L., May, C., Muller-Meskamp, L., and Leo, K., Highly Conductive PEDOT:PSS Electrode with Optimized Solvent and Thermal Post-Treatment for ITO-Free Organic Solar Cells. *Advanced Functional Materials*. **21**(6), 1076-1081 (2011)

[213] Claus, R.O., Goff, R.M., Homer, M., Hill, A.B., and Lalli, J.H., Ultralow modulus electrically conducting electrode materials. *Proc. SPIE*. **6168**, 61681O (2006)

[214] Hill, A.B., Claus, R.O., Lalli, J.H., Mecham, J.B., Davis, B.A., Goff, R.M., and Subrahmanyan, S., Metal Rubber™ Electrodes for Active Polymer Devices. *Proc. SPIE*. **5759**, 247 (2005)

[215] Graz, I.M., Cotton, D.P.J., and Lacour, S.P., Extended cyclic uniaxial loading of stretchable gold thin-films on elastomeric substrates. *Applied Physics Letters*. **94**(7), 071902-071902 (2009)

[216] Robinson, A.P., Minev, I., Graz, I.M., and Lacour, S.P., Microstructured silicone substrate for printable and stretchable metallic films. *Langmuir*. **27**(8), 4279-4284 (2011)

[217] Seker, E., Reed, M., Utz, M., and Begley, M.R., Flexible and conductive bilayer membranes of nanoporous gold and silicone: Synthesis and characterization. *Applied Physics Letters*. **92**(15), 154101-154101 (2008)

[218] Jones, J., Lacour, S.P., Wagner, S., and Suo, Z., Stretchable wavy metal interconnects. *Journal of Vacuum Science and Technology A: Vacuum, Surfaces and Films*. **22**(4), 1723-1725 (2004)

[219] Wang, X., Hu, H., Shen, Y., Zhou, X., and Zheng, Z., Stretchable conductors with ultrahigh tensile strain and stable metallic conductance enabled by prestrained polyelectrolyte nanoplatforms. *Advanced Materials*. **23**(27), 3090-3094 (2011)

[220] Wang, C., Zheng, W., Yue, Z., Too, C.O., and Wallace, G.G., Buckled, stretchable polypyrrole electrodes for battery applications. *Advanced Materials*. **23**(31), 3580-3584 (2011)

[221] Leosson, K., Ingason, A.S., Agnarsson, B., Kossoy, A., Olafsson, S., and Gather, M.C., Ultra-thin gold films on transparent polymers. *Nanophotonics*. **2**(1), 3-11 (2013)

[222] Xu, F., Wang, X., Zhu, Y., and Zhu, Y., Wavy ribbons of carbon nanotubes for stretchable conductors. *Advanced Functional Materials*. **22**(6), 1279-1283 (2012)

[223] Hyun, D.C., Park, M., Park, C., Kim, B., Xia, Y., Hur, J.H., Kim, J.M., Park, J.J., and Jeong, U., Ordered Zigzag Stripes of Polymer Gel/Metal Nanoparticle Composites for Highly Stretchable Conductive Electrodes. *Advanced Materials*. **23**(26), 2946-2950 (2011)

[224] Chun, K.Y., Oh, Y., Rho, J., Ahn, J.H., Kim, Y.J., Choi, H.R., and Baik, S., Highly conductive, printable and stretchable composite films of carbon nanotubes and silver. *Nature Nanotechnology*. **5**(12), 853-857 (2010)

[225] Lee, P., Ham, J., Lee, J., Hong, S., Han, S., Suh, Y.D., Lee, S.E., Yeo, J., Lee, S.S., Lee, D., and Ko, S.H., Highly Stretchable or Transparent Conductor Fabrication by a Hierarchical Multiscale Hybrid Nanocomposite. *Advanced Functional Materials*. **24**(36), 5671-5678 (2014)

[226] Kovacs, G., Düring, L., Michel, S., and Terrasi, G., Stacked dielectric elastomer actuator for tensile force transmission. *Sensors and Actuators A: Physical*. **155**(2), 299-307 (2009)

[227] Kornbluh, R.D., Pelrine, R., Pei, Q., Heydt, R., Stanford, S., Oh, S., and Eckerle, J. *Electroelastomers: applications of dielectric elastomer transducers for actuation, generation, and smart structures*. 2002.

[228] Ha, S.M., Yuan, W., Pei, Q., Pelrine, R., and Stanford, S., Interpenetrating Polymer Networks for High-Performance Electroelastomer Artificial Muscles. *Advanced Materials*. **18**(7), 887-891 (2006)

[229] Ha, S.M., Yuan, W., Pei, Q., Pelrine, R., and Stanford, S., Interpenetrating networks of elastomers exhibiting 300% electrically-induced area strain. *Smart Materials and Structures*. **16**(2), S280 (2007)

[230] Yu, Z., Yuan, W., Brochu, P., Chen, B., Liu, Z., and Pei, Q., Large-strain, rigid-to-rigid deformation of bistable electroactive polymers. *Applied Physics Letters*. **95**(19), 192904 (2009)

[231] Yu, Z., Niu, X., Brochu, P., Yuan, W., Li, H., Chen, B., and Pei, Q. *Bistable electroactive polymers (BSEP): large-strain actuation of rigid polymers*. 2010.

[232] Kofod, G., Paajanen, M., and Bauer, S., Self-organized minimum-energy structures for dielectric elastomer actuators. *Applied Physics A*. **85**(2), 141-143 (2006)

[233] Carpi, F., Salaris, C., and De Rossi, D., Folded dielectric elastomer actuators. *Smart Materials and Structures*. **16**(2), S300 (2007)

[234] Murray, C., McCoul, D., Sollier, E., Ruggiero, T., Niu, X., Pei, Q., and Di Carlo, D., Electro-adaptive microfluidics for active tuning of channel geometry using polymer actuators. *Microfluidics and nanofluidics*. **14**(1-2), 345-358 (2013)

[235] McCoul, D., Murray, C., Di Carlo, D., and Pei, Q. *Dielectric elastomer actuators for active microfluidic control*. in *SPIE Smart Structures and Materials+ Nondestructive Evaluation and Health Monitoring*. 2013. International Society for Optics and Photonics.

[236] Maffli, L., Rosset, S., and Shea, H., Zipping dielectric elastomer actuators: characterization, design and modeling. *Smart Materials and Structures*. **22**(10), 104013 (2013)

[237] Maffli, L., Rosset, S., and Shea, H.R. *Mm-size bistable zipping dielectric elastomer actuators for integrated microfluidics*. in *SPIE Smart Structures and Materials+ Nondestructive Evaluation and Health Monitoring*. 2013. International Society for Optics and Photonics.

[238] Maffli, L., O'Brien, B., Rosset, S., and Shea, H. *Pump it up*. in *SPIE Smart Structures and Materials+ Nondestructive Evaluation and Health Monitoring*. 2012. International Society for Optics and Photonics.

[239] Gebbers, P., Grätzel, C., Maffli, L., Stamm, C., and Shea, H. *Zipping it up: DEAs independent of the elastomer's electric breakdown field*. in *SPIE Smart Structures and Materials+ Nondestructive Evaluation and Health Monitoring*. 2012. International Society for Optics and Photonics.

[240] Price, A.K. and Culbertson, C.T., Generation of Nonbiased Hydrodynamic Injections on Microfluidic Devices Using Integrated Dielectric Elastomer Actuators. *Analytical chemistry*. **81**(21), 8942-8948 (2009)

[241] Akbari, S. and Shea, H., Microfabrication and characterization of an array of dielectric elastomer actuators generating uniaxial strain to stretch individual cells. *Journal of Micromechanics and Microengineering*. **22**(4), 045020 (2012)

[242] Goulbourne, N., Frecker, M.I., Mockensturm, E.M., and Snyder, A.J. *Modeling of a dielectric elastomer diaphragm for a prosthetic blood pump*. 2003.

[243] Niu, X., Brochu, P., Salazar, B., and Pei, Q. *Refreshable tactile displays based on bistable electroactive polymer*. in *SPIE Smart Structures and Materials+ Nondestructive Evaluation and Health Monitoring*. 2011. International Society for Optics and Photonics.

[244] Niu, X., Brochu, P., Stoyanov, H., Yun, S.R., and Pei, Q. *Bistable electroactive polymer for refreshable Braille display with improved actuation stability*. in *SPIE Smart Structures and Materials+ Nondestructive Evaluation and Health Monitoring*. 2012. International Society for Optics and Photonics.

[245] Ren, Z., Niu, X., Chen, D., Hu, W., and Pei, Q. *A new bistable electroactive polymer for prolonged cycle lifetime of refreshable Braille displays*. in *SPIE Smart Structures and Materials+ Nondestructive Evaluation and Health Monitoring*. 2014. International Society for Optics and Photonics.

[246] Carpi, F., Frediani, G., and De Rossi, D., Electroactive elastomeric haptic displays of organ motility and tissue compliance for medical training and surgical force feedback. *Biomedical Engineering, IEEE Transactions on*. **56**(9), 2327-2330 (2009)

[247] Carpi, F., Mannini, A., and De Rossi, D., Dynamic splint-like hand orthosis for finger rehabilitation. *Biomedical applications of electroactive polymer actuators. John Wiley & Sons Ltd, New York*. 443-461 (2009)

[248] Herr, H.M. and Kornbluh, R.D. *New horizons for orthotic and prosthetic technology: artificial muscle for ambulation*. 2004.

[249] Kovacs, G., Lochmatter, P., and Wissler, M., An arm wrestling robot driven by dielectric elastomer actuators. *Smart Materials and Structures*. **16**(2), S306 (2007)

[250] Carpi, F. and De Rossi, D. *Contractile folded dielectric elastomer actuators*. in *The 14th International Symposium on: Smart Structures and Materials & Nondestructive Evaluation and Health Monitoring*. 2007. International Society for Optics and Photonics.

[251] Pei, Q., Pelrine, R., Rosenthal, M.A., Stanford, S., Prahlad, H., and Kornbluh, R.D. *Recent progress on electroelastomer artificial muscles and their application for biomimetic robots*. 2004.

[252] Jung, K., Koo, J.C., Lee, Y.K., and Choi, H.R., Artificial annelid robot driven by soft actuators. *Bioinspiration & biomimetics*. **2**(2), S42 (2007)

[253] Jordi, C., Michel, S., and Fink, E., Fish-like propulsion of an airship with planar membrane dielectric elastomer actuators. *Bioinspiration & biomimetics*. **5**(2), 026007 (2010)

[254] Chiang, C.-C., K. Lin, C.-C., and Ju, M.-S., An implantable capacitive pressure sensor for biomedical applications. *Sensors and Actuators A: Physical*. **134**(2), 382-388 (2007)

[255] Carpi, F., Bauer, S., and De Rossi, D., Stretching Dielectric Elastomer Performance. *Science*. **330**(6012), 1759-1761 (2010)

[256] Kornbluh, R.D., Pelrine, R., Prahlad, H., and Heydt, R. *Electroactive polymers: an emerging technology for MEMS*. 2004.

[257] Yu, Z., Hu, L., Liu, Z., Sun, M., Wang, M., Grüner, G., and Pei, Q., Fully bendable polymer light emitting devices with carbon nanotubes as cathode and anode. *Applied Physics Letters*. **95**(20), 203304 (2009)

[258] Kim, D.-H., Viventi, J., Amsden, J.J., Xiao, J., Vigeland, L., Kim, Y.-S., Blanco, J.A., Panilaitis, B., Frechette, E.S., Contreras, D., Kaplan, D.L., Omenetto, F.G., Huang, Y., Hwang, K.-C., Zakin, M.R., Litt, B., and Rogers, J.A., Dissolvable films of silk fibroin for ultrathin conformal bio-integrated electronics. *Nat Mater*. **9**(6), 511-517 (2010)

[259] Baca, A.J., Ahn, J.-H., Sun, Y., Meitl, M.A., Menard, E., Kim, H.-S., Choi, W.M., Kim, D.-H., Huang, Y., and Rogers, J.A., Semiconductor Wires and Ribbons for High- Performance Flexible Electronics. *Angewandte Chemie International Edition*. **47**(30), 5524-5542 (2008)

[260] Rogers, J.A., Someya, T., and Huang, Y., Materials and mechanics for stretchable electronics. *Science*. **327**(5973), 1603-1607 (2010)

[261] Ko, S.H., Pan, H., Grigoropoulos, C.P., Luscombe, C.K., Fréchet, J.M.J., and Poulikakos, D., All-inkjet-printed flexible electronics fabrication on a polymer substrate by low-temperature high-resolution selective laser sintering of metal nanoparticles. *Nanotechnology*. **18**(34), 345202 (2007)

[262] Ju, S., Facchetti, A., Xuan, Y., Liu, J., Ishikawa, F., Ye, P., Zhou, C., Marks, T.J., and Janes, D.B., Fabrication of fully transparent nanowire transistors for transparent and flexible electronics. *Nat Nano*. **2**(6), 378-384 (2007)

[263] McAlpine, M.C., Friedman, R.S., and Lieber, C.M., High-Performance Nanowire Electronics and Photonics and Nanoscale Patterning on Flexible Plastic Substrates. *Proceedings of the IEEE*. **93**(7), 1357-1363 (2005)

[264] Kim, I.-D., Choi, Y., and Tuller, H.L., Low-voltage ZnO thin-film transistors with high-K Bi 1.5 Zn 1.0 Nb 1.5 O 7 gate insulator for transparent and flexible electronics. *Applied Physics Letters*. **87**(4), 043509-043509-3 (2005)

[265] Sun, Y. and Rogers, J.A., Inorganic semiconductors for flexible electronics. *Advanced Materials*. **19**(15), 1897-1916 (2007)

[266] Huang, D., Liao, F., Molesa, S., Redinger, D., and Subramanian, V., Plastic-compatible low resistance printable gold nanoparticle conductors for flexible electronics. *Journal of the electrochemical society*. **150**(7), G412-G417 (2003)

[267] Majewski, L., Grell, M., Ogier, S., and Veres, J., A novel gate insulator for flexible electronics. *Organic Electronics*. **4**(1), 27-32 (2003)

[268] Jain, K., Klosner, M., Zemel, M., and Raghunandan, S., Flexible electronics and displays: high-resolution, roll-to-roll, projection lithography and photoablation processing technologies for high-throughput production. *Proceedings of the IEEE*. **93**(8), 1500-1510 (2005)

[269] Cao, Q., Zhu, Z.-T., Lemaitre, M.G., Xia, M.-G., Shim, M., and Rogers, J.A., Transparent flexible organic thin-film transistors that use printed single-walled carbon nanotube electrodes. *Applied physics letters*. **88**(11), 113511 (2006)

[270] Hu, L., Kim, H.S., Lee, J.-Y., Peumans, P., and Cui, Y., Scalable coating and properties of transparent, flexible, silver nanowire electrodes. *ACS nano*. **4**(5), 2955-2963 (2010)

[271] Wang, Q., Zhang, L., and Zhao, X., Creasing to cratering instability in polymers under ultrahigh electric fields. *Physical review letters*. **106**(11), 118301 (2011)

[272] Dobretsov, S., Dahms, H.-U., and Qian, P.-Y., Inhibition of biofouling by marine microorganisms and their metabolites. *Biofouling*. **22**(1), 43-54 (2006)

[273] Akbari, S. and Shea, H.R., An array of 100μm× 100μm dielectric elastomer actuators with 80% strain for tissue engineering applications. *Sensors and Actuators A: Physical*. **186**, 236-241 (2012)

[274] Gossett, D.R., Weaver, W.M., Mach, A.J., Hur, S.C., Tse, H.T.K., Lee, W., Amini, H., and Di Carlo, D., Label-free cell separation and sorting in microfluidic systems. *Analytical and bioanalytical chemistry*. **397**(8), 3249-3267 (2010)

[275] Hsu, C.-H., Di Carlo, D., Chen, C., Irimia, D., and Toner, M., Microvortex for focusing, guiding and sorting of particles. *Lab on a Chip*. **8**(12), 2128-2134 (2008)

[276] Heim, J.R., Pelrine, R.E., Kornbluh, R.D., Eckerle, J.S., Rosenthal, M., and Heydt, R.P., *Electroactive polymer devices for controlling fluid flow*. 2008, U.S. Patent No. 7,320,457.

[277] Kovacs, G., Düring, L., Michel, S., and Terrasi, G., Field Induced Deformation of Active Structures Based on Dielectric Elastomers. (2008)

[278] Prisco, G.M. and Au, S., *Curved cannula surgical system control*. 2009, Google Patents.

[279] Wingert, A., Lichter, M.D., Dubowsky, S., and Hafez, M. *Hyper-redundant robot manipulators actuated by optimized binary-dielectric polymers*. in *SPIE's 9th Annual International Symposium on Smart Structures and Materials*. 2002. International Society for Optics and Photonics.

[280] Basdogan, C., De, S., Kim, J., Muniyandi, M., Kim, H., and Srinivasan, M.A., Haptics in minimally invasive surgical simulation and training. *Computer Graphics and Applications, IEEE*. **24**(2), 56-64 (2004)

[281] Kornbluh, R.D. and Pelrine, R.E., *Variable stiffness electroactive polymer systems*. 2005, Google Patents.

[282] Carpi, F., De Rossi, D., Kornbluh, R., Pelrine, R.E., and Sommer-Larsen, P., *Dielectric elastomers as electromechanical transducers: Fundamentals, materials, devices, models and applications of an emerging electroactive polymer technology*. 2011: Elsevier.

[283] Lipomi, D.J., Vosgueritchian, M., Tee, B.C.K., Hellstrom, S.L., Lee, J.A., Fox, C.H., and Bao, Z., Skin-like pressure and strain sensors based on transparent elastic films of carbon nanotubes. *Nature Nanotechnology*. **6**(12), 788-792 (2011)

[284] *Body Mapping: Podiatry*. March 19, 2012]; Available from: http://www.sensorprod.com/dynamic/footing.php.

[285] Ashley, S., Artificial Muscles. *Scientific American*. 53-59 (October 2003)

[286] Price, A.K., Anderson, K.M., and Culbertson, C.T., Demonstration of an integrated electroactive polymer actuator on a microfluidic electrophoresis device. *Lab on a Chip*. **9**(14), 2076-2084 (2009)

[287] Loverich, J.J., Kanno, I., and Kotera, H., Concepts for a new class of all-polymer micropumps. *Lab on a Chip*. **6**(9), 1147-1154 (2006)

[288] Grover, W.H., Skelley, A.M., Liu, C.N., Lagally, E.T., and Mathies, R.A., Monolithic membrane valves and diaphragm pumps for practical large-scale integration into glass microfluidic devices. *Sensors and Actuators B: Chemical*. **89**(3), 315-323 (2003)

[289] Unger, M.A., Chou, H.-P., Thorsen, T., Scherer, A., and Quake, S.R., Monolithic Microfabricated Valves and Pumps by Multilayer Soft Lithography. *Science*. **288**(5463), 113-116 (2000)

[290] Willis, P.A., Hunt, B.D., White, V.E., Lee, M.C., Ikeda, M., Bae, S., Pelletier, M.J., and Grunthaner, F.J., Monolithic Teflon® membrane valves and pumps for harsh chemical and low-temperature use. *Lab on a Chip*. **7**(11), 1469-1474 (2007)

[291] Vyawahare, S., Sitaula, S., Martin, S., Adalian, D., and Scherer, A., Electronic control of elastomeric microfluidic circuits with shape memory actuators. *Lab on a Chip*. **8**(9), 1530-1535 (2008)

[292] Graf, N.J. and Bowser, M.T., A soft-polymer piezoelectric bimorph cantilever-actuated peristaltic micropump. *Lab on a Chip*. **8**(10), 1664-1670 (2008)

[293] Pan, T., McDonald, S.J., Kai, E.M., and Ziaie, B., A magnetically driven PDMS micropump with ball check-valves. *Journal of Micromechanics and Microengineering*. **15**(5), 1021 (2005)

[294] Sollier, E., Murray, C., Maoddi, P., and Di Carlo, D., Rapid prototyping polymers for microfluidic devices and high pressure injections. *Lab on a Chip*. **11**(22), 3752-3765 (2011)

[295] VanDelinder, V. and Groisman, A., Separation of Plasma from Whole Human Blood in a Continuous Cross-Flow in a Molded Microfluidic Device. *Analytical Chemistry*. **78**(11), 3765-3771 (2006)

[296] VanDelinder, V. and Groisman, A., Perfusion in Microfluidic Cross-Flow: Separation of White Blood Cells from Whole Blood and Exchange of Medium in a Continuous Flow. *Analytical Chemistry*. **79**(5), 2023-2030 (2007)

[297] MacDonald, J.C., Biyikli, K., Zugic, B., Ebersole, G., and Allor, J., Nucleation and growth of polymorphs of barbital on chemically modified surfaces in microfluidic channels. *MRS Online Proceedings Library*. **901**, null-null (2005)

[298] Bélanger, M.C. and Marois, Y., Hemocompatibility, biocompatibility, inflammatory and in vivo studies of primary reference materials low-density polyethylene and polydimethylsiloxane: A review. *Journal of Biomedical Materials Research*. **58**(5), 467-477 (2001)

[299] Vaughan, T.E. and Weaver, J.C., Molecular change signal-to-noise criteria for interpreting experiments involving exposure of biological systems to weakly interacting electromagnetic fields. *Bioelectromagnetics*. **26**(4), 305-322 (2005)

[300] Higgs, B., Shorter, R.G., and Ellis, F.H., A study of the anatomy of the human esophagus with special reference to the gastroesophageal sphincter. *Journal of Surgical Research*. **5**(11), 503-507 (1965)

[301] Pert, J.H., Davidson, M., Almy, T.P., and Sleisenger, M.H., Esophageal catheterization studies. I. The mechanism of swallowing in normal subjects with particular reference to the vestibule (esophago-gastric sphincter). *Journal of Clinical Investigation*. **38**(2), 397 (1959)

[302] Pfitzner, J., Poiseuille and his law. *Anaesthesia*. **31**(2), 273-275 (1976)

[303] Sandler, R.S., Everhart, J.E., Donowitz, M., Adams, E., Cronin, K., Goodman, C., Gemmen, E., Shah, S., Avdic, A., and Rubin, R., The burden of selected digestive diseases in the United States. *Gastroenterology*. **122**(5), 1500-1511 (2002)

[304] Fennerty, M.B., The continuum of GERD complications. *Cleveland Clinic journal of medicine*. **70**(Suppl 5), S33 (2003)

[305] Starling, J.R., Hamilton, J.W., Reichelderfer, M., Yamato, D.T., Pellet, J.R., and Belzer, F.O., Assessment of the Angelchik prosthesis for treatment of symptomatic esophageal reflux. *World journal of surgery*. **11**(3), 350-354 (1987)

[306] Starling, J.R., Reichelderfer, M.O., Pellett, J.R., and Belzer, F.O., Treatment of symptomatic gastroesophageal reflux using the Angelchik prosthesis. *Annals of surgery*. **195**(6), 686 (1982)

[307] Fennerty, B.M. and Gold, B.D. *Heartburn, Gastroesophageal Reflux (GER), and Gastroesophageal Reflux Disease (GERD).* [cited 2007; NIH Publication No. 07-0882.:[Available from: http://digestive.niddk.nih.gov/ddiseases/pubs/gerd.

[308] Weaver, R. and Temple, J., The Angelchik prosthesis for gastro-oesophageal reflux: symptomatic and objective assessment. *Annals of the Royal College of Surgeons of England*. **67**(5), 299 (1985)

[309] Little, A.G., Mechanisms of action of antireflux surgery: theory and fact. *World journal of surgery*. **16**(2), 320-325 (1992)

[310] Angelchik, J.P., *Method for prevention of gastro esophageal reflux*. 1981, Google Patents.

[311] Kozarek, R.A., Phelps, J.E., Sanowski, R.A., Grobe, J.L., and Fredell, C.H., An anti-reflux prosthesis in the treatment of gastroesophageal reflux. *Annals of internal medicine*. **98**(3), 310-315 (1983)

[312] Kozarek, R., Brayko, C., Sanowski, R., Grobe, J., Phelps, J., Sarles Jr, H., and Fredell, C., Evaluation of Angelchik antireflux prosthesis. *Digestive diseases and sciences*. **30**(8), 723-732 (1985)

[313] Lipham, J.C., DeMeester, T.R., Ganz, R.A., Bonavina, L., Saino, G., Dunn, D.H., Fockens, P., and Bemelman, W., The LINX® reflux management system: confirmed safety and efficacy now at 4 years. *Surgical endoscopy*. **26**(10), 2944-2949 (2012)

[314] Forsell, P., *Controlled heartburn and reflux disease treatment*. 2002, Google Patents.

[315] Forsell, P., *Mechanical heartburn and reflux treatment*. 2002, Google Patents.

[316] *LINX is aimed at permanently curing reflux disease.* May 22, 2015]; Available from: http://southwestreflux.co.uk/reflux-disease/linx-surgery/.

[317] *Magnetic game changer device used to treat acid reflux patients.* May 22, 2015]; Available from: http://www.jsonline.com/news/health/magnetic-game-changer-device-used-to-treat-acid-reflux-patients-b99255482z1-257086871.html.

[318] Xia, F., Mao, J., Ding, J., and Yang, H., Observation of normal appearance and wall thickness of esophagus on CT images. *European journal of radiology*. **72**(3), 406-411 (2009)

[319] Bonavina, L., DeMeester, T., Fockens, P., Dunn, D., Saino, G., Bona, D., Lipham, J., Bemelman, W., and Ganz, R.A., Laparoscopic sphincter augmentation device eliminates reflux symptoms and normalizes esophageal acid exposure: one-and 2-year results of a feasibility trial. *Annals of surgery*. **252**(5), 857-862 (2010)

[320] Pandolfino, J.E., Ghosh, S.K., Zhang, Q., Jarosz, A., Shah, N., and Kahrilas, P.J., *Quantifying EGJ morphology and relaxation with high-resolution manometry: a study of 75 asymptomatic volunteers*. Vol. 290. 2006. G1033-G1040.

[321] Høeg, H., Slatkin, A.B., Burdick, J.W., and Grundfest, W.S. *Biomechanical modeling of the small intestine as required for the design and operation of a robotic endoscope*. in *Robotics and Automation, 2000. Proceedings. ICRA'00. IEEE International Conference on*. 2000. IEEE.

[322] 3M. *Industrial Adhesives & Tapes*. [cited 2015; Available from: http://solutions.3m.com/wps/portal/3M/en_US/Adhesives/Tapes/Brands/3M-VHB-Tape/.

[323] Bureau., U.C. *Statistical Abstract of the United States*. . September 30, 2011 Retrieved Sept. 5, 2012]; Available from: http://www.census.gov/compendia/statab/cats/health_nutrition/food_consumption_and_nutrition.html.

[324] Hughes, T. and Wiles, C., Clinical measurement of swallowing in health and in neurogenic dysphagia. *Qjm*. **89**(2), 109-116 (1996)

[325] Suvarna, S., Start, R., and Tayler, D., A prospective audit of pacemaker function, implant lifetime, and cause of death in the patient. *Journal of clinical pathology*. **52**(9), 677-680 (1999)

[326] Schuchert, A. and KUCK, K.H., Influence of internal current and pacing current on pacemaker longevity. *Pacing and Clinical Electrophysiology*. **17**(1), 13-16 (1994)

[327] Kim, S., Byun, J., Choi, S., Kim, D., Kim, T., Chung, S., and Hong, Y., Negatively Strain-Dependent Electrical Resistance of Magnetically Arranged Nickel Composites: Application to Highly Stretchable Electrodes and Stretchable Lighting Devices. *Advanced Materials*. **26**(19), 3094-3099 (2014)

[328] Tee, B.C.K., Wang, C., Allen, R., and Bao, Z., An electrically and mechanically self-healing composite with pressure- and flexion-sensitive properties for electronic skin applications. *Nat Nano*. **7**(12), 825-832 (2012)

[329] Zrnić, D.S. and Swatik, D.S., On the resistivity and surface tension of the eutectic alloy of gallium and indium. *Journal of the Less Common Metals* **18**(1), 67-68 (1969)

[330] Burdakin, A., Khlevnoy, B., Samoylov, M., Sapritsky, V., Ogarev, S., Panfilov, A., Bingham, G., Privalsky, V., Tansock, J., and Humpherys, T., Melting points of gallium and of binary eutectics with gallium realized in small cells. *Metrologia*. **45**(1), 75 (2008)

[331] Mavoori, H. and Jin, S., New, creep-resistant, low melting point solders with ultrafine oxide dispersions. *Journal of Electronic Materials*. **27**(11), 1216-1222 (1998)

[332] Siegel, A.C., Bruzewicz, D.A., Weibel, D.B., and Whitesides, G.M., Microsolidics: Fabrication of Three-Dimensional Metallic Microstructures in Poly(dimethylsiloxane). *Advanced Materials*. **19**(5), 727-733 (2007)

[333] Dickey, M.D., Chiechi, R.C., Larsen, R.J., Weiss, E.A., Weitz, D.A., and Whitesides, G.M., Eutectic Gallium-Indium (EGaIn): A Liquid Metal Alloy for the Formation of Stable Structures in Microchannels at Room Temperature. *Advanced Functional Materials* **18**(7), 1097-1104 (2008)

[334] Chiechi, R.C., Weiss, E.A., Dickey, M.D., and Whitesides, G.M., Eutectic Gallium–Indium (EGaIn): A Moldable Liquid Metal for Electrical Characterization of Self-Assembled Monolayers. *Angewandte Chemie* **120**(1), 148-150 (2008)

[335] Kim, H.J., Son, C., and Ziaie, B., A multiaxial stretchable interconnect using liquid-alloy-filled elastomeric microchannels. *Applied Physics Letters*. **92**(1), 011904-011904 (2008)

[336] Stoyanov, H., Kofod, G., and Gerhard, R., A Co-Axial Dielectric Elastomer Actuator. *Advances in Science and Technology*. **61**, 81-84 (2008)

[337] Kofod, G., Stoyanov, H., and Gerhard, R., Multilayer coaxial fiber dielectric elastomers for actuation and sensing. *Applied Physics A*. **102**(3), 577-581 (2011)

[338] Schueler, R., Petermann, J., Schulte, K., and Wentzel, H.-P., Agglomeration and electrical percolation behavior of carbon black dispersed in epoxy resin. *Journal of Applied Polymer Science*. **63**(13), 1741-1746 (1997)

[339] Zallen, R., *The Percolation Model*, in *The Physics of Amorphous Solids*. 1983, Wiley-VCH Verlag GmbH. p. 135-204.

[340] Bauhofer, W. and Kovacs, J., A review and analysis of electrical percolation in carbon nanotube polymer composites. *Composites Science and Technology*. **69**(10), 1486-1498 (2009)

[341] Winey, K.I., Kashiwagi, T., and Mu, M., Improving electrical conductivity and thermal properties of polymers by the addition of carbon nanotubes as fillers. *Mrs Bulletin*. **32**(04), 348-353 (2007)

[342] Kujawski, M., Pearse, J.D., and Smela, E., Elastomers filled with exfoliated graphite as compliant electrodes. *Carbon*. **48**(9), 2409-2417 (2010)

[343] Jiseok, K. and Woo Soo, K., Stretching Silver: Printed Metallic Nano Inks in Stretchable Conductor Applications. *Nanotechnology Magazine, IEEE*. **8**(4), 6-13 (2014)

[344] Lalli, J.H., Hill, A., Hannah, S., Bortner, M., Subrahmanyan, S., Mecham, J., Davis, B., and Claus, R.O., Self-Assembled Nanostructured Conducting Elastomeric Electrodes. *Proc. SPIE*. **5385**, 290-293 (2004)

[345] Yamada, T., Hayamizu, Y., Yamamoto, Y., Yomogida, Y., Izadi-Najafabadi, A., Futaba, D.N., and Hata, K., A stretchable carbon nanotube strain sensor for human-motion detection. *Nat Nanotechnol*. **6**(5), 296-301 (2011)

[346] Feng, C., Liu, K., Wu, J.S., Liu, L., Cheng, J.S., Zhang, Y., Sun, Y., Li, Q., Fan, S., and Jiang, K., Flexible, stretchable, transparent conducting films made from superaligned carbon nanotubes. *Advanced Functional Materials*. **20**(6), 885-891 (2010)

[347] Graudejus, O., Yu, Z., Jones, J., Morrison, B., and Wagner, S., Characterization of an Elastically Stretchable Microelectrode Array and Its Application to Neural Field Potential Recordings. *Journal of the Electrochemical Society*. **156**(6), 85-94 (2009)

[348] Graudejus, O., Jia, Z., Li, T., and Wagner, S., Size-dependent rupture strain of elastically stretchable metal conductors. *Scripta Materialia*. **66**(11), 919-922 (2012)

[349] Lacour, S.P., Chan, D., Wagner, S., Li, T., and Suo, Z.G., Mechanisms of reversible stretchability of thin metal films on elastomeric substrates. *Applied Physics Letters*. **88**(20), 204103-204103 (2006)

[350] Li, T. and Suo, Z., Deformability of thin metal films on elastomer substrates. *International journal of solids and structures* **43**(7), 2351-2363 (2006)

[351] Lacour, S.P., Jones, J., Wagner, S., Li, T., and Suo, Z., Stretchable Interconnects for Elastic Electronic Surfaces. *Proceedings of the IEEE*. **93**(8), 1459-1466 (2005)

[352] Douville, N.J., Li, Z., Takayama, S., and Thouless, M.D., Fracture of metal coated elastomers. *Soft Matter*. **7**(14), 6493-6500 (2011)

[353] Lu, N.S., Wang, X., Suo, Z.G., and Vlassak, J., Failure by simultaneous grain growth, strain localization, and interface debonding in metal films on polymer substrates. *Journal of Materials Research*. **24**(2), 379-385 (2009)

[354] Lu, N.S., Wang, X., Suo, Z.G., and Vlassak, J., Metal films on polymer substrates stretched beyond 50%. *Applied Physics Letters*. **91**(22) (2007)

[355] Li, T., Huang, Z.Y., Xi, Z.C., Lacour, S.P., Wagner, S., and Suo, Z., Delocalizing strain in a thin metal film on a polymer substrate. *Mechanics of Materials*. **37**(2–3), 261-273 (2005)

[356] Lu, N., Suo, Z., and Vlassak, J.J., The effect of film thickness on the failure strain of polymer-supported metal films. *Acta Materialia*. **58**(5), 1679-1687 (2010)

[357] Li, T., Huang, Z., Suo, Z., Lacour, S.P., and Wagner, S., Stretchability of thin metal films on elastomer substrates. *Applied Physics Letters*. **85**(16), 3435-3437 (2004)

[358] Sim, G.D., Won, S., Jin, C.Y., Park, I., Lee, S.B., and Vlassak, J.J., Improving the stretchability of as-deposited Ag coatings on poly-ethylene-terephthalate substrates through use of an acrylic primer. *Journal of Applied Physics*. **109**(7), 073511-073511 (2011)

[359] Chou, N., Yoo, S., and Kim, S., A Largely Deformable Surface Type Neural Electrode Array Based on PDMS. *Neural Systems and Rehabilitation Engineering*. **21**(4), 544 - 553 (2012)

[360] Wagner, S., Lacour, S.P., Jones, J., Hsu, P.H.I., Sturm, J.C., Li, T., and Suo, Z., Electronic skin: architecture and components. . *Low-dimensional Systems and Nanostructures* **25**(2), 326-334 (2004)

[361] Lacour, S.P., Wagner, S., Huang, Z., and Suo, Z., Stretchable gold conductors on elastomeric substrates. *Applied Physics Letters*. **82**(15), 2404-2406 (2003)

[362] Bowden, N., Brittain, S., Evans, A.G., Hutchinson, J.W., and Whitesides, G.M., Spontaneous formation of ordered structures in thin films of metals supported on an elastomeric polymer. *Nature*. **393**(6681), 146-149 (1998)

[363] Bowden, N., Huck, W.T.S., Paul, K.E., and Whitesides, G.M., The controlled formation of ordered, sinusoidal structures by plasma oxidation of an elastomeric polymer. *Applied Physics Letters*. **75**(17), 2557-2559 (1999)

[364] Lacour, S.P., Jones, J., Suo, Z., and Wagner, S., Design and performance of thin metal film interconnects for skin-like electronic circuits. *IEEE Electron Device Letters*. **25**(4), 179-181 (2004)

[365] Yu, C., Masarapu, C., Rong, J., Wei, B., and Jiang, H., Stretchable supercapacitors based on buckled single-walled carbon nanotube macrofilms. *Advanced Materials*. **21**(47), 4793-4797 (2009)

[366] Adrega, T. and Lacour, S.P., Stretchable gold conductors embedded in PDMS and patterned by photolithography: fabrication and electromechanical characterization. *Journal of Micromechanics and Microengineering*. **20**(5), 055025 (2010)

[367] Ghosh, D., Martinez, L., Giurgola, S., Vergani, P., and Pruneri, V., Widely transparent electrodes based on ultrathin metals. *Optics letters*. **34**(3), 325-327 (2009)

[368] Hu, L., Wu, H., and Cui, Y., Metal nanogrids, nanowires, and nanofibers for transparent electrodes. *MRS bulletin*. **36**(10), 760-765 (2011)

[369] O'Connor, B., Haughn, C., An, K.-H., Pipe, K.P., and Shtein, M., Transparent and conductive electrodes based on unpatterned, thin metal films. *Applied Physics Letters*. **93**(22), - (2008)

[370] Khang, D.-Y., Xiao, J., Kocabas, C., MacLaren, S., Banks, T., Jiang, H., Huang, Y.Y., and Rogers, J.A., Molecular Scale Buckling Mechanics in Individual Aligned Single-Wall Carbon Nanotubes on Elastomeric Substrates. *Nano Letters*. **8**(1), 124-130 (2007)

[371] Zhu, Y. and Xu, F., Buckling of aligned carbon nanotubes as stretchable conductors: A new manufacturing strategy. *Advanced Materials*. **24**(8), 1073-1077 (2012)

[372] Lamé, G. and Clapeyron, B., Mémoire sur l'équilibre intérieur des corps solides homogènes. *Journal für die reine und angewandte Mathematik*. **7**, 145-169 (1831)